MODELING CHALLENGES IN COMPUTATIONAL ELECTROMAGNETICS: LARGE PLANAR MULTILAYERED STRUCTURES AND FINITE-THICKNESS IRISES

THÈSE N^{O} 3212 (2005)

PRÉSENTÉE À LA FACULTÉ SCIENCES ET TECHNIQUES DE L'INGÉNIEUR

Institut de transmissions, ondes et photonique

SECTION DE GÉNIE ÉLECTRIQUE ET ÉLECTRONIQUE

ÉCOLE POLYTECHNIQUE FÉDÉRALE DE LAUSANNE

POUR L'OBTENTION DU GRADE DE DOCTEUR ÈS SCIENCES

PAR

Ivica STEVANOVIC

Dipl.-Ing. EE, Université de Belgrade, Serbie et Monténégro
et de nationalité serbe et monténégrine

acceptée sur proposition du jury:

Prof. J. R. Mosig, directeur de thèse
Prof. A. Djordjevic, rapporteur
Prof. E. Kuester, rapporteur
Prof. J. Rappaz, rapporteur

Lausanne, EPFL
2005

I hear and I forget.
I see and I remember.
I do and I understand.

(Confucius)

Abstract

Printed multilayered media with metallizations embedded between dielectric layers are one of the most successful technologies for manufacturing planar structures with a good performance-to-price ratio. These structures range from PC board circuits, through cavity backed antennas and antenna arrays used in satellite communications, to waveguide filters. The approach most commonly used to model and analyze the aforementioned structures is the Integral Equation (IE) technique solved with Method of Moments (MoM). Applying IE-MoM with subsectional basis functions to electromagnetically large structures is demanding in terms of both computer memory allocation and time needed to solve the problem. Computationally efficient techniques are thus needed to accelerate the IE-MoM procedures and allow modeling of large circuits and antennas on standard desktop PCs. Subdomain Multilevel Approach (SMA) with Macro-Basis Functions (MBF) is one of the acceleration techniques, developed in our laboratory. Its application to modeling large antenna arrays has already proven to be very efficient. However, this technique can be improved, especially when MoM matrix filling time is concerned. This thesis proposes an improvement of the SMA using equivalent moments in computing the interactions between macro-basis functions. It shows that, without significant loss of accuracy, we obtain a two-fold gain in computational time for structures with the number of unknowns of the order 10^4.

In structures operating at higher frequencies (thin films in millimeter and submillimeter wave bands) or with self supporting metallic plates, the thickness of metallic screens must be taken into account. Multilayered structures with apertures (holes) in thick conducting screens can be accurately modeled using the equivalence theorem and magnetic currents introduced at both aperture interfaces. This approach, however, doubles the number of unknowns as compared to that one of the zero-thickness case. Moreover, the thick aperture problem asks for the computation of cavity Green's functions, which is a difficult and time-consuming task for apertures of arbitrary cross-sections. This thesis addresses the problem of scattering by apertures in thick conducting screens by introducing an approximate and computationally efficient formulation. This formulation consists in treating the thick aperture as an infinitely thin one and in using the correction term in integral equation kernel that accounts for the screen thickness. The number of unknowns remains the same as in the zero-thickness screens and evaluation of complicated cavity Green's functions is obviated, which yields computationally efficient routines. The technique is successfully applied to self-supporting aperture antennas and thick irises within multilayered rectangular waveguides giving good results for apertures whose thickness is smaller than their lateral dimensions.

Résumé

Les milieux stratifiés planaires avec des métallisations entre les couches diélectriques représentent l'une des technologies les plus utilisées dans la fabrication des structures planaires avec un bon rapport performance/prix. Ces structures s'étendent des circuits imprimés aux filtres en guide d'ondes, en passant par les antennes à cavité et les réseaux d'antennes utilisés dans les communications par satellite. La technique de l'équation intégrale (IE) résolue avec la méthode des moments (MoM) est l'approche généralement la plus employée pour modéliser et analyser les structures susmentionnées. L'application de l'IE-MoM avec des fonctions de base subsectionnelles aux structures qui sont grandes du point de vue électromagnétique est exigeante en espace mémoire et en temps d'exécution. Des techniques efficaces sont donc nécessaires pour accélérer les procédures IE-MoM permettant de modéliser les circuits et antennes à grande échelle avec des ordinateurs standards. L'une des techniques d'accélération, développée au sein de notre laboratoire, est le "Subdomain Multilevel Approach" (SMA) avec les macro-fonctions de base (MBF). Cette technique s'est montrée très efficace dans la modélisation des réseaux d'antennes à grande échelle. Cependant, la technique peut être améliorée, particulièrement le paramètre temps, nécessaire pour remplir la matrice des moments est concerné. Cette thèse propose une amélioration de la technique SMA en utilisant les moments équivalents pour calculer les interactions entre les macro-fonctions de base. Elle permet, sans perte significative de précision, d'obtenir des simulations qui sont au moins deux fois plus rapides avec un nombre d'inconnues de l'ordre 10^4.

Dans les structures fonctionnant aux fréquences plus élevées, l'épaisseur des écrans métalliques doit être prise en considération. Des structures en milieux stratifiés avec des ouvertures (trous) dans les écrans métalliques épais peuvent être modélisées avec précision en utilisant le théorème d'équivalence et en introduisant les courants magnétiques sur les deux interfaces de l'ouverture. Cette approche double, cependant, le nombre d'inconnues par rapport au cas de l'épaisseur-nulle. Par ailleurs, le problème d'ouverture épaisse demande le calcul des fonctions de Green pour les cavités, ce qui devient une tâche difficile quant aux ouvertures de formes transversales arbitraires. Cette thèse résoud le problème de la dispersion par des ouvertures des écrans métalliques épais en présentant une formulation approximative et efficace. Cette formulation consiste à traiter l'ouverture en la considérant comme infiniment mince et en appliquant le terme de correction, qui prend en compte l'épaisseur de l'écran, au noyau de l'équation intégrale. Le nombre d'inconnues demeure le même que dans le cas des écrans infiniment minces et le calcul des fonctions de Green pour les cavités est évité. La technique appliquée avec succès aux antennes à ouvertures des écrans métalliques épais et aux iris épais des guides d'ondes rectangulaires multicouches donne de bons résultats pour les ouvertures dont l'épaisseur est plus petite que leurs dimensions latérales.

Kratak Pregled

Planarni višeslojni dielektrici sa metalizacijama štampanim izmedju substrata predstavljaju jednu od najčešće korišćenih tehnologija u proizvodnji planarnih struktura, koja istovremeno ostvaruje dobar kompromis izmedju performansi i cene. Planarne strukture obuhvataju široki spektar kola i antena: od štampanih ploča, preko mikrostrip antena i antenskih nizova do filtera u talasovodima. Pristup koji se smatra najefikasnijim za analizu i dizajn ovih struktura jeste korišćenje integralnih jednačina (IE) koje se rešavaju numerički upotrebom metode momenata (MoM). Medjutim, ovaj pristup u kombinaciji sa baznim funkcijama definisanim na delovima domena, na koje je čitava geometrija problema izdeljena, zahteva velike memorijske resurse i vodi dugim kompjuterskim simulacijama. Iz tog razloga su neophodne tehnike koje ubrzavaju IE-MoM procedure i omogućavaju analizu elektromagnetno velikih struktura na standardnim računarima. Jedna od takvih 'akceleratorskih' tehnika koja se pokazala veoma efikasnom, a koja je razvijena u laboratoriji za elektromagnetiku i akustiku (LEMA) na EPFL-u, je Subdomain Multilevel Approach (SMA) sa makro-baznim funkcijama (MBF). U ovoj tezi predložen je način kojim se SMA ubrzava korišćenjem ekvivalentih momenata pri izračunavanju interakcija izmedju makro-baznih funkcija. Bez značajnijeg gubitka u preciznosti, simulacije štampanih antenskih nizova (sa brojem nepoznatih reda 10^4) postaju najmanje dva puta brže.

Ova teza zatim predlaže približnu ali efikasnu formulaciju za rešavanje problema rasejanja na otvorima u metalnim ravnima konačnih debljina. Naime, konačna debljina metalnih ravni u strukturama koje rade na višim učestanostima (kao što je slučaj kod tankih metalnih filmova na milimetarskim i manjim talasnim dužinama) mora biti uzeta u obzir u elektromagnetnim simulacijama. Precizan način modelovanja višeslojnih sredina sa aperturama (otvorima) u debelim metalnim ravnima je korišćenjem teoreme ekvivalencije i uvodjenjem magnetskih struja na obe strane otvora. Na ovaj način se, medjutim, udvostručava broj nepoznatih u poredjenju sa otvorima u beskonačno tankim ravnima. Štaviše, ovaj pristup zahteva izračunavanje Grinovih funkcija za talasovode što postaje numerički veoma zahtevno u slučaju otvora proizvoljnog poprečnog preseka. U predloženom rešenju, metalna ravan konačne debljine se aproksimira beskonačno tankom ravni dok se debljina pojavljuje kao korekcijski faktor u jezgru integralne jednačine. Broj nepoznatih ostaje isti kao u slučaju beskonačno tanke ravni a računanje zahtevnih Grinovih funkcija u talasovodima proizvoljnog poprečnog preseka je izbegnuto. Ova tehnika pokazuje dobre rezultate u simulaciji antenna sa metalnim otvorima u debelim metalizacijama kao i u simulaciji otvora konačne debljine u talasovodima, sve dok je debljina manja od poprečnih dimenzija aperture.

Acknowledgements

First and foremost, to my thesis advisor, Prof. Juan R. Mosig, for supporting this research and for providing an excellent working environment, for dedicated help, inspiration and encouragement throughout my PhD, for providing sound advice and lots of good ideas, and for good company within and outside the laboratory.

My appreciation goes to my other committee members as well: Prof. Antonije Djordjević, from University of Belgrade, Prof. Edward Kuester from University of Colorado at Boulder, and Prof. Jacques Rappaz from EPFL, for having accepted to examine this work and for having provided valuable insights and contributed to the improvement of the quality of this thesis. My gratitude to Prof. Djordjević, not just for being in my committee, but for all of his guidance, assistance, and subtle sense of humor. Thanks are also due to Dr. Farhad Rachidi for chairing my thesis committee.

I firmly believe that the work environment makes the greater part of the learning experience and for this I would like to thank my colleagues in the Laboratory of Electromagnetics and Acoustics of the EPFL. Thank you especially to Prof. Anja Skrivervik for her valuable support and for proof-reading this thesis. My thanks also to J.-F. Zürcher for having provided me with the measurements of the breadboards used to verify the algorithms developed in this thesis. I have had two office mates, Michael Mattes and Pedro Crespo Valero, both of them have freely shared their time, opinions and expertise. Michael provided the necessary encouragement and valuable help throughout my PhD. In addition to my office mates, I would like to extend my gratitude to Katarina Blagović, Maria Eugenia Cabot, and Francisco Nuñez, for their generous company. Also thanks to Juliane Iten Simões, Grégoire Walckiers, Daniel Llorens del Río, Frédéric Bongard, Stefano Vaccaro, Ferdinando Tiezzi, Pablo Dosil Rosende, Olivier Vidémé Bossou, Rainer Koß, and Julien Peruisseau.

I am grateful to the secretaries Mrs. Eulalia Durussel and Mrs. Alix Wend for helping the lab to run smoothly and for assisting me in many different ways.

Thanks go to Katarina Blagović, Danica Stefanović, Maria Eugenia Cabot, Olivier Vidémé Bossou, and J.-F. Zürcher, for their help in writing Serbo-Croatian and French versions of the thesis abstract.

Out with the work setting, I would like to offer my fondest regards to my friends: Marina Milanović, Kristina Popović, Mirjana Rapajić, Aleksandar Veselinović, and Dušan Vobornik.

Finally, I would like to mention my family. I wish to thank my parents who raised me, supported me, taught me, and loved me. And to my loving sister, brother-in-law and their two wonderful kids: Andrea and Aleksandar. To them all I dedicate this thesis.

Table of Contents

1 Introduction

Computational electromagnetics is a fascinating discipline that creates a symbiosis between mathematics, physics, computer science, and various application fields ranging from the analysis of circuits and antennas to the study of biological media. The term electromagnetic (EM) simulation implies the numerical solution of Maxwell's equations for electromagnetic fields for a given structure and specified environment (boundary conditions) [1]. These field computations may be carried out either in time domain (when the response is obtained as a function of time) or in frequency domain (when the solution is obtained for sinusoidal excitation in a specified range of frequencies). Among the time-domain solution techniques, the most commonly used approach is the finite-difference time-domain method (FDTD) [2, 3] and is indispensable when nonlinear active devices (for which only time-domain models are available) are included in the simulated structures. The most commonly used techniques for frequency simulation are the the finite-element method (FEM) [2, 4] and the solution of integral equations by the method of moments (IE-MoM) [2, 5, 6]. The FEM is used for general three-dimensional (3-D) structures, while the IE-MoM technique is especially well-suited for analysis of planar microwave and millimeter wave circuits and antennas.

This thesis deals with EM phenomena in the micro and millimeter wave range. In these frequency ranges, the dimensions of typical devices are comparable to the operating wavelength and the "full-wave" version of Maxwell equations must be used. The computer aided design (CAD) of microwave and millimeter wave structures has reached a significant level of maturity and nowadays there exists a vast choice of commercial EM solvers with enhanced capabilities in modeling these structures. A nonexhaustive list would include `ANSOFT DESIGNER` and `HFSS` (based on FEM) [7], `WIPL-D` (IE-MoM) [8], `ADS-Momentum` (IE-MoM) [9], `CST Microwave Studio` (time-domain Finite Integration Technique) [10], `IE3D` (IE-MoM) [11], and `Empire` (FDTD) [12] to mention but a few. Although EM-field simulation based on Maxwell's equations is rigorous, any practical implementation of EM-simulation methods does require some approximations either in description of the structure (and surrounding environment) to be analyzed, or in terms of boundary conditions, or in terms of the computational implementation of the method itself [1].

Planar technologies, with metallizations embedded in layered dielectric media, have a good performance-to-price ratio when manufacturing circuits and antennas at microwaves and millimeter waves. IE-MoM based simulators of planar multilayered media assume infinite lateral extent of the substrates and ground planes (or a rectangular boundary with electric and/or magnetic walls). These assumptions allow the efficient construction and evaluation of the associated Green's functions. At the same time, the thickness of metallic patches and ground planes is neglected. However, in many configurations such as cavity backed antennas, irises in waveguide filters, aperture-fed patches, and thick coplanar lines, the conducting screen thickness has to be accounted for, because of the technology (self-supporting metallic plates rather

than printed sheets), the frequency (mm- and sub mm-waves) or both. The drive to analyze more complex environments yields the much more involved Green's functions, for which the older numerical tricks and recipes do not apply anymore and any speed-up in the calculation of Green's functions and of their convolutions is of paramount relevance.

Other difficulties in application of EM simulators arise because of the intensive computer central processing unit (CPU) time and memory occupation. The memory requirements of a problem with N unknowns grow as $\mathcal{O}(N^2)$, in case of fully populated matrices. Even when the number of unknowns is such that it fits the available memory, another resource becomes critical. The CPU time grows as $\mathcal{O}(N^3)$ when a direct solution is applied leading to prohibitively long simulations. Despite the constant growth in computer technology, the EM simulation of electrically large structures is made feasible only with the development of fast algorithms with reduced complexity and memory requirements [13]. Thus, the development of fast solution methods that are efficient in terms of computational complexity and memory requirements is of chief importance.

1.1 Objectives

The main research directions taken in this thesis, aside from a pure academic interest, are strongly motivated and driven by three projects for the European Space and Technology Center of the European Space Agency (ESA-ESTEC).

The ESA-ESTEC project number 11278/94/NL/PB: "Antenna CAD and Technology for Future SARs" has been done in collaboration with Saab Ericsson Space. Space born Synthetic Aperture Radars (SAR) for high resolution imaging of the Earth require antenna radiators with large frequency bands and efficiency. A specific microstrip structure was proposed for this purpose by Saab Ericsson Space and an IE-MoM electromagnetic solver especially suited for the design of this type of microstrip antenna arrays, has been developed in our laboratory. The numerical code is optimized to cope with microstrip structures having a large number of radiating elements and containing thin dielectric skins between feeding lines and metallic patches. The solver incorporates dedicated routines for computation of Green's function of microstrip structures with thin dielectric layers. In addition, the Subdomain Multilevel Approach (SMA) is implemented to cope with the electromagnetically large microstrip designs.

Within the ESA-ESTEC project number 12996/98/NL/DS: "Modelling of wide band dual polarization antenna arrays", a software tool `POLARIS` for computationally efficient modeling of the Low Tolerance Arrays (LTA) has been developed. The Low Tolerance Arrays belong to the wide-band, dual-polarized, multiple slot array family. The design of these antennas is of interest for several ground and space applications, including satellite TVRO (Television Receive Only) systems, multimedia and Very Small Aperture Terminals (VSAT) on board, large bandwidth array panels, and SAR (Synthetic Aperture Radar) antennas. `POLARIS` is an IE-MoM based solver for modeling multilayered structures with dielectrics supporting slotted ground planes and feeding printed lines, such as encountered in the LTA family. Since an LTA element can be backed by a ground plane or a rectangular cavity, efficient treatment of rectangular cavities has been implemented by incorporating the boxed Green's functions to the existing IEs. Ground planes can have a sizeable thickness to provide self-supporting antennas

and specially suited Green's functions based on perturbation theory are developed in order to model them without slowing down the simulation. Finally, the arrays are obtained by periodical repetition of basic elements or subarrays including beam forming networks (BFN). In order to speed-up the MoM procedure of structures with large number of unknowns, the subdomain multilevel approach with macro-basis functions is used. The graphical user interface (GUI) is developed by JAST SA [14]. It is written in Tcl/Tk and allows object LEGO-like approach to complex geometries with a structured mesher that follows the symmetry of the structures to be analyzed.

Another ESA-ESTEC project (number 15538/01/NL/JSC: "Integrated Electromagnetic Modeling of Satellite Antennas") resulted in a planar multilayered circuit and antenna solver `MIXSOLVER`. This solver has been integrated within `ADF-EMS` system [15] that is a global software tool, under development at the European Space Agency, enabling the design of antennas both in free-space and on a spacecraft. Apart from `MIXSOLVER`, `ADF-EMS` gathers together several electromagnetic modeling tools from other partners in this project. The `ADF-EMS` allows the designer to assess antenna performances when installed on the spacecraft taking into account interactions with structures and with other radiating/receiving systems. The equivalent current distributions (Huygens sources) are used to achieve large scale modeling problems and antenna farm interactions. The efficient computation of the near-fields and equivalent currents is thus a main feature of `MIXSOLVER`. In addition, output files in special binary formats are used in order to communicate the geometry and simulation result data with the rest of the framework. The Graphical User Interface is based on GiD [16] and again developed by JAST SA using Tcl/Tk.

1.2 Outline

This section summarizes the contents of the chapters of the thesis. Every chapter contains a selective literature review substantial for the material presented in it.

Chapter 2 surveys the basic steps in the efficient IE-MoM simulations of planar multilayered circuits, antennas and waveguides. It gathers and presents in an organized way the geometry discretization issues, the Green's function computation in free space, laterally unbounded and shielded multilayered media, the details of IE-MoM procedure, and the computation of circuit and antenna parameters such as scattering parameters, far and near-fields.

Chapter 3 presents an improved Subdomain Multilevel Approach (SMA), used to efficiently solve large complex-shaped antenna problems. This chapter first outlines the details of the SMA technique and the concept of Macro-Basis Functions (MBFs). Then it explains the possible improvements in terms of MoM matrix filling and proposes an efficient way of computing the MBF reaction terms by reducing them to equivalent moments. Finally, this chapter demonstrates the accuracy and efficiency of the proposed improvement by investigating three representantive examples, in which the technique is compared with a conventional MoM, unrefined SMA and measurements.

Chapter 4 focuses on a classical EM problem of scattering of an EM wave by an aperture in a thick conducting screen. First, it presents a detailed bibliography overview of the work previously done to successfully solve the aperture problem in both thick and zero-thickness screens. Then it examines in detail the numerical solution for infinitely thin metallic plates and apertures and establishes all the steps in applying the equivalence theorem. Finally, it reviews the thick aperture integral equation formulation and modifies it to make it continuously valid for any aperture thickness, including a vanishing thickness. It proposes the simplification of this formulation and claims that this simplification reduces significantly the computational burden while providing valid results for apertures of arbitrary cross-sections whose thicknesses remain small compared with their linear transverse dimensions.

Chapter 5 takes the approximate solution from Chapter 4 and incorporates it within the traditional integral equations for aperture antennas embedded in stratified media. It introduces the new complete set of integral equations for a printed-line fed slot antenna and provides further numerical verifications. It validates the developed model by comparing its numerical predictions with measurements for a set of aperture antennas of different shapes and thicknesses.

Chapter 6 extends the approximate solution to the problem of thick irises inside the multilayered rectangular waveguides. After a thorough overview of different techniques used in solving waveguide discontinuities, this chapter illustrates an efficient IE-MoM approach for solving rectangular waveguide discontinuities where a thin iris is considered as a new waveguide section. After validating the approach by comparing the simulated values to results from other solvers and measurements, this chapter introduces two original and efficient treatments similar to the approximate solution presented in Chapter 4 and 5. Finally, it discusses the accuracy of the two approaches by putting side by side the simulated and measured results.

Chapter 7 summarizes the concluding remarks and outlines the possible future research directions inspired by the work presented in this thesis.

1.3 Original Contributions

The primary original contributions of this thesis are summarized in what follows.

Chapter 2, Section 2.6.4 presents a "specially truncated set of images", a technique used to speed-up the convergence of the multilayered boxed Green's functions. The results of this work have been presented in one conference paper.

Chapter 2, Section 2.12 is a valuable benchmark for near-field computations in multilayered planar circuits and antennas presented in a conference paper.

Chapter 3 proposes an improvement of the SMA technique that consists in the computationally efficient way of filling the MoM matrix by reducing the MBFs into equivalent moments. This work has been presented in one conference and one journal paper.

Chapters 4 – 6 introduce a novel model for apertures of arbitrary cross-sections in thick conducting screens and extend the validity of the model to aperture antennas in stratified media and to the thin irises in multilayered rectangular waveguides. At the moment of writing this thesis, this work has resulted in three conference papers, two workshop presentations and one published journal paper.

For a complete list of publications, the reader is referred to the page 179 of this thesis.

References

[1] K. C. Gupta, "Emerging trends in millimeter-wave CAD," *IEEE Trans. Microwave Theory Tech.*, vol. 46, no. 6, pp. 747–755, June 1998.

[2] T. Itoh, Ed., *Numerical Techniques for Microwave and Millimeter-Wave Passive Structures.* New York: Wiley, 1989.

[3] A. Taflove, *Computational Electrodynamics: The Finite-Difference Time-Domain Method.* Boston, MA: Artech House, 1995.

[4] P. P. Silvester and R. L. Ferrari, *Finite Elements for Electrical Engineers*, 2nd ed. Cambridge, UK: Cambridge Univ. Press, 1990.

[5] R. Harrington, *Field Computation by Moment Methods*, 2nd ed. IEEE Press, New York, 1993.

[6] S. M. Rao, D. R. Wilton, and A. W. Glisson, "Electromagnetic scattering by surfaces of arbitrary shape," *IEEE Trans. Antennas Propagat.*, vol. 30, no. 3, pp. 409–418, May 1982.

[7] Ansoft Corporation. (2004) Products. [Online]. Available: http://www.ansoft.com/products/

[8] WIPL-D. (2004) Electromagnetic modeling of composite metallic and dielectric structures. [Online]. Available: http://www.wipl-d.com/

[9] Agilent Technologies. (2004) Advanced Design System Momentum Simulator. [Online]. Available: http://home.agilent.com/

[10] Sonnet Software. (2004) CST Microwave Studio- Full 3-D Electromagnetic Analysis Software. [Online]. Available: http://www.sonnetusa.com/products/cst/index.asp

[11] Zeland Software, Inc. (2004) IE3D: MoM-Based EM Simulator. [Online]. Available: http://www.zeland.com/ie3d.html

[12] IMST. (2004) Empire. [Online]. Available: http://www.empire.de/

[13] W. C. Chew, J. Jin, C. Lu, E. Michielssen, and J. M. Song, "Fast solution methods in electromagnetics," *IEEE Trans. Antennas Propagat.*, vol. 45, no. 3, pp. 533–543, Mar. 1997.

[14] (2004) JAST antenna systems. [Online]. Available: http://www.jast.ch/

[15] (2004) ADF-EMS Antenna Design Framework - Electromagnetic Satellite. [Online]. Available: http://www.adf.ids-spa.it

[16] International Center for Numerical Methods in Engineering. (2004) GID, The personal pre and post processor. [Online]. Available: http://gid.cimne.upc.es/

2 Numerical Modeling of Planar Multilayered Structures

2.1 Introduction

Planar technologies, in which thin metallizations are embedded within flat layered dielectric media, are one of the most popular and successful approaches to build circuits and antennas in microwaves and millimeter waves with a good performance-to-price ratio. Here, we broaden a little the original definition and include under the generic name "planar structures" many different geometries, ranging from shielded and boxed printed circuits, to cavity-backed microstrip antennas and waveguide discontinuities. The common denominator is the presence of planar dielectric layers and of metallic structures that are essentially one- or two-dimensional (printed lines, patches, apertures in ground planes).

In the microwave community, structures covered by metallic planes or partially or fully shielded (boxed) by metallic enclosures are usually considered from a waveguide standpoint. Here, we will formulate an "antenna" approach, where the problem is first formulated in an unbounded medium and metallic walls are successively added. This is an interesting and complementary vantage point, which allows the introduction of alternate numerical techniques.

From the point of view of mathematical and numerical modeling, one of the most successful approaches, providing a general framework for this type of antennas and circuits, is the Integral Equation model combined with a discretization procedure like the Method of Moments (IE-MoM) [1, 2]. Any integral equation formulation starts by setting up the boundary conditions that must be satisfied by electromagnetic field [3]. Boundary conditions can be used to generate an integral equation, and depending on the type of boundary conditions used, one can obtain the electric field integral equation (EFIE), magnetic field integral equations (MFIE) or combined field integral equations (CFIE). The EFIE can be solved either in spectral domain or in space domain introducing mixed potential integral equations (MPIE).

In addition, boundary conditions can be replaced by unknown equivalent sources using surface and/or volume equivalent principles [4]. With conductors always represented by surface equivalent sources and dielectric media replaced by either volume or surface equivalent sources, there exist surface-volume or surface-surface formulations. In both cases homogeneous Green's functions are used.

A computationally most efficient formulation for modeling multilayered structures, where the substrates can be approximated by flat layers of infinite transverse extent, and ground planes assumed to be of infinite dimensions, is by using surface equivalence theorem and stratified media Green's functions. In this formulation, conductors are replaced by surface electric currents and slots in conducting planes by surface magnetic currents. Therefore this kind of IE-MoM can be recognized as a technique belonging to the family of Boundary Element

Methods (BEM). In this formulation, the boundary conditions on different dielectric regions are included in the Green's functions [2, 3, 5].

The key step in any IE formulation is the construction and evaluation of the associated Green's functions. By using a flexible scheme in the definition of these functions it is possible to bring under the same roof all the mentioned geometries. Therefore, in addition to the original multilayered printed antenna, where the dielectric substrates are usually considered as of lateral infinite extent, the same approach is able to deal with boxed circuits, cavity-backed antennas and waveguide discontinuities, thus providing a seamless transition between the printed antenna and the waveguide worlds [6, 7].

In this chapter, a brief overview of all the steps that need to be undertaken in the efficient numerical simulations of planar multilayered circuits, antennas and waveguides is given, ranging from the geometry discretization, through the Green's function computation, to the recovery of the circuit parameters, such as input impedance, near and far fields. The last section of this chapter illustrates near field computation for a set of stratified media circuits and antennas. The examples of other circuit and antenna parameters, such as scattering parameters and far fields, will be presented in other chapters of this thesis.

2.2 A Basic Survey of a Generic IE Procedure

The following essential steps can be defined and identified in most IE-MoM implementations:

1. Discretization of the geometry and definition of basis functions.
2. Analytical construction of Green's functions.
3. Filling the MoM matrix.
   - 3a) Calculation of Green's functions.
   - 3b) Calculation of coupling integrals associated to matrix elements.
4. Definition of an excitation vector.
5. Solving the matrix equation.
6. Recovering equivalent circuit or system parameters of the structure.

2.2.1 Geometrical Discretization

The first step, geometrical discretization, is a rather generic problem, where the electromagnetics community has largely borrowed information from other technical communities, more advanced in the routine use of finite elements and related techniques for solving large-scale problems. Some specificities of the electromagnetic problems (for instance the need for vector edge elements) must be taken into account and there is an ongoing effort to adapt existing finite element tools and meshers from civil and mechanical engineering to specific electromagnetic problems. Nowadays, many directly usable tools are freely available and/or widely distributed (see for instance Triangle [8] and GiD [9] websites).

The basis functions used can be entire domain basis functions or subsectional basis functions. The advantage of using subsectional basis functions is that any geometry can be treated by dividing it into triangular, rectangular, quadrangular or more complex subdomains.

The fundamental reason for this subdivision is that the currents can be expanded in a basis of simple linear divergence and curl-conforming vector functions, also called rooftop function or surface doublets, which will satisfy the pertinent continuity equations and exhibit a locally constant charge distribution. The most important current continuity condition, in order for the currents to locally satisfy Kirchhoff's law, is for the normal component to be continuous across the boundaries of adjacent cells in the mesh.

Once the structure is discretized, the rooftop functions are associated with rectangular or triangular cells [10], quadrangular [11, 12, 13] or generalized polygonal basis functions defined over the arbitrary polygonal subdomains [14].

2.3 The Green's Function Formulation

For the sake of simplicity, let us illustrate the Green's function formulation with the specific geometry of a cavity backed antenna, which already contains two types of boundary conditions to be considered in this work [Fig. 2.1(a)]. The standard procedure [3] applies the equivalence theorem to the ground plane. Equivalent magnetic currents, equal but of opposite sign $\mathbf{M}_{\mathrm{U}} = -\mathbf{M}_{\mathrm{L}} = \mathbf{M}$, are then defined in both sides of the "filled" aperture and the problem is split into two parts (subproblems): an upper one ① and a lower one ② [Fig. 2.1(b-c)]. We define now equivalent electric currents $\mathbf{J}_{\mathrm{P}}$ in the upper patch P and $\mathbf{J}_{\mathrm{L}}$ in the lower printed line L. Assuming some excitation (incident) fields $\mathbf{E}^{\mathrm{i}}$, $\mathbf{H}^{\mathrm{i}}$ existing in the lower part, and using the usual convolution notation [3] we can write by direct inspection the following equations:

- Impedance (Leontovich) boundary condition for the tangential **E**-field in the upper patch P:

$$\mathbf{n} \times \left(\overleftrightarrow{\mathbf{G}}^{①}_{\mathrm{EJ}} \otimes \mathbf{J}_{\mathrm{P}} + \overleftrightarrow{\mathbf{G}}^{①}_{\mathrm{EM}} \otimes \mathbf{M} \right) = \mathbf{n} \times Z_{\mathrm{s}} \mathbf{J}_{\mathrm{P}} \tag{2.1}$$

- Continuity of the tangential **H**-field in both sides of the slot S:

$$\mathbf{n} \times \left(\overleftrightarrow{\mathbf{G}}^{①}_{\mathrm{HM}} \otimes \mathbf{M} \right) = \mathbf{n} \times \left(\mathbf{H}^{\mathrm{i}} + \overleftrightarrow{\mathbf{G}}^{②}_{\mathrm{HJ}} \otimes \mathbf{J}_{\mathrm{L}} + \overleftrightarrow{\mathbf{G}}^{②}_{\mathrm{HM}} \otimes (-\mathbf{M}) \right) \tag{2.2}$$

- Impedance (Leontovich) boundary condition for the tangential **E**-field in the lower line L:

$$\mathbf{n} \times \left(\mathbf{E}^{\mathrm{i}} + \overleftrightarrow{\mathbf{G}}^{②}_{\mathrm{EJ}} \otimes \mathbf{J}_{\mathrm{L}} + \overleftrightarrow{\mathbf{G}}^{②}_{\mathrm{EM}} \otimes (-\mathbf{M}) \right) = \mathbf{n} \times Z_{\mathrm{s}} \mathbf{J}_{\mathrm{L}} \tag{2.3}$$

These are the three coupled integral equations fully defining the problem of Fig. 2.1. In the above equations, $\overleftrightarrow{\mathbf{G}}^{N}_{\mathrm{PQ}} = \overleftrightarrow{\mathbf{G}}^{N}_{\mathrm{PQ}}(\mathbf{r}|\mathbf{r}')$ is a dyadic Green's function giving the vector field $\mathbf{P}$ at point $\mathbf{r}$ created by the point vector source $\mathbf{Q}$ at $\mathbf{r}'$ when both source and observer belong to

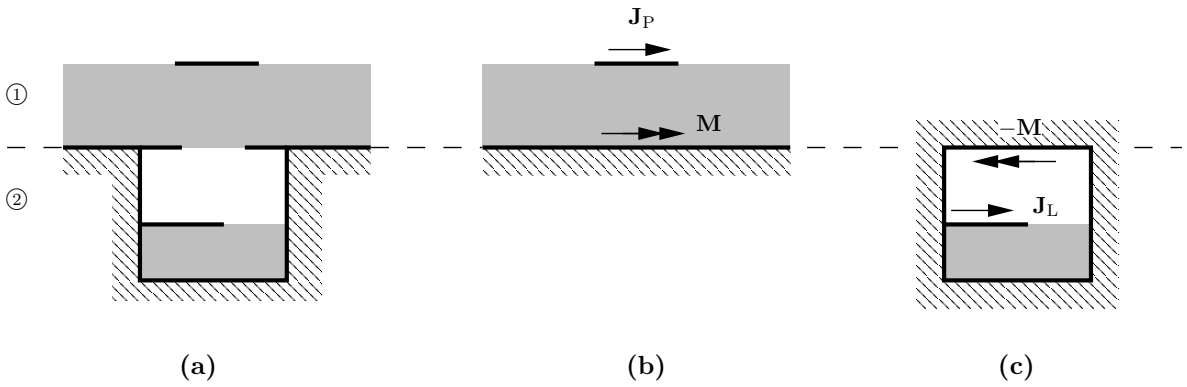

Figure 2.1: Equivalence theorem: (a) Original problem, (b) Upper equivalent subproblem, (c) Lower equivalent subproblem.

the subproblem N. And the convolution operator $\otimes$ is defined as:

$$\overleftrightarrow{\mathbf{G}} \otimes \mathbf{f} = \int_D \overleftrightarrow{\mathbf{G}}(\mathbf{r}|\mathbf{r}')\mathbf{f}(\mathbf{r}')\,\mathrm{d}D,$$

where D is the domain of definition of the source vector $\mathbf{f}$.

It is worth mentioning that alternative IE formulations do exist for many planar problems. For instance, for the geometries of Fig. 2.1, an "all-$\mathbf{J}$" formulation is possible. Instead of using the equivalence theorem and "filling" the aperture with magnetic currents, the "holed" planes are treated as standard metallizations and modeled by electric currents. In this case, there is no need to deal with subproblems and the only required convolutions are of type $\overleftrightarrow{\mathbf{G}}_\mathrm{EJ} \otimes \mathbf{J}$. But the number of unknowns can increase dramatically. Conversely, the equivalence theorem can be systematically applied to all the layers, hence defining as many subproblems as layers ("all-$\mathbf{M}$" formulation). Any horizontal metallization is considered as a part of a ground plane and the only required convolutions are of type $\overleftrightarrow{\mathbf{G}}_\mathrm{HM} \otimes \mathbf{M}$. Moreover, all the Green's functions correspond to a homogeneously filled parallel plate waveguide. This interesting approach could be competitive when most interfaces are densely filled by metal.

2.3.1 Mixed Potentials

Basic electromagnetic theory teaches us that the fields $\mathbf{E}$, $\mathbf{H}$ scattered by sources $\mathbf{J}$, $\mathbf{M}$ can be expressed not only as convolutions of the sources and the corresponding dyadic Green's functions, but also through auxiliary functions called potentials, namely a vector potential $\mathbf{A}$ and a scalar potential V for electric sources and a vector potential $\mathbf{F}$ and a scalar potential W for magnetic sources [4]:

$$\begin{aligned} \mathbf{E} &= \overleftrightarrow{\mathbf{G}}_\mathrm{EJ} \otimes \mathbf{J} + \overleftrightarrow{\mathbf{G}}_\mathrm{EM} \otimes \mathbf{M} &&= -\mathrm{j}\omega\mathbf{A} - \boldsymbol{\nabla}V - \tfrac{1}{\varepsilon}\boldsymbol{\nabla} \times \mathbf{F}, \\ \mathbf{H} &= \overleftrightarrow{\mathbf{G}}_\mathrm{HJ} \otimes \mathbf{J} + \overleftrightarrow{\mathbf{G}}_\mathrm{HM} \otimes \mathbf{M} &&= -\mathrm{j}\omega\mathbf{F} - \boldsymbol{\nabla}W + \tfrac{1}{\mu}\boldsymbol{\nabla} \times \mathbf{A}. \end{aligned} \tag{2.4}$$

The obvious question is whether we can define also Green's functions for the potentials and

how these new Green's functions are related to their field counterparts. The answer is not so straightforward as it could be expected and many publications have been dedicated to this subject. For our planar structures, it is possible to define Green's functions for the potentials but some precautions must be taken [15]. The final result generalizes what is well known in free space [3]

$$\begin{aligned} \overleftrightarrow{\mathbf{G}}_{\mathrm{EJ}} \otimes \mathbf{J} &= -\mathrm{j}\omega \overleftrightarrow{\mathbf{G}}_A \times \mathbf{J} - \boldsymbol{\nabla}(G_V \otimes q_{\mathrm{e}}), & \overleftrightarrow{\mathbf{G}}_{\mathrm{EM}} \otimes \mathbf{M} &= -\boldsymbol{\nabla} \times \left(\overleftrightarrow{\mathbf{G}}_F \otimes \mathbf{M} \right) / \varepsilon, \\ \overleftrightarrow{\mathbf{G}}_{\mathrm{HM}} \otimes \mathbf{M} &= -\mathrm{j}\omega \overleftrightarrow{\mathbf{G}}_F \times \mathbf{M} - \boldsymbol{\nabla}(G_W \otimes q_{\mathrm{m}}), & \overleftrightarrow{\mathbf{G}}_{\mathrm{HJ}} \otimes \mathbf{J} &= -\boldsymbol{\nabla} \times \left(\overleftrightarrow{\mathbf{G}}_A \otimes \mathbf{J} \right) / \mu, \end{aligned} \tag{2.5}$$

where q_{e} and q_{m} are respectively the electric and magnetic charge densities defined according to the continuity equation as $q_{\mathrm{e}} = -\boldsymbol{\nabla} \cdot \mathbf{J}/(\mathrm{j}\omega)$, and $q_{\mathrm{m}} = -\boldsymbol{\nabla} \cdot \mathbf{M}/(\mathrm{j}\omega)$. As it is well known [15], several numerical benefits can be drawn from the use of potentials. They have in general simpler expressions and milder singularities than the fields. For instance, we have in free space

$$\overleftrightarrow{\mathbf{G}}_A = \frac{\mu}{4\pi} \Psi \overleftrightarrow{\mathbf{I}}, \quad G_V = \frac{1}{4\pi\varepsilon} \Psi, \quad \Psi = \frac{\mathrm{e}^{-\mathrm{j}kR}}{R}, \quad R = \left| \mathbf{r} - \mathbf{r}' \right|, \tag{2.6}$$

while several components of the Green's functions for the fields have a strong singularity of type R^{-3}.

2.3.2 Method of Moments and Potentials

In the Method of Moments [1], the unknown currents are expanded as linear combinations of a set of N vector basis functions $\mathbf{f}_j$ and the integral equations are tested, via an internal product, against a set of vector weight functions $\mathbf{w}_i$. Several choices of weight functions are especially well suited, like "point-matching" ($\mathbf{w}_i = \delta(\rho - \rho_i)$, Dirac delta functions), "razor-testing" (integrating the integral equations along 1-D segments belonging to the surfaces where the currents are defined) [16], and Galerkin ($\mathbf{w}_i = \mathbf{f}_i$).

All of these choices transform the system of coupled integral equations into the system of linear equations (also known as the MoM system), which can be shortly written in a matrix form as

$$\mathbf{M}\mathbf{a} = \mathbf{v} \tag{2.7}$$

where $\mathbf{M} = [m_{ij}]_{N \times N}$ is the MoM matrix, $\mathbf{v} = [v_j]_{N \times 1}$ is the excitation vector, and $\mathbf{a} = [a_i]_{N \times 1}$ denotes the unknown coefficients that expand the electric and magnetic currents into a set of subsectional basis functions.

There are two types of interactions in the MoM matrix. If the source and the observer rooftops (basis and weight functions) belong to the same type of source (electric or magnetic), the potential Green's functions are used in order to obtain a milder singularity (R^{-1} instead of R^{-3} for fields). This allows for the integrals to be numerically solved in two possible ways. The singularity can be extracted, computed analytically [17] and added to the remaining regular part that can be computed using numerical integration. Another strategy is to solve the integral in polar coordinates, where the Jacobian of the transformation will cancel out the singularity, and the integral can be computed numerically [18, 19].

This means that in the final matrix of moments, every time that a convolution of type

$\overleftrightarrow{\mathbf{G}}_{\mathrm{EJ}} \otimes \mathbf{J}$ appears in the integral equation, it will contribute to corresponding MoM matrix element with the term

$$m_{ij} = \left\langle \mathbf{f}_i, \overleftrightarrow{\mathbf{G}}_{\mathrm{EJ}} \otimes \mathbf{f}_j \right\rangle = -\mathrm{j}\omega \left\langle \mathbf{f}_i, \overleftrightarrow{\mathbf{G}}_A \otimes \mathbf{f}_j \right\rangle - \frac{1}{\mathrm{j}\omega} \left\langle \boldsymbol{\nabla} \cdot \mathbf{f}_i, G_V \otimes (\boldsymbol{\nabla} \cdot \mathbf{f}_j) \right\rangle, \tag{2.8}$$

where the inner product is defined as

$$\langle \mathbf{w}_i, \mathbf{h}_j \rangle = \int_{S_i} \mathbf{w}_i \cdot \mathbf{h}_j \, \mathrm{d}S_i. \tag{2.9}$$

In the case of two rooftops belonging to different types of sources, field GFs are preferred (there is no singular interaction, since magnetic and electric currents are not supposed to share the same z-level) and the contribution to the corresponding MoM matrix element is

$$m_{ij} = \left\langle \mathbf{f}_i, \overleftrightarrow{\mathbf{G}}_{\mathrm{EM}} \otimes \mathbf{f}_j \right\rangle, \tag{2.10}$$

for the case when $\mathbf{f}_i$ belongs to the electric and $\mathbf{f}_j$ belongs to the magnetic source.

In all cases, the numerical integration is done using cubature rules specially adapted to triangular or rectangular domains [20].

Concerning the excitation vector terms, they can be expressed as

$$v_i = \begin{cases} \left\langle \mathbf{f}_i, \mathbf{E}^{\mathrm{i}} \right\rangle, & \text{if } \mathbf{f}_i \text{ belongs to an electric source} \\ \left\langle \mathbf{f}_i, \mathbf{H}^{\mathrm{i}} \right\rangle, & \text{if } \mathbf{f}_i \text{ belongs to a magnetic source} \end{cases} \tag{2.11}$$

The detailed expressions for MoM matrix elements and the excitation vector are given in Chapter 4, where the scattering from an infinitely thin patch and aperture is treated.

2.3.3 Space and Spectral Domains

It must be clear that direct calculation of Green's functions is not mandatory in the practical implementations of IE-MoM algorithms. The final quantities to be computed are given by equations of the type (2.8) combining internal products and convolutions. This has prompted many IE practitioners to skip step 3a) (calculation of Green's functions) and attack directly the computation of MoM matrix elements. The main tool here is the Fourier transform. Parseval theorem allows us to demonstrate that the expression in equation (2.8) can be written as

$$\left\langle \mathbf{w}_i, \overleftrightarrow{\mathbf{G}}_{\mathrm{EJ}} \otimes \mathbf{f}_j \right\rangle = \mathcal{F}^{-1} \left(\widetilde{\mathbf{w}}_i \overleftrightarrow{\mathbf{G}}_{\mathrm{EJ}} \widetilde{\mathbf{f}}_j \right), \tag{2.12}$$

where the tilde denotes a spectral magnitude obtained by Fourier transform $\widetilde{g} = \mathcal{F}^{-1}(g)$. All the techniques using this formulation can be called *spectral domain approaches* (SDAs) [21, 22, 23]. Reducing the calculation of every matrix element to the value at the origin of the inverse Fourier transform of the product of three Fourier transforms looks very appealing. The Fourier transforms of Green's functions (spectral values) and of basis and test functions are usually analytically known, and FFT techniques are readily available to compute Fourier transforms.

However, the involved functions show a complex set of singularities and bad convergence properties, which prevents a straightforward use of FFT, and special sophisticated numerical devices must be used. Therefore, remaining in the original space domain is not necessarily a drawback. Moreover, computing Greens functions could be an interesting investment in many cases and for several reasons.

1. When computing interactions between basis and test functions defined in faraway located domains, a reasonable approximation is:

$$\left\langle \mathbf{w}_i, \overleftrightarrow{\mathbf{G}} \otimes \mathbf{f}_j \right\rangle = \left(\int_{D_i} \mathbf{w}_i \, \mathrm{d}D_i \right) \overleftrightarrow{\mathbf{G}}(\mathbf{r}_i | \mathbf{r}'_j) \left(\int_{D_j} \mathbf{f}_j \, \mathrm{d}D_j \right),$$

   where $\mathbf{r}_k$ is the center of domain D_k.

2. Green's functions show usually strong symmetries and can be advantageously precomputed and stored for later retrieval and interpolation.

3. Green's functions properties offer a direct insight into the physical properties of the problem.

2.4 Free-space Dyadic Green's functions

In this section, the overview of formulas defining the Green's functions in free-space for both fields and potentials is presented.

2.4.1 Potential Green's Functions

Potential Green's functions in free-space are given by the following expressions

$$\overleftrightarrow{\mathbf{G}}_A = \frac{\mu_0}{4\pi} \Psi \overleftrightarrow{\mathbf{I}}, \quad G_V = \frac{1}{4\pi\varepsilon_0} \Psi, \tag{2.13a}$$

$$\overleftrightarrow{\mathbf{G}}_F = \frac{\varepsilon_0}{4\pi} \Psi \overleftrightarrow{\mathbf{I}}, \quad G_W = \frac{1}{4\pi\mu_0} \Psi, \tag{2.13b}$$

where

$$\Psi = \frac{\mathrm{e}^{-\mathrm{j}kR}}{R},$$

the distance between source and observer points is

$$R = \sqrt{(x - x')^2 + (y - y')^2 + (z - z')^2},$$

and the idem dyad expressed in matrix notation

$$\overleftrightarrow{\mathbf{I}} = \hat{x}\hat{x} + \hat{y}\hat{y} + \hat{z}\hat{z} = \begin{bmatrix} 1 & 0 & 0 \\ 0 & 1 & 0 \\ 0 & 0 & 1 \end{bmatrix}.$$

2.4.2 Electric Field Dyadic Green's functions

Electric source

The electric field dyadic Green's function for electric source can be expressed in terms of the potential Green's functions for an electric source in the following way

$$\overleftrightarrow{\mathbf{G}}_{\mathrm{EJ}}(\mathbf{r}|\mathbf{r}') = -\mathrm{j}\omega\overleftrightarrow{\mathbf{G}}_A(\mathbf{r}|\mathbf{r}') - \frac{1}{\mathrm{j}\omega}\boldsymbol{\nabla}\boldsymbol{\nabla}' G_V(\mathbf{r}|\mathbf{r}'), \tag{2.14}$$

where the operator $\boldsymbol{\nabla}\boldsymbol{\nabla}'$, acting on the electric scalar potential Green's function, will give as a result a dyad.

Taking into account equations (2.13a) and (2.14), one can write all the components of the electric field free space dyadic Green's function as

$$\overleftrightarrow{\mathbf{G}}_{\mathrm{EJ}} = \mu_0\kappa P \begin{bmatrix} (x-x')^2 - Q & (x-x')(y-y') & (x-x')(z-z') \\ (x-x')(y-y') & (y-y')^2 - Q & (y-y')(z-z') \\ (x-x')(z-z') & (y-y')(z-z') & (z-z')^2 - Q \end{bmatrix}$$

with

$$\kappa = \frac{\mathrm{j}\omega}{4\pi}\frac{\mathrm{e}^{-\mathrm{j}kR}}{kR^3},$$

$$P = \frac{k^2R^2 - 3\mathrm{j}kR - 3}{R^2},$$

and

$$Q = \frac{k^2R^2 - \mathrm{j}kR - 1}{P}.$$

Magnetic source

Having in mind that the electric field $\mathbf{E}$ can be expressed as a curl of the electric vector potential $\mathbf{F}$

$$\mathbf{E} = -\frac{1}{\varepsilon_0}\boldsymbol{\nabla} \times \mathbf{F}, \tag{2.15}$$

the electric field dyadic Green's function for a magnetic source can be written as

$$\overleftrightarrow{\mathbf{G}}_{\mathrm{EM}} = -\frac{1}{\varepsilon_0}\boldsymbol{\nabla} \times \overleftrightarrow{\mathbf{G}}_F, \tag{2.16}$$

where the curl operator acting on a dyad acts on every column of the dyad. The electric field dyadic Green's function for magnetic sources can be written as

$$\overleftrightarrow{\mathbf{G}}_{\mathrm{EM}} = -\frac{1}{4\pi}\frac{1+\mathrm{j}kR}{R^3}\mathrm{e}^{-\mathrm{j}kR}\begin{bmatrix} 0 & z-z' & -(y-y') \\ -(z-z') & 0 & x-x' \\ y-y' & -(x-x') & 0 \end{bmatrix}. \tag{2.17}$$

2.4.3 Magnetic Field Dyadic Green's functions

Electric source

Following the same procedure as in Section 2.4.2, the magnetic field dyadic Green's function for an electric source is given by

$$\overleftrightarrow{\mathbf{G}}_{\mathrm{HJ}} = \frac{1}{4\pi}\frac{1+\mathrm{j}kR}{R^3}\mathrm{e}^{-\mathrm{j}kR}\begin{bmatrix} 0 & z-z' & -(y-y') \\ -(z-z') & 0 & x-x' \\ y-y' & -(x-x') & 0 \end{bmatrix}. \tag{2.18}$$

Magnetic source

In an analogous way as presented in Section 2.4.2, the magnetic field dyadic Green's function for a magnetic source can be expressed as

$$\overleftrightarrow{\mathbf{G}}_{\mathrm{EJ}} = \varepsilon_0\kappa P\begin{bmatrix} (x-x')^2-Q & (x-x')(y-y') & (x-x')(z-z') \\ (x-x')(y-y') & (y-y')^2-Q & (y-y')(z-z') \\ (x-x')(z-z') & (y-y')(z-z') & (z-z')^2-Q \end{bmatrix}.$$

2.5 Green's Functions for Laterally Unbounded Planar Multilayered Structures

2.5.1 Spectral Domain

The study of Green's functions associated to sources embedded in a planar multilayered medium can be optimally done by solving an equivalent transmission line problem [2, 24] (Fig. 2.2). The source becomes a lumped generator and every layer corresponds to a transmission line section. The terminal impedance walls bounding the planar multilayered medium correspond to loading impedances. For instance, a semi-infinite terminal will be simulated by a matched load impedance.

Once the equivalent transmission line problem is solved, the knowledge of voltages and currents at any z-level allows a full solution of the original electromagnetic problem. In particular, voltages and currents at the connection points between transmission line sections give the fields and the potentials at the interfaces of the layered medium. Table 2.1 and Table 2.2 summarize the expressions that relate spectral domain field and potential Green's function components with voltages and currents in the equivalent transmission line model. In these tables, the primed variables designate the source, and the non-primed – the observer, k_z is the propagation constant in the z-direction, $k_\rho^2 = k_0^2\mu_r\varepsilon_r - k_z^2 = k_x^2 + k_y^2$ is the transverse

spectral variable, and the characteristic impedances for the TE and TM modes are given by, respectively,

$$Z_{\mathrm{c}}^{\mathrm{TE}} = \frac{\omega\mu_0\mu_r}{k_z} \text{ and } Z_{\mathrm{c}}^{\mathrm{TM}} = \frac{k_z}{\omega\varepsilon_0\varepsilon_r}.$$

Note also that a transversal electric source J_ρ and a normal magnetic source M_z correspond to the parallel current generator of $I_{\mathrm{g}} = 1/(2\pi)$, while a transversal magnetic source M_ρ and a normal electric source J_z correspond to the series voltage generator with $V_{\mathrm{g}} = 1/(2\pi)$.

The Sommerfeld choice for vector potentials reduces the full dyadic into only five non-zero components, but at the same time there is an additional component for the scalar potentials [25, 26] (Table 2.2). Note that throughout this work, only planar electric and magnetic sources (at $z = \text{const.}$) are considered.

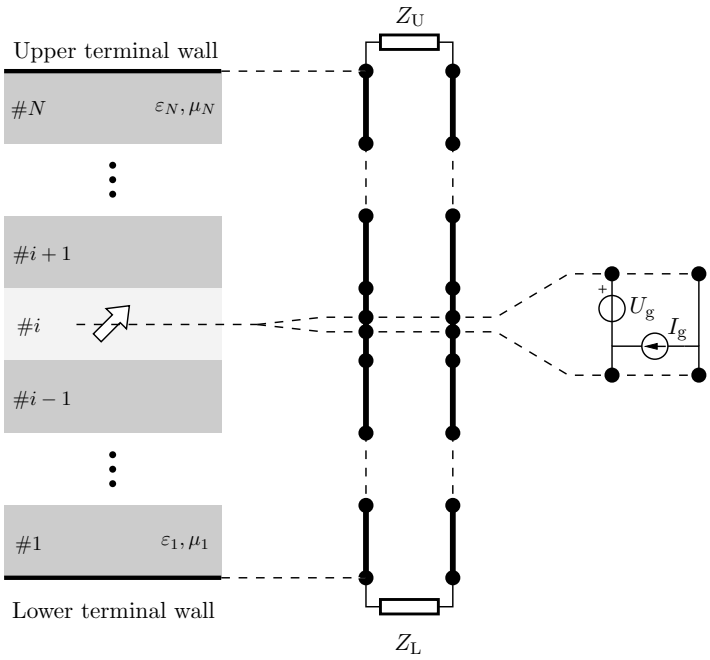

Figure 2.2: Equivalent transmission line model of the Green's function problem [24].

2.5.2 Spatial Domain

If a function G depends on tangential coordinates only through the radial source-observer distance $\rho = \sqrt{(x-x')^2 + (y-y')^2}$, then its spectral transform is only a function of the radial spectral coordinate $k_\rho = \sqrt{k_x^2 + k_y^2}$ and we can write the 2-D Fourier transformation

Electric Source	
$\widetilde{G}^{xx}_{\mathrm{EJ}} = -\frac{1}{k_\rho^2}\left(k_y^2 V^{\mathrm{TE}}_{J_\rho} + k_x^2 V^{\mathrm{TM}}_{J_\rho}\right)$	$\widetilde{G}^{xx}_{\mathrm{HJ}} = -\frac{k_x k_y}{k_\rho^2}\left(I^{\mathrm{TE}}_{J_\rho} - I^{\mathrm{TM}}_{J_\rho}\right)$
$\widetilde{G}^{yx}_{\mathrm{EJ}} = \frac{k_x k_y}{k_\rho^2}\left(V^{\mathrm{TE}}_{J_\rho} - V^{\mathrm{TM}}_{J_\rho}\right)$	$\widetilde{G}^{yx}_{\mathrm{HJ}} = -\frac{1}{k_\rho^2}\left(k_y^2 I^{\mathrm{TE}}_{J_\rho} + k_x^2 I^{\mathrm{TM}}_{J_\rho}\right)$
$\widetilde{G}^{zx}_{\mathrm{EJ}} = -\frac{k_x}{\omega\varepsilon} I^{\mathrm{TM}}_{J_\rho}$	$\widetilde{G}^{zx}_{\mathrm{HJ}} = -\frac{k_y}{\omega\mu} V^{\mathrm{TE}}_{J_\rho}$
$\widetilde{G}^{xy}_{\mathrm{EJ}} = \frac{k_x k_y}{k_\rho^2}\left(V^{\mathrm{TE}}_{J_\rho} - V^{\mathrm{TM}}_{J_\rho}\right)$	$\widetilde{G}^{xy}_{\mathrm{HJ}} = \frac{1}{k_\rho^2}\left(k_x^2 I^{\mathrm{TE}}_{J_\rho} + k_y^2 I^{\mathrm{TM}}_{J_\rho}\right)$
$\widetilde{G}^{yy}_{\mathrm{EJ}} = -\frac{1}{k_\rho^2}\left(k_x^2 V^{\mathrm{TE}}_{J_\rho} + k_y^2 V^{\mathrm{TM}}_{J_\rho}\right)$	$\widetilde{G}^{yy}_{\mathrm{HJ}} = \frac{k_x k_y}{k_\rho^2}\left(I^{\mathrm{TE}}_{J_\rho} - I^{\mathrm{TM}}_{J_\rho}\right)$
$\widetilde{G}^{zy}_{\mathrm{EJ}} = -\frac{k_y}{\omega\varepsilon} I^{\mathrm{TM}}_{J_\rho}$	$\widetilde{G}^{zy}_{\mathrm{HJ}} = \frac{k_x}{\omega\mu} V^{\mathrm{TE}}_{J_\rho}$
$\widetilde{G}^{xz}_{\mathrm{EJ}} = -\frac{k_x}{\omega\varepsilon'} V^{\mathrm{TM}}_{J_z}$	$\widetilde{G}^{xz}_{\mathrm{HJ}} = \frac{k_y}{\omega\varepsilon'} I^{\mathrm{TM}}_{J_z}$
$\widetilde{G}^{yz}_{\mathrm{EJ}} = -\frac{k_y}{\omega\varepsilon'} V^{\mathrm{TM}}_{J_z}$	$\widetilde{G}^{yz}_{\mathrm{HJ}} = \frac{k_x}{\omega\varepsilon'} I^{\mathrm{TM}}_{J_z}$
$\widetilde{G}^{zz}_{\mathrm{EJ}} = -\frac{k_\rho^2}{\omega^2\varepsilon\varepsilon'} I^{\mathrm{TM}}_{J_z}$	$\widetilde{G}^{zz}_{\mathrm{HJ}} = 0$

Magnetic Source	
$\widetilde{G}^{xx}_{\mathrm{EM}} = -\frac{k_x k_y}{k_\rho^2}\left(V^{\mathrm{TE}}_{M_\rho} - V^{\mathrm{TM}}_{M_\rho}\right)$	$\widetilde{G}^{xx}_{\mathrm{HM}} = -\frac{1}{k_\rho^2}\left(k_x^2 I^{\mathrm{TE}}_{M_\rho} + k_y^2 I^{\mathrm{TM}}_{M_\rho}\right)$
$\widetilde{G}^{yx}_{\mathrm{EM}} = \frac{1}{k_\rho^2}\left(k_x^2 V^{\mathrm{TE}}_{M_\rho} + k_y^2 V^{\mathrm{TM}}_{M_\rho}\right)$	$\widetilde{G}^{yx}_{\mathrm{HM}} = -\frac{k_x k_y}{k_\rho^2}\left(I^{\mathrm{TE}}_{M_\rho} - I^{\mathrm{TM}}_{M_\rho}\right)$
$\widetilde{G}^{zx}_{\mathrm{EM}} = \frac{k_y}{\omega\varepsilon} I^{\mathrm{TM}}_{M_\rho}$	$\widetilde{G}^{zx}_{\mathrm{HM}} = -\frac{k_x}{\omega\mu} V^{\mathrm{TE}}_{M_\rho}$
$\widetilde{G}^{xy}_{\mathrm{EM}} = -\frac{1}{k_\rho^2}\left(k_y^2 V^{\mathrm{TE}}_{M_\rho} + k_x^2 V^{\mathrm{TM}}_{M_\rho}\right)$	$\widetilde{G}^{xy}_{\mathrm{HM}} = -\frac{k_x k_y}{k_\rho^2}\left(I^{\mathrm{TE}}_{M_\rho} - I^{\mathrm{TM}}_{M_\rho}\right)$
$\widetilde{G}^{yy}_{\mathrm{EM}} = \frac{k_x k_y}{k_\rho^2}\left(V^{\mathrm{TE}}_{M_\rho} - V^{\mathrm{TM}}_{M_\rho}\right)$	$\widetilde{G}^{yy}_{\mathrm{HM}} = -\frac{1}{k_\rho^2}\left(k_y^2 I^{\mathrm{TE}}_{M_\rho} + k_x^2 I^{\mathrm{TM}}_{M_\rho}\right)$
$\widetilde{G}^{zy}_{\mathrm{EM}} = -\frac{k_x}{\omega\varepsilon} I^{\mathrm{TM}}_{M_\rho}$	$\widetilde{G}^{zy}_{\mathrm{HM}} = -\frac{k_y}{\omega\mu} V^{\mathrm{TE}}_{M_\rho}$
$\widetilde{G}^{xz}_{\mathrm{EM}} = -\frac{k_y}{\omega\mu'} V^{\mathrm{TE}}_{M_z}$	$\widetilde{G}^{xz}_{\mathrm{HM}} = -\frac{k_x}{\omega\mu'} I^{\mathrm{TE}}_{M_z}$
$\widetilde{G}^{yz}_{\mathrm{EM}} = \frac{k_x}{\omega\mu'} V^{\mathrm{TE}}_{M_z}$	$\widetilde{G}^{yz}_{\mathrm{HM}} = -\frac{k_y}{\omega\mu'} I^{\mathrm{TE}}_{M_z}$
$\widetilde{G}^{zz}_{\mathrm{EM}} = 0$	$\widetilde{G}^{zz}_{\mathrm{HM}} = -\frac{k_\rho^2}{\omega^2\mu\mu'} V^{\mathrm{TE}}_{M_z}$

Table 2.1: Analytical expressions of the field Green's function components in a multilayered medium in terms of currents and voltages in the equivalent transmission lines.

as a Henkel (Fourier-Bessel) transformation, also called Sommerfeld integral

$$G(\rho, z, z') = \mathcal{S}_n\left\{\widetilde{G}(k_\rho, z, z')\right\} = \\ = \int_0^\infty J_n(k_\rho\rho) k_\rho^{n+1} \widetilde{G}(k_\rho, z, z')\,\mathrm{d}k_\rho, \tag{2.19}$$

Electric Source	Magnetic Source
$\widetilde{G}_A^{xx} = \frac{1}{\mathrm{j}\omega} V_{J_\rho}^{\mathrm{TE}}$	$\widetilde{G}_F^{xx} = \frac{1}{\mathrm{j}\omega} I_{M_\rho}^{\mathrm{TM}}$
$\widetilde{G}_A^{zx} = \mathrm{j}\mu \frac{k_x}{k_\rho^2} \left(I_{J_\rho}^{\mathrm{TE}} - I_{J_\rho}^{\mathrm{TM}} \right)$	$\widetilde{G}_F^{zx} = -\mathrm{j}\varepsilon \frac{k_x}{k_\rho^2} \left(V_{M_\rho}^{\mathrm{TE}} - V_{M_\rho}^{\mathrm{TM}} \right)$
$\widetilde{G}_A^{yy} = \frac{1}{\mathrm{j}\omega} V_{J_\rho}^{\mathrm{TE}}$	$\widetilde{G}_F^{xx} = \frac{1}{\mathrm{j}\omega} I_{M_\rho}^{\mathrm{TM}}$
$\widetilde{G}_A^{zy} = \mathrm{j}\mu \frac{k_y}{k_\rho^2} \left(I_{J_\rho}^{\mathrm{TE}} - I_{J_\rho}^{\mathrm{TM}} \right)$	$\widetilde{G}_F^{zx} = -\mathrm{j}\varepsilon \frac{k_y}{k_\rho^2} \left(V_{M_\rho}^{\mathrm{TE}} - V_{M_\rho}^{\mathrm{TM}} \right)$
$\widetilde{G}_A^{zz} = -\frac{\mathrm{j}\mu}{\omega\varepsilon'} I_{J_z}^{\mathrm{TM}}$	$\widetilde{G}_F^{zz} = -\frac{\mathrm{j}\varepsilon}{\omega\mu'} V_{M_z}^{\mathrm{TE}}$
$\widetilde{G}_{V_\rho} = -\frac{\mathrm{j}\omega}{k_\rho^2} \left(V_{J_\rho}^{\mathrm{TE}} - V_{J_\rho}^{\mathrm{TM}} \right)$	$\widetilde{G}_{W_\rho} = \frac{\mathrm{j}\omega}{k_\rho^2} \left(I_{M_\rho}^{\mathrm{TE}} - I_{M_\rho}^{\mathrm{TM}} \right)$
$\widetilde{G}_{V_z} = -\frac{\mathrm{j}\omega}{{k'_z}^2} V_{J_z}^{\mathrm{TM}}(z', z)$	$\widetilde{G}_{W_z} = -\frac{\mathrm{j}\omega}{{k'_z}^2} I_{M_z}^{\mathrm{TE}}(z', z)$

Table 2.2: Analytical expressions of the potential Green's function components in a multilayered medium in terms of currents and voltages in the equivalent transmission lines.

where J_n is the Bessel function of order n and $\widetilde{G}$ is a generic Green's function depending on the variable $k_\rho = \sqrt{k_x^2 + k_y^2}$ and the vertical positions of the observer (z) and source (z') points. In the case of simple functions like the ones involved in the expressions from Tables 2.1 and 2.2, it can be shown that only the Sommerfeld transformations of order $n = 0$, $n = 1$ or the combinations of the two are used. The correspondence between the spectral and space domains for various expressions of $\widetilde{G}$ can be summarized as in Table 2.3 (ϕ is the angle in cylindrical coordinates). The numerical evaluation of Sommerfeld integrals can be efficiently performed using specially tailored algorithms [2, 27].

Spectral domain	Space domain
$\widetilde{G}$	$\mathcal{S}_0 \left\{ \widetilde{G} \right\}$
$\mathrm{j}k_x \widetilde{G}$	$-\cos\phi \, \mathcal{S}_1 \left\{ \widetilde{G} \right\}$
$\mathrm{j}k_y \widetilde{G}$	$-\sin\phi \, \mathcal{S}_1 \left\{ \widetilde{G} \right\}$
$\mathrm{j}k_x \mathrm{j}k_x \widetilde{G}$	$\frac{\cos(2\phi)}{\rho} \mathcal{S}_1 \left\{ \widetilde{G} \right\} - \cos^2\phi \, \mathcal{S}_0 \left\{ k_\rho^2 \widetilde{G} \right\}$
$\mathrm{j}k_y \mathrm{j}k_y \widetilde{G}$	$-\frac{\cos(2\phi)}{\rho} \mathcal{S}_1 \left\{ \widetilde{G} \right\} - \sin^2\phi \, \mathcal{S}_0 \left\{ k_\rho^2 \widetilde{G} \right\}$
$\mathrm{j}k_x \mathrm{j}k_y \widetilde{G}$	$\frac{\sin(2\phi)}{\rho} \mathcal{S}_1 \left\{ \widetilde{G} \right\} - \frac{1}{2}\sin(2\phi) \, \mathcal{S}_0 \left\{ k_\rho^2 \widetilde{G} \right\}$

Table 2.3: Correspondence between the spectral and space domain GFs.

2.6 Green's Functions for Shielded Planar Multilayered Structures

The starting point in computing the shielded Green's functions is the fact that the spectral values of any Green's function are readily available in closed-form for laterally unbounded stratified media [15]. This includes as a particular case the "covered" stripline geometry, where the layered medium is terminated by two metallic horizontal layers. From these spectral values, the spatial Green's functions are recovered as two-dimensional inverse Fourier transforms.

2.6.1 Space or Image Formulation

Let us assume that we know the covered Green's function G_C for a specific problem, and we want the shielded (boxed) Green's function G_B, corresponding to the introduction of four lateral vertical walls at $x = 0, a$ and $y = 0, b$ (Fig. 2.3). Using the image theory, we first define a "basic image set" (BIS) finding the images with respect to the walls $x = 0$ and $y = 0$. Thus, we have

$$G_{\mathrm{BIS}}(x, y|x', y') = \\ G_{\mathrm{C}}(x, y|x', y') + s_x G_{\mathrm{C}}(x, y|-x', y') + s_y G_{\mathrm{C}}(x, y|x', -y') + s_x s_y G_{\mathrm{C}}(x, y|-x', -y'), \quad (2.20)$$

where the dependence with z and z' is understood and suppressed. The "signs" s_x and s_y depend on the type of potentials [15]. Table 2.4 gives the values for the potential Green's functions for electric and magnetic sources.

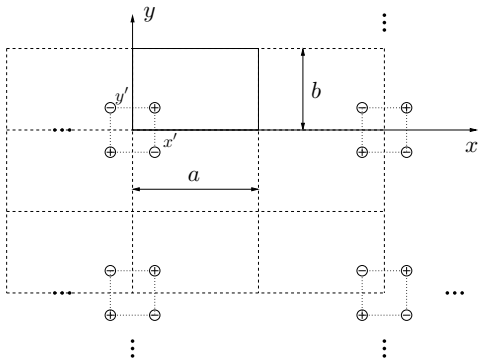

Figure 2.3: Spatial images for a single point charge needed to satisfy boundary conditions at lateral metallic walls.

Now, the boxed Green's function is just an infinite double sum of basic image sets periodically translated along the coordinates x and y

$$G_{\mathrm{B}} = \sum_{m=-\infty}^{\infty} \sum_{n=-\infty}^{\infty} G_{\mathrm{BIS}}(x, y|x' + 2ma, y' + 2nb). \quad (2.21)$$

-	s_x	s_y	$f_x(k,x)$	$f_y(k,y)$
G_A^{xx}	$+1$	-1	$\cos(kx)$	$\sin(ky)$
G_A^{yy}	-1	$+1$	$\sin(kx)$	$\cos(ky)$
G_V	-1	-1	$\sin(kx)$	$\sin(ky)$
G_F^{xx}	-1	$+1$	$\sin(kx)$	$\cos(ky)$
G_F^{yy}	$+1$	-1	$\cos(kx)$	$\sin(ky)$
G_W	$+1$	$+1$	$\cos(kx)$	$\cos(ky)$

Table 2.4: The signs associated to each electric and magnetic potential Green's function.

2.6.2 Spectral or Modal Formulation

If Poisson's sum formula [28] is applied to (2.21), we obtain the result

$$G_{\mathrm{B}} = \sum_{m=0}^{\infty}\sum_{n=0}^{\infty} \widetilde{G}(k_{xm}, k_{yn}) f_x(k_{xm}, x) f_x(k_{xm}, x') f_y(k_{yn}, y) f_y(k_{yn}, y'), \tag{2.22}$$

where $k_{xm} = m\pi/a$, $k_{yn} = n\pi/b$, and the factors f are sin / cos functions depending again on the type of potential (Table 2.4).

This is the modal formulation of the boxed Green's functions, since the functions f are directly related to the eigenmodes of a rectangular waveguide of a cross section $a \times b$. Indeed, the modal formulation can directly be obtained by starting with an infinite (along z) waveguide problem and matching all the necessary boundary conditions in the $z = \text{const.}$ planes. For other box sections (for instance circular cylindrical cavities), where the image approach is cumbersome, a direct evaluation of the modal Green's function, using the corresponding waveguide analysis, could be the best approach.

2.6.3 Algorithms for Acceleration of Slowly Convergent Series

Both infinite sums in (2.21) and (2.22) are slowly convergent. The image sum is converging faster when the observer point is close to the source point, since the singularity in the source point is perfectly included in the expression. However, close to the lateral cavity or waveguide walls, the image sum is converging very slowly, since the boundary conditions on the lateral walls are going to be satisfied only when infinite number of images is taken into account. The modal sum, on the other hand, behaves in the opposite way. Each term in the modal sum satisfies the boundary conditions at the lateral walls, and hence, the convergence of this sum is faster close to the walls. However, only infinite number of modes taken into account will recover the singularity at the source point, leading, therefore, to the slow convergence of the modal sum in the region close to the source point.

There is a number of acceleration techniques that can be used to speed-up the convergence of the image or modal sums, a thorough overview of which can be found in [29]. They can be divided into two main groups: general and specific methods. A general method can be applied to any sequence, which can be obtained from an infinite series. Examples of such methods are the Euler transformation [30], Shanks' transformation [31, 32, 33], Wynn's ε algo-

rithm [34], the Chebyshev-Toeplitz algorithm [35, 36], the Θ-algorithm [37, 38], and the Levin's T-transform [39]. On the other hand, specific methods are derived by analytically working on the kernel of a series and, therefore, can be applied only on their own types. In general, they usually work better than the general methods. The Kummer's transformation [32, 40, 41], summation by parts algorithm [42, 43], specially truncated set of images [42, 44], and the Ewald's transformation [45] are the examples. In the following sections, we will treat in more detail the specially truncated set of images technique, used to speed up the convergence of image sums, and the Ewald transform, as an example where modal and image formulations are successfully combined in a fast converging series.

2.6.4 Specially Truncated Set of Images[†]

This technique has been developed in order to try to alleviate the problem of the slow convergence rate of the spatial image series derived in (2.21). The idea behind the technique is simple and very intuitive, and it is based on the fact that there are two main features in any shielded Green's function that must be preserved in order to obtain accurate results, namely:

- The singular behavior when $\rho \to 0$.
- The boundary conditions on all lateral cavity walls.

The singular behavior is naturally preserved in the developed series of images, because it has been constructed using standard Green's functions. What remains then is the accurate imposition of the boundary conditions on the metallic walls. This can be approximately done by simply adding the first few image layers of the series, and then computing the needed strength of the images that remain in the last image layer so that the boundary conditions for the fields are strictly satisfied at the points on lateral metallic walls. The approach is, thus, based on the following approximation of the boxed Green's function

$$G_{\mathrm{B}}(\mathbf{r}|\mathbf{r}') \approx G_{\mathrm{C}}(\mathbf{r}|\mathbf{r}') + \sum_{k=1}^{N_{\mathrm{in}}} s(\mathbf{r}_{\mathrm{in}}^{(k)}) G_{\mathrm{C}}(\mathbf{r}|\mathbf{r}_{\mathrm{in}}^{(k)}) + \sum_{k=1}^{N_{\mathrm{out}}} q_k G_{\mathrm{C}}(\mathbf{r}|\mathbf{r}_{\mathrm{out}}^{(k)}), \tag{2.23}$$

where $\mathbf{r}$ is the point inside the cavity at which the Green's function is calculated and $\mathbf{r}'$ is the position of the source. In this approach the finite number of images N_{in} is taken with their original signs $s(\mathbf{r}_{\mathrm{in}}^{(k)}) \in \{-1, +1\}$ depending on the position of the image and the type of the source. The space of N layers contains $N_{\mathrm{in}} = (2N+1)^2 - 1$ images. The sum is truncated and the images around the last layer placed at the points $\mathbf{r}_{\mathrm{out}}^{(k)}$ have complex coefficients q_k in order to satisfy the boundary conditions on the lateral cavity walls. The number of these images is $N_{\mathrm{out}} = 8(N+1)$. In Fig. 2.4(a) an example with $N = 2$ image layers is shown.

Let S_x and S_y represent two sets of points placed on $x = 0$, a and $y = 0$, b cavity borders, respectively. The boundary conditions for potential Green's functions for electric source in a

[†] I. Stevanović and J. R. Mosig (2002), in *Proc. International Symposium on Antennas (JINA02)*, Nice, 12-14 Nov. 2002, vol. 1, pp. 35–38.

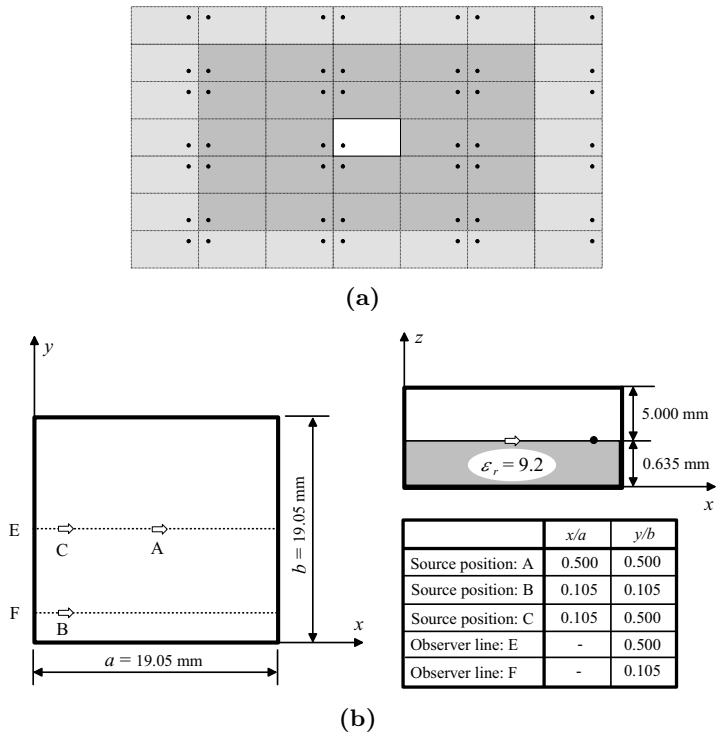

Figure 2.4: (a) Spatial images for the presented approach. (b) Studied boxed microstrip structure.

cavity can be expressed now as follows

$$G_{\mathrm{BV}}(\mathbf{r}) = 0, \;\; \mathbf{r} \in S_x \cup S_y \tag{2.24}$$

$$\begin{aligned} G^{xx}_{\mathrm{BA}}(\mathbf{r}) &= 0, \;\; \mathbf{r} \in S_y, \quad \frac{\partial}{\partial x} G^{xx}_{\mathrm{BA}}(\mathbf{r}) = 0, \;\; \mathbf{r} \in S_x, \\ G^{yy}_{\mathrm{BA}}(\mathbf{r}) &= 0, \;\; \mathbf{r} \in S_x, \quad \frac{\partial}{\partial y} G^{yy}_{\mathrm{BA}}(\mathbf{r}) = 0, \;\; \mathbf{r} \in S_y. \end{aligned} \tag{2.25}$$

After imposing the boundary conditions at points $\mathbf{r}_{\mathrm{o}}^{(l)}$, $l = 1, 2, ..., N_{\mathrm{out}}$, placed at the lateral cavity walls, the following systems of linear equations are obtained.

For the electric scalar potential Green's function G_{BV} one has

$$\sum_{k=1}^{N_{\mathrm{out}}} q_k G_{CV}(\mathbf{r}_{\mathrm{o}}^{(l)}|\mathbf{r}_{\mathrm{out}}^{(k)}) = -G_{CV}(\mathbf{r}_{\mathrm{o}}^{(l)}|\mathbf{r}') - \sum_{k=1}^{N_{\mathrm{in}}} s(\mathbf{r}_{\mathrm{in}}^{(k)}) G_{\mathrm{CV}}(\mathbf{r}_{\mathrm{o}}^{(l)}|\mathbf{r}_{\mathrm{in}}^{(k)}), \;\; l = 1, 2, ..., N_{\mathrm{out}} \tag{2.26}$$

The complex coefficients for the magnetic vector potential Green's function G^{xx}_{BA}, are given by the following system of equations

$$\sum_{k=1}^{N_{\mathrm{out}}} q_k G_{CA}(\mathbf{r}_{\mathrm{o}}^{(l)}|\mathbf{r}_{\mathrm{out}}^{(k)}) = \; - G_{\mathrm{CA}}(\mathbf{r}_{\mathrm{o}}^{(l)}|\mathbf{r}') - \sum_{k=1}^{N_{\mathrm{in}}} s(\mathbf{r}_{\mathrm{in}}^{(k)}) G_{CA}(\mathbf{r}_{\mathrm{o}}^{(l)}|\mathbf{r}_{\mathrm{in}}^{(k)}), \tag{2.27a}$$

where $\mathbf{r}_{\rm o}^{(l)} \in S_y,\ \ l = 1, 2, ..., N_{\rm out}$ and

$$\sum_{k=1}^{N_{\rm out}} q_k \left[G_{CA}(\mathbf{r}_{\rm o}^{(l)} + \Delta x \hat{x} | \mathbf{r}_{\rm out}^{(k)}) - G_{CA}(\mathbf{r}_{\rm o}^{(l)} | \mathbf{r}_{\rm out}^{(k)}) \right] =$$

$$- \left[G_{\rm CA}(\mathbf{r}_{\rm o}^{(l)} + \Delta x \hat{x} | \mathbf{r}') - G_{\rm CA}(\mathbf{r}_{\rm o}^{(l)} | \mathbf{r}') \right] - \sum_{k=1}^{N_{\rm in}} s(\mathbf{r}_{\rm in}^{(k)}) \left[G_{CA}(\mathbf{r}_{\rm o}^{(l)} + \Delta x \hat{x} | \mathbf{r}_{\rm in}^{(k)}) - G_{CA}(\mathbf{r}_{\rm o}^{(l)} | \mathbf{r}_{\rm in}^{(k)}) \right] \tag{2.27b}$$

where $\mathbf{r}_{\rm o}^{(l)} \in S_x,\ \ l = 1, 2, ..., N_{\rm out}$.

An analogous system of equations is obtained for the second dyad component of the magnetic vector potential Green's function $G_{\rm BA}^{yy}$. In the above expressions, G_{CV} and G_{CA} are covered scalar potential and vector potential GFs, respectively, calculated when no lateral walls are taken into account, and Δx is the vanishing distance used to numerically compute the derivatives appearing in the Neumann boundary conditions on the walls.

The unknown coefficients for every GF are easily found by solving these systems of linear equations. Then turning back to (2.23), the corresponding boxed Green's functions are recovered for every pair of source and observer points inside the cavity. It is interesting to note that the procedure holds also for any field GF, and one needs only to apply the right boundary conditions on the lateral metallic walls.

Some Numerical Results

As an example, we consider the geometry of Fig. 2.4(b) (a metallic box of dimensions $10.95 \times 10.95 \times 5.635\,\text{mm}^3$ along the x-, y- and z-axis, enclosing a ceramic-air configuration). The dielectric substrate (ceramic) has a thickness $h = 0.635$ mm and a dielectric constant $\varepsilon_r = 9.2$. We have located a point source in the air-dielectric interface at $x' = y' = 2$ mm (point B), i.e., rather close to a vertical edge of the box. We explore the behavior of the Green's function for the scalar potential as the observation point moves, also in the interface, along the straight line F, passing through the source [Fig. 2.4(b)]. Fig. 2.5 gives the obtained results for several frequencies: well below resonance [4 GHz, Fig. 2.5(a)], at resonance [10.49 GHz, Fig. 2.5(b)], and above the cavity's second resonance [24 GHz, Fig. 2.5(c)]. The results are computed using the new method developed in this section (solid line) and the summation by parts algorithm (•) [42, 43], showing that there is a very good agreement between the two approaches. In all computations, three image layers were taken into account (48 images with their original signs and 32 complex images). Fig. 2.6 shows G_A^{xx} and G_A^{yy} components of a dyadic magnetic vector potential Green's functions computed at different frequencies.

The solution obtained using the truncated set of images fulfills the reciprocity theorem, as it can be seen from Fig. 2.7. First, the source is fixed at the point B and the observer is being moved along the diagonal of the box (solid black line). Then, the roles between the source and the observer are interchanged, the observer is placed at the point B and the source is being moved along the diagonal (dashed gray line). The relative difference between two Green's functions computed this way is less than 0.1 % at the operating frequency $f = 24$ GHz.

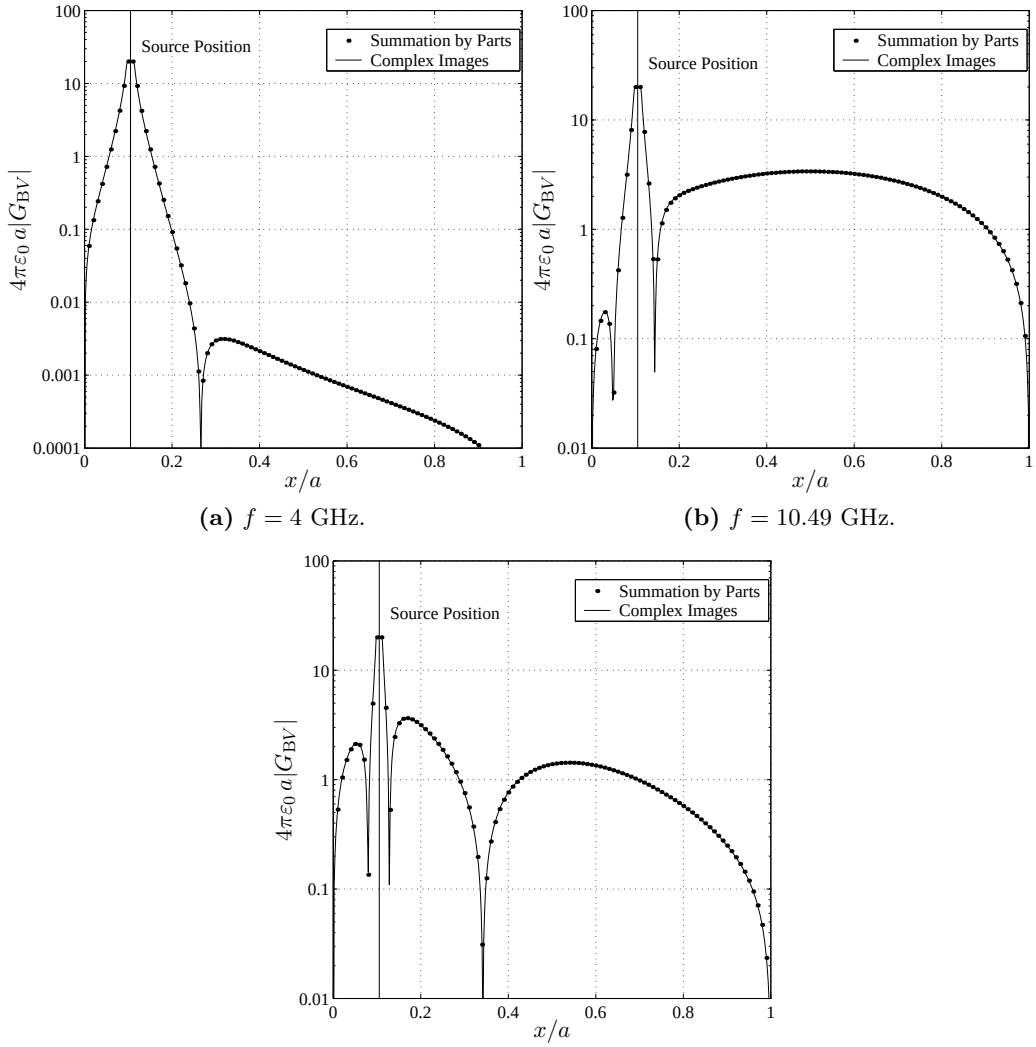

(a) $f = 4$ GHz.

(b) $f = 10.49$ GHz.

(c) $f = 24$ GHz.

Figure 2.5: Boxed potential Green's functions for the structure shown in Fig. 2.4(b). The source is at position B and the observer is moving along the line F. Boxed Green's functions are computed using the summation by parts algorithm (dotted) and specially truncated set of images (solid line).

Fig. 2.8 shows the results at the second resonance of the cavity ($f = 20.525$ GHz) for observation points located anywhere in the air-dielectric interface. The singularity of the function (lower-left corner) is dwarfed by the strong resonant behaviour of the boxed Green's function. The three-dimensional plot of Fig. 2.9 enlarges the information of Fig. 2.5(c), presenting the results at 24 GHz. Here the complex behavior of the boxed GFs is evident, combining singularity effects, zero values at the boundary and interesting patterns of standing waves, produced by the interaction between the different cavity modes.

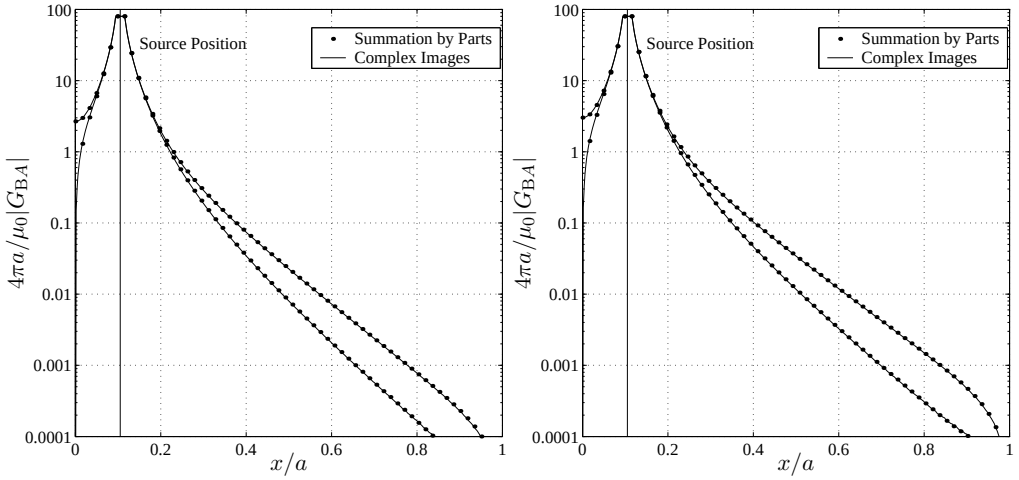

(a) $f = 4$ GHz.

(b) $f = 10.49$ GHz.

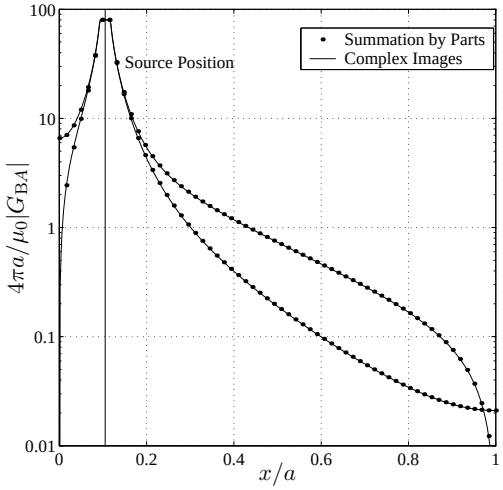

(c) $f = 24$ GHz.

Figure 2.6: Boxed magnetic vector potential Green's functions for the structure shown in Fig. 2.4(b). The source is at position B and the observer is moving along the line F. Boxed Green's functions are computed using the summation by parts algorithm (dotted) and specially truncated set of images (solid line).

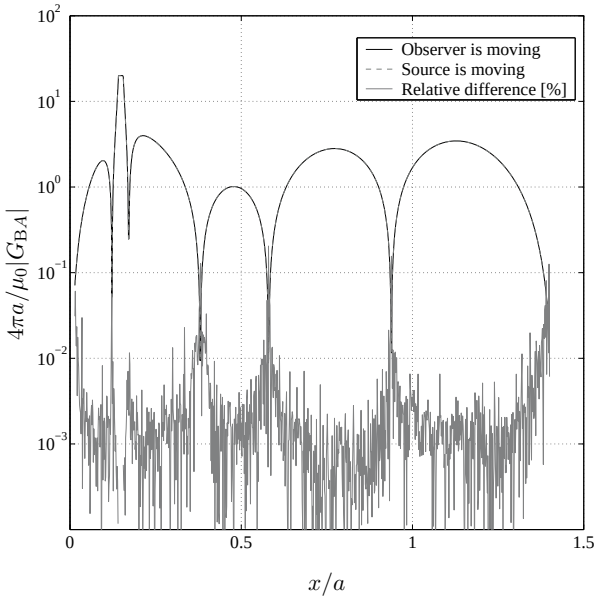

Figure 2.7: The reciprocity theorem.

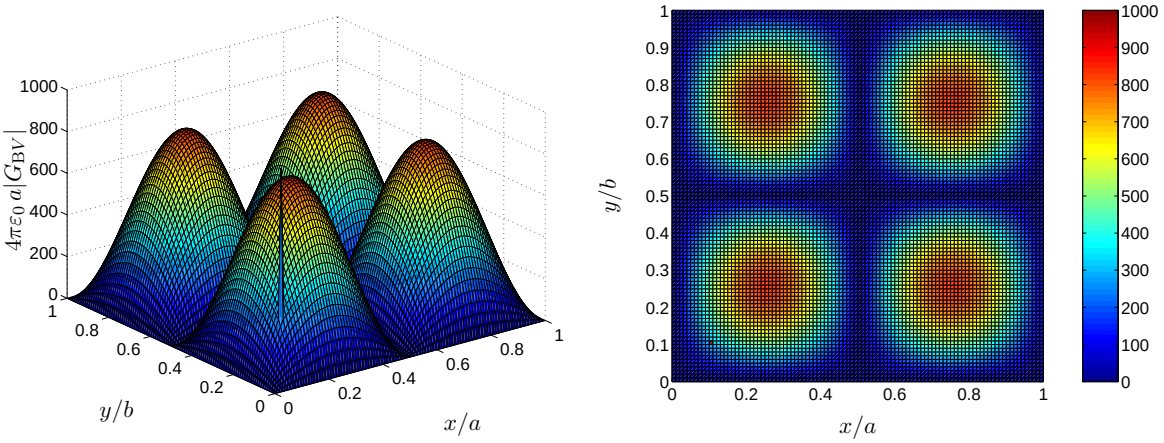

(a) Three-dimensional plot. **(b)** Contour plot.

Figure 2.8: Boxed electric scalar potential Green's function for the structure shown in Fig. 2.4(b) computed using specially truncated set of images. Second resonance of the box (f = 20.525 GHz).

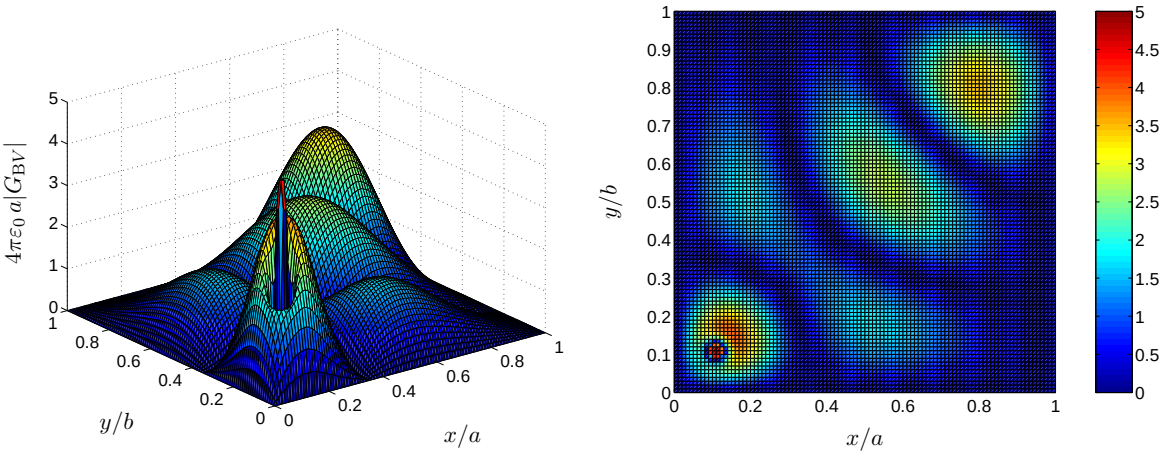

(a) Three-dimensional plot. **(b)** Contour plot.

Figure 2.9: Boxed electric scalar potential Green's function for the structure shown in Fig. 2.4(b) computed using specially truncated set of images. Frequency 24 GHz.

Discussion

The specially truncated set of images in computing boxed Green's functions uses Sommerfeld-type Green's functions for laterally unbounded stratified media. The computation of these functions is a standard and well-known procedure. The approach is valid for any field and potential Green's functions, provided the right boundary conditions at the lateral metallic walls. Convergence with the specially truncated set of images is relatively fast and using three inner image layers yields good accuracy when compared to the summation by parts algorithm.

However, there are some serious drawbacks in using this technique when solving boxed structures. The major one is the time needed for computing the Green's function.

For every position of the source point, there is a system of linear equations to be solved in order to obtain the unknown complex image values. If N image layers are used, the dimension of the system of linear equations is given by $N_{\mathrm{out}} = 8(N+1)$ and so the time for solving the system grows as $\mathcal{O}(N^3)$ when direct inversion is used. As the number of image layers grows, the accuracy of the computed Green's function is higher, but the time needed for computing the Green's function becomes larger, thus leading to prohibitively long simulations.

2.6.5 Ewald Transform

The Ewald transformation is a powerful method for various periodic problems that efficiently combines the modal and image formulations of the Green's functions. It has been successfully used in the efficient Green's function computation of 2-D free-space periodic structures [45, 46], rectangular waveguides [47], and rectangular cavities [48, 49]. The method has been extended to multilayered planar periodic structures [50], and shielded planar structures [51], being

computationally more expensive as it involves the approximation of spectral domain Green's functions by the Generalized Pencil-of-Function (GPOF) method [52].

In this section, we present the details of the Ewald method used to compute the rectangular cavity potential Green's functions.

Ewald Method Applied to Rectangular Cavity Potential Green's Functions

Any potential Green's function inside a rectangular cavity has in its expression the infinite sum of the basic image sets periodically translated along the x, y and z axes

$$\Psi = \frac{1}{4\pi} \sum_{m,n,p=-\infty}^{+\infty} \sum_{i=0}^{7} S_i \frac{\mathrm{e}^{-\mathrm{j}kR_{i,mnp}}}{R_{i,mnp}}, \tag{2.28}$$

where $S_i \in \{A_i^{ss}, F_i^{ss}, V_i, W_i\}$ represent the signs of the images in the basic image sets for the corresponding potential Green's function as defined in Tables 2.5 and 2.6. In the same expression, $R_{i,mnp}$ is given by

$$R_{i,mnp} = \sqrt{(X_i + 2ma)^2 + (Y_i + 2nb)^2 + (Z_i + 2pc)^2}, \tag{2.29}$$

where X_i, Y_i and Z_i are the distances between the observer and images in basic image set and their values are defined for every image in a basic image set in the same tables. Variables X_i, Y_i and Z_i depend on the position of the image in the basic image set. Figs. 2.10–2.13 illustrate the basic image sets for some potential Green's function components.

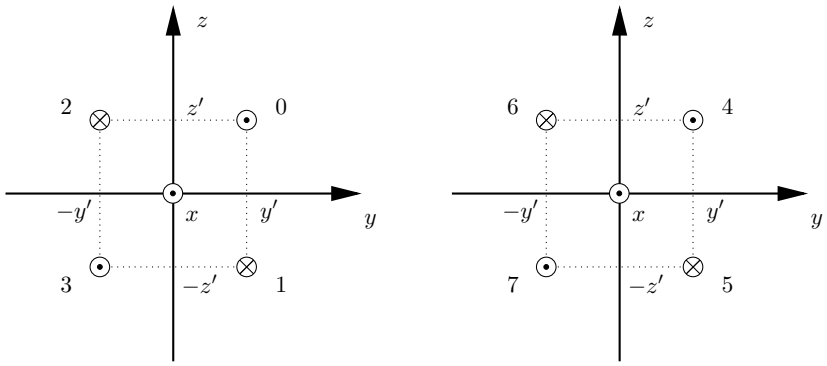

(a) $x = x'$. **(b)** $x = -x'$.

Figure 2.10: Basic Image Set for G_A^{xx}.

Following Ewald [45, 53], we use the identity

$$\frac{\mathrm{e}^{-\mathrm{j}kR}}{R} = \frac{2}{\sqrt{\pi}} \int_0^{\infty} \mathrm{e}^{-R^2 s^2 + \frac{k^2}{4s^2}} \, \mathrm{d}s. \tag{2.30}$$

The Green's function, given by (2.28), can be written in two parts by using (2.30) and splitting

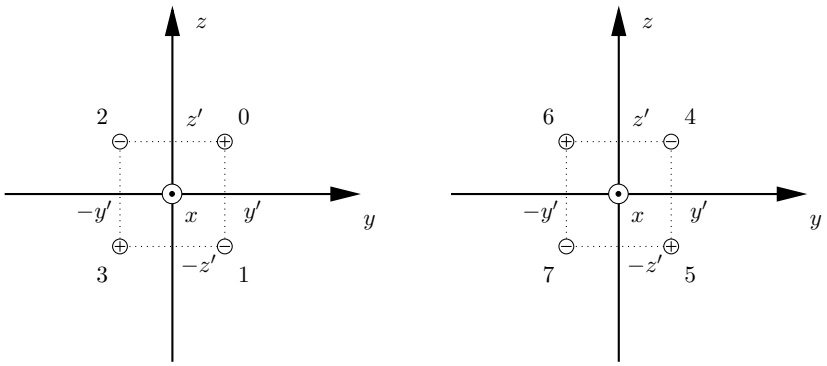

(a) $x = x'$. **(b)** $x = -x'$.

Figure 2.11: Basic Image Set for G_V.

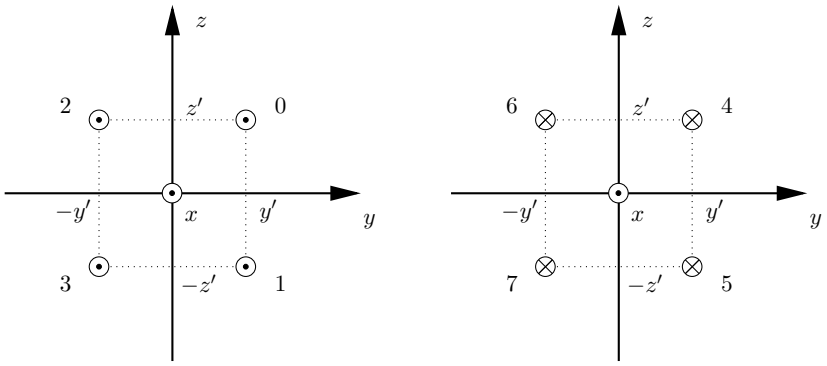

(a) $x = x'$. **(b)** $x = -x'$.

Figure 2.12: Basic Image Set for G_F^{xx}.

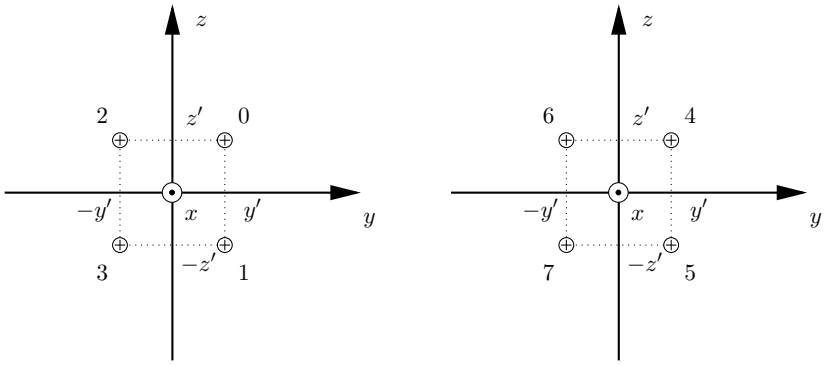

(a) $x = x'$. **(b)** $x = -x'$.

Figure 2.13: Basic Image Set for G_W.

i	position	X_i	Y_i	Z_i	A_i^{xx}	A_i^{yy}	A_i^{zz}	V_i
0	$(+x', +y', +z')$	$x - x'$	$y - y'$	$z - z'$	$+1$	$+1$	$+1$	$+1$
1	$(+x', +y', -z')$	$x - x'$	$y - y'$	$z + z'$	-1	-1	$+1$	-1
2	$(+x', -y', +z')$	$x - x'$	$y + y'$	$z - z'$	-1	$+1$	-1	-1
3	$(+x', -y', -z')$	$x - x'$	$y + y'$	$z + z'$	$+1$	-1	-1	$+1$
4	$(-x', +y', +z')$	$x + x'$	$y - y'$	$z - z'$	$+1$	-1	-1	-1
5	$(-x', +y', -z')$	$x + x'$	$y - y'$	$z + z'$	-1	$+1$	-1	$+1$
6	$(-x', -y', +z')$	$x + x'$	$y + y'$	$z - z'$	-1	-1	$+1$	$+1$
7	$(-x', -y', -z')$	$x + x'$	$y + y'$	$z + z'$	$+1$	$+1$	$+1$	-1

Table 2.5: Basic Image Set parameters associated to potential Green's functions of an electric source.

i	position	X_i	Y_i	Z_i	F_i^{xx}	F_i^{yy}	F_i^{zz}	W_i
0	$(+x', +y', +z')$	$x - x'$	$y - y'$	$z - z'$	$+1$	$+1$	$+1$	$+1$
1	$(+x', +y', -z')$	$x - x'$	$y - y'$	$z + z'$	$+1$	$+1$	-1	$+1$
2	$(+x', -y', +z')$	$x - x'$	$y + y'$	$z - z'$	$+1$	-1	$+1$	$+1$
3	$(+x', -y', -z')$	$x - x'$	$y + y'$	$z + z'$	$+1$	-1	-1	$+1$
4	$(-x', +y', +z')$	$x + x'$	$y - y'$	$z - z'$	-1	$+1$	$+1$	$+1$
5	$(-x', +y', -z')$	$x + x'$	$y - y'$	$z + z'$	-1	$+1$	-1	$+1$
6	$(-x', -y', +z')$	$x + x'$	$y + y'$	$z - z'$	-1	-1	$+1$	$+1$
7	$(-x', -y', -z')$	$x + x'$	$y + y'$	$z + z'$	-1	-1	-1	$+1$

Table 2.6: Basic Image Set parameters associated to potential Green's functions of a magnetic source.

the path of integration at E in (2.30):

$$\int_0^\infty (\cdot) = \int_0^E (\cdot) + \int_E^\infty (\cdot). \tag{2.31}$$

Thus we define

$$\Psi = \Psi_1 + \Psi_2, \tag{2.32}$$

where

$$\Psi_1 = \frac{1}{4\pi} \sum_{m,n,p} \sum_{i=0}^{7} S_i \frac{2}{\sqrt{\pi}} \int_0^E \mathrm{e}^{-R_{i,mnp}^2 s^2 + \frac{k^2}{4s^2}} \, \mathrm{d}s \tag{2.33}$$

and

$$\Psi_2 = \frac{1}{4\pi} \sum_{m,n,p} \sum_{i=0}^{7} S_i \frac{2}{\sqrt{\pi}} \int_E^\infty \mathrm{e}^{-R_{i,mnp}^2 s^2 + \frac{k^2}{4s^2}} \, \mathrm{d}s. \tag{2.34}$$

The integral in (2.33) can be solved using the Poisson 3-D summation formula, while (2.34)

is obtained straightforwardly applying the identity

$$\int_r^\infty \mathrm{e}^{-p^2s^2+\frac{q^2}{4s^2}}\,\mathrm{d}s = \frac{\sqrt{\pi}}{4p}\left(\mathrm{e}^{-\mathrm{j}pq}\,\mathrm{erfc}(pr-\mathrm{j}\frac{q}{2r}) + \mathrm{e}^{\mathrm{j}pq}\,\mathrm{erfc}(pr+\mathrm{j}\frac{q}{2r})\right). \tag{2.35}$$

Using the Ewald transformation, the potential Green's functions in rectangular cavity can be summarized by the following equations

$$G = \kappa\Psi \tag{2.36a}$$

$$\Psi = \Psi_1 + \Psi_2, \tag{2.36b}$$

$$\Psi_1 = \frac{1}{abc}\sum_{m,n,p=0}^{+\infty} \varepsilon_m\varepsilon_n\varepsilon_p k_{mnp} f(k_{x_m}x, k_{x_m}x')g(k_{y_n}y, k_{y_n}y')h(k_{z_p}z, k_{z_p}z') \tag{2.36c}$$

where

$$k_{mnp} = \frac{\mathrm{e}^{-\frac{\alpha_{mnp}^2}{4E^2}}}{\alpha_{mnp}^2}, \tag{2.36d}$$

$$\alpha_{mnp} = \left(\frac{m\pi}{a}\right)^2 + \left(\frac{n\pi}{b}\right)^2 + \left(\frac{p\pi}{c}\right)^2 - k^2 \tag{2.36e}$$

$$\varepsilon_\nu = \begin{cases} 1, & \nu = 0 \\ 2, & \nu > 0 \end{cases} \tag{2.36f}$$

$$\Psi_2 = \sum_{m,n,p}\sum_{i=0}^{7} \frac{S_i}{8\pi R_{i,mnp}}\left(\mathrm{e}^{-\mathrm{j}kR_{i,mnp}}\,\mathrm{erfc}(R_{i,mnp}E - \mathrm{j}\frac{k}{2E}) + \mathrm{e}^{\mathrm{j}kR_{i,mnp}}\,\mathrm{erfc}(R_{i,mnp}E + \mathrm{j}\frac{k}{2E})\right) \tag{2.36g}$$

where

$$X_i = \begin{cases} x - x', & i = 0,\ 1,\ 2,\ 3 \\ x + x', & i = 4,\ 5,\ 6,\ 7 \end{cases} \tag{2.36h}$$

$$Y_i = \begin{cases} y - y', & i = 0,\ 1,\ 4,\ 5 \\ y + y', & i = 2,\ 3,\ 6,\ 7 \end{cases} \tag{2.36i}$$

$$Z_i = \begin{cases} z - z', & i = 0,\ 2,\ 4,\ 6 \\ z + z', & i = 1,\ 3,\ 5,\ 7 \end{cases} \tag{2.36j}$$

$$R_{i,mnp} = \sqrt{(X_i + 2ma)^2 + (Y_i + 2nb)^2 + (Z_i + 2pc)^2} \tag{2.36k}$$

and A_i^{ss}, V_i, F_i^{ss}, W_i being defined in Tables 2.5 and 2.6.

The complementary error function which appears in both series Ψ_1 and Ψ_2 makes these series converge rapidly. The best choice for the splitting parameter E is the one that balances the rate of decay of the two series, making Ψ_1 and Ψ_2 contribute an equal number of terms

G	κ	$f(x,x')$	$g(y,y')$	$h(z,z')$	S_i
G_A^{xx}	μ	$\cos x \cos x'$	$\sin y \sin y'$	$\sin z \sin z'$	A_i^{xx}
G_A^{yy}	μ	$\sin x \sin x'$	$\cos y \cos y'$	$\sin z \sin z'$	A_i^{yy}
G_A^{zz}	μ	$\sin x \sin x'$	$\sin y \sin y'$	$\cos z \cos z'$	A_i^{zz}
G_V	$\frac{1}{\varepsilon}$	$\sin x \sin x'$	$\sin y \sin y'$	$\sin z \sin z'$	V_i
G_F^{xx}	ε	$\sin x \sin x'$	$\cos y \cos y'$	$\cos z \cos z'$	F_i^{xx}
G_F^{yy}	ε	$\cos x \cos x'$	$\sin y \sin y'$	$\cos z \cos z'$	F_i^{yy}
G_F^{zz}	ε	$\cos x \cos x'$	$\cos y \cos y'$	$\sin z \sin z'$	F_i^{zz}
G_W	$\frac{1}{\mu}$	$\cos x \cos x'$	$\cos y \cos y'$	$\cos z \cos z'$	W_i

Table 2.7: The parameters for the potential Green's functions in rectangular cavity, computed using Ewald transformation.

to the final value Ψ. The approximation to the optimal value of E for 2-D series (rectangular waveguide Green's functions or 2-D periodic Green's functions [45]), is given by

$$E = \frac{\pi}{\sqrt{ab}}.$$

In the case of 3-D sums, the optimal parameter is given by [54]

$$E = \left(\pi^2 \frac{\frac{1}{a^2} + \frac{1}{b^2} + \frac{1}{c^2}}{a^2 + b^2 + c^2} \right)^{1/4}.$$

Convergence Study

The method is tested on a rectangular cavity whose side dimensions ($a = b = c$) are all equal to $L = 0.998\lambda_0$ (the case when the operating frequency is very close to the resonance frequency of the cavity).

In Fig. 2.14 the convergence of the Green's function computed using the Ewald sum method for three different cases is shown. The source point is fixed at the center of the cavity ($x' = y' = z' = 0.5L$) and three observation points are selected along the diagonal of the cavity, far from the source point ($x = y = z = 0.1L$), near the source point ($x = y = z = 0.49L$), and around the midpoint of these two ($x = y = z = 0.3L$). The number of iterations N_{it} means that $m, n, p \in [0, N_{\text{it}}]$ for Ψ_1 in (2.36c) and $m, n, p \in [-N, N]$, for Ψ_2 in (2.36g), where $N = \lfloor \frac{N_{\text{it}}}{2} \rfloor$. The reference values are obtained by the Ewald sum method with sufficiently large number of terms (30 terms in both Ewald sums for every axis). Fig. 2.14 shows that the calculations by the Ewald sum method has very rapid convergence in all three cases considered.

2.7 Excitation and Port Description

The excitation and port description are very specific steps and tightly dependent on the nature of the problem (see [55, 56, 57] for some practical examples). These steps provide

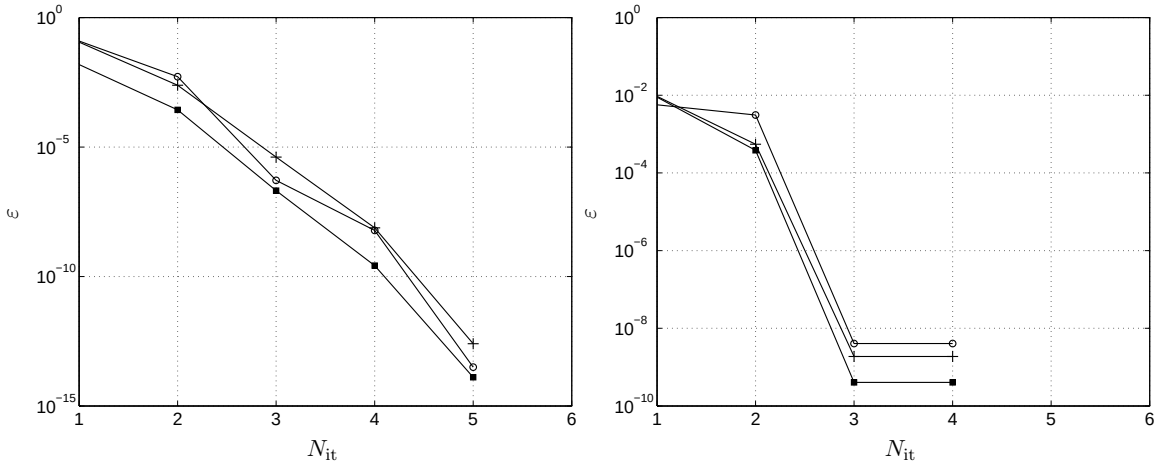

(a) $G_A^{xx} = G_A^{yy} = G_A^{zz}$. **(b)** G_V.

Figure 2.14: Typical convergence behaviour of a cavity potential Green's function computed using Ewald sum method: $x = y = z = 0.1L$ (○), $x = y = z = 0.3L$ (+), and $x = y = z = 0.49L$ (■).

the roundtrip transition between the physical world and the mathematical model. On one hand, the physical excitation (planar electromagnetic wave, waveguide mode, coaxial probe, small aperture, microstrip or CPW printed line, etc.) must be cast in terms of mathematical excitation, providing the vector of independent terms to the linear system. On the other hand, once the linear system is solved, the vector of unknowns (equivalent currents) must be translated into equivalent circuit or system parameters that are easily measurable in the real world (resonant frequencies, port impedances, scattering parameters, radiation patterns, etc). It must be said that although not time-consuming, those are frequently the most difficult steps and the weakest link in the chain. In any case, the relevance of these steps cannot be ignored. A superficial treatment will handicap the most sophisticated numerical implementation and will produce predictions which compare poorly with measurements, regardless of the quality of Green's functions and of the precision of the geometrical discretization.

In this section, two excitation models are treated, the plane wave and the voltage delta-gap model. The modal excitation for waveguides will be explained in Section 6.4 on page 142.

2.7.1 Plane Wave Excitation

Consider a plane wave ($\mathbf{E}^{\mathrm{i}}$, $\mathbf{H}^{\mathrm{i}}$) as shown in Fig. 2.15 with electric field $\mathbf{E}^{\mathrm{i}} = (E_\theta,\, E_\phi)$ and magnetic field $\mathbf{H}^{\mathrm{i}} = (H_\theta,\, H_\phi)$ traveling in a homogeneous medium with propagation direction $\hat{k} = \mathbf{k}/|\mathbf{k}|$

$$\mathbf{E}^{\mathrm{i}} = (\hat{\theta} E_\theta + \hat{\phi} E_\phi) \mathrm{e}^{-\mathrm{j}\mathbf{k}\cdot\mathbf{r}}, \tag{2.37a}$$

$$\mathbf{H}^{\mathrm{i}} = \frac{1}{\eta}\, \hat{k} \times \mathbf{E}^{\mathrm{i}}, \tag{2.37b}$$

where $\eta = \sqrt{\mu/\varepsilon}$ is the medium wave impedance.

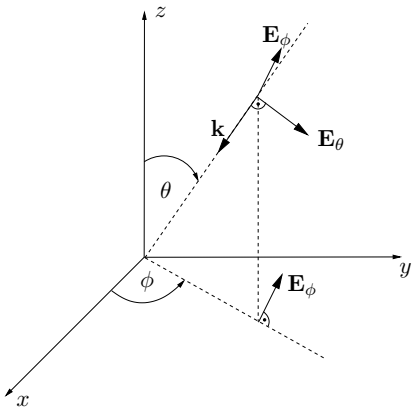

Figure 2.15: A uniform plane wave propagating in a homogeneous medium.

In this section the components of the electric field in Cartesian coordinates will be expressed in terms of the components of the electric field in spherical coordinates. This way the tangential components of the electric/magnetic field of the plane wave impinging on the aperture or metallic plate situated at $z = 0$ plane will be readily known.

From Fig. 2.15 directly follows

$$E_z = -E_\theta \sin\theta, \tag{2.38a}$$

$$E_y = E_\theta \cos\theta \sin\phi + E_\phi \cos\phi, \tag{2.38b}$$

$$E_x = E_\theta \cos\theta \cos\phi - E_\phi \sin\phi, \tag{2.38c}$$

and for the propagation direction one obtains

$$k_z = -k \cos\theta, \tag{2.39a}$$

$$k_y = -k \sin\theta \sin\phi, \tag{2.39b}$$

$$k_x = -k \sin\theta \cos\phi. \tag{2.39c}$$

Finally the equation of the plane wave in Cartesian coordinates can be written as

$$\mathbf{E}^{\mathrm{i}} = \begin{bmatrix} E_\theta \cos\theta \cos\phi - E_\phi \sin\phi \\ E_\theta \cos\theta \sin\phi + E_\phi \cos\phi \\ -E_\theta \sin\theta \end{bmatrix} \mathrm{e}^{\mathrm{j}k(x \sin\theta \cos\phi + y \sin\theta \sin\phi)} \mathrm{e}^{\mathrm{j}kz \cos\theta}, \tag{2.40a}$$

$$\mathbf{H}^{\mathrm{i}} = \frac{1}{\eta}\, \hat{k} \times \mathbf{E}^{\mathrm{i}}. \tag{2.40b}$$

Consider a special case when $E_\phi = 0$. This would mean, taking the plane $z = 0$ as a reference, that θ is the angle of the incidence and ϕ is the polarization angle of the electric field

$$\mathbf{E}^{\mathrm{i}} = E_0 \begin{bmatrix} \cos\theta\cos\phi \\ \cos\theta\sin\phi \\ -\sin\theta \end{bmatrix} \mathrm{e}^{\mathrm{j}k(x\sin\theta\cos\phi + y\sin\theta\sin\phi)} \mathrm{e}^{\mathrm{j}kz\cos\theta}, \tag{2.41a}$$

$$\mathbf{H}^{\mathrm{i}} = \frac{1}{\eta}\,\hat{k} \times \mathbf{E}^{\mathrm{i}}, \tag{2.41b}$$

where $E_0 = E_\theta$.

Once the expressions for electric and magnetic fields of the plane wave are known, they are plugged back in (2.11) to define the excitation vector needed to solve MoM matrix equation and compute the unknown surface currents. The plane wave excitation is of paramount importance in computing the radar cross section (RCS)

$$\sigma_{u,v} = \lim_{r\to\infty} 4\pi r^2 \frac{|E_u^s|^2}{|E_v^i|^2} \tag{2.42}$$

where E_u^s is the u-component of the scattered electric field coming from the induced surface currents and E_v^i is the v-component of the incident electric field.

2.7.2 Delta-Gap Generator

The delta-gap voltage generator is a point-like ideal voltage generator. In the delta-gap model, the port is assumed to be excited by a voltage source of magnitude V, applied within an infinitesimally small gap of length $\delta \to 0$ and across the extended ground-plane and the tip of the feeding line [58], as shown in Fig. 2.17.

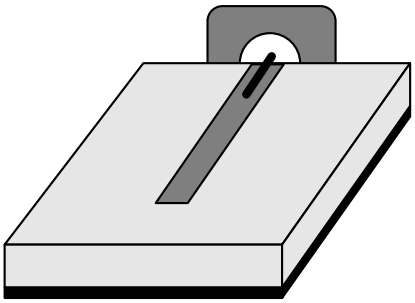

Figure 2.16: The physical excitation.

The delta-gap voltage generator at each port provides an impressed (or incident) excitation field described by the expression

$$\mathbf{E}^{\mathrm{i}} = V_{\mathrm{e}}\delta(\mathbf{r} - \mathbf{r}_{\mathrm{e}})\hat{n}_{\mathrm{e}}, \tag{2.43}$$

where $\mathbf{r}_{\mathrm{e}}$ is the location of the port and $\hat{n}_{\mathrm{e}}$ is the outward normal perpendicular to the side

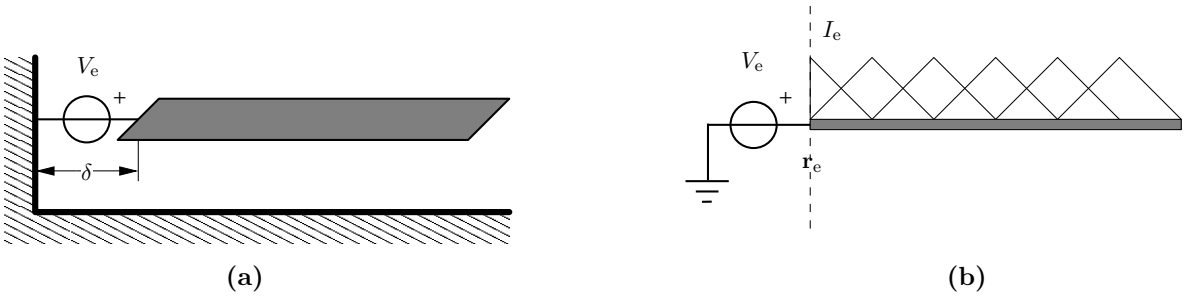

Figure 2.17: A delta-gap voltage generator exciting the microstrip line port (a) and the associated MoM description (b). For the MoM description, the first half-rooftop participates in the excitation vector.

on which the port is defined. As shown in Fig. 2.17, an induced current I_e flows through the voltage source, which spreads into a half-rooftop located at $\mathbf{r}_e$. Substituting (2.43) in the expression for MoM excitation vector (2.11) yields non-zero elements only for half-rooftop basis functions. Once the MoM equation has been solved for the unknown current coefficients, the circuit or antenna scattering parameters can be obtained in the way presented in Section 2.9. More details about the delta-gap voltage excitation and its equivalent impressed-current excitation can be found in [58].

2.8 Solving the Linear System

The discretization of complex planar geometries results in a very large number of unknowns. Typical printed antennas being currently analyzed and routinely built have $N = 10^4 - 10^6$ degrees of freedom [59, 60]. This is a tough challenge, since no sparse matrix techniques can be directly applied to BEM problems. Hence, solving the linear system has been usually considered as the bottleneck for a successful implementation of IEs in large electromagnetic problems. This is due to the well known fact that direct methods for solving linear systems have a complexity $\mathcal{O}(N^3)$, while filling the matrix is, in the worst case, $\mathcal{O}(N^2)$. Excitation and circuit parameter calculations are even faster $\mathcal{O}(N)$ procedures, and the Green's functions treatment is usually a fixed overhead scarcely depending on the number of unknowns N. These considerations have led in the past to optimization strategies where any improvement in the Green's functions treatment was met by the experts with a knowledgeable smile and judged as a waste of time and gray matter. However, the situation is quickly changing. On one side, the drive to analyze more complex environments has led to much more involved Green's functions, for which the older numerical tricks and recipes do not apply anymore. On the other hand, a big progress has been made in the last decade to solve large linear systems with full matrices (see for instance [59, 60, 61] and references therein) and we have just now witnessed the advent of the first "millionaire" techniques [62]. Therefore, it is expected that in the near future the bottleneck could be displaced to the matrix filling, step 3), particularly if the environment is complex and the number of unknowns not excessive. Then, any speed-up in the calculation

of Green's functions and of their convolutions will be of paramount relevance.

In this thesis, we address the problem of the approximate but efficient Green's function computation for multilayered planar structures containing apertures and irises in ground planes with finite thicknesses. This matter is presented in detail in Chapters 4–6. At the same time, Chapter 3 deals with the computationally efficient way of filling the MoM matrix when solving large and complex electromagnetic problems.

2.9 Scattering Parameters

The input parameters of a multiport device (antenna or circuit) can be computed in a two step procedure [2] using standard circuit theory. First, a canonical solution is computed, employing consecutively voltage delta-gap excitations to one port of the device, while all the other ports are short-circuited (Y-matrix definition). The elements of the intrinsic input admittance matrix $\mathbf{Y}$ of dimensions $N_\mathrm{g} \times N_\mathrm{g}$, where N_g is the number of input ports, are computed as the following scalar product

$$y_{p,q} = \mathbf{v}^{(p)} \cdot \mathbf{a}^{(q)}, \tag{2.44}$$

where $\mathbf{v}^{(p)}$ is the p^{th} column in the excitation matrix corresponding to p^{th} excitation (delta-gap), and $\mathbf{a}^{(q)}$ is the q^{th} column in the solution matrix corresponding to the response on the q^{th} port of the device. The intrinsic input impedance matrix $\mathbf{Z}$ is obtained as

$$\mathbf{Z} = \mathbf{Y}^{-1}. \tag{2.45}$$

The intrinsic input impedance matrix can be obtained directly if, instead of voltage delta-gap generator, an impressed-current excitation is used [2, 58]. In contrast to the voltage delta-gap excitation, here we employ consecutively impressed current excitation to one port of the device, while all the other ports remain open circuited. In that case, we would have

$$z_{p,q} = \mathbf{v}^{(p)} \cdot \mathbf{a}^{(q)}, \tag{2.46}$$

where $\mathbf{v}^{(p)}$ is now the p^{th} column in the excitation matrix corresponding to p^{th} excitation (impressed-current generator). The procedure explained here is equivalent to the classical "quadratic form" approach [58].

The embedded currents need to be computed in order to take into account that all the ports are simultaneously loaded and to find the radiation pattern, the near field, and the active input impedances. This is done by computing the effective vectors $\mathbf{V}^{\mathrm{emb}}$ and $\mathbf{I}^{\mathrm{emb}}$ at each excitation port as a function of the given excitation amplitudes $\mathbf{V}$ (Fig. 2.18). Let $\mathbf{G}$ denote the matrix containing, along the main diagonal, the internal impedances of the generators at each port

$$\mathbf{G} = \mathrm{diag}(Z_\mathrm{g}^{(1)}, Z_\mathrm{g}^{(2)}, \ldots, Z_\mathrm{g}^{(N_\mathrm{g})}), \tag{2.47}$$

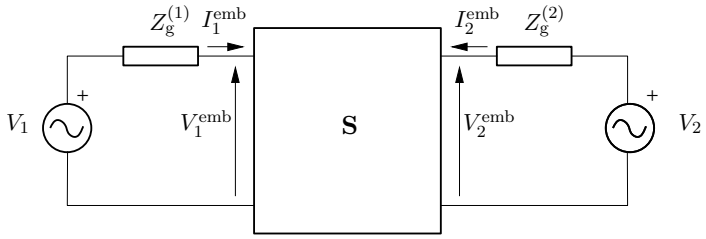

Figure 2.18: Two port network with the excitations.

then the input impedance at port p can be expressed as

$$\begin{aligned} \mathbf{I}^{\text{emb}} &= (\mathbf{Z}+\mathbf{G})^{-1}\mathbf{V}, \\ \mathbf{V}^{\text{emb}} &= \mathbf{Z}(\mathbf{Z}+\mathbf{G})^{-1}\mathbf{V}, \\ Z_p^{\text{in}} &= \frac{V_p^{\text{emb}}}{I_p^{\text{emb}}}, \quad p = 1, \ldots, N_{\text{g}}. \end{aligned} \tag{2.48}$$

The S-parameters can be obtained by simple matrix transform [63, 64]. Taking into account the load matrix, which has the generator impedances on the main diagonal, and the matrix $\mathbf{F}$, whose ith diagonal component is given by

$$\frac{1}{2\sqrt{\text{Re}(Z_{\text{g}}^{(i)})}},$$

the S-parameters can be expressed as

$$\mathbf{S} = \mathbf{F}(\mathbf{Z} - \mathbf{G}^{\text{H}})(\mathbf{Z}+\mathbf{G})^{-1}\mathbf{F}^{-1}, \tag{2.49}$$

where the superscript H indicates the complex conjugate transposed matrix.

2.10 Far Field Computation

Far field radiated by an antenna is an important parameter which gives the information on how the antenna radiates power in different directions of the space, on the directivity of the antenna, and the polarization of the radiated signal. Once the electric and magnetic currents induced in the structure are computed, the total radiated field can be computed using the convolution integrals that relate the fields with the sources. The usual far-field approximations [65] apply. However, for multilayered media, the Green's functions have to be computed for $\rho \to \infty$. Although not a trivial task, this can be done using the extraction of the asymptotic form of the multilayered media Green's functions and the details can be found in [5, 19].

Having computed the spherical component of the far field ($\mathbf{E}_\theta$, $\mathbf{E}_\phi$), the polarization and the axial ratio of the radiated wave can be derived using standard analytical techniques [66], and

the co- and cross-polarizations can be computed using different Ludwig's definitions [67].

2.11 Near Field Computation

Near fields are of paramount relevance in electromagnetic compatibility (EMC). An important cost reduction in complying to the EMC directives at system level can be gained by minimizing the radiation and susceptibility of subsystems such as printed circuit boards and high-frequency connectors. In this context, the characterization of the near fields in the vicinity of these subsystems is inevitable [68]. Computed or simulated near-field of an antenna can be used to determine the equivalent current sources over a fictitious surface. Once determined, these currents provide a powerful equivalent model of the antenna that can be used to compute its far fields but also to ascertain its interaction with any other close or far structure [69, 70, 71]. Some antenna platforms may impose unusual constraints, for example, the requirement to place other sensors very close to or on the antenna itself. The examination of the near field can give clues to the optimum location that minimizes an eventual degradation of the antenna performance.

The computation of near field is a straightforward procedure. Once the MoM matrix equation is solved for the unknown current coefficients, the electric and magnetic near fields are obtained as convolution integrals of the pertinent Green's functions and corresponding surface current densities.

2.12 Application Examples[†]

After having illustrated the survey of all theoretical and numerical tools needed to model planar multilayered structures, in this section we present first application examples that concern the computation of the near field. Numerous examples with computation of scattering parameters and far fields are going to be presented in other chapters of this thesis.

2.12.1 Near Field Computation and Probe Modeling

Providing information useful for diagnostic purposes, prototype design and an overall understanding of operational behaviour, near field computation and measurement has been given a lot of interest. There is now a variety of methods used for analysis of printed circuits and antennas and computation of their near field, ranging from hybrid FEM [72], time domain finite differences [73] to MPIE method in combination with FFT and biconjugate gradient [74]. In the latter, only rectangular basis functions and electric sources on one dielectric layer have been used. Here, we extend this work to both triangular and rectangular basis functions and mixed electric and magnetic sources embedded in a planar multilayered media structure. The results of near field numerical computation, based on mixed field dyadic Green's function, are then compared to experimental results. An approximate near field probe model has been

[†] I. Stevanović, P. Crespo-Valero, and J. R. Mosig (2004), in *Proc. International Symposium on Antennas (JINA'04)*, Nice, 8-11 Nov. 2004, pp. 58–59.

introduced that tries to interpret, in terms of the equations, the measurements method and this way better match the measurements results.

We will concentrate here on the near E-field but a complete analogous procedure can be established for the near H-field. After having solved the MoM system of equations, electric near field is found as a convolution integral between the surface current densities and pertinent field dyadic Green's functions

$$\mathbf{E}(\mathbf{r}) = \sum_{i=1}^{N_\mathrm{e}} \alpha_i \int_{S_\mathrm{e}^i} \overleftrightarrow{\mathbf{G}}_\mathrm{EJ}(\mathbf{r}|\mathbf{r}')\mathbf{f}_i(\mathbf{r}')\,\mathrm{d}S' + \sum_{j=1}^{N_\mathrm{m}} \beta_j \int_{S_\mathrm{m}^j} \overleftrightarrow{\mathbf{G}}_\mathrm{EM}(\mathbf{r}|\mathbf{r}')\mathbf{g}_j(\mathbf{r}')\,\mathrm{d}S', \tag{2.50}$$

where α_i is the electric current coefficient assigned to the ith basis function $\mathbf{f}_i$ on the electric planar surface S_e^i, β_j is the magnetic current coefficient assigned to the jth basis function $\mathbf{g}_j$ on the magnetic planar surface S_m^j, and N_e and N_m are, respectively, the number of electric and magnetic planar surfaces in the structure. The surface on which the near field is calculated is on a constant height from the antenna surface. The needed Green's functions are evaluated taking into account a supplementary dielectric layer of a height that corresponds to the height of the probe from the antenna surface (Fig. 2.19).

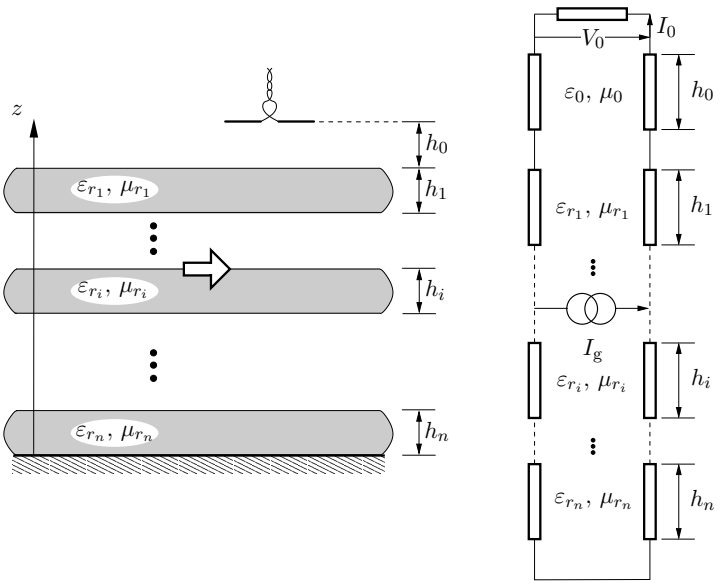

Figure 2.19: Near field measurement of the multilayered structure and its equivalent network representation.

In order to model the measurements procedure [75], an approximate model of the used near field probe must be taken into account. The near field probe consists here of a metallic dipole and a diode on its center that detects the field using the modulated scatterer principle [76].

Three main alternatives can be used for modeling the probe. In the first alternative, the probe is assimilated to a Hertz dipole. The field detected by the probe is then directly given by (2.50). The second approach consists of approximating the current density on the probe

using a triangular pulse [Fig. 2.20(a)]. The probe is replaced by a subsectional basis function, which has the same orientation and the same dimensions as the real probe. The measured near field is proportional to the convolution of the simulated near field with a supposed current density shape of the near field probe $\mathbf{d}(\mathbf{r})$

$$\sim \int_{S_d} \mathbf{d}(\mathbf{r})\mathbf{E}(\mathbf{r})\,\mathrm{d}S. \tag{2.51}$$

The third approach is the same as the previous one, but instead of triangular pulse, the sine function is used to approximate the current density on the probe [Fig. 2.20(b)].

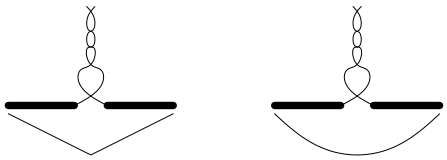

Figure 2.20: Near field probe and the current distribution approximations: (a) Triangular pulse approximation of the current distribution; (b) Sine approximation of the current distribution.

2.12.2 Results

Several planar circuit and antenna geometries have been used for comparison of simulated and measured near fields. The measured voltage is proportional to the square of the electric/magnetic field component of the device under test incident on the dipole and the details of the measurements procedure can be found in [75].

Four-Patch Array

In this section, the results of the near field simulations for a four patch antenna shown in Fig. 2.21 are presented. The results of the simulation using the above approaches are compared to the measurements in Fig. 2.22(a) – Fig. 2.22(d) for the x-component and in Fig. 2.23(a) – Fig. 2.23(d) for the y-component of the near electric field. The probe length is 10 mm and its diameter is 0.5 mm. The distance between the probe and the antenna surface is 2 mm. The measurements were done in 37 points along the x-axis and 9 points along the y-axis.

The slight asymmetry in the calculated results for the antenna structure which is perfectly symmetric is due to the unstructured mesh used to discretize the metallization surfaces of the antenna. It can be seen that the results that take into account the probe current distribution are closer to measurements. However, there is almost no difference in results for the two different shapes of the current distribution on the probe, which means that the triangular pulse function can be also considered as a good approximation.

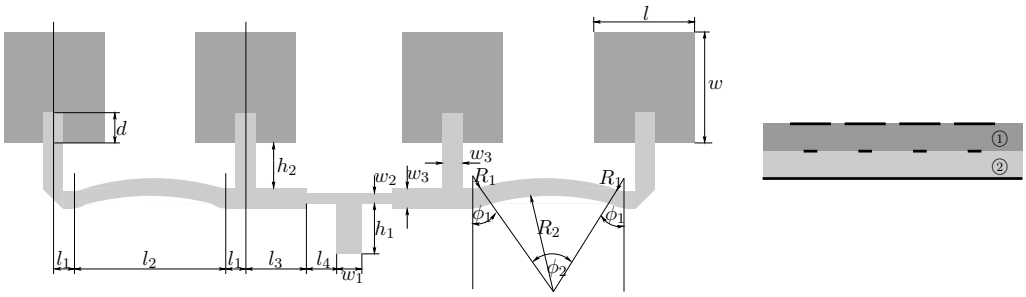

Figure 2.21: Four-patch antenna geometry: $l_1 = 4$, $l_2 = 42$, $l_3 = 13$, $l_4 = 9.5$, $h_1 = 9.25$, $h_2 = 7.5$, $w_1 = 5$, $w_2 = 1.5$, $w_3 = 4$, $R_1 = 8$, $R_2 = 30$, $\phi_1 = 30°$, $\phi_2 = 60°$, $l = 20$, $w = 23$, $d = 7$. Dielectric layers: $\varepsilon_{r1} = \varepsilon_{r2} = 2.33$, $\tan\delta_1 = \tan\delta_2 = 0.0012$, $h_1 = 1.57$, $h_2 = 0.51$. All dimensions given in mm.

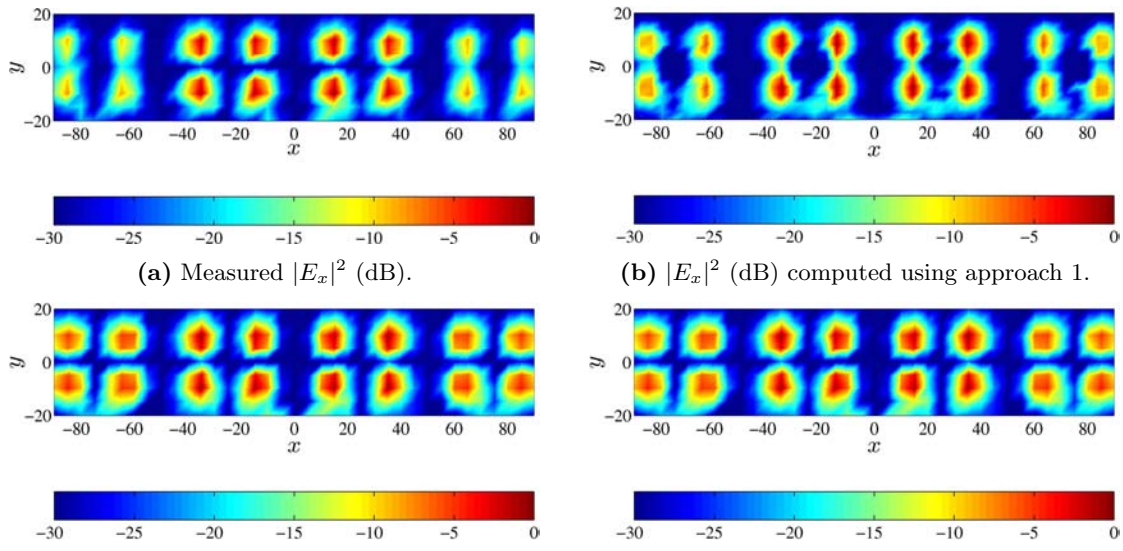

(a) Measured $|E_x|^2$ (dB).

(b) $|E_x|^2$ (dB) computed using approach 1.

(c) $|E_x|^2$ (dB) computed using approach 2.

(d) $|E_x|^2$ (dB) computed using approach 3.

Figure 2.22: Comparison between simulations and measurements for the x-component of the electric near field 2 mm above the antenna. Frequency 4.03 GHz.

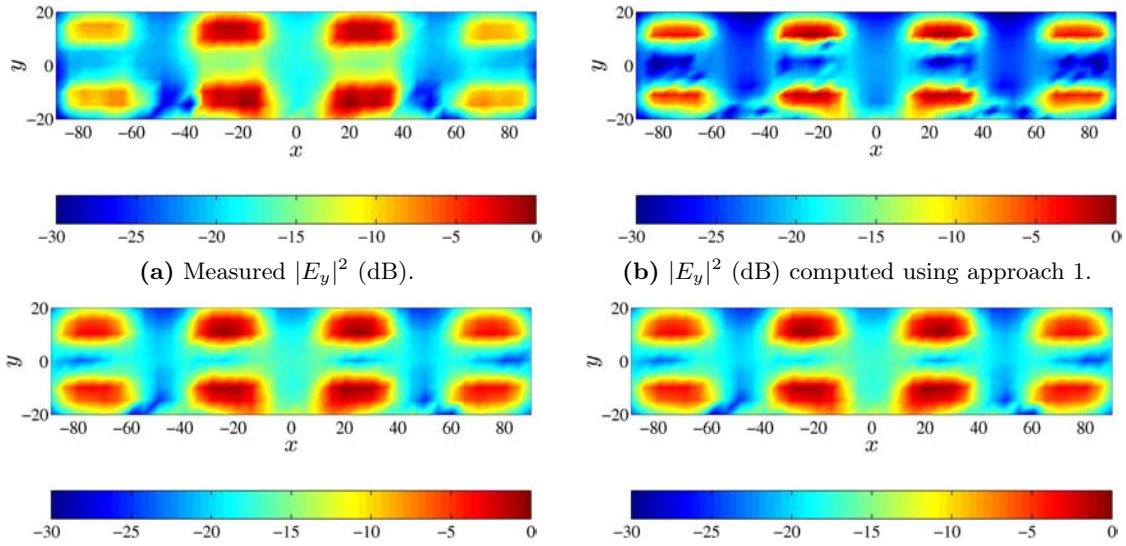

(a) Measured $|E_y|^2$ (dB).

(b) $|E_y|^2$ (dB) computed using approach 1.

(c) $|E_y|^2$ (dB) computed using approach 2.

(d) $|E_y|^2$ (dB) computed using approach 3.

Figure 2.23: Comparison between simulations and measurements for the y-component of the electric near field 2 mm above the antenna. Frequency 4.03 GHz.

Q-Hybrid

Canonical geometry of a Q-hybrid used to verify the results of simulation with both, measurements and theory, is shown in Fig. 2.24. Lower left port is excited while all the other ports are loaded with 50 Ω. From both, simulation in Fig. 2.25(b) and measurements in Fig. 2.25(a), it can be seen that the normal component of electric field is equally distributed to both right ports, while upper left port remains isolated.

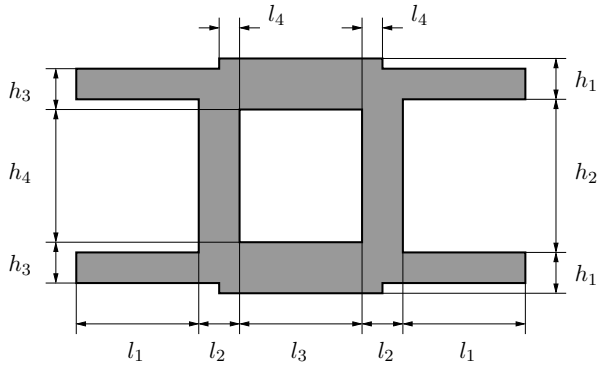

Figure 2.24: Q-hybrid geometry: $l_1 = 24.4$, $l_2 = 2.2$, $l_3 = 26.3$, $l_4 = 1.2$, $h_1 = 2.75$, $h_2 = 30$, $h_3 = 2.85$, and $h_4 = 28.5$. Dielectric: $\varepsilon_r = 2.485$, $\tan\delta = 0.0018$, $h = 0.76$, backed by a ground plane. All dimensions are given in mm.

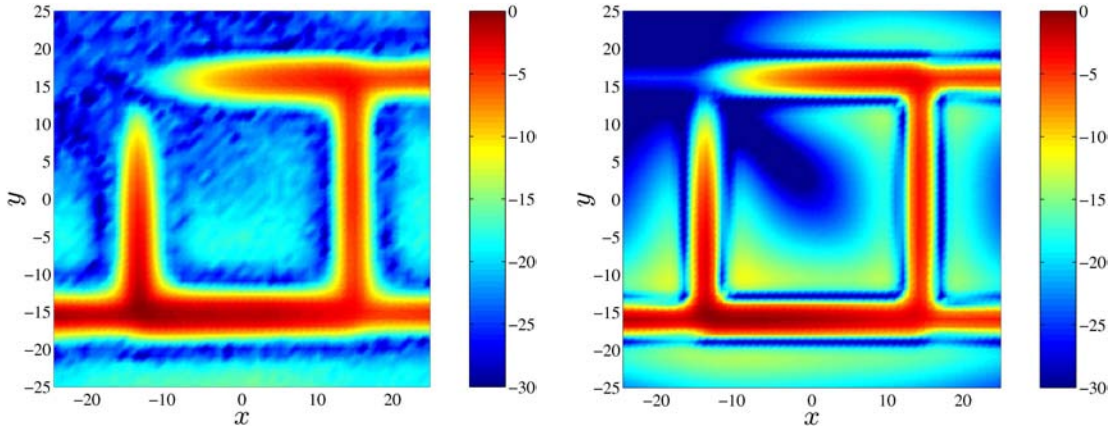

(a) Measured $|E_z|^2$ (dB). **(b)** $|E_z|^2$ (dB) computed using approach 1.

Figure 2.25: Comparison between simulations and measurements for the z-component of the electric near field 2 mm above the circuit. Frequency 1.85 GHz.

SSFIP Antenna

The geometry of an SSFIP (Strip-Slot-Foam-Inverted-Patch [77]) antenna with more complex vertical configuration and both electric and magnetic currents, is shown in Fig. 2.26.

Figs. 2.27–2.28 show good agreement between measured and simulated tangential components of the electric near field.

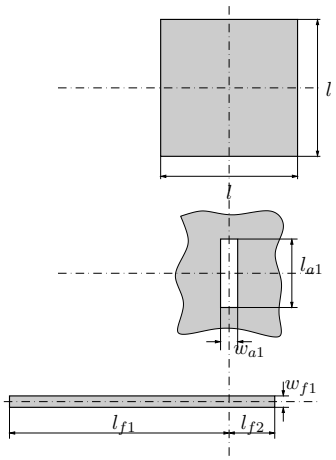

Figure 2.26: SSFIP antenna geometry: $l_{f1} = 50$, $l_{f2} = 28$, $w_{f1} = 1.5$, $l_{a1} = 54$, $w_{a1} = 1$, $l = 60$. Dielectric layers: $\varepsilon_{r1} = 2.33$, $\tan\delta_1 = 0.0012$, $h_1 = 0.51$, $\varepsilon_{r2} = 1.07$, $\tan\delta_2 = 0.001$, $h_2 = 7.2$, $\varepsilon_{r3} = 4.34$, $\tan\delta_3 = 0.01$, $h_3 = 0.8$. All dimensions given in mm.

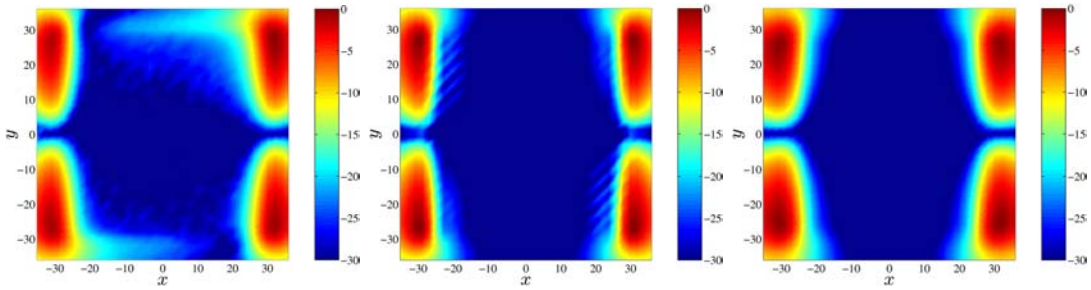

(a) Measured $|E_x|^2$ (dB). **(b)** $|E_x|^2$ (dB) – approach 1. **(c)** $|E_x|^2$ (dB) – approach 2.

Figure 2.27: Comparison between simulations and measurements for the x-component of the electric near field 2 mm above the antenna. Frequency 1.75 GHz.

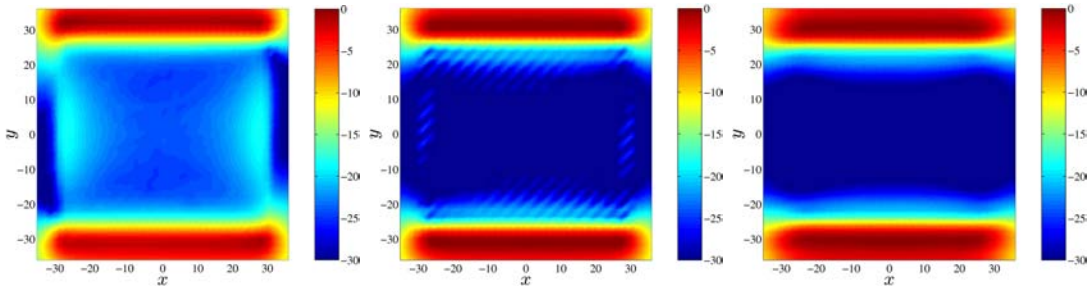

(a) Measured $|E_y|^2$ (dB). **(b)** $|E_y|^2$ (dB) – approach 1. **(c)** $|E_y|^2$ (dB) – approach 2.

Figure 2.28: Comparison between simulations and measurements for the y-component of the electric near field 2 mm above the antenna. Frequency: 1.75 GHz.

2.13 Conclusion

In this introductory chapter, an overview of all the necessary steps that are to be performed in most IE-MoM implementations has been presented. The chapter addressed geometry discretization issues, the Green's function computation in free space, laterally unbounded and shielded multilayered media, integral equations and their solution using the method of moments, and the computation of all parameters needed to characterize planar circuits, antennas and waveguides.

The present chapter was intended to give the basic tools that will be used in the subsequent chapters of this work, when more specific problems are tackled: efficient solving of large electromagnetic problems and scattering on apertures in metallic screens of finite thickness. Nevertheless, it contains two novel and original contributions.

In Section 2.6.4, a "specially truncated image set" used to speed up the convergence of the multilayered boxed Green's functions is presented. The results obtained from this method have been compared with another technique for fast calculation of boxed Green's functions in modal formulation. Numerical examples of Green's functions for printed boxed circuits have been presented and their properties discussed.

Section 2.12 illustrated the first application examples for the problem of the near-field computation in multilayered media circuits and antennas. An extensive measurements campaign has been performed in order to validate the developed and implemented models, resulting in a valuable benchmark for near field computations.

References

[1] R. Harrington, *Field Computation by Moment Methods*, 2nd ed. New York: IEEE Press, 1993.

[2] J. R. Mosig, "Integral-equation technique," in *Numerical Techniques for Microwave and Millimeter-Wave Passive Structures*, T. Itoh, Ed. New York: Wiley, 1989, ch. 3, pp. 133–213.

[3] ——, "Integral-equation techniques for three-dimensional microstrip structures," in *Review of Radio Science*, R. Stone, Ed. Oxford: URSI-Oxford Science Publications, 1992, ch. 6, pp. 127–152.

[4] C. A. Balanis, *Advanced Engineering in Electromagnetics*. New York: Wiley, 1989.

[5] J. R. Mosig, R. C. Hall, and F. E. Gardiol, "Numerical analysis of microstrip patch antennas," in *Handbook of Microstrip Antennas*, James and Hall, Eds. London: IEE - Peter Peregrinus, 1989, ch. 8, pp. 393–453.

[6] G. V. Eleftheriades, J. R. Mosig, and M. Guglielmi, "A fast integral equation technique for shielded planar circuits defined on nonuniform meshes," *IEEE Trans. Microwave Theory Tech.*, vol. 44, no. 12, pp. 2293–2296, Dec. 1996.

[7] A. Álvarez-Melcón, J. R. Mosig, and M. Guglielmi, "Efficient CAD of boxed microwave circuits based on arbitrary rectangular elements," *IEEE Trans. Microwave Theory Tech.*, vol. 47, no. 7, pp. 1045–1058, July 1999.

[8] J. R. Shewchuk. (2004) Triangle, A two-dimensional quality mesh generator and Delaunay triangulator. [Online]. Available: http://www-2.cs.cmu.edu/~quake/triangle.html

[9] International Center for Numerical Methods in Engineering. (2004) GID, The personal pre and post processor. [Online]. Available: http://gid.cimne.upc.es/

[10] S. M. Rao, D. R. Wilton, and A. W. Glisson, "Electromagnetic scattering by surfaces of arbitrary shape," *IEEE Trans. Antennas Propagat.*, vol. 30, no. 3, pp. 409–418, May 1982.

[11] B. M. Kolundžija, "On the locally continuous formulation of surface doublets," *IEEE Trans. Antennas Propagat.*, vol. 46, no. 12, pp. 1879–1883, Dec. 1998.

[12] B. M. Kolundžija and A. R. Djordjević, *Electromagnetic Modeling of Composite Metallic and Dielectric Structures*. Boston: Artech House, 2002.

[13] M. E. Cabot Barja, "Characterization techniques for antennas with highly convoluted topologies," Ph.D. dissertation, Ecole Polytechnique Fédérale de Lausanne, Switzerland, 2005, Thèse No. 3152.

[14] L. Knockaert, J. Sercu, and D. De Zutter, "Generalized Poisson-Neumann polygonal basis functions for the electromagnetic simulation of complex planar structures," *IEEE Trans. Microwave Theory Tech.*, vol. 52, no. 3, pp. 954–961, Mar. 2004.

[15] K. A. Michalski and J. R. Mosig, "Multilayered media Green's functions in integral equation formulations," *IEEE Trans. Antennas Propagat.*, vol. 45, no. 3, pp. 508–519, Mar. 1997.

[16] J. R. Mosig, "Arbitrarily shaped microstrip structures and their analysis with a Mixed Potential Integral Equation," *IEEE Trans. Microwave Theory Tech.*, vol. 36, no. 2, pp. 314–323, Feb. 1988.

[17] D. R. Wilton, S. M. Rao, A. W. Glisson, D. H. Schaubert, O. M. Al-Bundak, and C. M. Butler, "Potential integrals for uniform and linear source distributions on polygonal and polyhedral domains," *IEEE Trans. Antennas Propagat.*, vol. AP-32, no. 3, pp. 276–281, Mar. 1984.

[18] N. Morita, N. Kumagai, and J. Mautz, *Integral Equation Methods for Electromagnetics*. Boston, USA: Artech House, 1990.

[19] A. Álvarez-Melcón, "Application of the integral equation technique to the analysis and synthesis of multilayered printed shielded microwave circuits and cavity backed antennas," Ph.D. dissertation, Ecole Polytechnique Fédérale de Lausanne, Switzerland, 1998, Thèse No. 1901.

[20] R. Cools. (2004) Encyclopaedia of cubature formulas. [Online]. Available: http://www.cs.kuleuven.ac.be/~nines/research/ecf/ecf.html

[21] T. Uwaro and T. Itoh, "Spectral domain approach," in *Numerical Techniques for Microwave and Millimeter-Wave Passive Structures*, T. Itoh, Ed. New York: Wiley, 1989, ch. 5, pp. 334–380.

[22] S. L. Dvorak and E. F. Kuester, "A new method for computing the reaction between two rooftop basis functions in a planar structure," *International J. Micro. and Millimeter-Wave Computer-Aided Eng.*, vol. 1, no. 4, pp. 333–345, 1991.

[23] D. M. Pozar, "Microstrip antennas," *Proc. IEEE*, vol. 80, no. 1, pp. 79–91, Jan. 1992.

[24] J. R. Mosig, "On the calculation of Green's functions arising in the mixed potential integral equation formulation of multilayered printed antennas," Ecole Polytechnique Fédérale de Lausanne, Laboratory of Electromagnetics and Acoustics," Tutorial, Feb. 2001.

[25] K. A. Michalski and D. Zheng, "Electromagnetic scattering and radiation by surfaces of arbitrary shape in layered media, part I: Theory," *IEEE Trans. Antennas Propagat.*, vol. 38, no. 3, pp. 335–344, Mar. 1990.

[26] ——, "Electromagnetic scattering and radiation by surfaces of arbitrary shape in layered media, part II: Implementation and results for contigous half-spaces," *IEEE Trans. Antennas Propagat.*, vol. 38, no. 3, pp. 345–352, Mar. 1990.

[27] J. R. Mosig and F. E. Gardiol, "Analytical and numerical techniques in the Green's function treatment of microstrip antennas and scatterers," *IEE Proc-H*, vol. 130, no. 2, pp. 175–182, Mar. 1983.

[28] A. Papoulis, *The Fourier Integral and its Applications*. New York: McGraw-Hill, 1962.

[29] N. Kinayman and M. I. Aksun, "Comparative study of acceleration techniques for integrals and series in electromagnetic problems," *Radio Science*, vol. 30, no. 6, pp. 1713–1722, Nov.-Dec. 1995.

[30] F. B. Hildebrand, *Introduction to Numerical Analysis*. New York: McGraw-Hill, 1974.

[31] D. Shanks, "Non-linear transformations of divergent and slowly convergent sequences," *J. Math. Phys.*, vol. 34, pp. 1–42, 1955.

[32] S. Singh, W. F. Richards, J. R. Ziencker, and D. R. Wilton, "Accelerating the convergence of series representing the free space periodic Green's function," *IEEE Trans. Antennas Propagat.*, vol. 38, no. 12, pp. 1958–1962, Dec. 1990.

[33] S. Singh and R. Singh, "On the use of Shanks' transform to accelerate the summation of slowly converging series," *IEEE Trans. Microwave Theory Tech.*, vol. 39, no. 3, pp. 608–610, Mar. 1991.

[34] C. Brezinski and R. Zaglia, *Extrapolation Methods, Theory and Practice*. New York: North-Holland, 1991.

[35] J. Wimp, "Toeplitz arrays, linear sequence transformations, and orthogonal polynomials," *Numer. Math.*, vol. 23, pp. 1–17, 1974.

[36] S. Singh and R. Singh, "On the use of Chebyshev-Toeplitz algorithm in accelerating the numerical convergence of infinite series," *IEEE Trans. Microwave Theory Tech.*, vol. 40, no. 1, pp. 171–173, Jan. 1992.

[37] C. Brezinski, "Some new convergence acceleration methods," *Math. Comput.*, vol. 39, pp. 133–145, 1982.

[38] S. Singh and R. Singh, "A convergence acceleration procedure for computing slowly converging series," *IEEE Trans. Microwave Theory Tech.*, vol. 40, no. 1, pp. 168–171, Jan. 1992.

[39] ——, "On the use of Levin's T-transform in accelerating the summation of series representing the free-space periodic Green's function," *IEEE Trans. Microwave Theory Tech.*, vol. 41, no. 5, pp. 884–886, May 1993.

[40] R. Lampe, P. Klock, and P. Mayes, "Integral transforms useful for the accelerated summation of periodic, free-space Green's functions," *IEEE Trans. Microwave Theory Tech.*, vol. MTT-33, no. 8, pp. 734–736, Aug. 1985.

[41] S. Singh and R. Singh, "Application of transforms to accelerate the summation of periodic free-space Green's functions," *IEEE Trans. Microwave Theory Tech.*, vol. 38, no. 11, pp. 1746–1748, Nov. 1990.

[42] A. Álvarez-Melcón and J. R. Mosig, "Two techniques for the efficient numerical calculation of the green's function for planar shielded circuits and antennas," *IEEE Trans. Microwave Theory Tech.*, vol. 48, no. 9, pp. 1492–1504, Sept. 2000.

[43] J. R. Mosig and A. Álvarez-Melcón, "The summation-by-parts algorithm - A new efficient technique for the rapid calculation of certain series arising in shielded planar structures," *IEEE Trans. Microwave Theory Tech.*, vol. 50, no. 1, pp. 215–218, Jan. 2002.

[44] I. Stevanović and J. R. Mosig, "A specially truncated set of images used for solving Green's functions for boxed planar structures," in *Proc. International Symposium on Antennas (JINA'02)*, vol. 1, Nice, France, Nov. 12-14, 2002, pp. 35–38.

[45] K. E. Jordan, G. R. Richter, and P. Sheng, "An efficient numerical evaluation of the Green's function for the Helmholtz operator on periodic structures," *J. Comput. Phys.*, vol. 63, pp. 222–235, 1986.

[46] A. W. Mathis and A. F. Peterson, "Efficient electromagnetic analysis of a doubly infinite array of rectangular apertures," *IEEE Trans. Microwave Theory Tech.*, vol. 46, no. 1, pp. 46–54, Jan. 1998.

[47] M.-J. Park and S. Nam, "Rapid summation of the Green's function for the rectangular waveguide," *IEEE Trans. Microwave Theory Tech.*, vol. 46, no. 12, pp. 2164–2166, Dec. 1998.

[48] M.-J. Park, J. Park, and S. Nam, "Efficient calculation of the Green's function for the rectangular cavity," *IEEE Trans. Microwave Theory Tech.*, vol. 8, no. 3, pp. 124–126, Mar. 1998.

[49] F. Nuñez, I. Stevanović, and A. K. Skrivervik, "Simulation of cavity backed 3D structures using Ewald's transformation," in *Proc. International Symposium on Antennas (JINA'04)*, Nice, France, Nov. 8–11, 2004, pp. 56–57.

[50] M.-J. Park and S. Nam, "Efficient calculation of the Green's function for multilayered planar periodic structures," *IEEE Trans. Antennas Propagat.*, vol. 46, no. 10, pp. 1582–1583, Oct. 1998.

[51] ——, "Rapid calculation of the Green's function in the shielded planar structures," *IEEE Microwave Guided Wave Lett.*, vol. 7, no. 10, pp. 326–328, Oct. 1997.

[52] Y. Hua and T. K. Sarkar, "Generalized Pencil-of-Function method for extracting poles of an EM system from its transient response," *IEEE Trans. Antennas Propagat.*, vol. 374, no. 2, pp. 229–234, Feb. 1989.

[53] P. P. Ewald, "Die Berechnung Optischer und Elektrostatischer Gitterpotentiale," *Ann. Phys.*, vol. 64, pp. 253–287, 1921.

[54] A. Kustepeli and A. Q. Martin, "On the splitting parameter in the Ewald method," *IEEE Microwave Guided Wave Lett.*, vol. 10, no. 5, pp. 168–170, May 2000.

[55] R. C. Hall and J. R. Mosig, "The analysis of arbitrarily shaped aperture-coupled patch antennas via a mixed-potential integral equation," *IEEE Trans. Antennas Propagat.*, vol. 44, no. 5, pp. 608–614, May 1996.

[56] P. Otero, G. V. Eleftheriades, and J. R. Mosig, "Modeling the coplanar transmission line excitation of planar antennas in the method of moments," *Microwave Opt. Technol. Lett.*, vol. 16, no. 4, pp. 219–225, Nov. 1997.

[57] F. Tiezzi, A. Álvarez-Melcón, and J. R. Mosig, "A new excitation model for probe-fed printed antennas on finite ground planes," *Applied Computational Electromagnetics Society Journal*, pp. 115–125, July 2000.

[58] G. V. Eleftheriades and J. R. Mosig, "On the network characterization of planar passive circuits using the method of moments," *IEEE Trans. Microwave Theory Tech.*, vol. 44, no. 3, pp. 438–445, Mar. 1996.

[59] J. Rius, J. Parron, E. Ubeda, and J. R. Mosig, "MLMDA for Analysis of Electrically Large Electromagnetic Problems in 3D," *Microwave Opt. Technol. Lett.*, vol. 22, no. 3, pp. 178–182, Aug. 1999.

[60] E. Suter and J. R. Mosig, "A subdomain multilevel approach for the efficient MoM analysis of large planar antennas," *Microwave Opt. Technol. Lett.*, vol. 26, no. 4, pp. 270–277, Aug. 2000.

[61] I. Stevanović and J. R. Mosig, "Efficient evaluation of Macro-Basis-Function reaction terms in the Subdomain Multilevel Approach," *Microwave Opt. Technol. Lett.*, vol. 42, no. 2, pp. 138–143, July 2004.

[62] A. Heldring, J. M. Rius, and L. Ligthart, "New block ILU preconditioner scheme for numerical analysis of very large electromagnetic problems," *IEEE Trans. Magn.*, vol. 38, no. 2, pp. 337–340, Mar. 2002.

[63] K. Kurokawa, "Power waves and the scattering matrix," *IEEE Trans. Microwave Theory Tech.*, vol. 13, no. 2, pp. 194–202, Mar. 1965.

[64] F. Gardiol, *Microstrip Circuits*. New York: Wiley, 1994.

[65] C. A. Balanis, *Antenna Theory: Analysis and Design*, 2nd ed. New York: Wiley, 1997.

[66] R. E. Collin, *Antennas and Radiowave Propagation*. New York: McGraw-Hill, 1985.

[67] A. C. Ludwig, "The definition of cross polarization," *IEEE Trans. Antennas Propagat.*, vol. 21, no. 1, pp. 116–119, Jan. 1973.

[68] S. Criel, L. Martens, D. De Zutter, A. Frannchois, R. De Smedt, and P. De Langhe, "Theoretical and experimental quantitative characterization of the near-fields of printed circuit board interconnection structures," in *Proc. IEEE Int. Symp. Electromagnetic Compatibility*, Aug. 14–18, 1995, pp. 471–474.

[69] T. K. Sarkar and A. Taaghol, "Near-field to near/far-field transformation for arbitrary near-field geometry utilizing an equivalent electric current and MoM," *IEEE Trans. Antennas Propagat.*, vol. 47, no. 3, pp. 566–573, Mar. 1999.

[70] T. B. Hansen and A. D. Yaghjian, "Planar near-field scanning in the time domain, Part 2: sampling theorems and computation schemes," *IEEE Trans. Antennas Propagat.*, vol. 42, no. 9, pp. 1292–1300, Sept. 1994.

[71] J.-J. Laurin, J.-F. Zürcher, and F. E. Gardiol, "Near-field diagnostics of small printed antennas using the equivalent magnetic current approach," *IEEE Trans. Antennas Propagat.*, vol. 49, no. 5, pp. 814–828, May 2001.

[72] J. M. Jin and J. L. Volakis, "Radiation and scattering analysis of microstrip patch antennas via a hybrid finite element method," in *Proc. Second Int. Conf. Electromagnetics in Aerospace Applications*, Torino, Italy, Sept. 17–20, 1991, pp. 195–198.

[73] C. Wu, K. L. Wu, Z. Q. Bi, and J. Litva, "Accurate characterization of planar printed antennas using the finite difference time domain model," *IEEE Trans. Antennas Propagat.*, vol. 40, no. 5, pp. 526–534, May 1992.

[74] S. A. Bokhari, J.-F. Zürcher, J. R. Mosig, and F. E. Gardiol, "Near fields of microstrip antennas," *IEEE Trans. Antennas Propagat.*, vol. 43, no. 2, pp. 188–196, Feb. 1995.

[75] J.-F. Zürcher, "A near field measurement method applied to planar structures," *Microwave Engineering Europe*, pp. 43–51, June/July 1992.

[76] J.-C. Bolomey and F. E. Gardiol, *Engineering Applications of the Modulated Scatterer Technique*. Boston-London: Artech House, 2001.

[77] J.-F. Zürcher, "The SSFIP: A global concept for high performance broadband planar antennas," *Electron. Lett.*, vol. 24, no. 23, pp. 1433–1435, Nov. 1988.

3 Efficient Evaluation of Macro-Basis Function Reaction Terms in the Subdomain Multilevel Approach[†]

3.1 Introduction

Using the conventional Method of Moments (MoM) with subsectional basis functions becomes highly inefficient when large electromagnetic problems are to be solved. The size of the MoM matrix grows rapidly as the dimensions of the EM problems become large (in terms of wavelength) or a fine mesh density is used to guarantee good accuracy of results for structures with complex shapes. The memory needed for solving a problem of N unknowns increases with $\mathcal{O}(N^2)$. Even when the number of unknowns is such that the MoM matrix fits into the available memory, another resource becomes critical: the CPU time increases as $\mathcal{O}(N^3)$ in the direct solution, thus leading to prohibitively long simulations.

There are a number of techniques used to accelerate the MoM calculations and improve the $\mathcal{O}(N^2)$ and $\mathcal{O}(N^3)$ factors [1]. The fast multiple method (FMM) [2], the multilevel fast multiple algorithm (MLFMA) [3], the impedance matrix localization (IML) [4], the adaptive integral method (AIM) [5], and the multilevel matrix decomposition algorithm (MLMDA) [6] are all iterative techniques keeping the same number of unknowns but using very efficient matrix-vector product schemes. Another large group of approaches is based on the size-reduction of the matrix and nonexhaustive list includes the diakoptics-based multilevel moments method (MMM) [7], the synthetic basis function (SBF) [8], the characteristic basis function (CBF) [9], and the sub-entire-domain (SED) basis function methods [10].

In this chapter we present further improvements in the subdomain multilevel approach (SMA) with macro-basis functions (MBF) [11, 12, 13, 14], a technique that belongs to the latter group and that has proven to be very efficient in modeling the large printed antenna arrays. The basic idea of the method is to break a given complex geometry into smaller regions (subdomains) and perform numerical solutions for them. The set of isolated solutions on the individual subsectional basis functions belonging to a given subdomain is merged into so-called macro-basis functions (MBFs). These are, in turn, fit into the global MoM system, taking into account the symmetries and mutual coupling. The result is then a compressed MoM system of equations for the global problem with a significantly reduced number of unknowns, which is easily solved. Finally, the solution for every single unknown is recovered by a simple expansion from the compressed solution.

This powerful method can be improved, especially when the interactions between two different MBFs are concerned. In a large electromagnetic problem, where the memory occupation

[†] I. Stevanović and J. R. Mosig (2004), *Microwave Opt. Technol. Lett.*, Vol. 42(2):138-143

and computational time have been already significantly reduced using the SMA, the calculation of MBF reaction terms remains the most time-consuming part of the procedure. This thesis introduces a new and decisive improvement in the SMA by developing an original and efficient way of computing MBF reaction terms. It will be shown conclusively in this chapter that with this improvement, the SMA becomes a very competitive approach to solve large and complex printed or planar structures. The strategy for improving the SMA in terms of computational time is based on reducing MBFs to the equivalent moments. An MBF is cut into subregions, the number of which depends on the size of the MBF with respect to the operating wavelength. Instead of computing the reaction terms between every pair of subsectional basis functions belonging to two different MBFs and then summing them up, the MBF reaction term is computed as a sum of a significantly lower number of equivalent moment-reaction terms.

This chapter is organized as follows. First, we illustrate the Subdomain Multilevel Approach and the concept of the Macro-Basis Functions. Next, we explain an efficient way of computing the MBF reaction terms by reducing them to equivalent moments. Finally, we compare the numerical results obtained using the improved SMA with the conventional (brute-force) MoM, the (unrefined or standard) SMA and the measurements, demonstrating conclusively the power and efficiency of the new proposed technique.

3.2 Subdomain Multilevel Approach – the Basic Concept

To introduce the basic concept of the SMA, let us consider a wire antenna as shown in Fig. 3.1, of the length L and placed horizontally at a height h above a ground plane. Let the wire be excited on the left end by a current generator with an impressed current I_0, and let it be terminated with an open circuit on the right end. Depending on the electric length βL, this structure will either behave as a nonradiating open-ended stub or as an antenna. The current distribution on the line may be obtained using the Method of Moments (MoM) with N subsectional basis functions, as is sketched in Fig. 3.1. This would lead to a linear system of equations with the moment matrix $[Z]$, whose elements Z_{ij} are the interactions between rooftops i and j. However, we know that, at least at low frequencies ($\beta L < 1$), we should obtain a current distribution, which closely follows the transmission-line prediction [15], that is

$$I(z) = I_0 \frac{\sin \beta(L-z)}{\sin \beta L}, \quad 0 < z < L. \tag{3.1}$$

Now, what will happen if we split the line into two sections of lengths d and $L-d$ and try to recover the behavior of the full structure by studying the two isolated parts? From the point of view of antenna theory, the prospects are quite pessimistic. What we are trying to do is to divide the original MoM matrix into four blocks, and to omit the out-of-diagonal blocks, whose elements are obviously non-zero. This way we should expect to lose significant information, and to arrive to incorrect results. On the other hand, from the transmission-line point of view, we obviously can analyze the section of length d as a two-port device, alternately excited at one port with the current generator I_0 and leaving open-circuited the other one. For the first section of the line ($0 < z < d$) with a source at $z = 0$ and an open end at $z = d$

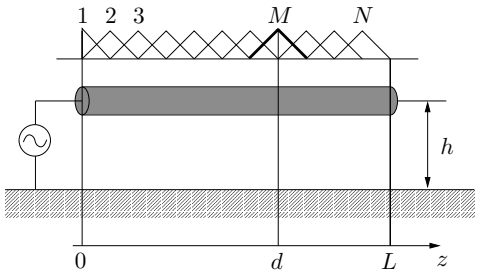

Figure 3.1: Wire antenna of length L, horizontally placed at height h above a ground plane and cut at $z = d$.

(Fig. 3.1), the current distribution becomes

$$I_{1a}(z) = I_0 \frac{\sin \beta(d - z)}{\sin \beta d} \tag{3.2a}$$

In turn, with an open end at $z = 0$ and a virtual generator at $z = d$, we obtain

$$I_{1b}(z) = I_0 \frac{\sin \beta z}{\sin \beta d} \tag{3.2b}$$

Similarly, the right-hand section of the line ($d < z < L$) is computed with a virtual generator at $z = d$ and an open end at $z = L$, leading to the current distribution

$$I_2(z) = I_0 \frac{\sin \beta(L - z)}{\sin \beta(L - d)}. \tag{3.3}$$

Finally, the global current $I(z)$ on the whole wire as given in (3.1), can be recovered easily by a linear combination of the latter three

$$I(z) = \begin{cases} c_{1a} I_{1a} + c_{1b} I_{1b}, & 0 < z < d \\ c_2 I_2, & d < z < L \end{cases} \tag{3.4}$$

with the constants

$$c_{1a} = 1, \qquad c_{1b} = c_2 = \frac{\sin \beta(L - d)}{\sin \beta L}.$$

What the previous developments tell us is that the non-radiation component of the current in any structure can be reconstructed from the values obtained by analyzing unconnected parts of them. Trivial as it may be from the point of view of circuit theory, the above fact is overlooked in many numerical approximations used in antenna theory. In other words, mutual coupling is irrelevant in the component of the current, which is controlled by transmission line theory. This fact already has long-reaching consequences since, in many practical situations (e.g., in printed antenna arrays), the antenna's structure includes beamforming networks of complex shape, which contribute heavily to the final MoM matrix size, but very weakly to the overall antenna radiation.

Concerning a printed radiating structure, it exhibits, in addition to the in-phase transmission-line-like current, a second component, in-quadrature with the excitation current [16]. This is the current responsible for radiation and the radiation resistance. As is well known, its behavior depends on the shape and the size of the structure, that is, the current's shape is governed by the resonances and eigenvalues of the structure, and is practically independent of the position of the generator. Thus, the quadrature component of the current has a very different physical behavior than the in-phase component, and any numerical approach giving the same treatment to both parts of the current will not provide accurate results.

This means that the linear combination of the isolated solutions should be separated with respect to the real and imaginary parts. For example, in the case of the wire antenna, we write, instead of (3.4),

$$I(z) = \begin{cases} c_{1a}^{\mathrm{r}}\mathrm{Re}(I_{1a}) + \mathrm{j}c_{1a}^{\mathrm{i}}\mathrm{Im}(I_{1a}) + c_{1b}^{\mathrm{r}}\mathrm{Re}(I_{1b}) + \mathrm{j}c_{1b}^{\mathrm{i}}\mathrm{Im}(I_{1b}), & 0 < z < d \\ c_{2}^{\mathrm{r}}\mathrm{Re}(I_{2}) + \mathrm{j}c_{2}^{\mathrm{i}}\mathrm{Im}(I_{2}), & d < z < L \end{cases} \tag{3.5}$$

where $\mathrm{Re}(\cdot)$ and $\mathrm{Im}(\cdot)$ denote the real and imaginary part, respectively. Indeed, for the case of a dissipative transmission line [15], it can be shown analytically that such a decomposition is necessary in order to exactly recover the global current from the partial solutions.

In practice, the success of this strategy will depend on the ability of introducing a block decomposition of the original MoM matrix such that the original eigenvalue spectrum is preserved as much as possible. This means to avoid cutting the structure at points where obvious resonances are destroyed or heavily coupled parts are disconnected.

3.3 Subdivision of the MoM Computation

In this section, we will replace the used analytic approximations by a method of moments computation of the wire problem. It will be shown how the numerical computation is split into sub-problems, and how the isolated solutions are fit together into an accurate global solution.

Prior to applying the method of moments, we refer to the electric surface current model [16] that formulates the wire problem by the following integral equation

$$\mathcal{L}(\mathbf{J}) = -\mathbf{E}_{\mathrm{t}}^{\mathrm{i}}. \tag{3.6}$$

Here, the operator $\mathcal{L}$ stands for the integral-equation kernel that acts on the unknown surface current $\mathbf{J}$ and $\mathbf{E}_{\mathrm{t}}^{\mathrm{i}}$ is the tangential component of the impressed electric field on the wire surface due to a known excitation.

Now, as sketched in Fig. 3.1, we will expand the current on the wire into a set of N subsectional basis functions [17] with unknown amplitudes α_i

$$\mathbf{J} = \sum_{i=1}^{N} \alpha_i \mathbf{f}_i \tag{3.7}$$

including $N-1$ rooftops distributed along the line and a half rooftop modeling the entering current at the generator. Using this expansion, the method of moments [18] transforms the

integral equation (3.6) into the system of linear equations

$$\sum_{i=1}^{N} \alpha_i \left\langle \mathbf{w}_j, \mathcal{L}(\mathbf{f}_i) \right\rangle = \left\langle \mathbf{w}_j, -\mathbf{E}_{\mathrm{t}}^{\mathrm{i}} \right\rangle, \quad j = 1, 2, \ldots, N \tag{3.8}$$

with $\mathbf{w}_j$ being a set of so-called weighting or testing functions and $\langle \cdot, \cdot \rangle$ an appropriate inner product. Or, in matrix notation, the linear system (3.8) can be written as

$$[Z][J] = [V] \tag{3.9}$$

with $[Z]$ being the impedance matrix of dimension $N \times N$ and the elements $Z_{ji} = \langle \mathbf{w}_j, \mathcal{L}(\mathbf{f}_i) \rangle$, and the vectors $[J]$, $[V]$ of dimensions $N \times 1$ and elements $J_i = \alpha_i$ and $V_j = \left\langle \mathbf{w}_j, -\mathbf{E}_{\mathrm{t}}^{\mathrm{i}} \right\rangle$, respectively.

For large complex problems, the matrix system (3.9) is to be solved for typically thousands of unknowns, which becomes difficult in terms of computer memory and computer running time since they increase as $\mathcal{O}(N^2)$ and $\mathcal{O}(N^3)$, respectively. In this context, the idea to break the large computation into several smaller subproblems seems to be an efficient way to mitigate the practical difficulties linked to a brute-force computation.

Thus, in the wire problem of Fig. 3.1, we assume again to split the computation into two parts, where the cut line is placed at $z = d$, defined by the rooftop M $(1 < M < N)$. This rooftop we call a "bridge rooftop". The resulting right-hand part of the antenna $d < z < L$ is an open stub, which can be solved similarly to the original problem, introducing a virtual generator at the cut position $z = d$ (Fig. 3.2). This way, an isolated MoM system $[\hat{Z}][\hat{J}] = [\hat{V}]$ of order $N - M + 1$ is set up. Excluding the terms linked to the virtual half-rooftop, the impedance matrix $[\hat{Z}]$ is a block-diagonal submatrix of the global impedance matrix $[Z]$. The solution of the isolated problem yields a set of $N - M$ coefficient $\hat{\alpha}_i$, but obviously, they are not a subset of the original solution α_i. However, as shown in (3.5), the shape of $\hat{\alpha}_i$ should follow closely that of α_i, $i = M + 1, \ldots, N$ in the corresponding part of the antenna $d < z < L$. Therefore, we merge the individual rooftop basis functions on the right-hand stub into a macro-basis function (MBF), that is defined as [11]

$$\mathbf{m}_1 = \sum_{i=M+1}^{N} \hat{\alpha}_i \mathbf{f}_i. \tag{3.10}$$

If we insert the MBF $\mathbf{m}_1$ into the global expansion (3.7), the N unknowns are reduced to $M + 1$ unknowns, namely, the remaining individual basis functions on the left-hand part and an additional unknown β_1 for the MBF

$$\mathbf{J} = \sum_{i=1}^{M} \alpha_i \mathbf{f}_i + \beta_1 \mathbf{m}_1. \tag{3.11}$$

The computational steps of the SMA are schematically highlighted in Fig. 3.2. In corre-

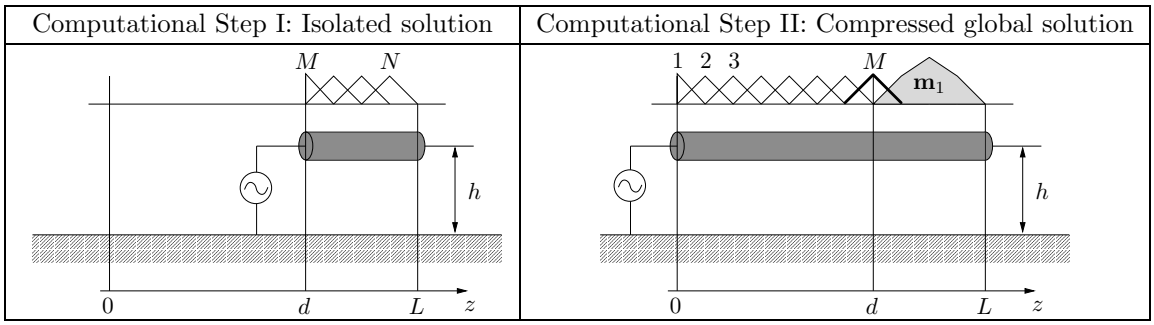

Figure 3.2: Sketch of computational steps in the SMA applied to the wire antenna problem of Fig. 3.1.

spondance with (3.11), we define an appropriate set W' of Galerkin testing functions

$$W' = \{\mathbf{f}_1, \mathbf{f}_2, \ldots, \mathbf{f}_M, \mathbf{m}_1\}\,. \tag{3.12}$$

Finally, we combine the reduced sets of expansion (3.11), which leads to a compressed MoM system of equations of dimension $(M+1)$

$$\begin{bmatrix} \langle \mathbf{f}_1, \mathcal{L}(\mathbf{f}_1)\rangle & \langle \mathbf{f}_1, \mathcal{L}(\mathbf{f}_2)\rangle & \cdots & \langle \mathbf{f}_1, \mathcal{L}(\mathbf{m}_1)\rangle \\ \langle \mathbf{f}_2, \mathcal{L}(\mathbf{f}_1)\rangle & \langle \mathbf{f}_2, \mathcal{L}(\mathbf{f}_2)\rangle & \cdots & \langle \mathbf{f}_2, \mathcal{L}(\mathbf{m}_1)\rangle \\ \vdots & \vdots & \ddots & \vdots \\ \langle \mathbf{m}_1, \mathcal{L}(\mathbf{f}_1)\rangle & \langle \mathbf{m}_1, \mathcal{L}(\mathbf{f}_2)\rangle & \cdots & \langle \mathbf{m}_1, \mathcal{L}(\mathbf{m}_1)\rangle \end{bmatrix} \begin{bmatrix} \alpha_1 \\ \alpha_2 \\ \vdots \\ \beta_1 \end{bmatrix} = \begin{bmatrix} \langle \mathbf{f}_1, -\mathbf{E}_\mathrm{t}^\mathrm{i}\rangle \\ \langle \mathbf{f}_2, -\mathbf{E}_\mathrm{t}^\mathrm{i}\rangle \\ \vdots \\ \langle \mathbf{m}_1, -\mathbf{E}_\mathrm{t}^\mathrm{i}\rangle \end{bmatrix}. \tag{3.13}$$

The solution of this shrunk MoM system of equations, yields the factor β_1 for the MBF and the remaining individual coefficients α_i, $i = 1, \ldots, M$. The current on the stub is recovered from the compressed solution by a simple multiplication $\alpha_i = \beta_i \hat{\alpha}_i$, $i = M+1, \ldots, N$.

The general case of several MBFs is straightforward, and for the two MBFs, we write, for instance

$$\begin{bmatrix} \langle \mathbf{f}_1, \mathcal{L}(\mathbf{f}_1)\rangle & \langle \mathbf{f}_1, \mathcal{L}(\mathbf{f}_2)\rangle & \cdots & \langle \mathbf{f}_1, \mathcal{L}(\mathbf{m}_1)\rangle \\ \langle \mathbf{f}_2, \mathcal{L}(\mathbf{f}_1)\rangle & \langle \mathbf{f}_2, \mathcal{L}(\mathbf{f}_2)\rangle & \cdots & \langle \mathbf{f}_2, \mathcal{L}(\mathbf{m}_1)\rangle \\ \vdots & \vdots & \ddots & \vdots \\ \langle \mathbf{m}_1, \mathcal{L}(\mathbf{f}_1)\rangle & \langle \mathbf{m}_1, \mathcal{L}(\mathbf{f}_2)\rangle & \cdots & \langle \mathbf{m}_1, \mathcal{L}(\mathbf{m}_1)\rangle \\ \langle \mathbf{m}_2, \mathcal{L}(\mathbf{f}_1)\rangle & \langle \mathbf{m}_2, \mathcal{L}(\mathbf{f}_2)\rangle & \cdots & \langle \mathbf{m}_2, \mathcal{L}(\mathbf{m}_2)\rangle \end{bmatrix} \begin{bmatrix} \alpha_1 \\ \alpha_2 \\ \vdots \\ \beta_1 \\ \beta_2 \end{bmatrix} = \begin{bmatrix} \langle \mathbf{f}_1, -\mathbf{E}_\mathrm{t}^\mathrm{i}\rangle \\ \langle \mathbf{f}_2, -\mathbf{E}_\mathrm{t}^\mathrm{i}\rangle \\ \vdots \\ \langle \mathbf{m}_1, -\mathbf{E}_\mathrm{t}^\mathrm{i}\rangle \\ \langle \mathbf{m}_2, -\mathbf{E}_\mathrm{t}^\mathrm{i}\rangle \end{bmatrix}. \tag{3.14}$$

In order to guarantee high accuracy, the different physical behaviour of the in-phase and quadrature part of the extracted MBFs are accounted for as suggested in (3.5). Therefore, we split the MBF into its real and imaginary parts, giving an additional degree of freedom in the expansion of the surface current

$$\mathbf{J} = \sum_{i=1}^{M} \alpha_i \mathbf{f}_i + \beta_1^\mathrm{r}\mathrm{Re}(\mathbf{m}_1) + \mathrm{j}\beta_1^\mathrm{i}\mathrm{Im}(\mathbf{m}_1). \tag{3.15}$$

3.4 Three Basic Steps of the SMA

The SMA algorithm can be summarized in three steps [13].

A. Cut and Estimate: Cut the whole structure into a number of subdomains S_p ($p = 0, 1, \ldots, N_s$). S_0 is a special subdomain, called the root domain, that contains at least all the excitations (subsectional basis functions where circuit ports are defined). The root domain may include subsectional basis functions that have been considered irrelevant for the SMA procedure and where no MBFs will be defined. The remaining subdomains $S_p\,(p = 1, \ldots, N_s)$ will be the support for the MBFs in the SMA. Depending on the geometry, subdomains may or may not be connected between them by subsectional basis functions $\mathbf{f}_k^{\mathrm{b}}$, called "bridge rooftops". Each subdomain $S_p\,(p = 1, \ldots, N_s)$ is solved now independently, using some artificial excitations that somewhat translate the effect of the outside world on the subdomain. Typically, bridge rooftops with unit current are used as excitations. Thus, a set of values for the currents $[\hat{\alpha}_k^p]$ in the isolated subdomain under a given excitation is obtained and stored.

B. Compress: The p^{th} MBF defined over the subdomain S_p is expanded using the stored coefficients $[\hat{\alpha}_k^p]$:

$$\mathbf{m}_p = \sum_k \hat{\alpha}_k^p \mathbf{f}_k^p \tag{3.16}$$

where $\mathbf{f}_k^p$ denotes all the subsectional basis functions defined over surfaces $\sigma_k^p \subset S_p$. Now, the global current is expanded using the subsectional basis functions $[\alpha_k^0]$ on the root domain S_0, the MBFs $[\beta_p]$ defined over the subdomains S_p, and the bridge basis functions $[\alpha_k^b]$ that connect them:

$$\mathbf{J} = \sum_k \alpha_k^0 \mathbf{f}_k^0 + \sum_k \alpha_k^{\mathrm{b}} \mathbf{f}_k^{\mathrm{b}} + \sum_p \beta_p \mathbf{m}_p$$

resulting in a compressed MoM matrix. The number of unknowns in the MoM matrix equation is reduced, as all the subsectional basis functions belonging to a subdomain are merged into an MBF. The compression of the MoM submatrices that contain all the interaction integrals between two subdomains S_p and S_q can be done using vector-matrix-vector multiplication:

$$\begin{aligned}\langle \mathbf{m}_p, \mathcal{L}\mathbf{m}_q \rangle &= \int_{S_p}\int_{S_q} \mathbf{m}_p(\mathbf{r}) \cdot \overleftrightarrow{\mathbf{G}}(\mathbf{r}|\mathbf{r}') \cdot \mathbf{m}_q(\mathbf{r}')\,\mathrm{d}S\,\mathrm{d}S' \\ &= \sum_k \hat{\alpha}_k^p \sum_l \hat{\alpha}_l^q \int_{\sigma_k^q}\int_{\sigma_l^p} \mathbf{f}_k^p \cdot \overleftrightarrow{\mathbf{G}} \cdot \mathbf{f}_l^q\,\mathrm{d}S\,\mathrm{d}S' = [\hat{\alpha}_k^p]^T [Z_{k,l}^{pq}][\hat{\alpha}_l^q]\end{aligned} \tag{3.17}$$

where

$$Z_{k,l}^{pq} = \int_{\sigma_k^q}\int_{\sigma_l^p} \mathbf{f}_k^p \cdot \overleftrightarrow{\mathbf{G}} \cdot \mathbf{f}_l^q\,\mathrm{d}S\,\mathrm{d}S'$$

designates the elements of the MoM submatrix that correspond to the interactions between subsectional basis functions belonging to the subdomains S_p and S_q. It should be noted here that the mutual coupling between different subdomains is accounted for through these MoM elements and that none of the MoM elements is set to zero. The final MoM matrix is reduced

in size, but still fully populated.

The solution of the compressed system gives the unknowns for subsectional basis functions over the root domain, for bridge basis functions and for MBFs β_p, $p = 1, \ldots, N_s$.
C. Expand: The solution over the compressed subdomains is finally recovered through a superposition of the MBFs and their global solutions

$$\alpha_k^p = \beta_p \hat{\alpha}_k^p.$$

This way the problem is solved for every single unknown. MBFs can be considered as "entire-domain" basis functions numerically defined on every subdomain S_p for a set of specific excitations. The different MBFs can be obtained by changing the position of the excitation (orthogonal space harmonics) or by using different frequencies. Another very simple possibility, which performs very well for structures near resonance, is to consider as separate MBFs, the real and imaginary parts of the original complex one. The success of this approach is due to the different physical behaviour of in-phase and quadrature parts of the current, related respectively to the radiation and induced fields [16]. The real part is close to the eigencurrent and rather independent of excitations, while the imaginary part is strongly connected to the specific nature and position of the excitation. A linear combination of both should fit better the actual current. The proposed expansion shows now an additional degree of freedom:

$$\mathbf{J} = \sum_k \alpha_k^0 \mathbf{f}_k^0 + \sum_k \alpha_k^{\mathrm{b}} \mathbf{f}_k^{\mathrm{b}} + \sum_p \beta_p^{\mathrm{r}} \mathrm{Re}\{\mathbf{m}_p\} + \mathrm{j}\beta_p^{\mathrm{i}} \mathrm{Im}\{\mathbf{m}_p\}.$$

3.5 Reaction Term Evaluation

Consider two subdomains p and q (Fig. 3.3) in a large electromagnetic problem being solved using the SMA. Let the subdomains p and q have N_p and N_q subsectional basis functions, each defined on a couple of cells, (σ_p^i, σ_p^j) and (σ_q^i, σ_q^j), respectively. In the SMA, an isolated MoM system of equations with virtual sources on the interfaces connecting the subdomain to the rest of the structure is solved for every subdomain [13]. In our case, this yields the coefficient sets $\hat{\alpha}_i^p$, $(i = 1, \ldots, N_p)$ and $\hat{\alpha}_i^q$, $(i = 1, \ldots, N_q)$, corresponding to the two considered sub-domains p and q. Each coefficient set and the corresponding set of subsectional basis functions define a macro-basis function (MBF) as follows

$$\mathbf{m}_p = \sum_{i=1}^{N_p} \hat{\alpha}_i^p \mathbf{f}_i^p, \quad \text{and} \quad \mathbf{m}_q = \sum_{j=1}^{N_q} \hat{\alpha}_j^q \mathbf{f}_j^q, \tag{3.18}$$

where $\mathbf{f}_i^p$, $(i = 1, \ldots, N_p)$ and $\mathbf{f}_j^q$, $(j = 1, \ldots, N_q)$ are the subsectional basis functions included in the macro-basis functions $\mathbf{m}_p$ and $\mathbf{m}_q$.

Now, the reaction term between two macro-basis functions can be expressed by the following general expression

$$c_{p,q} = \langle \mathbf{m}_p, \mathcal{L}(\mathbf{m}_q) \rangle \tag{3.19}$$

where $\mathcal{L}(\cdot)$ is a self-adjoint integral operator, and $\langle \cdot, \cdot \rangle$ is a shorthand notation for the inner

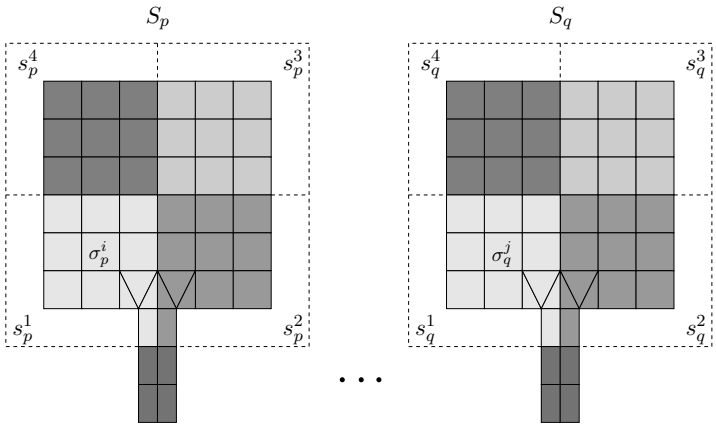

Figure 3.3: Two macro-basis functions split into subregions.

product of two functions.

In unrefined SMA procedures, the reaction term $c_{p,q}$ is computed by decomposing each MBF into its subsectional basis functions (BFs) and evaluating the reaction terms between every pair of BFs belonging to a couple of MBFs. The strategy for improving the SMA when interactions between two MBFs are concerned is based on reducing MBFs to the equivalent moments. An MBF is cut into subregions, the number of which depends upon the size of the MBF with respect to the operating wavelength. This way, instead of computing reaction terms between every pair of BFs belonging to two different MBFs and then summing them up, we compute the equivalent moments for every subregion of the two MBFs. Once these are known, the MBF reaction term will consist of the sum of a significantly lower number of equivalent moment-reaction terms.

Let the MBF $\mathbf{m}_p$ be defined over a surface S_p and the MBF $\mathbf{m}_q$ over a surface S_q. Let these two surfaces be subdivided into K and L subregions, respectively, given by

$$S_p = \bigcup_{k=1}^{K} s_p^k \quad \text{and} \quad S_q = \bigcup_{l=1}^{L} s_q^l$$

and let the centers of every subregion be denoted by $\mathbf{r}_{\mathrm{c}_k}^p \in s_p^k$, $k = 1, \ldots, K$ and $\mathbf{r}_{\mathrm{c}_l}^q \in s_q^l$, $l = 1, \ldots, L$.

Then the MBF reaction term $c_{p,q}$ can be approximated as follows

$$c_{p,q} = \langle \mathbf{m}_p, \mathcal{L}(\mathbf{m}_q) \rangle = \int_{S_p} \int_{S_q} \mathbf{m}_p(\mathbf{r}) \overleftrightarrow{\mathbf{G}}(\mathbf{r}|\mathbf{r}') \mathbf{m}_q(\mathbf{r}') \, \mathrm{d}S \, \mathrm{d}S' \approx$$

$$\approx \sum_{k=1}^{K} \sum_{l=1}^{L} \left(\int_{s_p^k} \mathbf{m}_p(\mathbf{r}) \, \mathrm{d}S \right) \overleftrightarrow{\mathbf{G}}(\mathbf{r}_{\mathrm{c}_k}^p | \mathbf{r}_{\mathrm{c}_l}^q) \left(\int_{s_q^l} \mathbf{m}_q(\mathbf{r}') \, \mathrm{d}S' \right). \tag{3.20}$$

One way of defining the subregions and corresponding moments in an MBF is as follows. A

maximum area that a given MBF occupies, $[x_{\min}, x_{\max}]\times[y_{\min}, y_{\max}]$, is found and rectangular subregions are equally distributed in it. Let λ be the operating wavelength and n given number of moments per wavelength. The number of moments in the x and y directions is then defined as

$$N_x = n\left\lfloor \frac{x_{\max}-x_{\min}}{\lambda}\right\rfloor + 1, \quad N_y = n\left\lfloor \frac{y_{\max}-y_{\min}}{\lambda}\right\rfloor + 1$$

where $\lfloor x\rfloor$ denotes the floor function. The subregions will be defined by the following grid

$$x^i_{\min} = x_{\min} + (i-1)\Delta_x, \quad x^i_{\max} = x_{\min} + i\Delta_x,$$

$$y^j_{\min} = y_{\min} + (j-1)\Delta_y, \quad y^j_{\max} = y_{\min} + j\Delta_y,$$

where

$$i = 1, \ldots, N_x, \quad j = 1, \ldots, N_y$$

and

$$\Delta_x = \frac{x_{\max}-x_{\min}}{N_x}, \quad \Delta_y = \frac{y_{\max}-y_{\min}}{N_y}.$$

Once the subregions are defined, for each subregion, all the cells in MBF that belong to it are found, and the overall moment of BFs defined on these cells is computed. The center of the moment is computed as an arithmetic mean of all the centers of BFs taken into account.

In the following, the results obtained applying the SMA with fast MBF interactions are given, showing good accuracy and a significant gain in computational time for large electromagnetic problems.

3.6 Results

3.6.1 Four-Patch Array Antenna

This antenna consists of four patches electromagnetically coupled to an underlying feeding network (Fig. 3.4). The details concerning the geometry and the dielectric parameters of this structure can be found in Fig. 2.21 on page 42. In the brute-force treatment of the problem, the structure is subdivided into 1093 subsectional basis functions. In the SMA, we have four isolated blocks, each of which includes a radiating patch together with a little portion of the underlying feeding line. Another subdomain contains the remaining beam forming network, including the excitation (Fig. 3.4). Each patch subdomain has 176 basis functions, and the subdomain including the excitation consists of 345 basis functions.

In Fig. 3.5, the error in the computed input impedance for different moment densities is shown. The unrefined SMA is taken as a reference for the error evaluation. The error is shown for 1, 6, 10, 14 and 20 moments per operating wavelength. It can be seen that the error decreases as the number of moments that approximate the MBF increases. Indeed, the error falls below 1 % when 20 moments per wavelength (mpλ) are used to represent the MBF. In Fig. 3.6, the input impedance for the four-patch array is shown. The solid line represents the result obtained applying the brute-force approach, the line with circles represents the result obtained applying the unrefined SMA and the dashed line – the results obtained applying

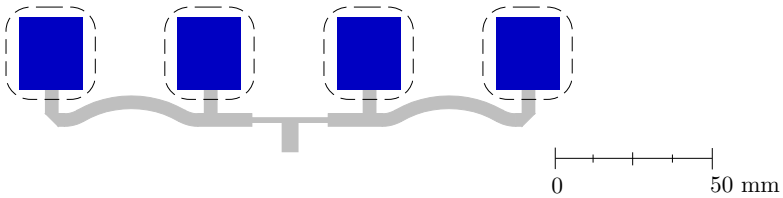

Figure 3.4: Four-patch antenna divided in subdomains. The dashed lines enclose the basic isolated subdomains (the patches with parts of underlying feeding lines).

the SMA with 1 mpλ. Applying 20 moments per wavelength, we obtain practically the same results as in the case of the unrefined SMA. The Smith's chart in Fig. 3.6(b) shows that not only the magnitudes of the reflection coefficients obtained using these three approaches are in good agreement, but the phases as well.

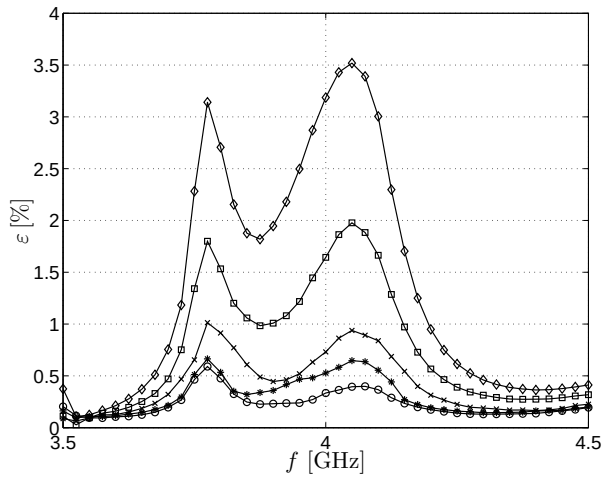

Figure 3.5: Relative error vs. number of moments per wavelength. The error decreases as the number of moments grows: $N = 1$ ($\diamond$), $N = 6$ ($\square$), $N = 10$ ($\times$), $N = 14$ ($*$), $N = 20$ ($\circ$).

On a PC with Linux operating system, a 1.4 GHz processor and 512 MB of RAM, the computational time per frequency point was 70 s when the brute-force approach was applied. Applying the unrefined SMA, the simulation time dropped to 17.4 s and further to 15.5 s, when the SMA with 20 mpλ was used. Both the SMA and the fast SMA yield results that coincide very well with the brute-force approach, the fast SMA having the advantage of a faster computational time. The example shown here is chosen to prove the validity of the idea behind the SMA with fast MBF interactions. The gain in computational time will become significant when the number of unknowns increases (typically, 10^4 or more), and/or when more complicated electromagnetic structures with a larger number of macro-basis functions are used.

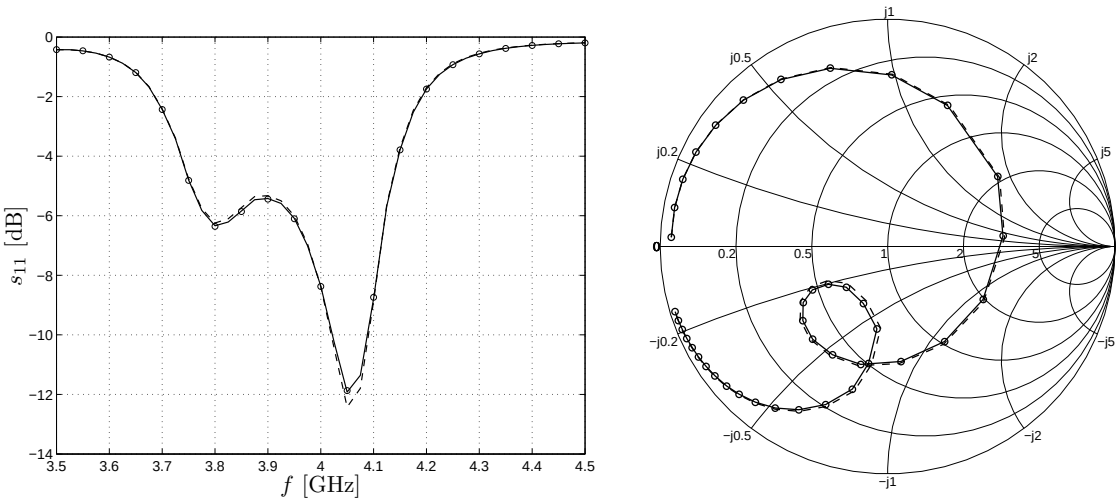

(a) The reflection coefficient.

(b) The input impedance.

Figure 3.6: Four-patch antenna. Results obtained using the brute-force approach (solid line), the SMA (line with circles ○) and the SMA with 1 mpλ (dashed line).

3.6.2 Subarray Element of a SAR Antenna

The second example is a dual polarized eight element subarray for a C-band SAR antenna with center frequency $f = 5.3$ GHz. The design of the antenna was proposed by Saab Ericsson Space and studied by our Laboratory within a common ESA research project [19].

The basic radiating element of this structure consists of two orthogonal slotted patches, which are etched on the two faces of a thin substrate. The structure of the radiating element is presented in Fig. 3.7. The distance between the lower skin-substrate and the ground plane is 1 mm and the distance between the two skins is 2.6 mm. The slotted patches of the vertical polarization are etched on the upper faces of the two skins, while the patches of the horizontal polarization are on the lower faces. The feeding lines of the horizontal polarization are etched on the upper face of the lower skin, while the vertical polarization feeding lines are on the lower face of the lower skin. The spacings between different layers are obtained using steel frames.

The subarray antenna as shown in Fig. 3.8 consists of eight radiating elements and the design is completed with a corporate feeding network. A reasonably detailed modeling of this antenna yields 8469 subsectional basis functions with rectangular or triangular supports. The brute-force approach requires a large amount (1.15 GB) of computer memory. Using the SMA, the problem is split into smaller subproblems. In Fig. 3.8, dashed lines define the subdomains in which the whole structure is divided. Each of the eight subdomains consists of the radiating elements with the end portions of the feed lines included and spans over the four metallization levels. The two subdomains (extreme left and right) have three interfaces with the rest of the structure (which defines the ninth subdomain), whereas the inner six subdomains have four. The number of interfaces automatically defines the number of MBFs that are defined on each subdomain. In the first computational step of the SMA, MoM equations of 858 and 900

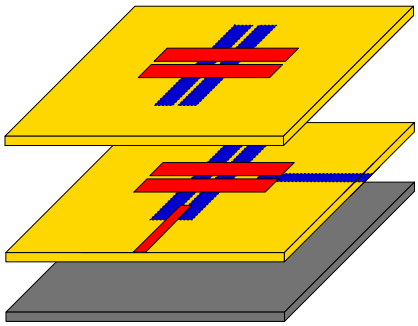

Figure 3.7: The structure of the radiating element. The thickness of the skin dielectric layers is $t = 0.15$ mm and the dielectric properties are $\varepsilon_r = 2.95$, $\tan\delta = 0.004$ [19].

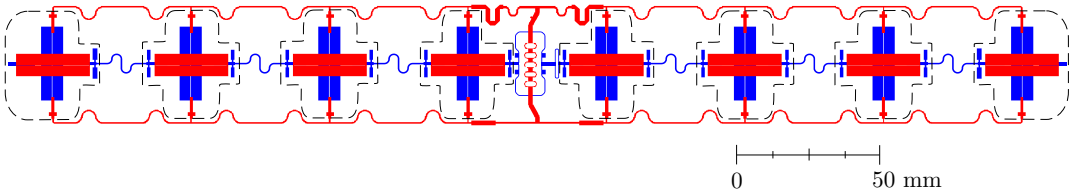

Figure 3.8: The SAR antenna subarray layout.

unknowns, for the end and the inner block are solved, respectively. In the second step, the MBFs are plugged into the global equation system, resulting in a compressed MoM equation of only 1428 unknowns. Compared to 8469 unknowns from the brute-force approach, the SMA brings the reduction in the memory occupation from 1.15 GB to 32 MB. On a PC with Linux operating system, a 1.4 GHz processor and with 512 MB of RAM this leads to computation time of 27.5 min. In the SMA with fast MBF interactions, the choice of having 20 mpλ results in a sizeable drop of the CPU time, which is now only 20 minutes. The memory occupation and time needed for solving the problem are shown in Table 3.1.

Method:		Brute-force	SMA	Fast SMA
Step I	Dim.	-	858 / 900	
	Mem.	-	11.8 / 13 MB	
Step II	Dim.	8469	1428	
	Mem.	1.15 GB	32.6 MB	
Time		-	27.5 min	20.8 min

Table 3.1: Matrix dimensions, memory requirements and time per frequency point needed for solving the SAR subarray using the brute-force, the standard SMA, and the SMA with fast MBF interactions.

Finally, we compare the computed radiation patterns against the measured ones, provided by Saab Ericsson. The patterns are shown for the vertical polarization. Fig. 3.9(a) shows the computed radiation pattern using the SMA and the measurements. In the measured

field, solid and dashed lines represent the co- and cross-polarization components, respectively. The computed results are depicted with circles (co-polar) and squares (cross-polar). The simulated co-polarization pattern shows good agreement with the measured one, while the predicted cross polarization is less accurate, but on a much lower dB-level. In Fig. 3.9(b) we compare radiation patterns computed using the unrefined SMA (solid and dashed lines) and the SMA with fast MBF interactions (circles and squares). The agreement in both co- and cross-polarization components is very good (which implies an excellent stability of the numerical technique) with a gain of 24 % in computational time, as compared to that of the unrefined SMA.

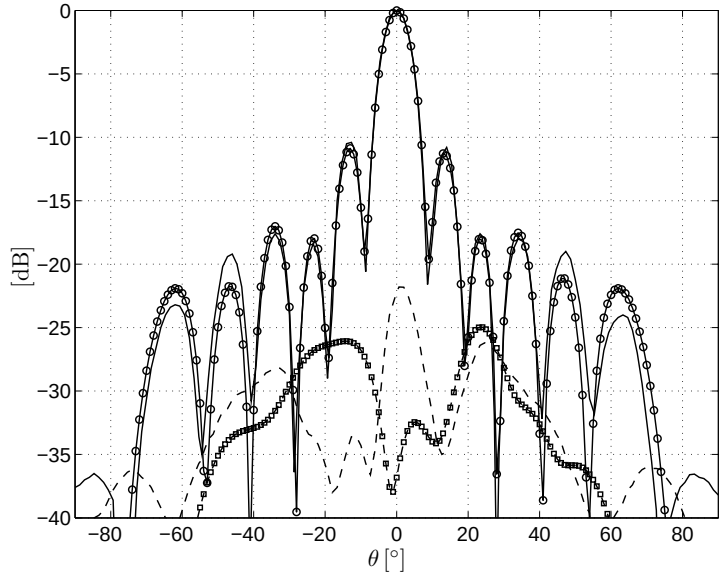

(a) Measured co-polar (solid line), measured cross-polar (dashed line), co-polar (circles) and cross-polar (squares) components computed using the standard SMA.

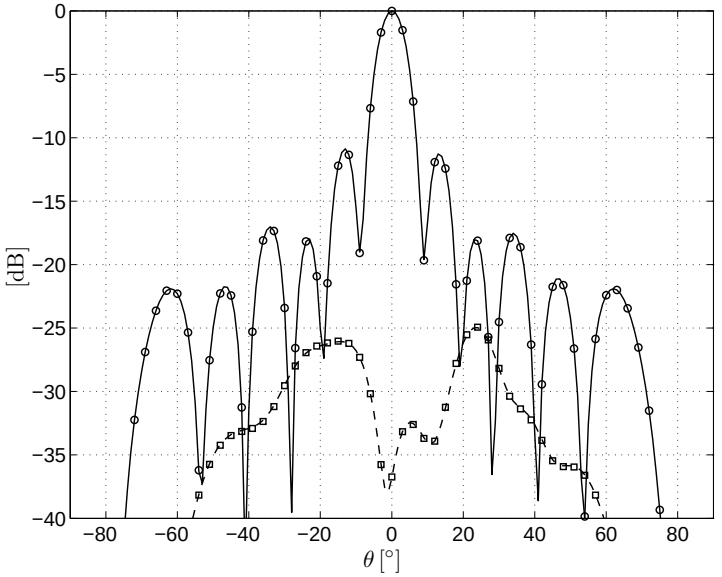

(b) Co-polar (solid line) and cross-polar (dashed line) components computed using the standard SMA. Co-polar (circles) and cross-polar (squares) components computed using the SMA with fast MBF interactions.

Figure 3.9: The radiation pattern of the SAR subarray in the $\phi = 0$ plane for the vertical polarization. $f = 5.3$ GHz.

3.6.3 8×8 Corporate Fed Patch Array

As a third example, we consider the 8×8 corporate-fed array of patches based on [20]. The geometry of the array is shown in Fig. 3.10 and the layout of the built test-sample in Fig. 3.11 [14]. The antenna consists of a single layered microstrip design with a combination of lines entering straight into the patches.

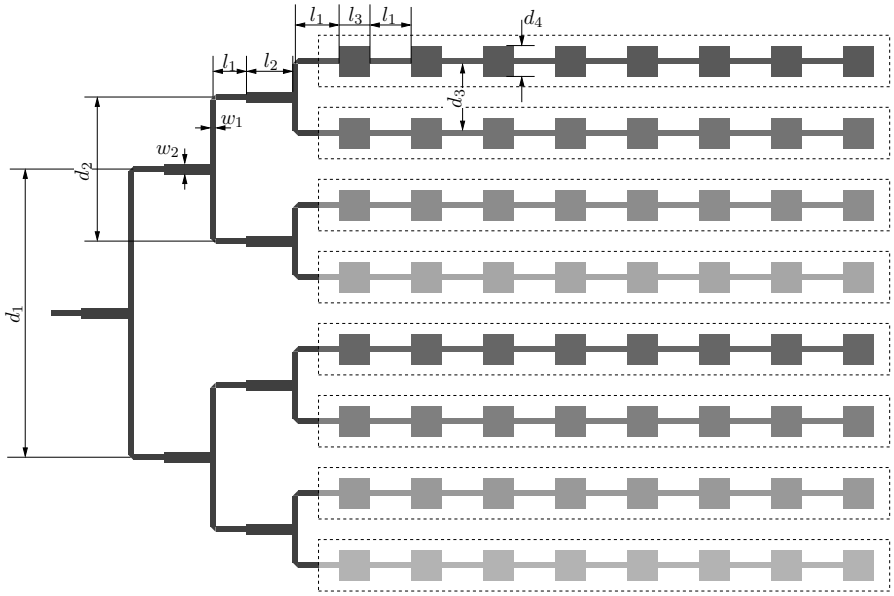

Figure 3.10: The geometry of the antenna array. $w_1 = 1.3$, $w_2 = 3.93$, $d_1 = 94.32$, $d_2 = 47.16$, $d_3 = 23.58$, $d_4 = 11.79$, $l_1 = 12.32$, $l_2 = 18.48$, $l_3 = 10.08$. All dimensions given in mm. Printed on Duroid-5870 with $\varepsilon_r = 2.35$, $\tan\delta = 0.0012$ and $h = 1.57$ mm. The dashed lines define the eight subdomains (fingers) in which the whole structure is subdivided.

The feeding lines and patches are densely meshed, which leads to a large number of $N = 9947$ triangular and rectangular basis functions for the whole antenna array and to the memory occupation of 1.6 GB. An AMD Athlon 1.4 GHz PC with 512 MB of RAM has been used in the simulations. Solving the problem using the conventional MoM could not be done on this PC because of the lack of the available memory (1.6 GB needed against the available 512 MB). The antenna structure with mesh density that yields 4000 unknowns is solved in 190 min per frequency point on this PC. Taking into account that the time dependency on the number of unknowns in the direct solution is $\mathcal{O}(N^3)$, the time needed for solving the problem with the mesh density fine enough to lead the accurate results (9947) would take about 54 hours per frequency point. This value is extrapolated and it does not take into account the memory resources. Actual time would be even longer due to the inevitable swapping to the hard disk.

Using the SMA, the structure is split into nine parts: the corporate feed network on the left hand side and eight "fingers", each including eight patches (Fig. 3.10). Although nothing prevents theoretically the definition of MBFs on the corporate beamforming network, this option has not been retained here. The beamforming network is a non-resonant structure that appears only once in the problem. Approximating the currents on it would certainly

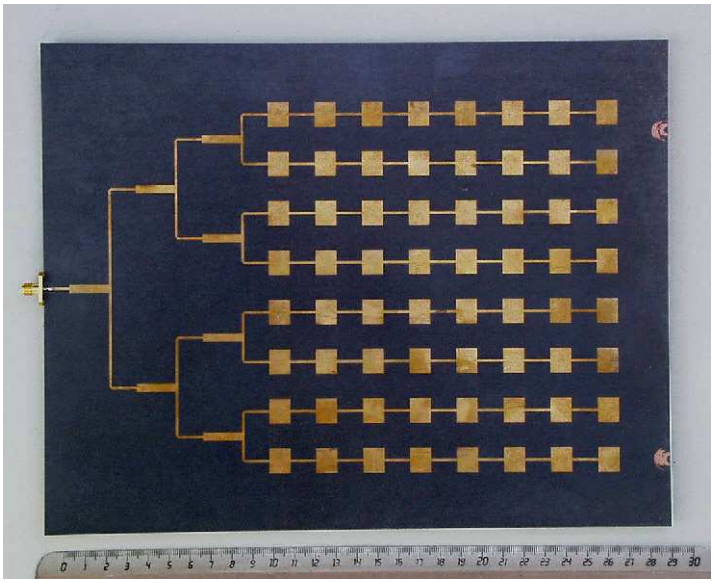

Figure 3.11: The layout of the built test-sample [14].

require more than one complex MBF and the lack of geometric redundancy minimizes the eventual benefits. The SMA computation starts with the evaluation of the currents on the isolated fingers, each with $N = 1131$ BFs being merged into a complex MBF. The global system of equations is then compressed to 923 unknowns, what corresponds to a memory drop from 1.6 GB to 13 MB. The direct solution is used for solving the compressed MoM system. The time needed per frequency point is 24.35 min. This is equivalent to a reduction of computer time by a factor greater than 100.

Method:		Brute-force	unrefined SMA
Step I	Dim.	-	1131
	Mem.	-	20.5 MB
Step II	Dim.	9947	923
	Mem.	1.58 GB	13 MB
Time		-	24.35 min

Table 3.2: Matrix dimensions, memory requirements and time per frequency point needed for solving the 8×8 antenna array using the conventional MoM and the unrefined SMA.

By inspecting our 8×8 array, we can see that 8 subdomains (fingers) are identical. A block of the MoM matrix for one subdomain could be filled, compressed, and repeated in the MoM matrix 7 more times. In addition, the solution for the subdomain could be computed only once and then reused in compressing the MoM submatrices that correspond to the interactions between different subdomains. However, the eight subdomains need to have the same mesh and basis function numbering scheme. However, all this presumes that the eight subdomains

are not only geometrically equal, but that they have exactly the same mesh and exactly the same basis function numbering scheme. By reconstructing the mesh and including the concept of repeated subdomains in our solver, further improvements in the computational time in addition to these obtained using the unrefined SMA (that does not take into account the repetitive subdomains) are achieved. The same structure is solved in only 12 min per frequency point, giving exactly the same input impedance and the radiation pattern as before. The computational time as compared to that one of the unrefined SMA has been reduced to 49 %.

As a final step, we use the concept of equivalent moments to represent the Macro-Basis Functions when computing their mutual interactions. With 20 equivalent moments per wavelength, the antenna is solved in 5.7 min, which is only 23.5 % (four times faster) of the time needed for the unrefined SMA.

In Fig. 3.12, the error in the computed input impedance for different moment densities is shown. The unrefined SMA is taken as a reference for the error evaluation. The error is shown for 2, 8, 14 and 20 moments per operating wavelength. The choice of 20 moments per wavelength leads once again to an error of less than 1 %.

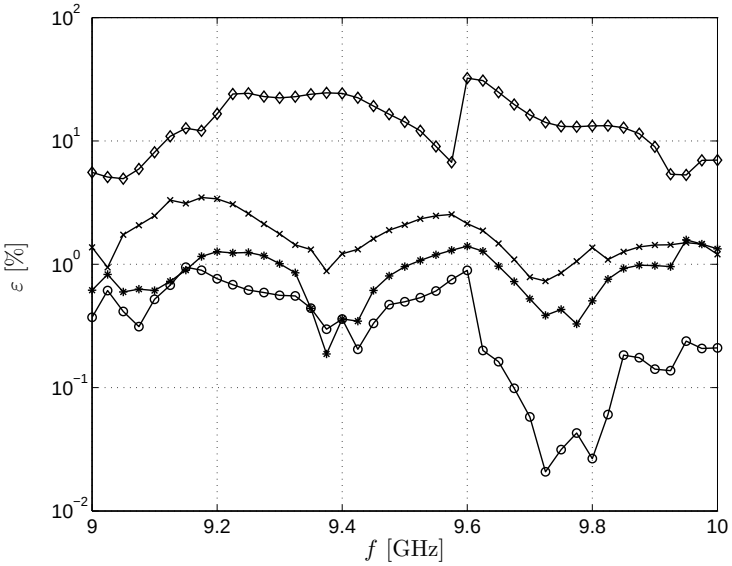

Figure 3.12: The relative error in input impedance. The error decreases as the number of moments per wavelength increases $N = 2$ ($\diamond$), $N = 8$ ($\times$), $N = 14$ ($*$), $N = 20$ ($\circ$).

Fig. 3.13 shows the CPU time as a function of the number of unknowns of the studied problem. The CPU time needed to solve the problem using a conventional MoM with direct solution grows with the number of unknowns as $\mathcal{O}(N^3)$. The time for solving the problem decreases as we use the unrefined SMA ($*$), the SMA with repeated subdomains ($+$) and it becomes minimal when the SMA with repeated subdomains and 20 mpλ in MBF mutual interactions are used ($\square$).

The reflection coefficient of the antenna is shown in Fig. 3.14. In this figure, three different results can be seen. The unrefined SMA (solid line) and the SMA with repeated subdomains

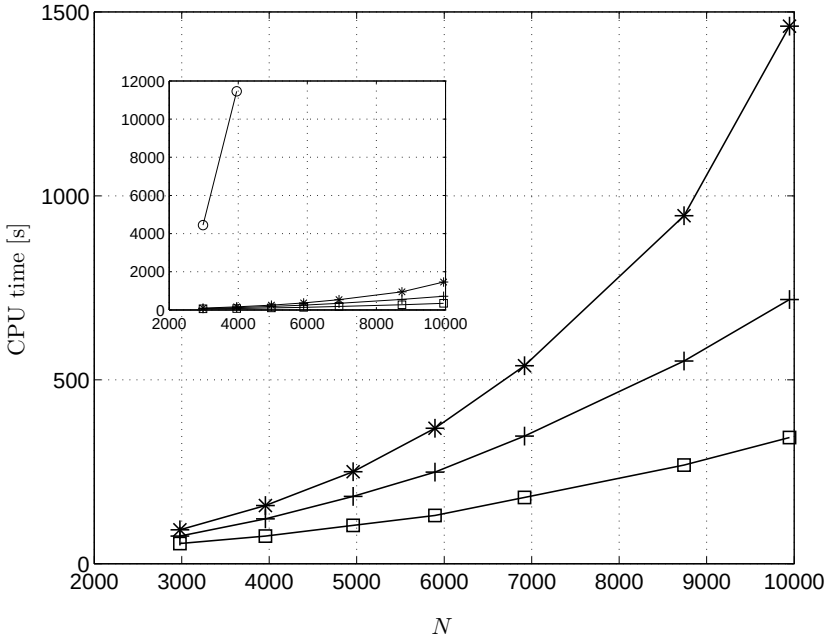

Figure 3.13: CPU time vs. number of unknowns using unrefined SMA ($*$), SMA with repeated subdomains ($+$) and SMA with repeated subdomains and fast mutual interactions with 20 mpλ ($\square$). In the upper left corner, the time needed for direct solution of the conventional MoM system of equations is shown.

and 20 mpλ ($\circ$) give practically the same results, the only difference being in more advantageous computational time. The results taken from [6] and obtained using another approximate technique, the Multilevel Matrix Decomposition Algorithm (MLMDA), are presented using a dash-dotted line. By inspecting the third curve (dashed line), which represents the measured values, one can conclude that the differences between the compared numerical methods are of the order of the differences from the measured values. Our method provides, therefore, an accuracy comparable to the MLMDA.

Fig. 3.15 shows the co-polar radiation patterns of the 8×8 corporate-fed patch array. Solid lines represent measured values, dashed lines represent the results obtained using the SMA with repeated subdomains and 20 mpλ in MBF mutual interactions, and circles – the results obtained using the conventional MoM. In the conventional MoM, the solution of the problem that takes 1.6 GB of memory on a PC with 512 MB of RAM was made possible using the block ILU preconditioner scheme [21], where matrix blocks are stored on the hard disk and swapped to memory. One can observe a very good agreement of the SMA results and the ones obtained using the conventional MoM with the measurements in both E- [Fig. 3.15(a)] and H-planes [Fig. 3.15(b)].

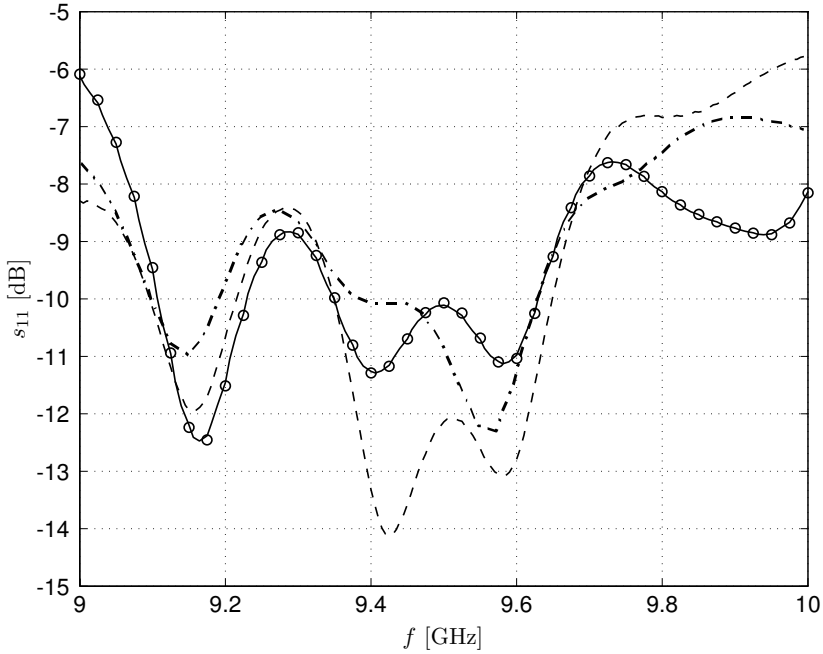

Figure 3.14: The reflection coefficient of the 8×8 corporate-fed patch array. Measurements (dashed line), MLMDA [6] (dash-dotted line), the unrefined SMA (solid line) and the SMA with repeated subdomains and 20 mpλ ($\circ$).

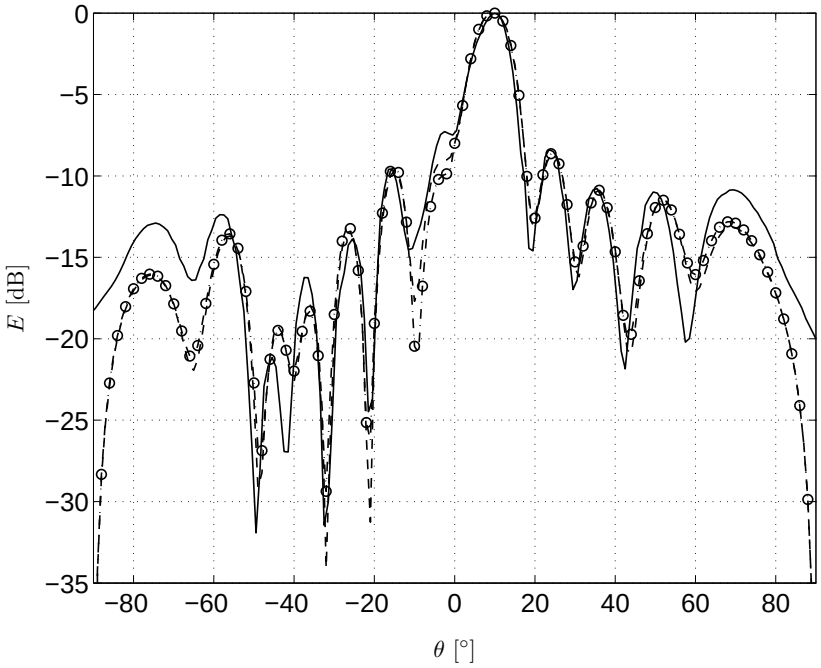

(a) E–plane.

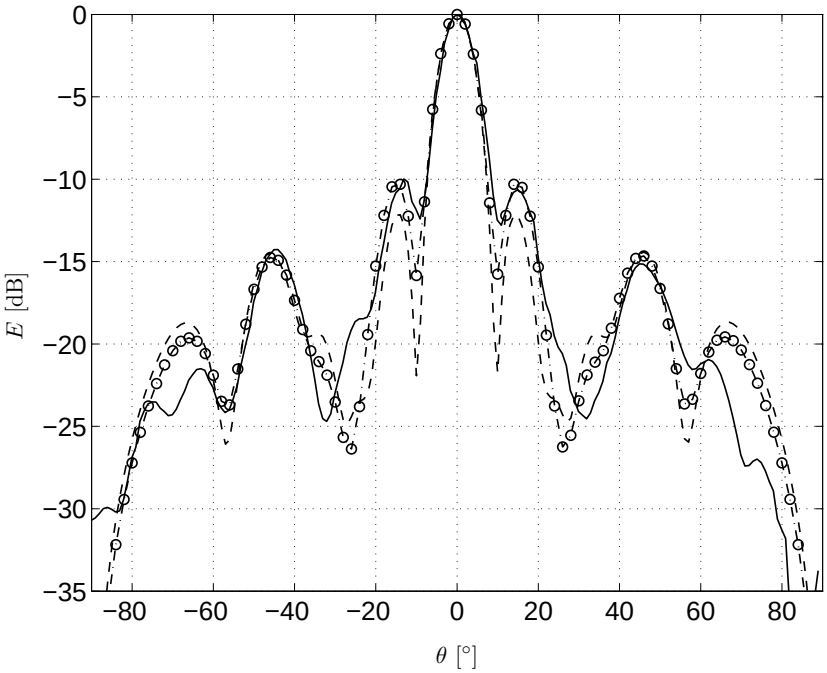

(b) H–plane.

Figure 3.15: Co-polar radiation patterns of the 8×8 corporate-fed patch array at $f = 9.43$ GHz. Measurements (solid lines), conventional MoM solved using [21] (○), and SMA with repeated subdomains and 20 mpλ (dashed lines).

3.7 Conclusion

In this chapter, we have presented an improved Subdomain Multilevel Approach (SMA), used to solve large complex-shaped antenna problems. The technique reduces the macro-basis functions into equivalent moments, which are then used in the efficient evaluation of MBF reaction terms. This procedure bypasses the bottleneck of the standard unrefined SMA, where the potential advantages are hindered by the effort spent in the computation of the reaction terms between macro-basis functions. Moreover, a welcome flexibility is introduced at the level of these computations. The technique presented here can be viewed as the physical counterpart of a matrix block decomposition, followed by an eigenvalue search or a singular value decomposition [22] of the blocks. Although it may require a little manual tuning and some expert system to divide the geometry under study, the technique presented here is very simple, easy to implement and competitive when compared with other available approaches.

The accuracy of the proposed method has been verified by investigating three representative examples, in which this technique is compared with a brute-force approach, with the unrefined SMA and with measurements. The results show excellent agreement between all the approaches for both input impedance and radiation patterns. The computational gain versus the unrefined SMA depends upon the size of the problem and upon the density of moments used to represent the macro-bases. For the problems studied here ($\sim 10^4$ unknowns), a reduction of up to 50 % of the CPU time has been observed. The improvement factor will quickly increase for larger problems or if a small reduction in accuracy can be accepted. Moreover, the use of symmetries and equivalent moments, as shown in the last section of this chapter, allows a further reduction in CPU time by a factor of four or better.

References

[1] W. C. Chew, J. Jin, C. Lu, E. Michielssen, and J. M. Song, "Fast solution methods in electromagnetics," *IEEE Trans. Antennas Propagat.*, vol. 45, no. 3, pp. 533–543, Mar. 1997.

[2] R. Coifman, V. Roklhin, and S. Wandzura, "The fast multiple method for the wave equation: A pedestrian prescription," *IEEE Antennas Propagat. Mag.*, vol. 35, no. 3, pp. 7–12, June 1993.

[3] J. M. Song, C. C. Lu, and W. C. Chew, "Multilevel fast multiple algorithm for solving combined field integral equations of electromagnetic scattering," *Microwave Opt. Technol. Lett.*, vol. 10, no. 1, pp. 14–19, Sept. 1995.

[4] F. X. Canning, "Improved impedance matrix localization method," *IEEE Trans. Antennas Propagat.*, vol. AP-41, no. 5, pp. 659–667, May 1993.

[5] E. Bleszynski, M. Bleszynski, and T. Jaroszewicz, "AIM: Adaptive integral method for solving large-scale electromagnetic scattering and radiation problems," *Radio Sci.*, vol. 31, no. 5, pp. 1225–1251, Sept. 1996.

[6] J. Parron, J. M. Rius, and J. R. Mosig, "Application of the multilevel decomposition algorithm to the frequency analysis of large microstrip antenna arrays," *IEEE Trans. Magn.*, vol. 38, no. 2, pp. 721–724, Mar. 2002.

[7] S. Ooms and D. De Zutter, "A new iterative diakoptics-based multilevel moments method for planar circuits," *IEEE Trans. Microwave Theory Tech.*, vol. 46, no. 3, pp. 280–291, Mar. 1998.

[8] L. Matekovits, G. Vecchi, G. Dassano, and M. Orefice, "Synthetic function analysis of large printed structures: The solution space sampling approach," in *Proc. IEEE AP-S Int. Symp.*, Boston, MA, July 2001, pp. 568–571.

[9] J. Yeo, V. V. S. Prakash, and R. Mitra, "Efficient analysis of a class of microstrip antennas using the characteristic basis function method cbfm," *Microwave Opt. Technol. Lett.*, vol. 39, no. 6, pp. 456–464, Dec. 2003.

[10] W. B. Lu, T. J. Cui, Z. G. Qian, X. X. Yin, and W. Hong, "Accurate analysis of large-scale periodic structures using an efficient sub-entire-domain basis function method," *IEEE Trans. Antennas Propagat.*, vol. 52, no. 11, pp. 3078–3085, Nov. 2004.

[11] E. Suter and J. R. Mosig, "A subdomain multilevel approach to moment methods," in *Proc. International Symposium on Antennas (JINA'98)*, Nice, France, Nov. 17–19, 1998, pp. 157–160.

[12] J. R. Mosig and E. Suter, "A multilevel divide and conquer approach to moment method computations," in *International Symposium on Recent Advances in Microwave Technology (ISRAMT'99)*, Malaga, Spain, Dec. 13-17, 1999, pp. 9–12.

[13] E. Suter and J. R. Mosig, "A subdomain multilevel approach for the efficient MoM analysis of large planar antennas," *Microwave Opt. Technol. Lett.*, vol. 26, no. 4, pp. 270–277, Aug. 2000.

[14] E. Suter, "Efficient numerical modelling of large scale planar antennas using a subdomain multilevel approach," Ph.D. dissertation, Ecole Polytechnique Fédérale de Lausanne, Switzerland, 2000, Thèse No. 2286.

[15] S. K. Schelkunoff and H. T. Friis, *Antennas: Theory and Practice*. New York: Wiley, 1952.

[16] J. R. Mosig, "Integral-equation technique," in *Numerical Techniques for Microwave and Millimeter-Wave Passive Structures*, T. Itoh, Ed. New York: Wiley, 1989, ch. 3, pp. 133–213.

[17] S. M. Rao, D. R. Wilton, and A. W. Glisson, "Electromagnetic scattering by surfaces of arbitrary shape," *IEEE Trans. Antennas Propagat.*, vol. 30, no. 3, pp. 409–418, May 1982.

[18] R. F. Harrington, *Field Computation by Moment Methods*, 2nd ed. New York: IEEE Press, 1993.

[19] A. Carlström, M. Viberg, P. Tatalias, J. R. Mosig, E. Suter, and M. Bandinelli, "Antenna CAD and Technology for Future SARs," Summary Report, July 2001, ESTEC No. 11279/94/NL/PB.

[20] C. Wang, F. Ling, and J. Jin, "A fast full-wave analysis of scattering and radiation from large finite arrays of microstrip antennas," *IEEE Trans. Antennas Propagat.*, vol. 46, no. 10, pp. 1467–1474, Oct. 1998.

[21] A. Heldring, J. M. Rius, and L. Ligthart, "New block ILU preconditioner scheme for numerical analysis of very large electromagnetic problems," *IEEE Trans. Magn.*, vol. 38, no. 2, pp. 337–340, Mar. 2002.

[22] R. Hall, Z. Cendes, and D. Wu, "Recent advances in planar moment method CAD tools," in *Millennium Conference on Antennas and Propagation*, Davos, Switzerland, Apr. 9-14, 2000.

4 Arbitrarily-Shaped Slots in Thick Conducting Screens: An Approximate Solution

4.1 Introduction

A classical problem in EM-theory is the scattering of an electromagnetic wave by an aperture in a thick conducting screen. This problem has countless applications in modern technology, ranging from waveguide filters using interconnecting wall holes and irises to cavity-backed slot-fed antennas and passing through many problems of field penetration through slits and holes, of paramount relevance in electromagnetic compatibility. In addition, very recently discovered enhanced transmission of light through subwavelength hole arrays made in optically thick metal films has numerous potential applications in photonics and optoelectronics [1, 2].

In a general case (Fig. 4.1), the screen may be curved and have a non-zero thickness, the aperture will have arbitrary shape and dimensions and even the lateral metallic walls associated to the aperture rim may have an irregular profile, thus leading to a truly three-dimensional problem. In this work, we will concentrate on the case where the thick conducting screen is bound by two parallel surfaces and is locally flat. Even with this simplification, the problem remains three-dimensional and for analysis purposes, a reduction to two dimensions has been traditionally obtained in two ways. With reference to Fig. 4.1, either the screen thickness is neglected and then we formulate the problem in two coordinates (x, y) locally tangential to the screen, or a translational symmetry along one tangential coordinate (y) is assumed, and then we work in a two-dimensional cut of the problem defined by its profile in the (x, z) coordinates.

Historically, the first model analyzed was the zero-thickness screen (frequently but improperly called the zero-thickness slot geometry). This problem can be traced back to Lord Rayleigh in 1897 [3] and was extensively analyzed in a series of classical papers authored by Bethe [4], Levine and Schwinger [5, 6], Collin [7], Bouwkamp [8], Van Bladel [9], and Rahmat-Samii and Mittra [10] to mention but a few pioneers. In these studies, the transverse dimensions of the aperture were always supposed to be small and, consequently, quasi-static or low frequency approximations were used, together with the concept of polarizability [11]. On the other hand, specific techniques were also developed for large apertures, using geometrical [12] and spectral [10] theories of diffraction. The rigorous formulation of a zero-thickness aperture with arbitrary size and shape is made through the use of the equivalence theorem and equivalent magnetic currents. This leads to an integral equation problem solved with the use of dyadic Green's functions [13]. This nowadays classical formulation is summarized in both vintage [14] and recent [15] electromagnetic textbooks. It was also extensively discussed

in an excellent review paper [16] and translated into the framework of a generalized network approach [17].

The second 2-D model, assuming translational invariance and valid for long, thin apertures (slits) was solved using asymptotic Wiener-Hopf techniques [18] or coupled integral equations [19]. These works deal essentially with thick slots having rectangular profiles in the plane. The integral equation approach was extended to arbitrary profiles [20] and was also combined with finite elements to cope with more general configurations possibly including inhomogeneous media [21, 22].

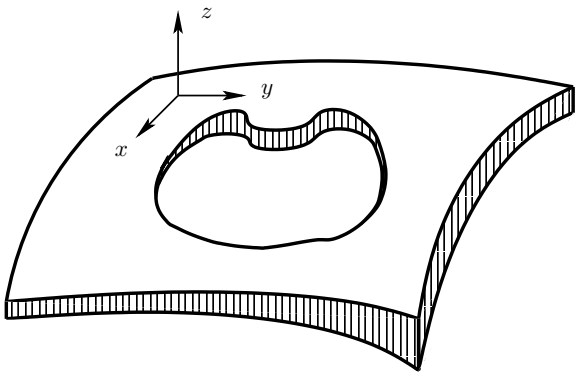

Figure 4.1: General geometry for an arbitrarily shaped aperture in a conducting curved screen of variable thickness.

Back to the general 3-D aperture problem of Fig. 4.1, it can be formally solved by using equivalence principles leading to a set of coupled equations. Typically, the two outer problems (outside the thick slot) will be formulated as integral equations and the inner problem (inside the thick slot) as a cavity problem where the Helmholtz equation is to be satisfied. In practice, the numerical implementation will be a difficult task, asking in the external regions for complicated Green's functions and 2-D-boundary elements, which must be coupled to 3-D-finite elements inside the slot. A clever simplified implementation, based on the reciprocity principle [23] has been used to analyze microstrip antennas fed through reasonably thick rectangular slots [24].

Finally, it must be mentioned that the circular aperture case is of particular relevance in optics, and that the thick case has been solved by Roberts in an optical context [25], emphasizing the determination of plane wave reflection and transmission coefficients.

In the first part of this chapter, the problems of scattering from an infinitely thin metallic plate and aperture are addressed. The problem of the scattering from an aperture perforated in an infinitely thin metallic screen is, from the electromagnetic point of view, dual to the problem of the scattering from an infinitely thin metallic plate. Having this in mind, we will first develop the Mixed Potential Integral Equation (MPIE) for the thin plate problem and numerically solve it using the Method of Moments (MoM). Next, we deal with the problem of the infinitely thin aperture, which is less straightforward as it involves the use of magnetic currents and the equivalence theorem. We present the steps in applying the equivalence theorem in detail as they will be useful later when the problem of the thick aperture is solved.

After having presented the solutions for both problems, we illustrate the duality among them, by proving Babinet's principle [26]. Finally, we show some numerical results that are in good agreement with the results available in literature, and that are going to be used afterwards when the problem of apertures in thick metallic screens is addressed.

The second part of the chapter follows closely the ideas introduced by Mosig [27] and develops them in full detail. The integral equation formulation of the thick aperture problem is reviewed and modified to make it continuously valid for any aperture thickness. Hence, the new proposed thick aperture formulation is free from the difficulties usually encountered when applying it to a vanishing thickness slot. Afterwards, a simplification of the formulation is proposed, which reduces dramatically the computational burden while providing valid results for apertures whose thicknesses remain small compared with their linear transverse dimensions (or with the square root of their surface) but having otherwise arbitrary shapes and sizes. Finally, some preliminary numerical results with scattering on thick metallic apertures and slits are performed in order to validate the theory presented in this chapter.

4.2 Scattering from Infinitely Thin Plates and Apertures

4.2.1 Scattering from an Infinitely Thin Perfectly Conducting Metallic Plate

Let S_{P} be a perfectly conducting plate of an arbitrary shape situated at the interface of two semi-infinite homogeneous media (taken as the $z = 0$ plane). The plate is assumed to be illuminated with an obliquely-incident plane wave. The geometry of the problem is shown in Fig. 4.2.

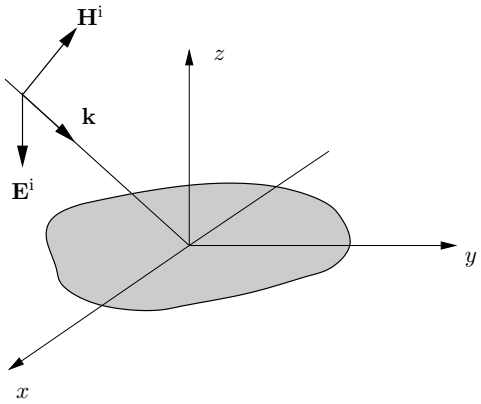

Figure 4.2: Infinitely thin metallic plate illuminated with an obliquely-incident plane wave.

An incident electric field $\mathbf{E}^{\mathrm{i}}$ induces on the plate the surface currents of a density $\mathbf{J}$, which in turn produce a scattered electric field $\mathbf{E}^{\mathrm{s}}$. Since the plate is perfectly conducting, the boundary condition that has to be satisfied on its surface is

$$\hat{z} \times (\mathbf{E}^{\mathrm{i}}(\mathbf{r}) + \mathbf{E}^{\mathrm{s}}(\mathbf{r})) = 0, \qquad \mathbf{r} \in S_{\mathrm{P}}. \tag{4.1}$$

The scattered electric field, knowing the dyadic Green's function $\overleftrightarrow{\mathbf{G}}_{\mathrm{EJ}}$, can be expressed as

$$\mathbf{E}^{\mathrm{s}}(\mathbf{r}) = \int_{S'} \overleftrightarrow{\mathbf{G}}_{\mathrm{EJ}}(\mathbf{r}|\mathbf{r}') \cdot \mathbf{J}(\mathbf{r}')\,\mathrm{d}S' = \overleftrightarrow{\mathbf{G}}_{\mathrm{EJ}} \otimes \mathbf{J}. \tag{4.2}$$

where $\otimes$ is a shorthand notation [28] for the convolution integral from (4.2). Introducing the potential Green's functions yields

$$\overleftrightarrow{\mathbf{G}}_{\mathrm{EJ}} \otimes \mathbf{J} = -\mathrm{j}\omega\overleftrightarrow{\mathbf{G}}_{A} \otimes \mathbf{J} - \boldsymbol{\nabla}\left(G_V \otimes \rho_{\mathrm{e}}\right), \tag{4.3}$$

where $\overleftrightarrow{\mathbf{G}}_{A}$ and G_V are the magnetic vector potential Green's function and electric scalar potential Green's function, respectively, and ρ_{e} is the surface charge density associated with the surface current density through the continuity equation

$$\rho_{\mathrm{e}} = -\frac{1}{\mathrm{j}\omega}\boldsymbol{\nabla}' \cdot \mathbf{J}. \tag{4.4}$$

In the last equation $\boldsymbol{\nabla}'$ is the operator that acts on the primed coordinates only. This way (4.3) can be written in terms of the surface current density $\mathbf{J}$ as

$$\overleftrightarrow{\mathbf{G}}_{\mathrm{EJ}} \otimes \mathbf{J} = -\mathrm{j}\omega\overleftrightarrow{\mathbf{G}}_{A} \otimes \mathbf{J} + \frac{1}{\mathrm{j}\omega}\boldsymbol{\nabla}\left(G_V \otimes \boldsymbol{\nabla}' \cdot \mathbf{J}\right). \tag{4.5}$$

The tangential component of the scattered electric field can be expressed now as follows

$$\mathbf{E}^{\mathrm{s}}_{\mathrm{t}}(\mathbf{r}) = -\mathrm{j}\omega \int_{S'} \overleftrightarrow{\mathbf{G}}_{A}(\mathbf{r}|\mathbf{r}') \cdot \mathbf{J}(\mathbf{r}')\,\mathrm{d}S' + \frac{1}{\mathrm{j}\omega}\boldsymbol{\nabla} \int_{S'} G_V(\mathbf{r}|\mathbf{r}')\boldsymbol{\nabla}' \cdot \mathbf{J}(\mathbf{r}')\,\mathrm{d}S', \tag{4.6}$$

where for the plate situated in free space $\overleftrightarrow{\mathbf{G}}_{A} = \frac{\mu}{4\pi}\Psi\overleftrightarrow{\mathbf{I}}$, $G_V = \frac{1}{4\pi\varepsilon}\Psi$, $\Psi = \frac{\mathrm{e}^{-\mathrm{j}k|\mathbf{r}-\mathbf{r}'|}}{|\mathbf{r}-\mathbf{r}'|}$ and for only tangential component of the electric field taken into account, the idem dyad is defined as $\overleftrightarrow{\mathbf{I}} = \hat{x}\hat{x} + \hat{y}\hat{y}$.

Taking into account (4.1), we can write

$$\mathbf{E}^{\mathrm{s}}_{\mathrm{t}}(\mathbf{r}) = -\mathbf{E}^{\mathrm{i}}_{\mathrm{t}}(\mathbf{r}), \qquad \mathbf{r} \in S_{\mathrm{P}} \tag{4.7}$$

and (4.6) becomes

$$-\mathbf{E}^{\mathrm{i}}_{\mathrm{t}}(\mathbf{r}) = -\mathrm{j}\omega \int_{S'} \overleftrightarrow{\mathbf{G}}_{A}(\mathbf{r}|\mathbf{r}') \cdot \mathbf{J}(\mathbf{r}')\,\mathrm{d}S' + \frac{1}{\mathrm{j}\omega} \int_{S'} \boldsymbol{\nabla} G_V(\mathbf{r}|\mathbf{r}')\boldsymbol{\nabla}' \cdot \mathbf{J}(\mathbf{r}')\,\mathrm{d}S'. \tag{4.8}$$

where the $\boldsymbol{\nabla}$ operator can be introduced inside the integral as it affects the unprimed coordinates only. In solving the integral equation (4.8), the method of moments technique (MoM) is applied. The function of the electric current surface density is expanded using subsectional

rooftop basis functions $\mathbf{f}_l$ defined on rectangular or triangular domains

$$\mathbf{J} = \sum_l \alpha_l \mathbf{f}_l(\mathbf{r}'), \qquad l = 1, \ldots, N. \tag{4.9}$$

Introducing (4.9) into (4.8), one obtains

$$-\mathbf{E}_{\mathrm{t}}^{\mathrm{i}}(\mathbf{r}) = \sum_l \alpha_l \left(-\mathrm{j}\omega \int_{S'} \overleftrightarrow{\mathbf{G}}_A(\mathbf{r}|\mathbf{r}') \cdot \mathbf{f}_l(\mathbf{r}')\, \mathrm{d}S' + \frac{1}{\mathrm{j}\omega} \int_{S'} \boldsymbol{\nabla} G_V(\mathbf{r}|\mathbf{r}') \boldsymbol{\nabla}' \cdot \mathbf{f}_l(\mathbf{r}')\, \mathrm{d}S' \right). \tag{4.10}$$

The Galerkin procedure is now completed if we choose for the testing functions the same set of functions as we have used before for the basis functions. Multiplying (4.10) with the set of testing functions $\mathbf{f}_k$ and integrating over the corresponding test surfaces, the following system of linear equations is obtained

$$\begin{aligned} -\int_S \mathbf{E}_{\mathrm{t}}^{\mathrm{i}}(\mathbf{r}) \cdot \mathbf{f}_k(\mathbf{r})\, \mathrm{d}S = \sum_l \alpha_l \Bigg(& -\mathrm{j}\omega \int_S \int_{S'} \mathbf{f}_k(\mathbf{r}) \cdot \overleftrightarrow{\mathbf{G}}_A(\mathbf{r}|\mathbf{r}') \cdot \mathbf{f}_l(\mathbf{r}')\, \mathrm{d}S'\, \mathrm{d}S + \\ & + \frac{1}{\mathrm{j}\omega} \int_S \int_{S'} \mathbf{f}_k(\mathbf{r}) \cdot \boldsymbol{\nabla} G_V(\mathbf{r}|\mathbf{r}') \boldsymbol{\nabla}' \cdot \mathbf{f}_l(\mathbf{r}')\, \mathrm{d}S\, \mathrm{d}S' \Bigg). \end{aligned} \tag{4.11}$$

The surface divergence theorem is used to transfer the gradient from the scalar potential Green's function to the testing function. First we have

$$\int_S \mathbf{f}_k \cdot \boldsymbol{\nabla} G_V\, \mathrm{d}S = \int_S \boldsymbol{\nabla} \cdot (\mathbf{f}_k G_V)\, \mathrm{d}S - \int_S \boldsymbol{\nabla} \cdot \mathbf{f}_k G_V\, \mathrm{d}S \tag{4.12}$$

and then we apply the surface divergence theorem

$$\int_S \boldsymbol{\nabla} \cdot (\mathbf{f}_k G_V)\, \mathrm{d}S = \oint_l G_V \mathbf{f}_k \cdot \hat{e}_l\, \mathrm{d}l = 0 \tag{4.13}$$

where $\hat{e}_l$ is the unit outward vector, normal to the line l that bounds the surface S. The last integral is zero due to the definition of the rooftop functions. Namely, we have two parts of the integration path, one where the value of the basis function is zero so the integral over this part is also zero (valid for rectangular rooftops), and the other where the basis function vector is perpendicular to the unit outward vector of the integration path and the scalar product between them gives zero (valid for both rectangular and triangular rooftops).

When we incorporate

$$\int_S \mathbf{f}_k \boldsymbol{\nabla} G_V\, \mathrm{d}S = -\int_S \boldsymbol{\nabla} \cdot \mathbf{f}_k G_V\, \mathrm{d}S \tag{4.14}$$

into (4.11), we obtain the following system of linear equations

$$\sum_l (a_{k,l} + v_{k,l})\alpha_l = e_k, \tag{4.15a}$$

where, for k, $l = 1, \ldots, N$,

$$a_{k,l} = \mathrm{j}\omega \int_S \int_{S'} \mathbf{f}_k(\mathbf{r}) \cdot \overleftrightarrow{\mathbf{G}}_A(\mathbf{r}|\mathbf{r}') \cdot \mathbf{f}_l(\mathbf{r}')\, \mathrm{d}S'\, \mathrm{d}S, \tag{4.15b}$$

$$v_{k,l} = \frac{1}{\mathrm{j}\omega} \int_S \int_{S'} \boldsymbol{\nabla} \cdot \mathbf{f}_k(\mathbf{r}) G_V(\mathbf{r}|\mathbf{r}') \boldsymbol{\nabla}' \cdot \mathbf{f}_l(\mathbf{r}')\, \mathrm{d}S'\, \mathrm{d}S, \tag{4.15c}$$

$$e_k = \int_S \mathbf{E}^{\mathrm{i}}_{\mathrm{t}}(\mathbf{r}) \cdot \mathbf{f}_k(\mathbf{r})\, \mathrm{d}S. \tag{4.15d}$$

4.2.2 Electromagnetic Penetration through an Aperture

In this section we will treat a problem which is from electromagnetic point of view dual to the problem discussed in the previous section. We will consider an aperture in a perfectly conducting screen, of vanishing thickness and infinite extent, separating half spaces of different electromagnetic characteristics. Fig. 4.3 depicts a step-by-step reduction of the lower half-space ($z < 0$) problem to a simple equivalent problem in a form which readily suggests how one may develop an expression for the lower half space total magnetic field $\mathbf{H}^-$. Fig. 4.3(a) depicts the original problem, a plane wave impinging from the lower half space on the infinitely thin metallic screen with an aperture (which can be of arbitrary shape). In Fig. 4.3(b) the aperture-perforated screen is seen to be replaced by a perfectly conducting (shorted aperture) plane with the original tangential electric field in the aperture at $z = 0^-$ ($\mathbf{E}^{\mathrm{a}}_{\mathrm{t}}$) restored by an appropriate magnetic surface current density $\mathbf{M}$, which is specified to have a value

$$\mathbf{M} = -(-\hat{z}) \times \mathbf{E}^{\mathrm{a}}_{\mathrm{t}} = \hat{z} \times \mathbf{E}^{\mathrm{a}}_{\mathrm{t}}. \tag{4.16}$$

Next, from the image theory, one removes the conducting screen and arrives at the lower half-space equivalent problem of Fig. 4.3(c). In addition to the images of the magnetic surface current $\mathbf{M}$, the images of the sources producing the original incident plane wave ($\mathbf{E}^{\mathrm{i}}$, $\mathbf{H}^{\mathrm{i}}$) have to be also taken into account. These images will produce so-called "mirrored" plane wave ($\mathbf{E}^{\mathrm{m}}$, $\mathbf{H}^{\mathrm{m}}$), which will assure that there will be no tangential component of the electric field on the perfectly conducting metallic screen

$$\hat{z} \times (\mathbf{E}^{\mathrm{m}}(\mathbf{r}) + \mathbf{E}^{\mathrm{i}}(\mathbf{r})) = 0, \qquad \mathbf{r} \in \{(x, y, z) | (x, y) \in \mathbb{R}^2,\ z = 0\} \tag{4.17}$$

and in consequence

$$\hat{z} \times (\mathbf{H}^{\mathrm{m}}(\mathbf{r}) - \mathbf{H}^{\mathrm{i}}(\mathbf{r})) = 0, \qquad \mathbf{r} \in \{(x, y, z) | (x, y) \in \mathbb{R}^2,\ z = 0\}. \tag{4.18}$$

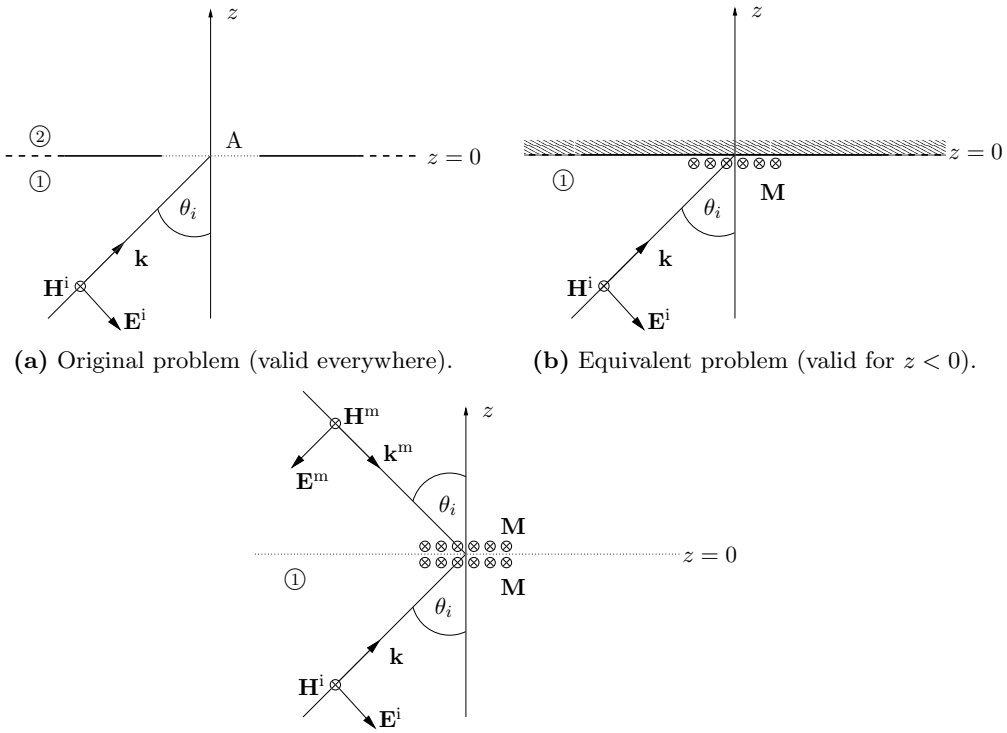

(a) Original problem (valid everywhere).

(b) Equivalent problem (valid for $z < 0$).

(c) Equivalent problem (valid for $z < 0$).

Figure 4.3: Lower half-space equivalent problems.

In Fig. 4.4 the equivalent problem valid for the upper half-space ($z > 0$) is shown.

The total lower half-space electromagnetic field ($\mathbf{E}^-$, $\mathbf{H}^-$) is the sum of the field radiated by $\mathbf{M}$ plus its image and that radiated by the lower half-space sources plus their images, that is, the incident and the mirror fields, all radiating in an infinite, homogeneous space characterized by electromagnetic properties of the lower half-space medium. For the upper half-space, the electromagnetic field ($\mathbf{E}^+$, $\mathbf{H}^+$) is the field radiated by magnetic surface current $-\mathbf{M}$ plus its image radiating in an infinite, homogeneous space characterized by electromagnetic properties of the upper half-space medium. Equations for the magnetic fields in the lower and the upper half-spaces have the following form

$$\mathbf{H}^-(\mathbf{r}) = \mathbf{H}^{\mathrm{i}}(\mathbf{r}) + \mathbf{H}^{\mathrm{m}}(\mathbf{r}) + \int_{S'} \overleftrightarrow{\mathbf{G}}^{(-)}_{\mathrm{HM}}(\mathbf{r}|\mathbf{r}') \cdot \mathbf{M}(\mathbf{r}')\, \mathrm{d}S', \tag{4.19a}$$

$$\mathbf{H}^+(\mathbf{r}) = -\int_{S'} \overleftrightarrow{\mathbf{G}}^{(+)}_{\mathrm{HM}}(\mathbf{r}|\mathbf{r}') \cdot \mathbf{M}(\mathbf{r}')\, \mathrm{d}S', \tag{4.19b}$$

where $\overleftrightarrow{\mathbf{G}}^{(-)}_{\mathrm{HM}}$ and $\overleftrightarrow{\mathbf{G}}^{(+)}_{\mathrm{HM}}$ are the magnetic field dyadic Green's functions for the lower and the upper half-spaces, respectively. It must be highlighted that these two Green's functions take

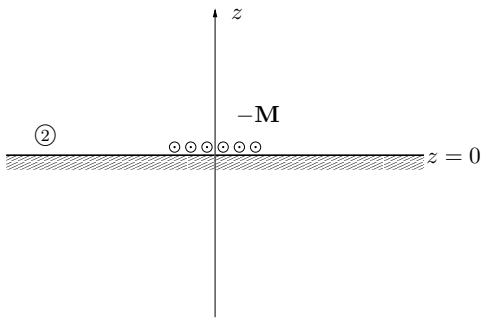

Figure 4.4: Equivalent upper half-space problem.

into account the images from the infinite perfectly conducting metallic screen and that this is the reason why in equations $\mathbf{M}$ is written instead of $2\mathbf{M}$.

Requiring that the magnetic field be continuous in any point belonging to the aperture $\mathbf{r} \in \mathrm{A}$

$$\hat{z} \times (\mathbf{H}^{+}(\mathbf{r}) - \mathbf{H}^{-}(\mathbf{r})) = 0, \tag{4.20}$$

denoting tangential components of the magnetic field with a subscript "t" and taking into account (4.18), the following integral equation is obtained

$$-2\mathbf{H}_{\mathrm{t}}^{\mathrm{i}}(\mathbf{r}) = \int_{S'} \left(\overleftrightarrow{\mathbf{G}}_{\mathrm{HM}}^{(+)}(\mathbf{r}|\mathbf{r}') + \overleftrightarrow{\mathbf{G}}_{\mathrm{HM}}^{(-)}(\mathbf{r}|\mathbf{r}') \right) \cdot \mathbf{M}(\mathbf{r}')\, \mathrm{d}S' = \int_{S'} \overleftrightarrow{\mathbf{G}}_{\mathrm{HM}}(\mathbf{r}|\mathbf{r}') \cdot \mathbf{M}(\mathbf{r}')\, \mathrm{d}S'. \tag{4.21}$$

If the electric vector potential Green's function $\overleftrightarrow{\mathbf{G}}_F$ and scalar magnetic potential Green's function G_W are introduced

$$\overleftrightarrow{\mathbf{G}}_{\mathrm{HM}} \otimes \mathbf{M} = -\mathrm{j}\omega \overleftrightarrow{\mathbf{G}}_F \otimes \mathbf{M} - \boldsymbol{\nabla} \left(G_W \otimes \rho_{\mathrm{m}} \right), \tag{4.22}$$

and the same MoM procedure from Section 4.2.1 is applied, one obtains the following system of linear equations

$$\sum_{l} (f_{k,l} + w_{k,l}) \alpha_l = h_k, \tag{4.23a}$$

where, for $k,\, l = 1, \ldots, N$,

$$f_{k,l} = \mathrm{j}\omega \int_{S} \int_{S'} \mathbf{f}_k(\mathbf{r}) \cdot \overleftrightarrow{\mathbf{G}}_F(\mathbf{r}|\mathbf{r}') \cdot \mathbf{f}_l(\mathbf{r}')\, \mathrm{d}S'\, \mathrm{d}S, \tag{4.23b}$$

$$w_{k,l} = \frac{1}{\mathrm{j}\omega} \int_{S} \int_{S'} \boldsymbol{\nabla} \cdot \mathbf{f}_k(\mathbf{r}) G_W(\mathbf{r}|\mathbf{r}') \boldsymbol{\nabla}' \cdot \mathbf{f}_l(\mathbf{r}')\, \mathrm{d}S'\, \mathrm{d}S, \tag{4.23c}$$

$$h_k = 2 \int_{S} \mathbf{H}_{\mathrm{t}}^{\mathrm{i}}(\mathbf{r}) \cdot \mathbf{f}_k(\mathbf{r})\, \mathrm{d}S. \tag{4.23d}$$

If the perforated metallic screen is placed in a homogeneous medium of dielectric permittivity ε and magnetic permeability μ, then the potential Green's functions can be written as follows

$$\overleftrightarrow{\mathbf{G}}_F(\mathbf{r}|\mathbf{r}') = 4\,\frac{\varepsilon}{4\pi}\,\frac{\mathrm{e}^{-\mathrm{j}k|\mathbf{r}-\mathbf{r}'|}}{|\mathbf{r}-\mathbf{r}'|}\,\overleftrightarrow{\mathbf{I}}, \tag{4.24a}$$

$$G_W(\mathbf{r}|\mathbf{r}') = 4\,\frac{1}{4\pi\mu}\,\frac{\mathrm{e}^{-\mathrm{j}k|\mathbf{r}-\mathbf{r}'|}}{|\mathbf{r}-\mathbf{r}'|}. \tag{4.24b}$$

where the factor "4" comes from the equivalence theorem and image theory applied to the thin aperture problem.

4.2.3 Babinet's Principle

Consider a metallic, perfectly conducting rectangular strip situated in a homogeneous medium with an intrinsic impedance η. Let the strip be excited by means of a generator at its center [Fig. 4.5(a)]. The generator can be modeled as an external field $(\mathbf{E}_1^{\mathrm{i}}, \mathbf{H}_1^{\mathrm{i}})$ concentrated in a small area at the center of the strip. The integral equation of the problem can be represented as follows (see Section 4.2.1)

$$-\mathbf{E}_1^{\mathrm{i}} = \overleftrightarrow{\mathbf{G}}_{\mathrm{EJ}} \otimes \mathbf{J}_1, \tag{4.25}$$

where $\overleftrightarrow{\mathbf{G}}_{\mathrm{EJ}}$ is the free space dyadic electric field Green's function for electric dipole excitation, $\mathbf{J}_1$ the induced electric surface current density on the strip and the symbol $\otimes$ stands for the convolution integral.

Consider the complementary problem, a rectangular slot of the same dimensions as dimensions of the metallic strip, cut in an infinite, plane, perfectly conducting thin sheet of metal. The slot is now excited by means of a generator connected between its opposite edges as shown in Fig. 4.5(b). The generator is modeled by an external electromagnetic field $(\mathbf{E}_2^{\mathrm{i}}, \mathbf{H}_2^{\mathrm{i}})$, where magnetic and electric quantities have the same values but interchanged directions when compared to the original problem.

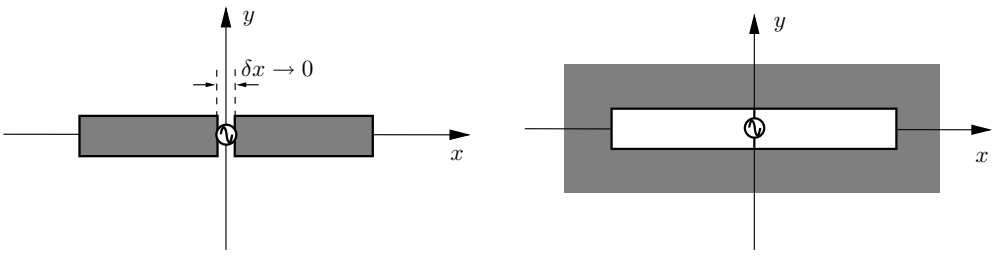

(a) Rectangular strip. **(b)** Rectangular slot.

Figure 4.5: Rectangular strip and complementary slot.

It has been shown in Section 4.2.2 that, using the equivalence principle, the integral equation for the complementary problem can be written as follows

$$-\mathbf{H}_2^{\mathrm{i}} = 2\overleftrightarrow{\mathbf{G}}_{\mathrm{HM}} \otimes \mathbf{M}_2, \tag{4.26}$$

where $\vec{\mathbf{G}}_{\mathrm{HM}}$ is the free space dyadic magnetic field Green's function for magnetic dipole excitation and $\mathbf{M}_2$ induced magnetic surface current density over the slot.

Since both $\mathbf{H}_2^{\mathrm{i}}$ and $\mathbf{E}_1^{\mathrm{i}}$ have the same direction, and $|\mathbf{E}_1^{\mathrm{i}}| = \eta|\mathbf{H}_2^{\mathrm{i}}|$, the resulting surface current densities will satisfy the following relation

$$\frac{\mathbf{J}_1}{|\mathbf{E}_1^{\mathrm{i}}|} = 2\frac{\mathbf{M}_2}{|\mathbf{H}_2^{\mathrm{i}}|}, \tag{4.27}$$

that is

$$\mathbf{J}_1 = \frac{2}{\eta}\mathbf{M}_2. \tag{4.28}$$

In the following we demonstrate that the geometric mean of the driving-point impedances of a strip and a complementary slot is equal to half the intrinsic impedance of the surrounding medium (Babinet's principle) [26].

Using the reaction concept, the driving point impedance of the metallic strip can be defined as

$$Z_1 = -\frac{1}{|I_1|^2}\int_{S_1} \mathbf{E}_1 \cdot \mathbf{J}_1^* \,\mathrm{d}S, \tag{4.29}$$

with $\mathbf{E}_1$ being the scattered electric field, $\mathbf{J}_1$, as before, the electric surface current density and I_1 the driving current of the strip generator

$$I_1 = \int_y \mathbf{J}_1 \cdot \hat{x}\,\mathrm{d}y. \tag{4.30}$$

For the complementary slot, the driving point admittance can be defined as

$$Y_2 = -\frac{1}{|V_2|^2}\int_{S_2} \mathbf{H}_2 \cdot \mathbf{M}_2^* \,\mathrm{d}S, \tag{4.31}$$

where the magnetic current, that is, the driving voltage of the generator, is obtained by integrating across the width of the slot along the y axis

$$V_2 = \int_y \mathbf{M}_2 \cdot \hat{x}\,\mathrm{d}y. \tag{4.32}$$

Using (4.28), we have the following relation between the current of the generator in strip problem and the voltage of the generator in the slot problem

$$V_2 = \int_y \mathbf{M}_2 \cdot \hat{x}\,\mathrm{d}y = \int_y \frac{\eta}{2}\mathbf{J}_1 \cdot \hat{x}\,\mathrm{d}y = \frac{\eta}{2}I_1. \tag{4.33}$$

The equation corresponds to the equation (20) in [26]. From (4.29), (4.31) and (4.33) the

product of the strip and complementary slot impedances can be written as follows

$$Z_1 Z_2 = \frac{Z_1}{Y_2} = \frac{|V_2|^2}{|I_1|^2} \frac{\int\limits_{S_1} \mathbf{E}_1 \cdot \mathbf{J}_1^* \, \mathrm{d}S}{\int\limits_{S_2} \mathbf{H}_2 \cdot \mathbf{M}_2^* \, \mathrm{d}S} = \frac{\eta^2}{4} \frac{\int\limits_{S_1} \mathbf{E}_1 \cdot \mathbf{J}_1^* \, \mathrm{d}S}{\int\limits_{S_2} \mathbf{H}_2 \cdot \mathbf{M}_2^* \, \mathrm{d}S}. \tag{4.34}$$

The last step in the development will be to show that the ratio between the powers dissipated by generators in both cases is equal to one, that is

$$\int\limits_{S_2} \mathbf{H}_2 \cdot \mathbf{M}_2^* \, \mathrm{d}S = \int\limits_{S_1} \mathbf{E}_1 \cdot \mathbf{J}_1^* \, \mathrm{d}S. \tag{4.35}$$

First, by applying the equivalence principle we have represented the original slot problem by two free space problems: 1) in the lower half space we had magnetic surface current density $2\mathbf{M}_2$ radiating in free space, and 2) in the upper half space we had magnetic surface current density $-2\mathbf{M}_2$ radiating in free space. The whole generator power is therefore dissipated equally in the upper and lower half spaces, so we can write

$$\int\limits_{S_2} \mathbf{H}_2 \cdot \mathbf{M}_2^* \, \mathrm{d}S = \int\limits_{S_2^+} \mathbf{H}_2 \cdot \mathbf{M}_2^* \, \mathrm{d}S + \int\limits_{S_2^-} \mathbf{H}_2 \cdot \mathbf{M}_2^* \, \mathrm{d}S = 2 \int\limits_{S_2^+} \mathbf{H}_2 \cdot \mathbf{M}_2^* \, \mathrm{d}S. \tag{4.36}$$

The surface S_2^+ of the slot (in the upper half space problem) corresponds to the surface S_1 of the strip, therefore

$$\int\limits_{S_2} \mathbf{H}_2 \cdot \mathbf{M}_2^* \, \mathrm{d}S = 2 \int\limits_{S_1} \mathbf{H}_2 \cdot \mathbf{M}_2^* \, \mathrm{d}S = 2 \int\limits_{S_1} \frac{1}{\eta} \mathbf{E}_1 \cdot \frac{\eta}{2} \mathbf{J}_1^* \, \mathrm{d}S = \int\limits_{S_1} \mathbf{E}_1 \cdot \mathbf{J}_1^* \, \mathrm{d}S. \tag{4.37}$$

Taking into account the last equation (4.37), from (4.34) directly follows

$$Z_1 Z_2 = \frac{\eta^2}{4}. \tag{4.38}$$

Thus we have verified the validity of Babinet's principle and found the particular form it adopts in our case.

4.2.4 Numerical Results

Zero Incidence Plane Wave

Let us first consider an infinitesimally thin square metallic plate of dimensions $\lambda \times \lambda$. The plate is assumed to be situated in an unbounded homogeneous medium (air) and to be illuminated with a plane wave. For convenience, the plate is assumed to be located in the xy plane of a Cartesian system of coordinates, whose origin is at the center of the plate. The geometry of the problem is shown in Fig. 4.6 with two possible cases of incidence

- TE case [Fig. 4.6(a)], where $\mathbf{E}^{\mathrm{i}} = -\hat{y}E_0 \mathrm{e}^{-\mathrm{j}\mathbf{k}\cdot\mathbf{r}}$
- TM case [Fig. 4.6(b)], where $\mathbf{H}^{\mathrm{i}} = \hat{y}\frac{1}{\eta}E_0 \mathrm{e}^{-\mathrm{j}\mathbf{k}\cdot\mathbf{r}}$

In the case when the incident angle θ_{i} is zero, TE incidence and TM incidence are equivalent, so the results for zero TM incidence will be shown.

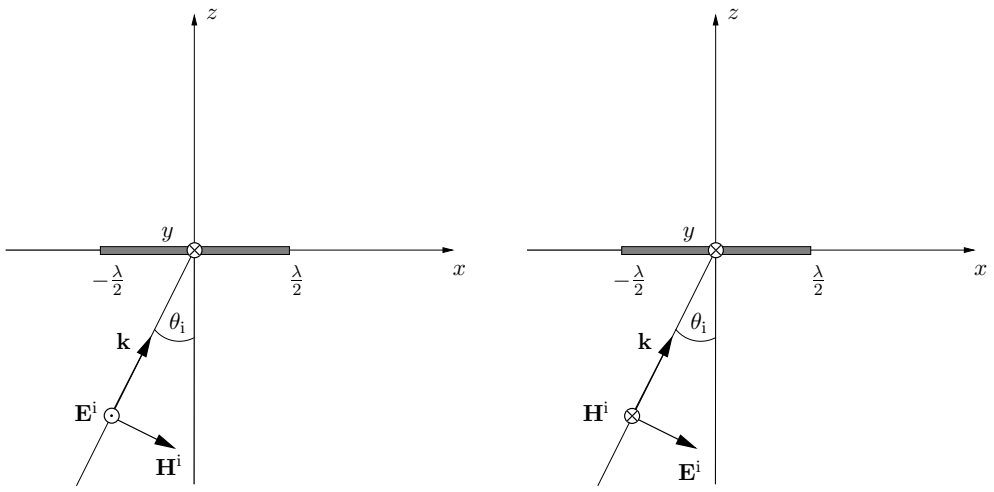

(a) TE incidence. **(b)** TM incidence.

Figure 4.6: Infinitesimally thin square plate illuminated with a plane wave.

Let us suppose that the plane wave has the following form

$$\mathbf{E}^{\mathrm{i}} = \hat{x}E_0 \mathrm{e}^{-\mathrm{j}kz}. \tag{4.39}$$

Figs. 4.7 and 4.8 show distribution of the magnitude, the real and imaginary parts of the x and y current components over the square $\lambda \times \lambda$ metallic plate, normalized with magnetic field intensity of the incident plane wave. It is supposed that the magnitude of the plane wave electric field is $E_0 = 1$ V/m. These results are in excellent agreement with the benchmark results that can be found in [29].

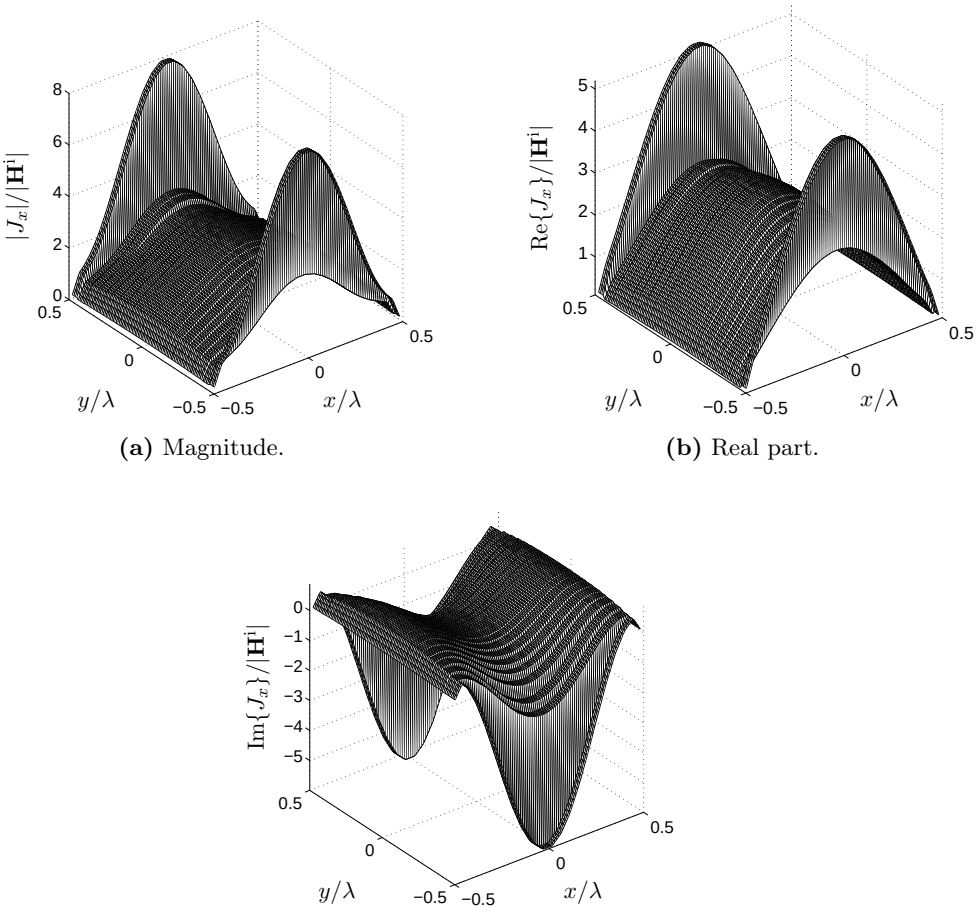

(a) Magnitude.

(b) Real part.

(c) Imaginary part.

Figure 4.7: The x-component of the electric surface current over $\lambda \times \lambda$ plate illuminated with a zero incidence plane wave.

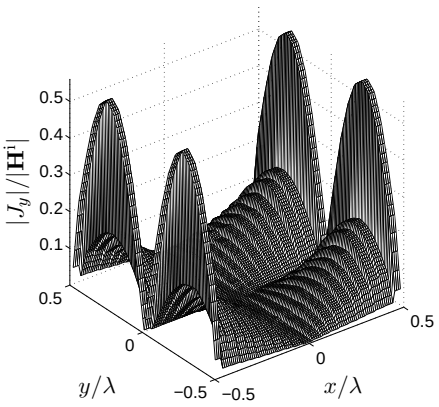

(a) Magnitude.

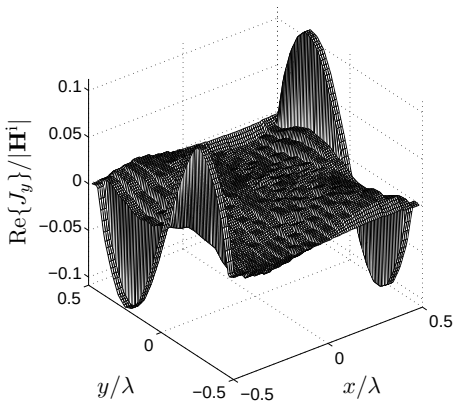

(b) Real part.

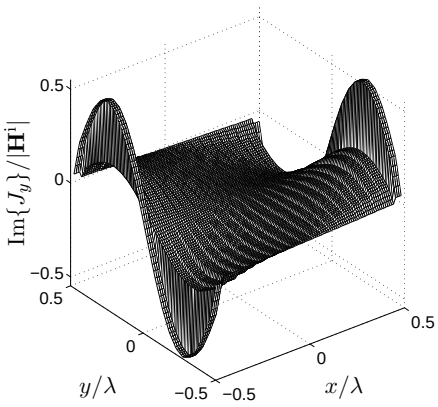

(c) Imaginary part.

Figure 4.8: The y-component of the electric surface current over $\lambda \times \lambda$ plate illuminated with a zero incidence plane wave.

Next, we will consider an infinitely thin square aperture of the same dimensions as the dimensions of the plate to be illuminated with a plane wave, whose magnetic field has the following form (electromagnetically dual problem)

$$\mathbf{H}^{\mathrm{i}} = \hat{x} H_0 \mathrm{e}^{-\mathrm{j}kz}, \tag{4.40}$$

where $H_0 = 1$ A/m. In Figs. 4.9 and 4.10, the x-components of the induced electric (magnetic) surface current densities along the $x = 0$ and $y = 0$ lines are shown for the case of the plate (aperture) with a zero incidence plane wave illumination. It can be noticed that the normalized magnetic current (normalization being done with the magnitude of the electric field intensity) is twice smaller than the corresponding normalized electric current.

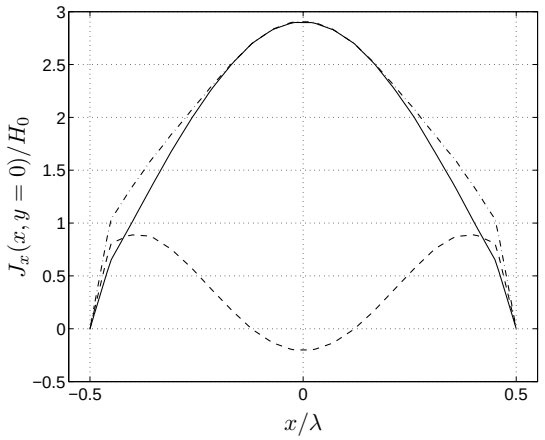

(a) The x-component of the electric surface current along the x-axis.

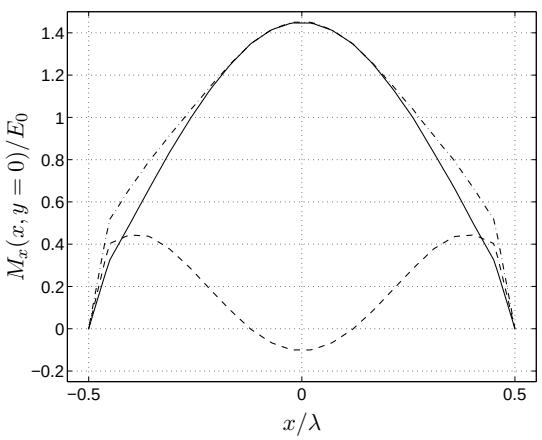

(b) The x component of the magnetic surface current along the x-axis.

Figure 4.9: The x-component of the currents induced on a square patch/aperture along the x-axis. Solid line: real part, dashed line: imaginary part, dash-dotted line: magnitude.

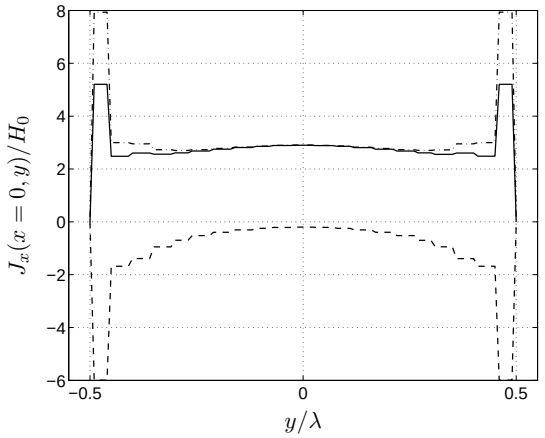

(a) The x-component of the electric surface current along the y-axis.

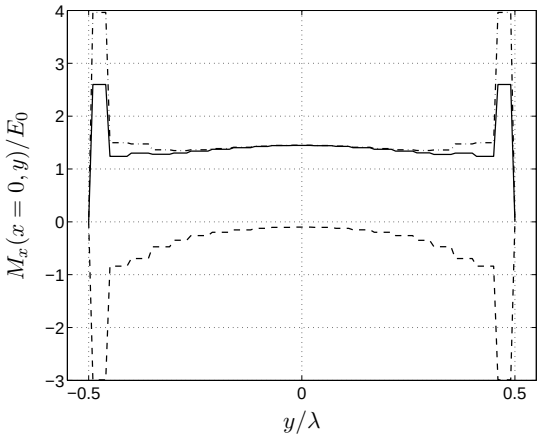

(b) The x-component of the magnetic surface current along the y-axis.

Figure 4.10: The x-component of currents induced on a square patch/aperture along the y-axis. Solid line: real part, dashed line: imaginary part, dash-dotted line: magnitude.

Oblique Plane Wave Incidence

We consider the case of an oblique plane wave incidence on a rectangular narrow slot of dimensions $L = 10\lambda$, $W = \lambda/10$, with its longer side oriented in the x direction. Let the tangential component of the incident magnetic field have only the x-direction (Fig. 4.11).

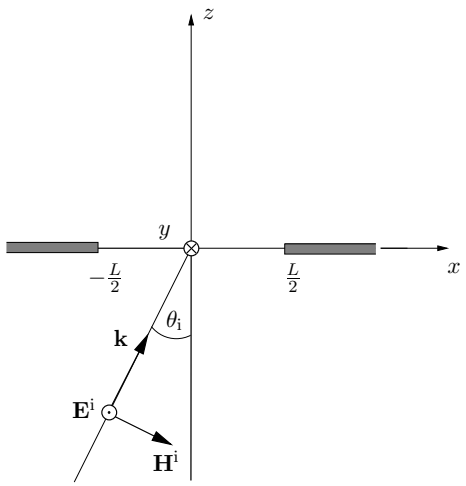

Figure 4.11: TE case of a planewave incidence on a narrow rectangular aperture.

In Fig. 4.12, Fig. 4.13, and Fig. 4.14 the current distribution and radiation pattern of a long aperture when illuminated with a plane wave impinging from the lower half space with incident angles $\theta_i = 15°$, $\theta_i = 45°$, and $\theta_i = 75°$, respectively, are shown. As it can be seen from the radiation patterns, the radiated field is maximum in the direction from which incident plane wave impinges to the aperture. Radiation patterns are compared to the radiation patterns obtained assuming that the electric field in the aperture follows the incident electric field, that is, $\mathbf{M} = \hat{z} \times \mathbf{E}^i$. This last assumption is the equivalent of the Physical Optics (PO) model for scattering from apertures. Since it assumes an unperturbated traveling wave in the aperture, unaffected by edge effects, it is frequently called the "traveling wave approach".

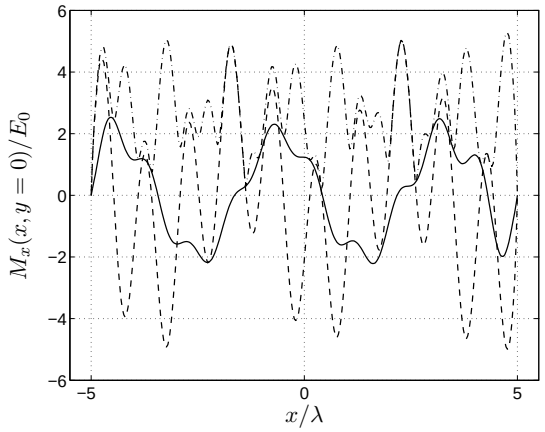

(a) The x-component of magnetic current along x-axis. Solid line: real part, dashed line: imaginary part, dash-dotted line: magnitude.

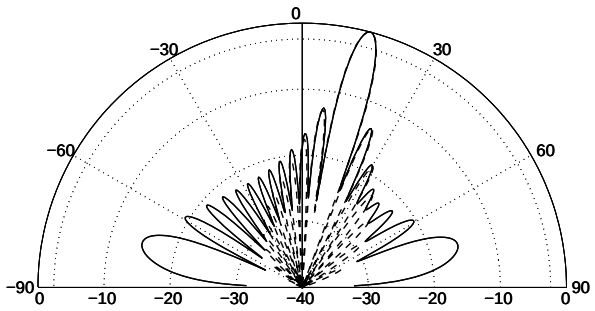

(b) Radiation pattern in $\phi = 0$ plane. E_ϕ component of the radiated field. Simulation (solid line) and traveling wave (dashed).

Figure 4.12: $\theta_\mathrm{i} = 15°$.

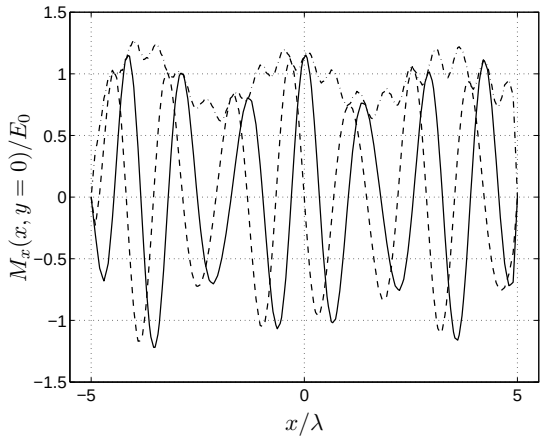

(a) The x-component of magnetic current along x-axis. Solid line: real part, dashed line: imaginary part, dash-dotted line: magnitude.

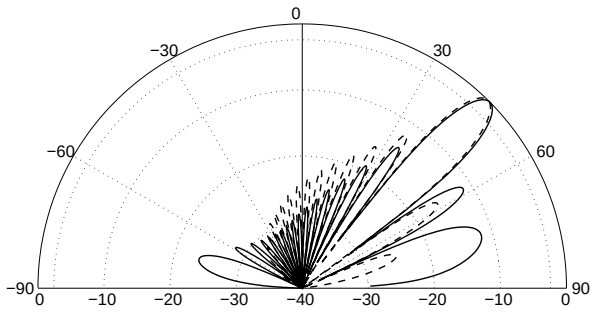

(b) Radiation pattern in $\phi = 0$ plane. E_ϕ component of the radiated field. Simulation (solid line) and traveling wave (dashed).

Figure 4.13: $\theta_\mathrm{i} = 45°$.

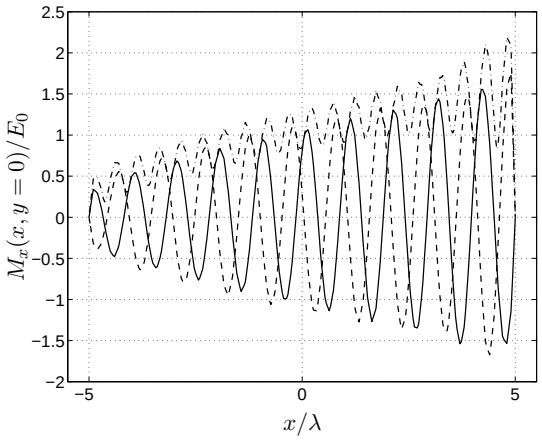

(a) The x-component of magnetic current along x-axis. Solid line: real part, dashed line: imaginary part, dash-dotted line: magnitude.

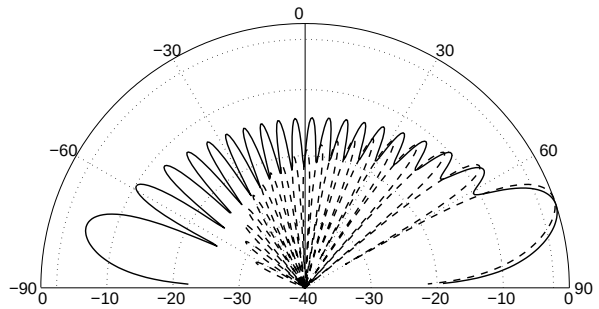

(b) Radiation pattern in $\phi = 0$ plane. E_ϕ component of the radiated field. Simulation (solid line) and traveling wave (dashed).

Figure 4.14: $\theta_\mathrm{i} = 75^\circ$.

4.3 Thick Slot Integral Equations

The procedure leading to the coupled integral equations which solve the problem of a thick slot is well known [19, 21, 22, 30]. We will briefly recall it here for the sake of completeness and for introducing the notation used throughout this chapter. Consider the generic problem of Fig. 4.15(a), in which two arbitrary inhomogeneous regions ① and ② are originally separated by a thick conducting wall. The region ① also includes a set of impressed currents $\mathbf{J}^{\mathrm{i}}$, $\mathbf{M}^{\mathrm{i}}$ (sources). A portion of the screen is suppressed, leaving a 3D-hole, which defines a new region Ⓒ, connecting ① and ② [Fig. 4.15(a)]. As stated in the introduction, in most problems of practical interest the conducting screen is limited by two parallel surfaces and is locally flat. Also, the region Ⓒ is usually a cylindrical volume with arbitrary but constant cross-section in the xy-plane and with its axis parallel to the screen's normal coordinate z. Nevertheless, the theory which follows is also formally valid for the more general geometry of Fig. 4.1.

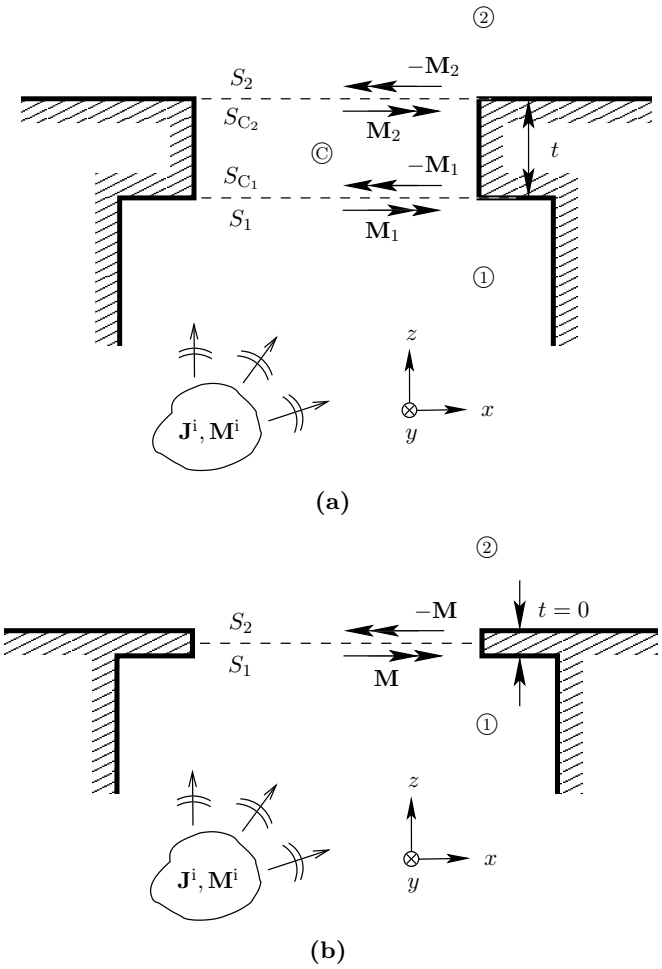

Figure 4.15: Two arbitrary regions connected through a slot on a conducting screen of finite (a) and zero (b) thickness.

Following the standard procedure, we replace the two openings of the thick aperture by zero-thickness conducting surfaces. The two sides of the surface separating regions ① and Ⓒ will be denoted S_1 and S_{C_1}, while the two sides of the surface separating regions Ⓒ and ② will be denoted S_{C_2} and S_2. Now, according to the equivalence theorem, we define unknown equivalent magnetic surface currents in the following way [Fig. 4.15(a)]

$$\mathbf{M}_1 \text{ on } S_1;\ -\mathbf{M}_1 \text{ on } S_{C_1};\ \mathbf{M}_2 \text{ on } S_{C_2};\ -\mathbf{M}_2 \text{ on } S_2. \tag{4.41}$$

Since surface magnetic currents are cross products of unit normal vectors and electric fields, the continuity of the tangential electric field is automatically fulfilled in the interfaces between our three regions. The introduction of the conducting surfaces allows the consideration of three formally independent problems, one for each region, that are indirectly coupled through the equivalent magnetic currents. In particular the region Ⓒ becomes a cavity fully bounded by conducting walls. We use now the well known concept of "short-circuited excitation fields" $\mathbf{E}^{\text{exc}}$, $\mathbf{H}^{\text{exc}}$ [9], defined as the fields created by the impressed sources in the region where they exist (here ①) but *with the aperture opening covered by the conducting surface*. With the introduction of the scattered fields $\mathbf{H}_1$, $\mathbf{H}_2$, $\mathbf{H}_C$ existing in each region, the boundary conditions imposing the continuity of the tangential components of the total magnetic field across the two interfaces are written as

$$\begin{aligned} \mathbf{H}^{\text{exc}} + \mathbf{H}_1|_{\text{on } S_1} &= \mathbf{H}_C|_{\text{on } S_{C_1}} \\ \mathbf{H}_2|_{\text{on } S_2} &= \mathbf{H}_C|_{\text{on } S_{C_2}} \end{aligned} \tag{4.42}$$

where, to keep the notation simple, we have avoided to show the cross product with the normal unit vector $\hat{z}$, but it is understood from now on that we only consider the tangential x, y components of the fields.

The transposition of these boundary conditions into integral equations should be straightforward. Invoking linearity and superposition, we can write the scattered fields due to any induced or equivalent source as a convolution of the source with the pertinent dyadic Green's functions over the source's domain of existence S. For instance, the magnetic field of a magnetic current is

$$\mathbf{H}^{\text{s}}(\mathbf{r}) = \int_S \overleftrightarrow{\mathbf{G}}_{\text{HM}}(\mathbf{r}|\mathbf{r}') \cdot \mathbf{M}(\mathbf{r}')\, \mathrm{d}S' = \overleftrightarrow{\mathbf{G}}_{\text{HM}} \otimes \mathbf{M}, \tag{4.43}$$

where as before $\otimes$ represents the convolution integral. To develop the first boundary condition in (4.42), we remark that the scattered magnetic field in the region ① is that created by $\mathbf{M}_1$ on S_1, while in region Ⓒ the fields are due to $-\mathbf{M}_1$ on S_{C_1} and to $\mathbf{M}_2$ on S_{C_2}. When we consider the fields at the interface, the three above mentioned currents act through convolution with, respectively, the three Green's functions

$$\overleftrightarrow{\mathbf{G}}^{1}_{\text{HM}}(S_1|S_1),\ \overleftrightarrow{\mathbf{G}}^{\text{C}}_{\text{HM}}(S_{C_1}|S_{C_1}) \text{ and } \overleftrightarrow{\mathbf{G}}^{\text{C}}_{\text{HM}}(S_{C_1}|S_{C_2})$$

that we abridge as, respectively, $\overleftrightarrow{\mathbf{G}}_{11}$, $\overleftrightarrow{\mathbf{G}}_{C_1C_1}$ and $\overleftrightarrow{\mathbf{G}}_{C_1C_2}$. These Green's functions are also "short-circuited", i.e. they are the Green's functions associated to the respective regions when they are isolated (decoupled) from each other by conducting zero thickness walls placed in

the thick aperture surfaces.

Applying an identical reasoning to the second boundary condition, we can now translate directly the set (4.42) into the following system of two coupled integral equations

$$\begin{aligned} \mathbf{H}^{\text{exc}} + \overleftrightarrow{\mathbf{G}}_{11} \otimes \mathbf{M}_1 &= \overleftrightarrow{\mathbf{G}}_{\text{C}_1\text{C}_1} \otimes (-\mathbf{M}_1) + \overleftrightarrow{\mathbf{G}}_{\text{C}_1\text{C}_2} \otimes \mathbf{M}_2, \\ \overleftrightarrow{\mathbf{G}}_{22} \otimes (-\mathbf{M}_2) &= \overleftrightarrow{\mathbf{G}}_{\text{C}_2\text{C}_1} \otimes (-\mathbf{M}_1) + \overleftrightarrow{\mathbf{G}}_{\text{C}_2\text{C}_2} \otimes \mathbf{M}_2. \end{aligned} \tag{4.44}$$

The system of equations (4.44) for the unknowns $\mathbf{M}_1$ and $\mathbf{M}_2$ fully defines the thick slot problem. Although in theory they can be used for the general problem of Fig. 4.1, the calculation of Green's functions would be too much involved. Hence, we will restrict from now on our analysis to the simpler geometries of the kind illustrated in Fig. 4.15(a), leaving the general problem to numerically intensive techniques like finite elements or finite differences.

4.4 Cavity Green's Functions and the Zero Thickness Slot

If we start from the very beginning considering a zero thickness slot, the cavity region Ⓒ shrinks to a null volume and we only need to consider two regions ① and ② separated by an interface in whose sides S_1 and S_2 we define equivalent surface magnetic currents $\mathbf{M}$ and $-\mathbf{M}$ [Fig. 4.15(b)]. The single integral equation is now [see the equation (4.21) on page 84]

$$\mathbf{H}^{\text{exc}} + \overleftrightarrow{\mathbf{G}}_{11} \otimes \mathbf{M} = \overleftrightarrow{\mathbf{G}}_{22} \otimes (-\mathbf{M}). \tag{4.45}$$

Therefore if we solve the system of equations (4.44) associated to the thick slot problem in the limiting case of a vanishing slot thickness $t \to 0$, we should end up with the result $\mathbf{M}_1 = \mathbf{M}_2 = \mathbf{M}$, which is the solution of the integral equation (4.45). Unfortunately, this is not the case in practice, as the cavity Green's functions show a divergent behavior when the cavity thickness vanishes. This fact deserves further consideration and will be investigated now.

The four cavity Green's functions $G_{\text{C}_i\text{C}_j}$ correspond to the four interactions shown in Fig. 4.16(a). Electromagnetic reciprocity ensures that we must have

$$\overleftrightarrow{\mathbf{G}}_{\text{C}_1\text{C}_2} = \overleftrightarrow{\mathbf{G}}_{\text{C}_2\text{C}_1} = \overleftrightarrow{\mathbf{G}}_{\text{m}}, \tag{4.46}$$

where the subscript "m" reminds us that this Green's functions correspond to a "mutual" interaction between the two parallel surfaces bounding the slot and hence the cavity. With this simplified notation, the set of coupled integral equations (4.44) can be cast into a convenient matricial form

$$\begin{bmatrix} \overleftrightarrow{\mathbf{G}}_{11} + \overleftrightarrow{\mathbf{G}}_{\text{C}_1\text{C}_1} & -\overleftrightarrow{\mathbf{G}}_{\text{m}} \\ -\overleftrightarrow{\mathbf{G}}_{\text{m}} & \overleftrightarrow{\mathbf{G}}_{22} + \overleftrightarrow{\mathbf{G}}_{\text{C}_2\text{C}_2} \end{bmatrix} \otimes \begin{bmatrix} \mathbf{M}_1 \\ \mathbf{M}_2 \end{bmatrix} = \begin{bmatrix} -\mathbf{H}^{\text{exc}} \\ 0 \end{bmatrix}, \tag{4.47}$$

where electromagnetic reciprocity ensures the symmetry of the Green's functions matrix. A further simplification can be used if the interior of the cavity is homogeneous or it is

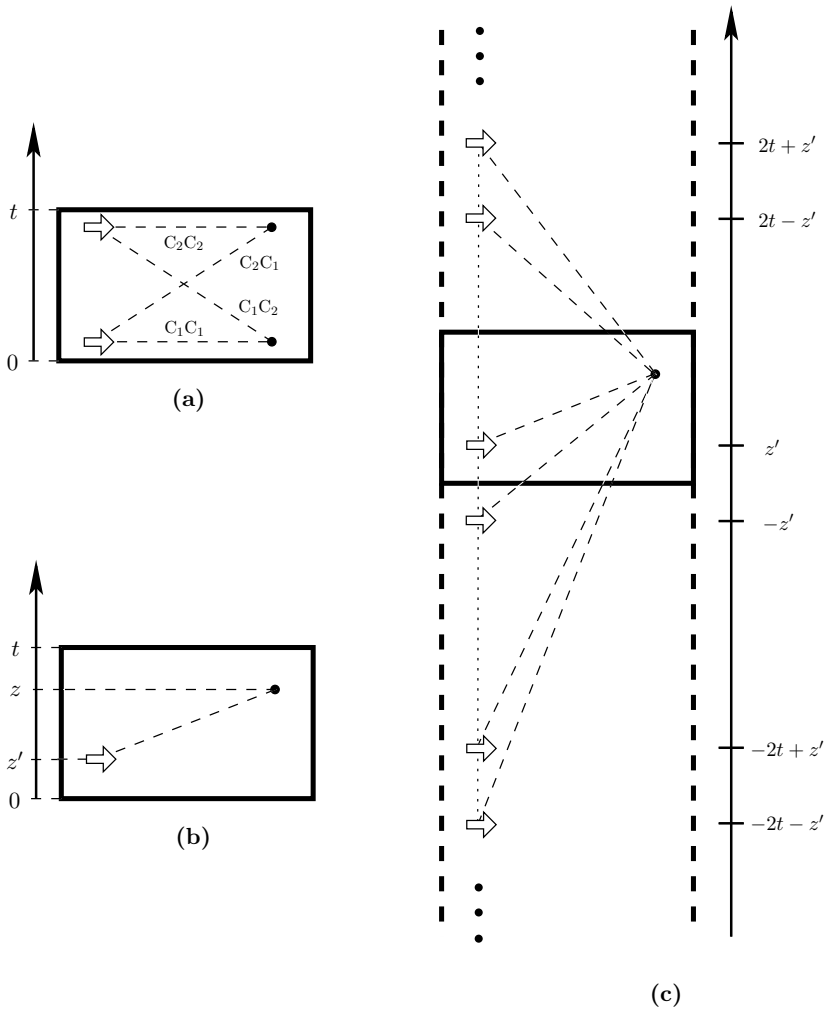

Figure 4.16: (a) The four cavity Green's functions, (b) a generic situation, (c) its solution by images.

symmetrically filled with dielectric media, because then we would have by symmetry

$$\overleftrightarrow{\mathbf{G}}_{\mathrm{C_1C_1}} = \overleftrightarrow{\mathbf{G}}_{\mathrm{C_2C_2}} = \overleftrightarrow{\mathbf{G}}_{\mathrm{s}}, \tag{4.48}$$

where the subscript "s" reminds us that this Green's functions correspond to a "self" interaction of one of the surfaces bounding the slot and hence the cavity with itself.

In all cases, the four cavity Green's functions $G_{\mathrm{C}_i\mathrm{C}_j}$ correspond all to particular cases of the situation depicted in Fig. 4.16(b). Formally, we can solve this problem by transforming the cavity into an infinite waveguide. This is achieved by taking images of the source with respect to both the lower and upper cavity walls as in Fig. 4.16(c). But in this situation, it is well known that all the images will keep the sign of the original magnetic source. Therefore, all the $G_{\mathrm{C}_i\mathrm{C}_j}$ Green's functions (which are of the HM-type) will diverge in the limiting case,

as all the images coalesce into a single source of infinite intensity.

This heuristic conclusion will be confirmed later on by a rigorous analytic development in a more specific geometry. At this time, let us simply point out the evident consequence: in its current formulation (4.47), the thick aperture problem cannot be solved numerically in the limiting case of a zero thickness slot, since all the elements in the Green's function matrix would diverge. Indeed, numerical difficulties should be expected when trying to solve (4.47) for small values of the thickness t, and alternate forms must be investigated to provide a smooth transition to the zero-thickness case.

4.5 An Algebraic Interlude

To throw some extra light on the problems revealed in the previous section, let us consider the algebraic counterpart of the integral equation system (4.47), namely the linear system

$$\begin{bmatrix} g_1 + c_{11} & -c_{12} \\ -c_{21} & g_2 + c_{22} \end{bmatrix} \begin{bmatrix} x_1 \\ x_2 \end{bmatrix} = \begin{bmatrix} h \\ 0 \end{bmatrix}, \tag{4.49}$$

where the coefficients c_{ij} play the role of the potentially diverging cavity Green's functions and $c_{12} = c_{21}$. The formal solution of this system is

$$\begin{aligned} x_2 &= \frac{c_{21}}{(c_{11}c_{22} - c_{12}c_{21}) + c_{22}g_1 + c_{11}g_2 + g_1g_2} h, \\ x_1 &= \frac{g_2 + c_{22}}{c_{21}} x_2. \end{aligned} \tag{4.50}$$

Now, we can easily see that if under a certain condition ($t \to 0$) all the c_{ij} coefficients diverge but in such a way that the following conditions are satisfied

$$\lim_{t\to 0}(c_{11}c_{22} - c_{12}c_{21}) = 0; \quad \lim_{t\to 0} \frac{c_{21}}{c_{11}} = \lim_{t\to 0} \frac{c_{21}}{c_{22}} = 1, \tag{4.51}$$

then we obtain the limit solution

$$x_2 = x_1 = \frac{1}{g_1 + g_2} h, \tag{4.52}$$

which is indeed the solution of the algebraic equation equivalent to the zero-thickness slot integral equation (4.45). The conclusion is that the thick slot equations (4.47) contains as a particular case the zero-thickness slot solution, if the cavity Green's functions fulfill conditions equivalent to (4.51). These conditions will be checked in a coming section. But even with these conditions satisfied, the presence of the convolution operator prevents the use of the equation (4.47) in situations approaching the zero thickness case and an improved formulation of the thick slot problem must be sought after. To get some hints about what must be done, let us progress a further step in the simplification of our problem and move from algebra to

arithmetic by introducing a set of numerical values for the coefficients, namely

$$\begin{aligned} c_{11} = c_{22} = 1000, \quad c_{12} = c_{21} = 998, \\ g_1 = 2, \quad g_2 = 4, \quad h = 10, \end{aligned} \tag{4.53}$$

which reproduce quite faithfully the numerical conditions arising in a typical thin-slot situation. The corresponding linear system is

$$\begin{aligned} 1002x_1 - 998x_2 = 10, \\ -998x_1 + 1004x_2 = 0. \end{aligned} \tag{4.54}$$

A close look to this system with engineer eyes reveals two very similar equations (the information about the field values in both sides of the slot). Therefore, the logical thought is to replace the original equations by their sum and difference

$$\begin{aligned} 4x_1 + 6x_2 = 10, \\ 2000x_1 - 2002x_2 = 10. \end{aligned} \tag{4.55}$$

We also have two close unknowns (the values of the magnetic currents in both sides of the slot). So, the meaningful quantities are their average and their deviation from average. Therefore, we replace also the unknowns by their half-sum and half-difference

$$x_1 = x_\Sigma + x_\Delta, \quad x_2 = x_\Sigma - x_\Delta, \tag{4.56}$$

with the result

$$\begin{aligned} 10x_\Sigma - 2x_\Delta = 10, \\ -2x_\Sigma + 4002x_\Delta = 10. \end{aligned} \tag{4.57}$$

We have here finally uncovered the clue for a successful attack to problem. The combination $-2x_\Delta$ in the first equation of (4.57) includes both a small coefficient and a small unknown and hence can be safely neglected. Therefore by starting with $x_\Delta = 0$, the first equation provides directly the initial guess for the average value $x_\Sigma = 1$. This is already an excellent estimation of the true solutions of the original system (4.54), namely $x_1 = 1.0036$, $x_2 = 0.9976$. If we need a better estimation providing different values for the unknowns, we just replace $x_\Sigma = 1$ in the second equation and obtain directly $x_\Delta = 0.0030$, and therefore $x_1 = 1.0030$ and $x_2 = 0.9970$. If still better accuracy is needed, the cyclic iteration can be pursued indefinitely. Now, coming back to formal algebra, let us symbolize our linear system (4.54) by the matrix equation

$$\mathbf{Ax} = \mathbf{b}. \tag{4.58}$$

It is easy to show that replacing the original individual equations by their sum and difference, is equivalent to pre-multiplication by a matrix $\mathbf{R}$ and the linear system (4.55) corresponds to the matrix equation

$$\mathbf{RAx} = \mathbf{Rb} \text{ with } \mathbf{R} = \begin{bmatrix} 1 & 1 \\ 1 & -1 \end{bmatrix}. \tag{4.59}$$

By the same token, replacing the original unknowns by their half-sum and half-difference can be also related to this $\mathbf{R}$ matrix since

$$\mathbf{x} = \begin{bmatrix} x_1 \\ x_2 \end{bmatrix} = \begin{bmatrix} 1 & 1 \\ 1 & -1 \end{bmatrix} \begin{bmatrix} x_\Sigma \\ x_\Delta \end{bmatrix} = \mathbf{R}\mathbf{x}^* \tag{4.60}$$

and therefore the final transformed problem (4.57), easily amenable to an iterative solution, is formally given by

$$\mathbf{R}\mathbf{A}\mathbf{R}\mathbf{x}^* = \mathbf{R}\mathbf{b}. \tag{4.61}$$

But $\mathbf{R}$ is just a scaled version of the unitary 45 degrees rotation matrix

$$\mathbf{R} = \sqrt{2} \begin{bmatrix} \cos(\pi/4) & \sin(\pi/4) \\ \sin(\pi/4) & -\cos(\pi/4) \end{bmatrix}. \tag{4.62}$$

Hence, we conclude that the potentially useful transformation of our linear system is just achieved by pre- and post-multiplying by a 45° rotation matrix.

4.6 Thick Slot Integral Equations and Rotation Matrices

Let's apply to our thick slot matrix integral equation (4.47) the pre- and post-multiplications by the rotation matrix $\mathbf{R}$ as indicated in (4.61). The final result is given in (4.63)

$$\begin{bmatrix} -\mathbf{H}^{\text{exc}} \\ -\mathbf{H}^{\text{exc}} \end{bmatrix} = \begin{bmatrix} \vec{\mathbf{G}}_{11} + \vec{\mathbf{G}}_{22} + (\vec{\mathbf{G}}_{C_1C_1} + \vec{\mathbf{G}}_{C_2C_2} - 2\vec{\mathbf{G}}_{\text{m}}) & \vec{\mathbf{G}}_{11} - \vec{\mathbf{G}}_{22} \\ \vec{\mathbf{G}}_{11} - \vec{\mathbf{G}}_{22} + (\vec{\mathbf{G}}_{C_1C_1} - \vec{\mathbf{G}}_{C_2C_2}) & \vec{\mathbf{G}}_{11} + \vec{\mathbf{G}}_{22} + (\vec{\mathbf{G}}_{C_1C_1} + \vec{\mathbf{G}}_{C_2C_2} + 2\vec{\mathbf{G}}_{\text{m}}) \end{bmatrix} \otimes \begin{bmatrix} \mathbf{M}_\Sigma \\ \mathbf{M}_\Delta \end{bmatrix} \tag{4.63}$$

where we have introduced the "average" and "deviation" values of the magnetic currents in the slot

$$\mathbf{M}_\Sigma = \frac{\mathbf{M}_1 + \mathbf{M}_2}{2}, \quad \mathbf{M}_\Delta = \frac{\mathbf{M}_1 - \mathbf{M}_2}{2}. \tag{4.64}$$

The matrix equation (4.63) looks much more complicated than the original one (4.47) and it could be feared that we have worsened our chances. But, as in the numerical example of the previous section, the first line in the system (4.63) is the clue, since none of its elements will diverge when the slot thickness vanishes, if conditions (4.51) are fulfilled. We can therefore start with the assumption $\mathbf{M}_\Delta = 0$ and solve the first equation in the system (4.63) to obtain a first estimation of $\mathbf{M}_\Sigma$. It is remarkable indeed that if media ① and ② in both sides of the slot are identical (for instance, free space), then we have $\vec{\mathbf{G}}_{11} - \vec{\mathbf{G}}_{22} = 0$ and then the first equation in (4.63) becomes uncoupled, directly providing the *exact* value of $\mathbf{M}_\Sigma$.

To clarify these ideas, let's fully develop the proposed procedure in the case of a slot filled by an homogeneous or symmetrically disposed dielectric medium, and therefore satisfying the symmetry condition (4.48). In this case, the notation can be greatly simplified by introducing

the combinations

$$\overleftrightarrow{\mathbf{G}}_{\Sigma} = \overleftrightarrow{\mathbf{G}}_{\mathrm{s}} + \overleftrightarrow{\mathbf{G}}_{\mathrm{m}}, \quad \overleftrightarrow{\mathbf{G}}_{\Delta} = \overleftrightarrow{\mathbf{G}}_{\mathrm{s}} - \overleftrightarrow{\mathbf{G}}_{\mathrm{m}} \tag{4.65}$$

that we can call the "sigma" and "delta" cavity Green's functions (sigma = self + mutual and delta = self − mutual). For a vanishing thickness slot, the sigma Green's function will diverge but the delta one will vanish. With this notation, it is a straightforward matter to show that the matrix equation (4.63) is equivalent to

$$\begin{bmatrix} \overleftrightarrow{\mathbf{G}}_{11} + \overleftrightarrow{\mathbf{G}}_{22} + 2\overleftrightarrow{\mathbf{G}}_{\Delta} & \overleftrightarrow{\mathbf{G}}_{11} - \overleftrightarrow{\mathbf{G}}_{22} \\ \overleftrightarrow{\mathbf{G}}_{22} + \overleftrightarrow{\mathbf{G}}_{\Delta} & -\overleftrightarrow{\mathbf{G}}_{22} - \overleftrightarrow{\mathbf{G}}_{\Sigma} \end{bmatrix} \otimes \begin{bmatrix} \mathbf{M}_{\Sigma} \\ \mathbf{M}_{\Delta} \end{bmatrix} = \begin{bmatrix} -\mathbf{H}^{\mathrm{exc}} \\ 0 \end{bmatrix}. \tag{4.66}$$

This is a great improvement with respect to the original matrix equation (4.47)! When the slot thickness vanishes, the only divergent term is $\overleftrightarrow{\mathbf{G}}_{\Sigma}$. Therefore, the second line in (4.66) automatically gives the result $\mathbf{M}_{\Delta} = 0$, and the first line reduces to the zero-thickness slot equation.

Hence, we can set up the following procedure for thin slots:

(i) assume $\mathbf{M}_{\Delta} = 0$

(ii) solve a modified zero-thickness slot equation to obtain a first estimate of $\mathbf{M}_{\Sigma}$

$$(\overleftrightarrow{\mathbf{G}}_{11} + \overleftrightarrow{\mathbf{G}}_{22} + 2\overleftrightarrow{\mathbf{G}}_{\Delta}) \otimes \mathbf{M}_{\Sigma} = -\mathbf{H}^{\mathrm{exc}} \tag{4.67}$$

(iii) estimate $\mathbf{M}_{\Delta}$ by solving the equation

$$(\overleftrightarrow{\mathbf{G}}_{22} + \overleftrightarrow{\mathbf{G}}_{\Sigma}) \otimes \mathbf{M}_{\Delta} = (\overleftrightarrow{\mathbf{G}}_{22} + \overleftrightarrow{\mathbf{G}}_{\Delta}) \otimes \mathbf{M}_{\Sigma}$$

(iv) improve, if necessary, the estimation of $\mathbf{M}_{\Sigma}$ by solving

$$(\overleftrightarrow{\mathbf{G}}_{11} + \overleftrightarrow{\mathbf{G}}_{22} + 2\overleftrightarrow{\mathbf{G}}_{\Delta}) \otimes \mathbf{M}_{\Sigma} = -\mathbf{H}^{\mathrm{exc}} - (\overleftrightarrow{\mathbf{G}}_{11} - \overleftrightarrow{\mathbf{G}}_{22}) \otimes \mathbf{M}_{\Delta}$$

(v) go to step (iii)

It is worth mentioning that all the above steps are single uncoupled integral equations. In most cases, stopping after the step (ii) will be enough to predict the first order deviation from the zero-thickness case introduced by a reasonable slot thickness. In fact, step (ii) is identical to the zero-thickness slot integral equation (4.45), but with the Green's function kernel corrected by an additive term $2\overleftrightarrow{\mathbf{G}}_{\Delta}$. Therefore, if the "delta" cavity Green's functions could be approximated by an easily computable expression, the step (ii) would provide first corrections for thick slots with no increase in the computational complexity. The next section proposes some reasonable expressions for the "delta" Green's function.

4.7 Approximations for Delta and Sigma Green's Functions

First of all we move from fields to potentials and introduce the convenient formalism of the "Mixed Potential Integral Equation" [28, 31]. Till now, all the Green's functions referred in previous section are of the HM-type (magnetic field due to a magnetic current). Therefore any generic convolution in the previous sections can be expanded in terms of potentials

$$\mathbf{H} = \overleftrightarrow{\mathbf{G}} \otimes \mathbf{M} = -\mathrm{j}\omega\mathbf{F} - \boldsymbol{\nabla} W = -\mathrm{j}\omega\overleftrightarrow{\mathbf{G}}_F \otimes \mathbf{M} - \boldsymbol{\nabla}(G_W \otimes \rho_{\mathrm{m}}), \tag{4.68}$$

where $\mathbf{F}$ and W are the vector and scalar potentials associated with transverse magnetic currents $\mathbf{M}$ and ρ_{m} is the equivalent magnetic charge.

As it is well known, in free space we have for the mixed potential Green's functions the values

$$\overleftrightarrow{\mathbf{G}}_F = \frac{\varepsilon_0}{4\pi}\overleftrightarrow{\mathbf{I}}\Psi, \quad G_W = \frac{1}{4\pi\mu_0}\Psi, \tag{4.69}$$

with the free space scalar Green's function Ψ given by

$$\Psi = \Psi_0 = \frac{\mathrm{e}^{-\mathrm{j}k_0|\mathbf{r}-\mathbf{r}'|}}{|\mathbf{r}-\mathbf{r}'|}. \tag{4.70}$$

The question is how to compute these quantities in the cavity geometry. The problem is not trivial and will depend obviously on the cavity's shape and on the medium filling it. In general, for arbitrary shaped slots, the answer can be obtained only by intensive numerical procedures. But we may try to introduce a powerful approximation, which should lead to reasonable results if the slot's transverse dimensions are not smaller than the slot thickness: we just neglect the lateral conducting walls of the cavity. Although the validity of this assumption can only be judged a posteriori, its appeal is enormous. First, the cavity delta and sigma Green's functions will have "universal" expressions independent of the slot/cavity shape. And secondly, these expressions will be reasonably simple.

Fig. 4.17 shows the parallel plate waveguide configuration which remains when we neglect the lateral walls. In this case, relations (4.69) are still valid, but the scalar Green's function Ψ is no longer the free-space one (4.70). Its calculation is easily performed in the spectral domain [28]. For a source located on the lower wall ($z' = 0$) we get the result

$$\tilde{\Psi} = \frac{2}{u}\left[\mathrm{e}^{-uz} + \frac{\mathrm{e}^{-ut}\cosh(uz)}{\sinh(ut)}\right], \text{ where } u^2 = k_\rho^2 - k_0^2. \tag{4.71}$$

A partial check of the above result is provided by the fact that if we let t go to infinity (the parallel plate waveguide reduces to its lower plate), we obtain $\tilde{\Psi} = (2/u)\exp(-uz)$, which is the expected result, twice the free space value. Keeping now t finite and particularizing to the values $z = 0$ and $z = t$, we get the potential versions of our cavity "self" and "mutual" Green's functions (4.46), (4.48) and making sums and differences with them we get the potential

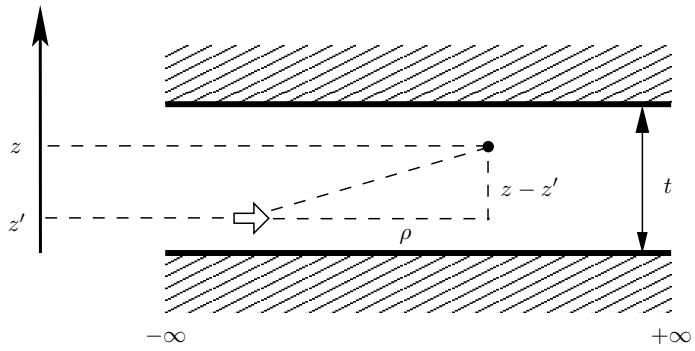

Figure 4.17: Approximating arbitrarily shaped cylindrical cavities by a parallel plate waveguide.

versions of our cavity "sigma" and "delta" Green's functions (4.65):

$$\tilde{\Psi}_\Sigma = \frac{2}{u\tanh(\frac{ut}{2})}, \quad \tilde{\Psi}_\Delta = \frac{2}{u}\tanh\left(\frac{ut}{2}\right). \tag{4.72}$$

We have here a clear confirmation of our theoretical predictions. While the "self", "mutual" and "sigma" cavity Green's functions diverge for a vanishing slot thickness $t \to 0$, the "delta" function goes to zero. Moreover, it is straightforward to show that these Green's functions fulfill the conditions equivalent to (4.51). Moving from the spectral domain to the space domain, we can write the "delta" potential Green's function as a Sommerfeld integral

$$\Psi_\Delta = \int_0^\infty J_0(k_\rho\rho)\frac{2}{u}\tanh\left(\frac{ut}{2}\right)k_\rho\,\mathrm{d}k_\rho, \tag{4.73}$$

where ρ is the radial source-observer distance. A series expansion of the hyperbolic tangent in the above equation will result in a series expression for the delta Green's function. The amazing result is that the delta Green's function can be expressed as an alternating-sign infinite series identical to the scalar potential of an electric point charge when both source and observer are in the mid-plane of the parallel plate waveguide. To obtain specific information about the near field (quasistatic) behavior, we look at the asymptotical spectral behavior for $k_\rho \to \infty$. Since in this case the hyperbolic tangent becomes unity, the delta Green's function corresponds in the near field to twice the free space Green's function Ψ_0. This behavior is confirmed by the numerical evaluation of the Sommerfeld integral (4.73) using well tested algorithms [32, 33].

Fig. 4.18 shows the normalized potential delta Green's function $\Psi_\Delta/(2k_0)$ for three slot thicknesses of 0.001, 0.01 and 0.1 free space wavelengths. It is evident at a glance how in the near field Ψ_Δ behaves as $2\Psi_\Delta$, since the diagonal line in Fig. 4.18 is $\Psi_0/k_0 = 1/(k_0\rho)$. As a rule of thumb, we could infer from Fig. 4.18 that the delta Green's functions remain close to twice the free space Green's function while the radial distance is smaller than the slot thickness (say $\rho < t/(2\pi)$). But for greater radial distances, the values of the delta Green's

function decay very fast and it should be possible to neglect it.

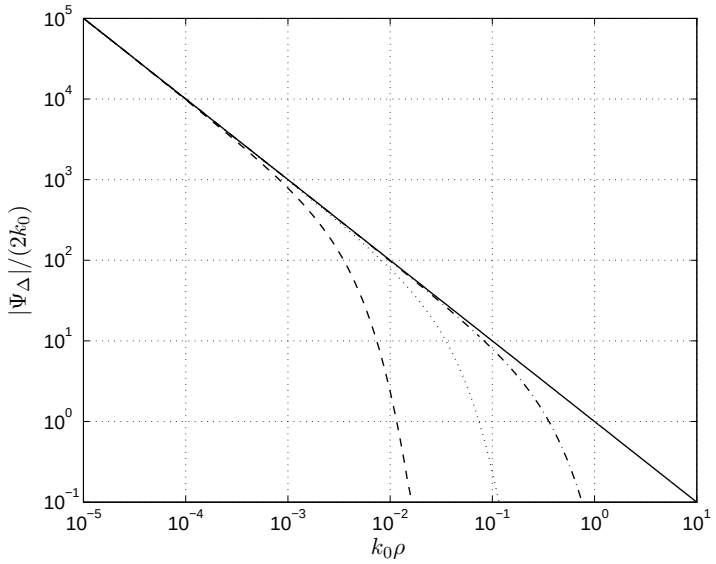

Figure 4.18: Modulus of the normalized delta Green's function for several slot thicknesses: $t = \lambda/1000$ (dashed line), $t = \lambda/100$ (dotted line) and $t = \lambda/10$ (dash-dotted line). The straight solid line is the free space Green's function.

To put these results in perspective, let's consider a slot in a thick conducting screen separating two semi-infinite free spaces. The equation to be solved is (4.67) or rather its mixed potential MPIE form. Hence, applying (4.68) to (4.67) we will get for instance a combination $G_{W_{11}} + G_{W_{22}} + 2G_{W_\Delta}$ for the scalar potential. We can easily demonstrate using image theory that the potential Green's functions $G_{W_{11}}$ and $G_{W_{22}}$, associated with the seminfinite media, are both given by twice the free space Green's function Ψ_0. Therefore, $G_{W_{11}} + G_{W_{22}}$ is just $4\Psi_0$. But the correction term $2G_{W_\Delta}$ also behaves in the near field as $4\Psi_0$ and therefore the total kernel is expected to have a quasistatic behavior of type $8\Psi_0$. It could be objected that an additive "correction" identical to the corrected term shouldn't be called a correction, being much more than this. But this is only the limiting near-field situation, when the source-observer distance is smaller than the slot thickness. For larger radial distances, the delta Green's function decays very fast (Fig. 4.18) and so does its "correcting" effect.

4.8 Preliminary Results

4.8.1 Scattering from a Square Slot

To check the validity of our assumptions and of our proposed equations, a very simple numerical experiment has been performed on a rather thick square slot (transverse dimensions $\lambda_0 \times \lambda_0$ and thickness $0.1\lambda_0$) (Fig. 4.19). The slot has been made in a screen separating two semiinfinite free space regions and it is excited with a normally incident plane wave having its electric field along the y–coordinate. The main and more interesting component of the

magnetic current is then along x. We have considered this component along the two medians of the square slot, a "longitudinal" one $x = \lambda_0/2$ and the transverse one $y = \lambda_0/2$ (Fig. 4.19). The problem has been first solved with a rigorous treatment, where the set of equations (4.44) is used, together with exact expressions for the Green's functions in the cavity. This "full wave cavity" model gives then the most accurate expressions for the currents $\mathbf{M}_1$ and $\mathbf{M}_2$ in both sides of the slot, represented by circles and squares in Figs. 4.20–4.21. They show the expected behavior from a $\lambda_0 \times \lambda_0$ slot. But it must be pointed out that the full wave cavity approach is a time consuming method, mainly due to the bad convergence of cavity Green's functions and their lack of translational symmetry. And the situation will be much worse, not to say untractable, for an arbitrarily shaped slot. Even disregarding the cavity problem, we should expect an important slowdown with respect to the zero thickness case, since we have twice more unknowns.

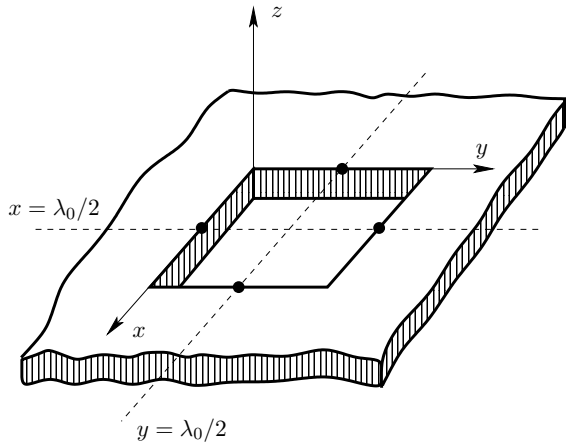

Figure 4.19: Thick $\lambda_0 \times \lambda_0$ slot of thickness $\lambda_0/10$ illuminated by normally incident plane wave having its electric field along the y–coordinate.

The snag with the zero-thickness formulation (4.45) is that it gives unsatisfactory results, since we get a unique current $\mathbf{M}$ (stars in Figs. 4.20–4.21) that only matches the true values on one side of the aperture (in this case, the excitation side). Using our corrected equation (4.67), we obtain a first estimation for $\mathbf{M}_\Sigma$, which happens to be an almost perfect average value (diamonds in Figs. 4.20 and 4.21).

4.8.2 Scattering from a Rectangular Slit

In order to see the influence on the radiation pattern, the scattering from a rectangular slit of length $10\lambda_0$ and width $\lambda_0/10$, oriented with its longer side in the x-direction, has been simulated. Radiation patterns in the E-plane ($\phi = 0°$) obtained using the presented and the full-wave cavity approaches are shown in Fig. 4.22. Two different incidence angles $\theta_i = 15°$ and $\theta_i = 45°$ of a plane wave with magnetic field polarized in the x-direction impinging from below were simulated. As expected, the difference between the two approaches in case of $\lambda_0/100$ thickness can hardly be seen. In the case of $\lambda_0/10$ thickness, the difference, although

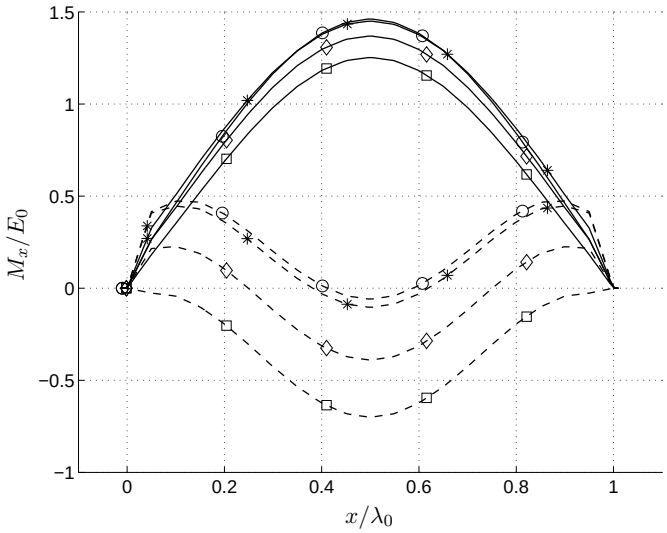

Figure 4.20: Normalized x–component of magnetic current along the line $y = \lambda_0/2$ over a square $\lambda_0 \times \lambda_0$ aperture of thickness $\lambda_0/10$. Normal incidence plane wave illumination. $\circ$ – M_1, $\square$ – M_2, $\diamond$ – M_Σ, $*$ – zero-thickness slot. Solid line – real part, dashed line – imaginary part.

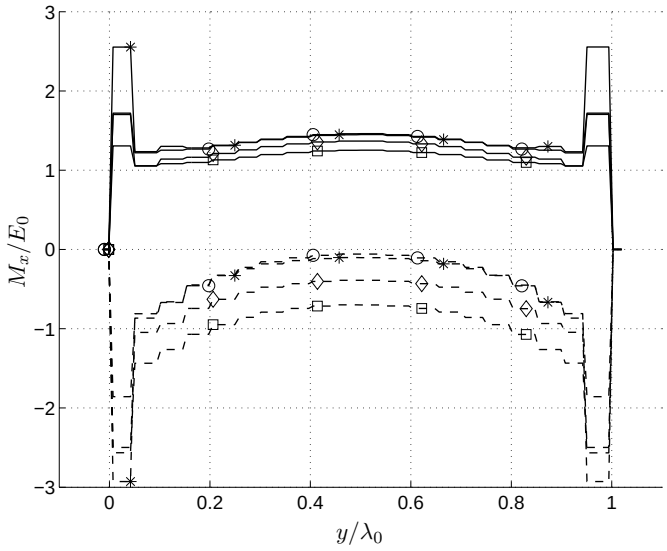

Figure 4.21: Normalized x–component of magnetic current along the line $x = \lambda_0/2$ over a square $\lambda_0 \times \lambda_0$ aperture of thickness $\lambda_0/10$. Normal incidence plane wave illumination. $\circ$ – M_1, $\square$ – M_2, $\diamond$ – M_Σ, $*$ – zero-thickness slot. Solid line – real part, dashed line – imaginary part.

not excessive, is noticeable in the side-lobe levels. The approximate approach already provides a much better result than the zero-thickness approach (dash-dotted lines) and with no increase in computational complexity.

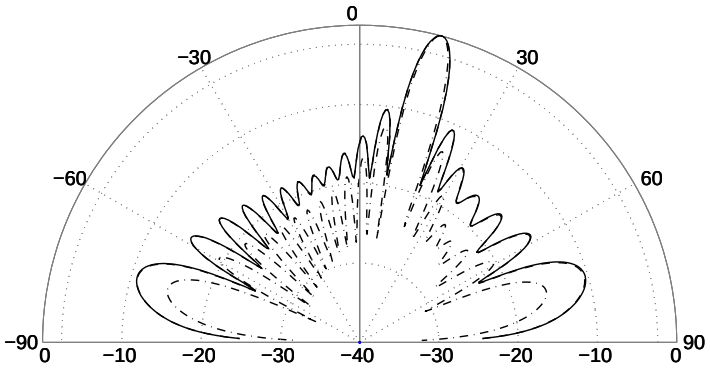

(a)

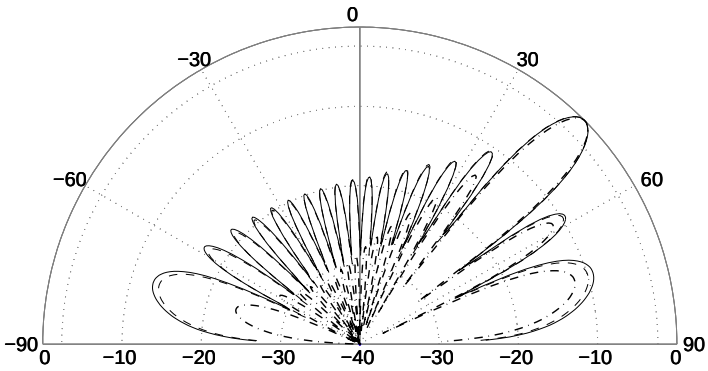

(b)

Figure 4.22: Radiation patterns produced by currents induced by a plane wave impinging on the aperture from below for different thicknesses, computed using presented approach (solid lines) and full-wave cavity approach (dashed lines) and for the case of the zero-thickness (dash-dotted lines). (a) $t = \lambda_0/100$ and incidence angle $\theta_\mathrm{i} = 15°$. (b) $t = \lambda_0/10$ and incidence angle $\theta_\mathrm{i} = 45°$.

4.9 Conclusion

In this chapter, we have presented a rigorous integral equation formulation of the thick aperture problem providing a smooth transition to the zero-thickness case, inspired by an analogy with an algebraic problem. The full usefulness of the new formulation is only evident if the cavity Green's functions can be easily calculated or at least efficiently approximated. In this chapter, we proposed to use as a starting point the zero-thickness case. Consequently, a logical approximation is to neglect the internal lateral walls of the slot and to assume that the equivalent cavity is a parallel plate waveguide. The final result is a new integral equation whose unknown is the average value of the magnetic currents in both sides of the thick slot. And this new equation has exactly the same degree of complexity as the zero thickness slot equation, since the only modification is the addition of a correcting "delta" term for the Green's functions, that can be analytically approximated and that disappears naturally in the zero-thickness limiting case.

The formulation presented is this chapter is very flexible and combines naturally well with the integral equation based models currently used for cavity backed antennas, thick irises in waveguide filters, slot-fed patches and thick coplanar lines. These configurations and many related ones are of paramount relevance in innovative and emerging applications, where conducting wall thickness cannot be any more neglected, because of the technology (self-supporting metallic plates rather than printed sheets), the frequency (mm- and sub mm-waves) or both. In the next chapter we will present an intensive numerical exploration of some of these geometries, including predictions of very sensitive near-field quantities like multiport scattering parameters, that provides a more detailed appraisal of the scope of this theory and of its accuracy.

References

[1] L. Martín-Moreno, F. J. García-Vidal, H. J. Lezec, K. M. Pellerin, T. Thio, J. B. Pendry, and T. W. Ebbesen, "Theory of extrodinary optical transmission through subwavelength hole arrays," *Phys. Rev. Lett.*, vol. 86, no. 6, pp. 1114–1117, Feb. 2001.

[2] G. P. Wang, Y. Yi, and B. Wang, "Evanescent coupling of transmitted light through an array of holes in a metallic film assisted by transverse surface current," *J. Phys.: Condens. Matter*, vol. 15, pp. 8147–8156, Nov. 2003.

[3] Lord Rayleigh, "On the incidence of aerial and electric waves upon small obstacles in the form of ellipsoids or elliptic cylinders, and on the passage of electric waves through a circular aperture in a conducting screen," *Phil. Mag.*, vol. 44, no. 5, pp. 28–52, July 1897.

[4] H. A. Bethe, "Theory of Diffraction by Small Holes," *Phys. Rev.*, vol. 66, no. 7 - 8, pp. 163–182, Oct. 1944.

[5] H. Levine and J. Schwinger, "On the theory of difraction by an aperture in an infinite plane screen I," *Phys. Rev.*, vol. 74, pp. 958–974, 1948.

[6] ——, "On the theory of difraction by an aperture in an infinite plane screen II," *Phys. Rev.*, vol. 75, pp. 1423–1432, 1949.

[7] R. E. Collin, *Field Theory of Guided Waves*. New York: McGraw-Hill, 1960.

[8] C. J. Bouwkamp, "Diffraction theory," *Rep. Prog. Phys.*, vol. 17, pp. 35–100, 1954.

[9] J. Van Bladel, *Electromagnetic Fields*. New York: McGraw-Hill, 1964.

[10] Y. Rahmat-Samii and R. Mittra, "Electromagnetic coupling through small apertures in a conducting screen," *IEEE Trans. Antennas Propagat.*, vol. AP-25, no. 2, pp. 180–187, Mar. 1977.

[11] S. B. Cohn, "The electric polarizability of apertures of arbitrary shape," *Proc. IRE*, vol. 40, pp. 1069–1071, Sept. 1952.

[12] J. B. Keller, "Geometrical theory of diffraction," *J. Appl. Phys.*, vol. 28, pp. 426–444, 1962.

[13] P. M. Morse and H. Feshbach, *Methods of Theoretical Physics*. New York: McGraw-Hill, 1953.

[14] R. F. Harrington, *Time-Harmonic Electromagnetic Fields*. New York: McGraw-Hill, 1961.

[15] C. A. Balanis, *Antenna Theory: Analysis and Design*, 2nd ed. New York: Wiley, 1997.

[16] C. M. Butler, Y. Rahmat-Samii, and R. Mittra, "Electromagnetic penetration through apertures in conducting surfaces," *IEEE Trans. Antennas Propagat.*, vol. AP-26, no. 1, pp. 82–93, Jan. 1978.

[17] R. Harrington and J. Mautz, "A generalized network formulation for aperture problems," *IEEE Trans. Antennas Propagat.*, vol. 24, no. 6, pp. 870–873, Nov. 1976.

[18] S. C. Kashyap and M. A. K. Hamid, "Diffraction characteristics of a slit in a thick conducting screen," *IEEE Trans. Antennas Propagat.*, vol. AP-19, no. 4, pp. 499–507, July 1971.

[19] F. L. Neerhoff and G. Mur, "Diffraction of a plane electromagnetic wave by a slit in a thick screen placed between two different media," *Appl. Sci. Res.*, vol. 28, pp. 73–88, July 1973.

[20] D. T. Auckland and R. F. Harrington, "A nonmodal formulation for electromagnetic transmission through a filled slot of arbitrary cross-section in a thick conducting screen," *IEEE Trans. Microwave Theory Tech.*, vol. MTT-28, no. 6, pp. 548–555, June 1980.

[21] J. Jin and J. Volakis, "TM scattering by an inhomogeneously filled aperture in a thick conducting plane," *IEE Proc-H*, vol. 137, no. 3, pp. 153–159, June 1990.

[22] S. Gedney and R. Mittra, "Electromagnetic transmission through inhomogeneously filled slots in a thick conducting plane - arbitrary incidence," *IEEE Trans. Electromagn. Compat.*, vol. 34, no. 4, pp. 404–415, Nov. 1992.

[23] D. M. Pozar, "A microstrip antenna aperture coupled to a microstrip line," *Electron. Lett.*, vol. 21, pp. 49–50, 1985.

[24] P. Haddad and D. Pozar, "Characterisation of aperture coupled microstrip patch antenna with thick ground plane," *Electron. Lett.*, vol. 30, no. 14, pp. 1106–1107, July 1994.

[25] A. Roberts, "Electromagnetic theory of diffraction by a circular aperture in a thick, perfectly conducting screen," *J. Opt. Soc. Amer. A, Opt. Image Sci.*, vol. 4, no. 10, pp. 1970–1983, Oct. 1987.

[26] H. G. Booker, "Slot aerials and their relation to complementary wire aerials (Babinet's Principle)," *J. Inst. Elect. Eng.*, vol. III-A, pp. 620–627, May 1946.

[27] J. R. Mosig, "Scattering by arbitrarily-shaped slots in thick conducting screens: an approximate solution," *IEEE Trans. Antennas Propagat.*, vol. 52, no. 8, pp. 2109–2117, Aug. 2004.

[28] ——, "Integral-equation technique," in *Numerical Techniques for Microwave and Millimeter-Wave Passive Structures*, T. Itoh, Ed. New York: Wiley, 1989, ch. 3, pp. 133–213.

[29] B. M. Kolundžija, "Accurate solution of square scatterer as benchmark for validation of electromagnetic modeling of plate structures," *IEEE Trans. Antennas Propagat.*, vol. 46, no. 7, pp. 1009–1014, July 1998.

[30] C. A. Balanis, *Advanced Engineering Electromagnetics*. New York: Wiley, 1989.

[31] K. A. Michalski and J. R. Mosig, "Multilayered media Green's functions in integral equation formulations," *IEEE Trans. Antennas Propagat.*, vol. 45, no. 3, pp. 508–519, Mar. 1997.

[32] J. R. Mosig, R. C. Hall, and F. E. Gardiol, "Numerical analysis of microstrip patch antennas," in *Handbook of Microstrip Antennas*, J. R. Jones and R. C. Hall, Eds. London: Peter Peregrinus, 1989, ch. 8, pp. 393–452.

[33] K. A. Michalski, "Extrapolation methods for Sommerfeld integral tails," *IEEE Trans. Antennas Propagat.*, vol. 46, no. 10, pp. 1405–1418, Oct. 1998.

5 Line-Fed Aperture Antennas in Thick Conducting Screens[†]

5.1 Introduction

A number of radiating structures including apertures is traditionally analyzed considering the aperture in a zero-thickness screen. These structures include slot-fed patch antennas, cavity backed antennas with feeding irises, waveguide slot antennas and the simple slot antenna fed by a printed line. However, the use of new technologies (for instance, self-standing bulk ground planes instead of printed ones) and the drive for higher frequencies are calling for the inclusion of finite thickness effects in the currently existing models.

Harrington and Mautz [1] were the first to address this problem employing a transmission line model. Other researchers have recently followed this approach [2, 3] to compute aperture coupled microstrip antennas. A similar approach, based on reciprocity has been reported in [4]. Another way to tackle the problem is to treat the aperture volume as a cavity or a waveguide. In [5] and [6] the Integral Equation (IE) formulation is combined with the Finite Element Method (FEM) for the cavity. These methods are very versatile, and able to model arbitrary cross sections filled with inhomogeneous dielectrics. However, both require a separate FEM solution to be integrated into the IE framework. The MPIE formulation for the outer regions combined with an IE field formulation for the cavity (aperture; inner region), using a modal expansion of the Green's function, is outlined in [7]. This method has the advantage of a consistent IE approach, which produces well conditioned matrices and leads to highly accurate results. Also several layers of dielectrics, even with embedded metallizations can be treated within the apertures. A drawback of the method is the difficulty in computing the required modal functions, since computations in cross sections other than rectangular and circular ones becomes a difficult task. Moreover, for any aperture geometry, the summation of the modal series calls for specially tailored acceleration schemes [8, 9]. The line-fed thick aperture antennas have been one of the most important challenges for our Laboratory in the last years. Therefore, two complementary ways of attacking the problem were planned and successfully developed, each one leading to a Ph.D. thesis. In the approach developed by Llorens del Río [10, 11], the thick slot is modeled by a parallel plate waveguide with vertical electric currents added to account for the metallic walls. The method is capable of modeling apertures of arbitrary thicknesses and shapes filled with arbitrary number of dielectric layers. However, it introduces a very complex IE since boundary conditions for both the **E** and the **H** field must be enforced inside the slot and therefore all four dyadic Green's functions (EJ, EM, HJ, HM) must be used.

[†]I. Stevanović and J. R. Mosig (2004), *IEEE Trans. Antennas Propagat.*, Vol. 52(11):2896-2903.

The above mentioned methods can deal with very general aperture problems. But they lack the simplicity and internal coherence of the straightforward integral equation model that can be used in the case of zero-thickness apertures. In Chapter 4, a new approximate approach for slots on thick screens has been presented [12]. The slot thickness appears only as a modification in the Green's functions of the problem, but otherwise the slot is treated as a two-dimensional object.

In this chapter we fully develop this conjuncture and show that the aperture model can be, with minor modifications, fully incorporated into the traditional integral equations for slots and patch antennas embedded in stratified media. Indeed, this brings the study of slot thickness effects under the reach of traditional planar integral equation codes.

After introducing the new complete set of integral equations for a printed-line fed slot antenna, which involves both electric and magnetic currents, this chapter explores and unthreads some computational relevant aspects of the model presented in the previous chapter and provides further numerical verifications. Finally, the new complete integral equation model is validated by comparing its numerical predictions with measurements for a set of slot antennas with different shapes and thicknesses.

5.2 Formulation of Integral Equations

Consider a structure composed of a planar printed line or patch and an aperture of finite thickness $t = z_2 - z_1$ embedded into stratified dielectric layers as shown in Fig. 5.1. Using the equivalence principle, the interfaces of the aperture are short-circuited, i.e., continuous perfect electric screens are introduced at $z = z_1$ and $z = z_2$ and the continuity of the tangential components of the electric fields on aperture interfaces is ensured by introducing the equivalent surface magnetic currents $\mathbf{M}_{1,2}$ [13]. This way, the original problem can be decoupled into three equivalent ones: lower region ($z < z_1$), closed aperture or cavity region ($z_1 \leq z < z_2$), and upper region ($z \geq z_2$). Assuming an incident electromagnetic field ($\mathbf{E}^{\mathrm{i}}$, $\mathbf{H}^{\mathrm{i}}$) present in the lower region $z < z_1$, the boundary conditions at the patch and the lower and the upper interface of the aperture become

$$\hat{z} \times \mathbf{E}(\mathbf{r}_0) = -\hat{z} \times \mathbf{E}^{\mathrm{exc}}, \quad \mathbf{r}_0 \in S_0, \tag{5.1a}$$

$$\hat{z} \times [\mathbf{H}^{+}(\mathbf{r}_1) - \mathbf{H}^{-}(\mathbf{r}_1)] = \hat{z} \times \mathbf{H}^{\mathrm{exc}}, \quad \mathbf{r}_1 \in S_1, \tag{5.1b}$$

$$\hat{z} \times [\mathbf{H}^{+}(\mathbf{r}_2) - \mathbf{H}^{-}(\mathbf{r}_2)] = 0, \quad \mathbf{r}_2 \in S_2, \tag{5.1c}$$

where $\mathbf{r}_i$, $i = 0, 1, 2$ is the position vector with respect to the global coordinate system, $\mathbf{H}^{\pm}$ and $\mathbf{E}$ are the scattered fields produced by magnetic ($\mathbf{M}_{1,2}$) and electric ($\mathbf{J}$) currents, and the superscripts $(+)$ and $(-)$ refer to, respectively, the regions above and below the corresponding z coordinate. $\mathbf{H}^{\mathrm{exc}}$ is the sum of the incident magnetic field $\mathbf{H}^{\mathrm{i}}(\mathbf{r}_1)$ and its image (so called short-circuit magnetic field [14]), and $\mathbf{E}^{\mathrm{exc}} = \mathbf{E}^{\mathrm{i}}(\mathbf{r}_0)$.

Following the procedure outlined in Chapter 4, all the scattered fields are expressed as convolutions between the corresponding sources and the pertinent stratified media Green's

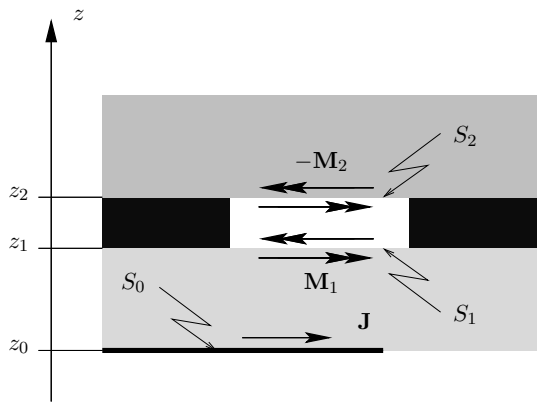

Figure 5.1: Aperture in a thick conducting shield embedded in a layered structure.

functions. Further, we introduce another couple of magnetic unknowns, the half-sum $\mathbf{M}_\Sigma = (\mathbf{M}_1 + \mathbf{M}_2)/2$ and the half-difference $\mathbf{M}_\Delta = (\mathbf{M}_1 - \mathbf{M}_2)/2$. Moreover, in the closed aperture region, taking into account the symmetry and reciprocity [15], we only need two different Green's functions of the magnetic-magnetic (HM) type, namely, $\overleftrightarrow{\mathbf{G}}_{\mathrm{HM}}^{(\mathrm{c})=}$ (the cavity Green's function with source and observer at the same horizontal interface) and $\overleftrightarrow{\mathbf{G}}_{\mathrm{HM}}^{(\mathrm{c})\times}$ (the cavity Green's function with source and observer at different horizontal interfaces). Then, according to [12], we define the sum and the difference cavity Green's functions as

$$\overleftrightarrow{\mathbf{G}}_{\mathrm{HM}}^{(\mathrm{c})\Sigma} = \overleftrightarrow{\mathbf{G}}_{\mathrm{HM}}^{(\mathrm{c})=} + \overleftrightarrow{\mathbf{G}}_{\mathrm{HM}}^{(\mathrm{c})\times}, \tag{5.2a}$$

$$\overleftrightarrow{\mathbf{G}}_{\mathrm{HM}}^{(\mathrm{c})\Delta} = \overleftrightarrow{\mathbf{G}}_{\mathrm{HM}}^{(\mathrm{c})=} - \overleftrightarrow{\mathbf{G}}_{\mathrm{HM}}^{(\mathrm{c})\times}. \tag{5.2b}$$

Introducing all these definitions in the boundary condition (5.1), we obtain, after some straightforward algebraic manipulations, the following set of coupled integral equations (Fig. 5.1)

$$\overleftrightarrow{\mathbf{G}}_{\mathrm{EJ}} \otimes \mathbf{J} + \overleftrightarrow{\mathbf{G}}_{\mathrm{EM}} \otimes \mathbf{M}_\Sigma + \overleftrightarrow{\mathbf{G}}_{\mathrm{EM}} \otimes \mathbf{M}_\Delta = -\mathbf{E}_{\mathrm{t}}^{\mathrm{exc}}, \tag{5.3a}$$

$$(\overleftrightarrow{\mathbf{G}}_{\mathrm{HM}}^{(1)} + \overleftrightarrow{\mathbf{G}}_{\mathrm{HM}}^{(\mathrm{c})\Delta}) \otimes \mathbf{M}_\Sigma - \overleftrightarrow{\mathbf{G}}_{\mathrm{HJ}} \otimes \mathbf{J} = (\overleftrightarrow{\mathbf{G}}_{\mathrm{HM}}^{(2)} + \overleftrightarrow{\mathbf{G}}_{\mathrm{HM}}^{(\mathrm{c})\Sigma}) \otimes \mathbf{M}_\Delta, \tag{5.3b}$$

$$(\overleftrightarrow{\mathbf{G}}_{\mathrm{HM}}^{(1)} + \overleftrightarrow{\mathbf{G}}_{\mathrm{HM}}^{(2)} + 2\overleftrightarrow{\mathbf{G}}_{\mathrm{HM}}^{(\mathrm{c})\Delta}) \otimes \mathbf{M}_\Sigma + (\overleftrightarrow{\mathbf{G}}_{\mathrm{HM}}^{(1)} - \overleftrightarrow{\mathbf{G}}_{\mathrm{HM}}^{(2)}) \otimes \mathbf{M}_\Delta - \overleftrightarrow{\mathbf{G}}_{\mathrm{HJ}} \otimes \mathbf{J} = -\mathbf{H}_{\mathrm{t}}^{\mathrm{exc}}, \tag{5.3c}$$

where $\otimes$ is, like before, a shorthand notation for the convolution integral, $\mathbf{E}_{\mathrm{t}}^{\mathrm{exc}} = \hat{z} \times \mathbf{E}^{\mathrm{exc}}$, and $\mathbf{H}_{\mathrm{t}}^{\mathrm{exc}} = \hat{z} \times \mathbf{H}^{\mathrm{exc}}$. $\overleftrightarrow{\mathbf{G}}_{\mathrm{EJ}}$ is the electric field Green's function with both observer and electric source situated at $z = z_0$, $\overleftrightarrow{\mathbf{G}}_{\mathrm{EM}}$ is the electric field Green's function with observer at $z = z_0$ and magnetic source at $z = z_1$, and $\overleftrightarrow{\mathbf{G}}_{\mathrm{HJ}}$ is the magnetic field Green's function with observer at $z = z_1$ and electric source situated at $z = z_0$. These three Green's functions should satisfy the boundary conditions for fields on the perfect electric screen situated in the plane $z = z_1$.

In addition to the cavity Green's function, two more Green's function of HM type are needed $\overleftrightarrow{\mathbf{G}}_{\mathrm{HM}}^{(1)}$ – Green's function of the stratified lower half-space with both source and observer at $z = z_1$ and the boundary conditions for magnetic field satisfied on the perfect electric screen at $z = z_1$, and $\overleftrightarrow{\mathbf{G}}_{\mathrm{HM}}^{(2)}$ – Green's function of the stratified upper half-space with both source and observer at $z = z_2$ and the boundary conditions for magnetic field satisfied on the perfect electric screen at $z = z_2$.

In apertures of practical thicknesses, there exists a rather strong correlation between $\mathbf{M}_1$ and $\mathbf{M}_2$ and therefore it is reasonable to assume that the difference of the two currents is zero $\mathbf{M}_\Delta \approx 0$. This approximation, which is exact in the limiting zero-thickness case, transforms the system (5.3) into

$$\overleftrightarrow{\mathbf{G}}_{\mathrm{EJ}} \otimes \mathbf{J} + \overleftrightarrow{\mathbf{G}}_{\mathrm{EM}} \otimes \mathbf{M}_\Sigma = -\mathbf{E}_{\mathrm{t}}^{\mathrm{exc}}, \tag{5.4a}$$

$$(\overleftrightarrow{\mathbf{G}}_{\mathrm{HM}}^{(1)} + \overleftrightarrow{\mathbf{G}}_{\mathrm{HM}}^{(2)} + 2\overleftrightarrow{\mathbf{G}}_{\mathrm{HM}}^{(\mathrm{c})\Delta}) \otimes \mathbf{M}_\Sigma - \overleftrightarrow{\mathbf{G}}_{\mathrm{HJ}} \otimes \mathbf{J} = -\mathbf{H}_{\mathrm{t}}^{\mathrm{exc}}. \tag{5.4b}$$

The set of equations (5.4) clearly shows that the strategy introduced in Chapter 4 can be generalized to more complex structures involving both, electric and magnetic currents. Indeed, equations (5.4) are identical to the zero-thickness case save for the use of $\mathbf{M}_\Sigma$ instead of a unique current $\mathbf{M}$ and the correcting term $2\overleftrightarrow{\mathbf{G}}_{\mathrm{HM}}^{(\mathrm{c})\Delta}$. In principle, the remaining equation (5.3b) could be used afterwards to find a non-zero estimation of $\mathbf{M}_\Delta$, and eventually start an iterative process.

5.3 Calculation of the Cavity Green's Functions

By introducing the electric and magnetic surface charge densities, $\rho_{\mathrm{e}} = -\frac{1}{\mathrm{j}\omega}\boldsymbol{\nabla} \cdot \mathbf{J}$ and $\rho_{\mathrm{m}} = -\frac{1}{\mathrm{j}\omega}\boldsymbol{\nabla} \cdot \mathbf{M}$, we can always set up the relation between the field and potential Green's functions [16]

$$\overleftrightarrow{\mathbf{G}}_{\mathrm{EJ}} \otimes \mathbf{J} = -\mathrm{j}\omega\overleftrightarrow{\mathbf{G}}_A \otimes \mathbf{J} - \boldsymbol{\nabla}(G_V \otimes \rho_{\mathrm{e}}), \tag{5.5a}$$

$$\overleftrightarrow{\mathbf{G}}_{\mathrm{HM}} \otimes \mathbf{M} = -\mathrm{j}\omega\overleftrightarrow{\mathbf{G}}_F \otimes \mathbf{M} - \boldsymbol{\nabla}(G_W \otimes \rho_{\mathrm{m}}), \tag{5.5b}$$

where $\overleftrightarrow{\mathbf{G}}_A$ and G_V, and $\overleftrightarrow{\mathbf{G}}_F$ and G_W are the dyadic and scalar potential Green's function for the electric and magnetic sources, respectively. With the MPIE formulation, the correction term will consist of the self and mutual interactions of the potential cavity Green's functions

$$\overleftrightarrow{\mathbf{G}}_F^{(\mathrm{c})\Delta} = \overleftrightarrow{\mathbf{G}}_F^{(\mathrm{c})=} - \overleftrightarrow{\mathbf{G}}_F^{(\mathrm{c})\times}, \tag{5.6a}$$

$$G_W^{(\mathrm{c})\Delta} = G_W^{(\mathrm{c})=} - G_W^{(\mathrm{c})\times}. \tag{5.6b}$$

The cavity Green's functions can be expanded in terms of the eigenfunctions that depend on the shape of the cavity cross-section. However, if the lateral dimensions of the cavity are big enough compared to its length (large aperture), the guiding properties of the corresponding shallow cavity will be weak. And with the problem discretized into a number of subsectional

basis functions, the appropriate currents in the center of the aperture will be only slightly affected by the cavity borders. Therefore, the problem can be treated as a parallel plate problem. The approximation will not be very accurate for the current coefficients belonging to the basis functions near the cavity borders. However, the form of the cavity is taken into account by the lateral distribution of the basis functions. Approximating the rigorous cavity formulation we avoid at the same time the summation of slowly convergent modal series [8, 9], and, maybe even more advantageous, the evaluation of the modal eigenfunctions for cavities with cross-sections of arbitrary shapes. It should be noted however that this approximation will remain valid for all shapes of the aperture as long as the aperture thickness is sufficiently small compared to its minimal lateral dimension.

For a parallel plate problem, the equivalent transmission line network given in Fig. 5.2 is valid. The excitation with a voltage generator corresponds to a magnetic surface current on the interface and yields the two currents

$$I_1^{\mathrm{TM/TE}} = \frac{1}{2\pi} \frac{1}{\mathrm{j} Z_{\mathrm{c}}^{\mathrm{TM/TE}} \tan k_z t}, \tag{5.7a}$$

$$I_2^{\mathrm{TM/TE}} = \frac{1}{2\pi} \frac{1}{\mathrm{j} Z_{\mathrm{c}}^{\mathrm{TM/TE}} \sin k_z t}, \tag{5.7b}$$

where $Z_{\mathrm{c}}^{\mathrm{TM/TE}}$ is the characteristic impedance of the respective mode, namely $k_z/(\omega\varepsilon)$ for the TM mode and $\omega\mu/k_z$ for the TE mode, $k_z = \sqrt{k_0^2 - k_\rho^2}$ and $t = z_2 - z_1$ is the thickness of the considered aperture.

Let us define

$$I_\Delta^{\mathrm{TM/TE}} = I_1^{\mathrm{TM/TE}} - I_2^{\mathrm{TM/TE}}. \tag{5.8}$$

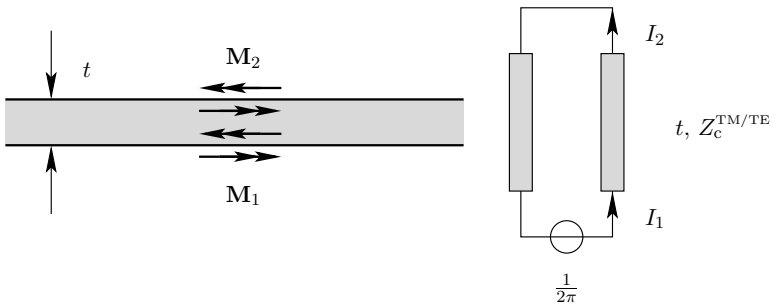

Figure 5.2: Equivalent TL network for a parallel plate problem.

The correction terms of the potential Green's functions are then obtained applying the zero order inverse Sommerfeld transformation [17]

$$G_F^{(\mathrm{c})\Delta\, xx} = G_F^{(\mathrm{c})\Delta\, yy} = \mathcal{S}_0 \left[\frac{1}{\mathrm{j}\omega} I_\Delta^{\mathrm{TM}} \right], \tag{5.9a}$$

$$G_W^{(\mathrm{c})\Delta} = \mathcal{S}_0 \left[\frac{\mathrm{j}\omega}{k_\rho^2} \left(I_\Delta^{\mathrm{TE}} - I_\Delta^{\mathrm{TM}} \right) \right]. \tag{5.9b}$$

The same approach remains valid for the multilayered media inside the aperture. In this case the equivalent circuit will consist of a cascade of transmission lines with different characteristic impedances corresponding to different layers in the aperture. It should be noted that both currents $I_{1,2}^{\mathrm{TM/TE}}$ go to infinity when the thickness of the aperture t approaches zero. However, their difference

$$I_\Delta^{\mathrm{TM/TE}} = \frac{\mathrm{j}}{Z_{\mathrm{c}}^{\mathrm{TM/TE}}} \tan \frac{k_z t}{2}$$

converges to zero when $t \to 0$, ensuring this way a smooth transition to the zero thickness case.

Consider an aperture in a thick conducting screen separating two semi-infinite free spaces. Using the MPIE form, the Integral Equation will have a Green's function kernel that consist of

$$\overleftrightarrow{\mathbf{G}}_F = \overleftrightarrow{\mathbf{G}}_F^{(1)} + \overleftrightarrow{\mathbf{G}}_F^{(2)} + 2\overleftrightarrow{\mathbf{G}}_F^{(\mathrm{c})\Delta}$$

for the electric vector potential and

$$G_W = G_W^{(1)} + G_W^{(2)} + 2G_W^{(\mathrm{c})\Delta}$$

for the magnetic scalar potential. Fig. 5.3 depicts the normalized electric vector potential Green's function kernel $\Psi = G_F^{xx} = G_F^{yy}$ computed using the presented approach for different aperture thicknesses, as a function of normalized distance.

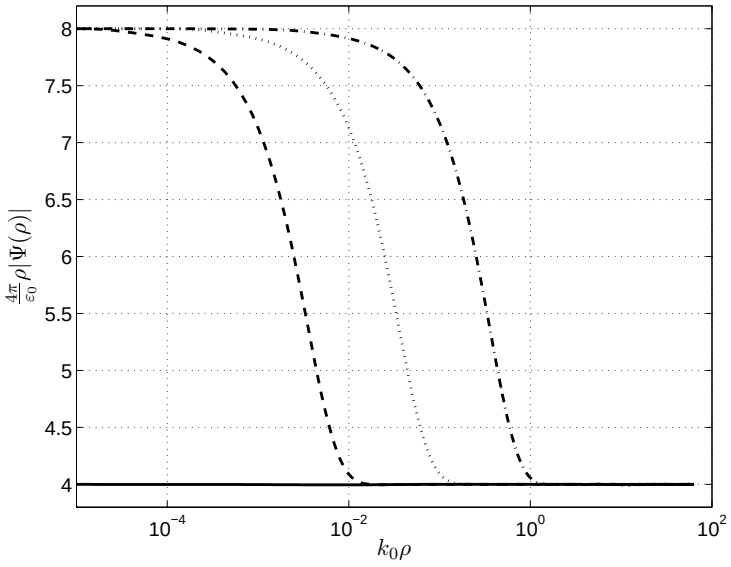

Figure 5.3: Influence of the correcting term on the potential Green's function. Zero-thickness case (solid line), $t = \lambda/1000$ (dashed line), $t = \lambda/100$ (dotted line), $t = \lambda/10$ (dash-dotted line).

5.4 Results for Thick Slot Configurations

Extensive numerical experiments have been carried out to assess the performance and limitations of the presented method. In this section we present comparisons against results obtained with a full-wave cavity approach and with measurements.

5.4.1 Currents for a Plane Wave Excitation

Let us consider a square aperture of dimensions $3\lambda/2 \times 3\lambda/2$ milled in a metallic plate of finite thickness. The aperture is assumed to be located in air in the xy plane and to be illuminated by a plane wave impinging with the incident angle $\theta_\mathrm{i} = 0$ from below having the magnetic field polarized in the x–direction: $\mathbf{H}^\mathrm{i} = \hat{x} H_0 \mathrm{e}^{-\mathrm{j}kz}$. In Fig. 5.4 the magnitudes of magnetic currents over the aperture are shown for the case of $\lambda/10$ thickness computed using the full-wave cavity approach [7] and the presented approach. As can be seen, the shape of the magnetic currents on the top and bottom aperture interfaces is similar to that on of the magnetic current obtained with the presented approach. The x-components of magnetic currents over the lines $y = 3\lambda/4$ (middle line) and $y = 3\lambda/20$ (line close to the aperture border) are given in Fig. 5.5. The real parts of currents are shown with solid lines and the imaginary parts using dashed ones. $\mathbf{M}_\Sigma$ computed using our proposed approach is shown with diamonds, while $\mathbf{M}_1$ and $\mathbf{M}_2$, computed using the full-wave cavity approach, are represented with circles and squares, respectively. The figure shows that both real and imaginary parts are close to half the sum of the currents on the lower and the upper interface of the aperture [Fig. 5.5(a)]. This relation is, however, deteriorated close to the aperture border [Fig. 5.5(b)].

In Fig. 5.6 the simulation time needed for solving the considered problem as a function of the number of unknowns is shown for both the full-wave cavity approach (circles) and the approximate approach (crosses). Using the approximate approach, we have discretized the aperture in 20×20 cells which corresponds to $N_1 = 760$ unknowns and the time needed for solving the problem on a Pentium IV processor with 2.4 GHz and 512 MB of RAM was $t_1 = 17.6$ s. If we want the same discretization density, using the full-wave cavity approach, we have to discretize both (upper and lower) aperture interfaces into 20×20 cells, which leads to twice as much unknowns $N_2 = 2N_1 = 1520$ and the time needed for solving the problem is $t_2 = 248$ s. The gain in computation time of 14 times is more than advantageous and it is due to, on the one hand, the adoption of the parallel plate Green's function for the cavity which accounts for the bulk of the computational savings (as it obviates the time consuming computation of the cavity Green's function). On the other hand, the number of unknowns is twice smaller as we consider the aperture having only one interface.

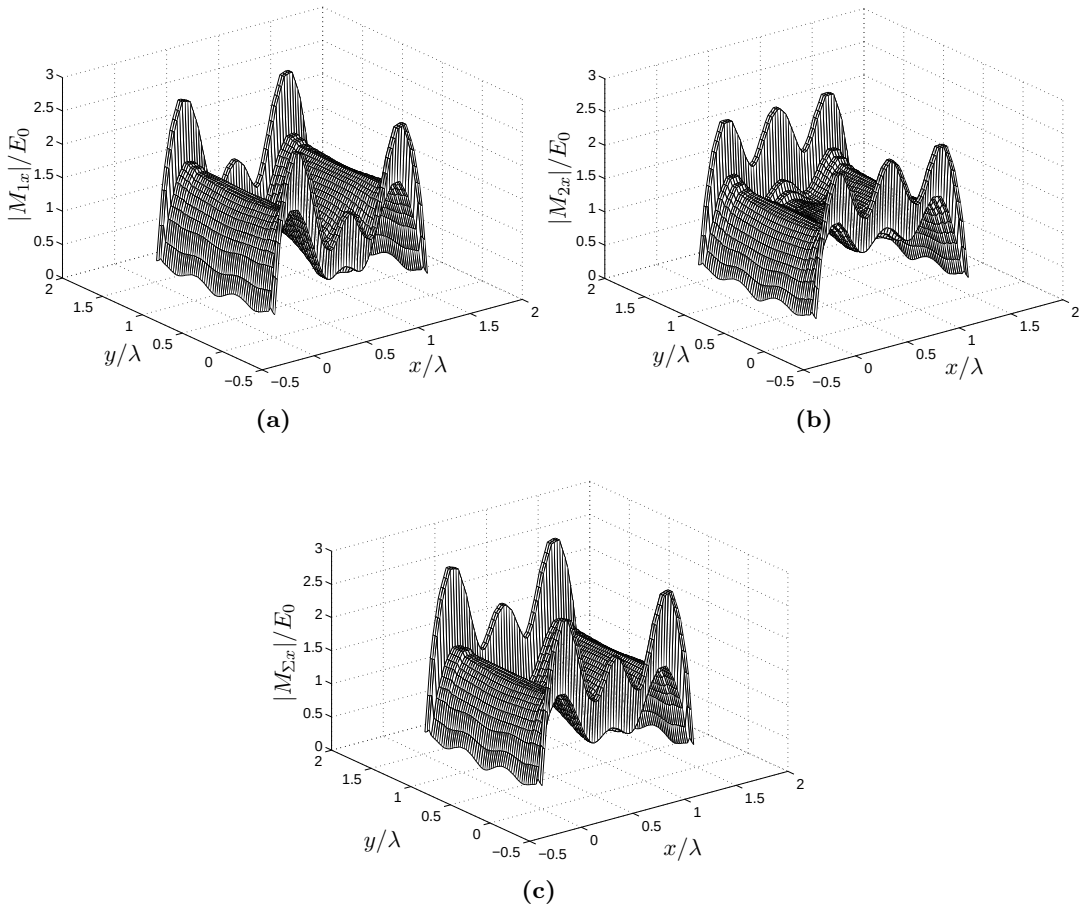

Figure 5.4: Normalized magnitude of the x-component of magnetic currents over a $\frac{3\lambda}{2} \times \frac{3\lambda}{2}$ aperture of thickness $\lambda/10$ illuminated by a plane wave impinging from below and having magnetic field polarized in the x-direction. (a) Lower aperture interface (full cavity approach). (b) Upper aperture interface (full cavity approach). (c) Average value using this technique.

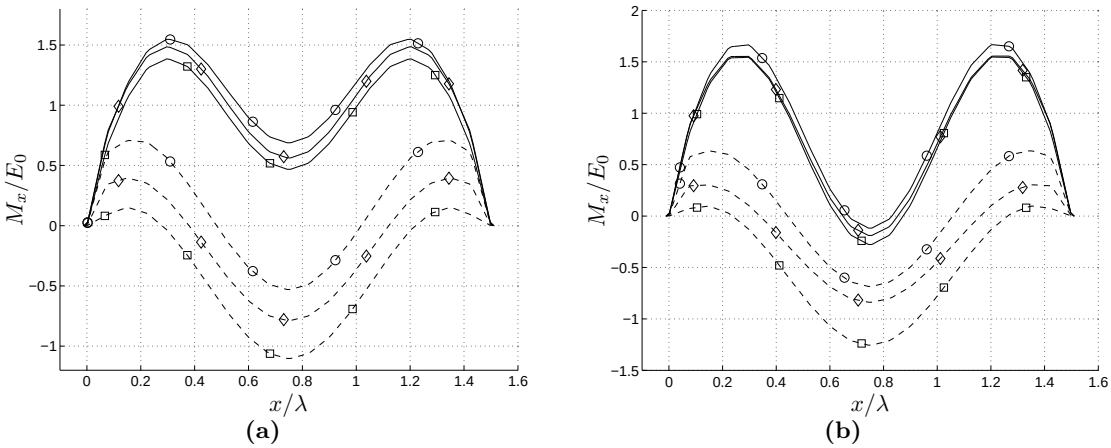

Figure 5.5: Normalized magnetic currents over the square $3\lambda/2 \times 3\lambda/2$ aperture of $\lambda/10$ thickness. $\diamond$ – $\mathbf{M}_\Sigma$, $\circ$ – $\mathbf{M}_1$, $\square$ – $\mathbf{M}_2$. Solid line – real part, dashed line – imaginary part. (a) $y = 3\lambda/4$. (b) $y = 3\lambda/20$.

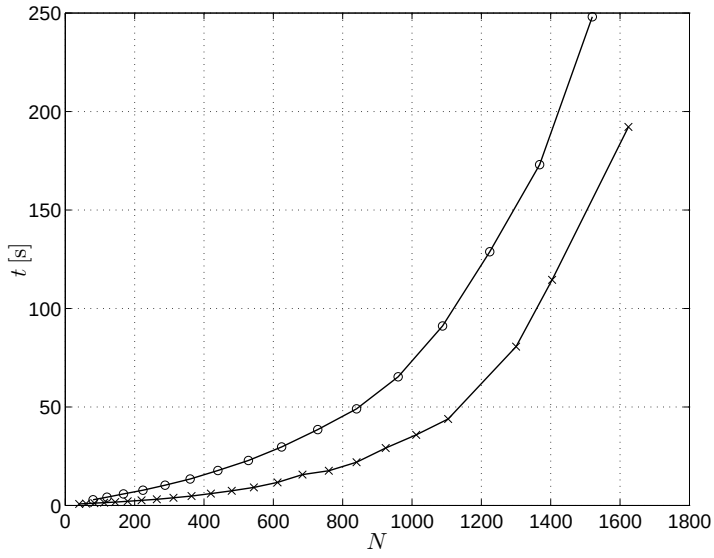

Figure 5.6: Computational time versus number of unknowns for the presented approach ($\times$) and the full-wave cavity approach ($\circ$) for a $\frac{3\lambda}{2} \times \frac{3\lambda}{2}$ aperture of thickness $\lambda/10$.

5.4.2 Comparison with a Rigorous Full Cavity Approach

To test the accuracy and validity of the proposed approximate model, we have compared it with a rigorous full-wave cavity approach in the case of a square aperture electromagnetically fed by a microstrip line in a two-layer configuration (Fig. 5.7). In this case the incident field is modeled in a standard way using the delta-gap model and introducing half-rooftops along the edge the port is connected to. Fig. 5.8 gives the reflection coefficients obtained for a slot thickness of 0.5 mm ($\sim 0.01\lambda$ at the resonant frequency). For the sake of completeness, the results obtained by the standard zero thickness integral equation are also included (dashed line). It can be seen that our model matches the full cavity model and hence predicts correctly the deviation from the zero thickness. Figs. 5.9 and 5.10 present similar predictions when the slot thickness is two and four times larger (1 mm and 2 mm), respectively. As it could be expected, here the predictions of the presented model start to deviate from those ones more rigorously obtained with the full cavity model, but the agreement is still reasonable.

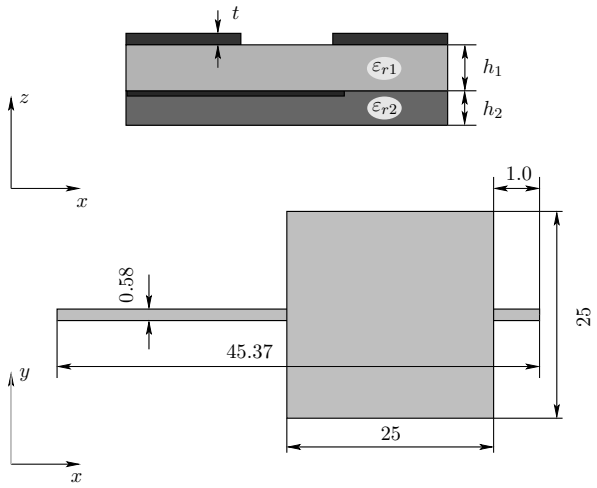

Figure 5.7: Square thick aperture antenna. Dielectrics: $h_1 = 1.0$ mm, $\varepsilon_{r1} = 1.0$, $h_2 = 0.635$ mm, $\varepsilon_{r2} = 10.7$, $\tan\delta = 0.0024$. All dimensions given in mm.

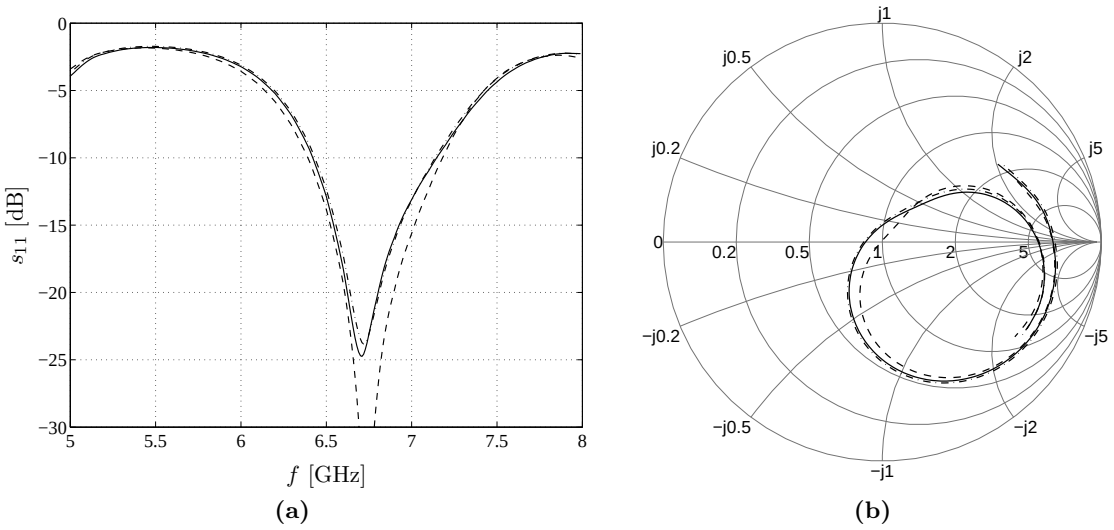

(a) **(b)**

Figure 5.8: Aperture thickness $t = 0.5$ mm. Presented approach (solid line), full-wave cavity approach (dash-dotted line), and zero thickness case (dashed line).

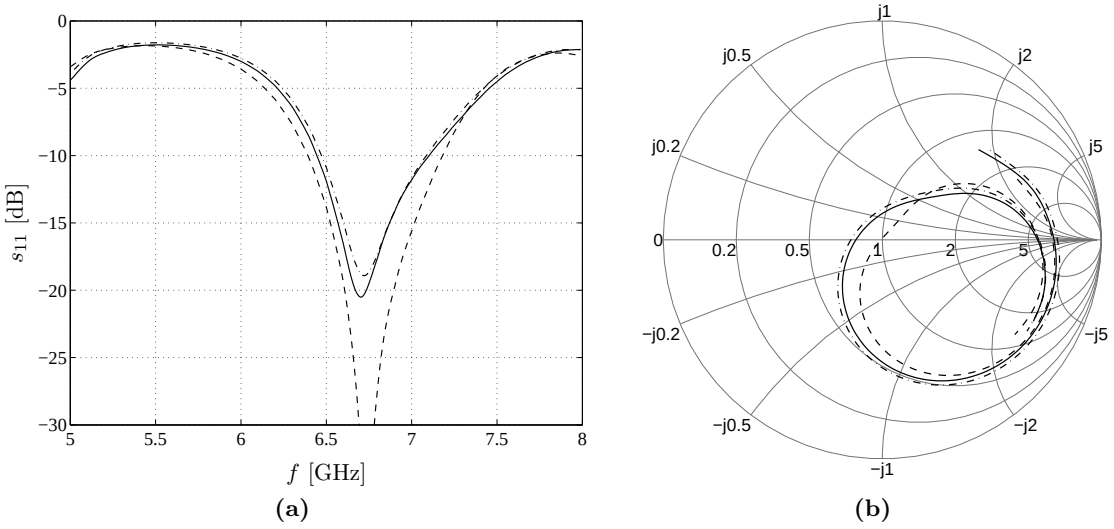

(a) **(b)**

Figure 5.9: Aperture thickness $t = 1.0$ mm. Presented approach (solid line), full-wave cavity approach (dash-dotted line), and zero thickness case (dashed line).

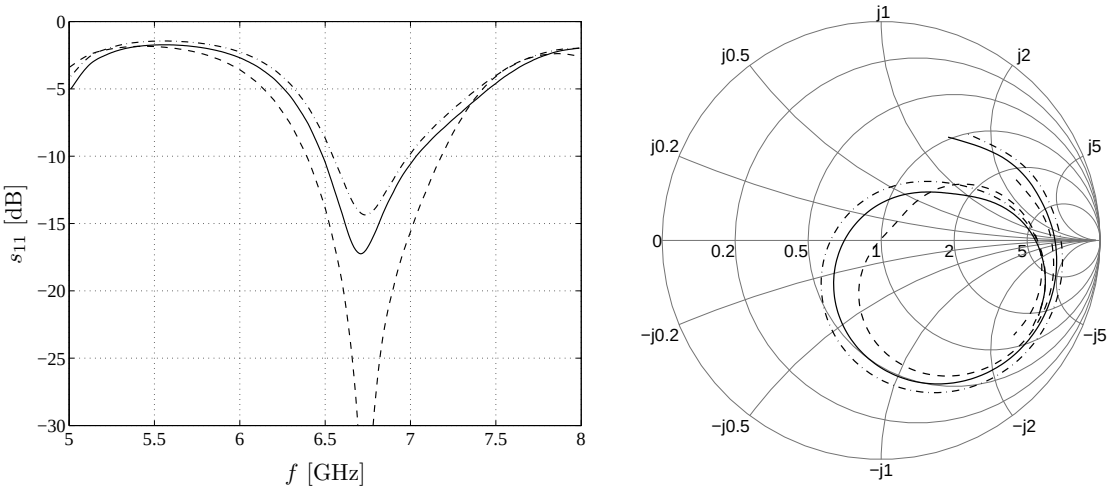

Figure 5.10: Aperture thickness $t = 2.0$ mm. Presented approach (solid line), full-wave cavity approach (dash-dotted line), and zero thickness case (dashed line).

5.4.3 Thick Rectangular Aperture Antenna: Comparison with Measurements

In order to check the results of the presented method against real-life measurements of input impedances, a set of rectangular aperture antennas with different aperture thicknesses has been realized in our Laboratory (Fig. 5.11). The metallic screens are made of aluminum and the apertures are carefully manufactured by electric erosion, what guarantees very sharp corners of the rectangular shape. The aluminum bodies are mounted on the metallization of the substrate and they are tied together with plastic bolts. For the sake of reduced weight, the aluminum bodies do not cover the whole metallization of the substrate. This set of variable thickness apertures has been carefully measured with the purpose of creating an accurate benchmark. The validity of all the numerical models developed in our laboratory and elsewhere can thus be checked, and the accuracy and range of validity of each one can be easily ascertained. These considerations also apply to the dog-bone apertures considered in the next section 5.4.4.

The computed and measured antenna input characteristics are shown in Fig. 5.12, for the zero thickness aperture, and in Figs. 5.13 and 5.14 for two different metallization thicknesses ($t = 1$, 3 mm). These two last figures include both a third curve reflecting the results obtained with a full-wave cavity approach that considers the aperture as a cavity section.

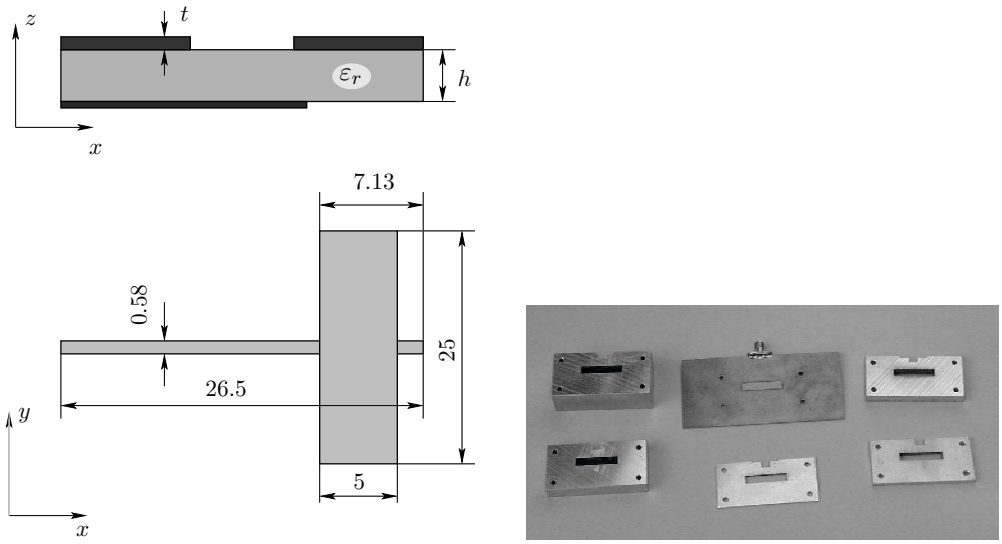

Figure 5.11: Test antenna sample. A set of conducting screens of various thicknesses and with rectangular apertures can be fixed on the basic antenna. Dielectric made of RT-Duroid 6010: $h = 0.635$ mm, $\varepsilon_r = 10.5$, $\tan\delta = 0.0024$. All dimensions given in mm.

The substrate thickness (and hence the distance between electric currents in the feeding line and magnetic currents in the slot) is only 0.635 mm and it is smaller than the thinnest slot considered ($t = 1$ mm). Therefore, this is a very challenging case for our approach (where the effect of lateral electric walls in the slot is only included indirectly) and it must be considered as a worst case revealing the limitations of our approach. However, the results presented

in Figs. 5.13 and 5.14 are still quite satisfactory, although the presented approach does not follow the measurements as well as the cavity approach, which is very good in this situation, but at the expense of much more demanding computation time. The evaluation of the cavity Green's function is a time consuming process and results in about 10 to 20 times longer simulations, when compared to the code with the new formulation. So, even in this worst-case situation, the delta function remains an interesting alternative and its predictions should improve dramatically when substrate layers thicker than the slots are used, like predicted in the previous section.

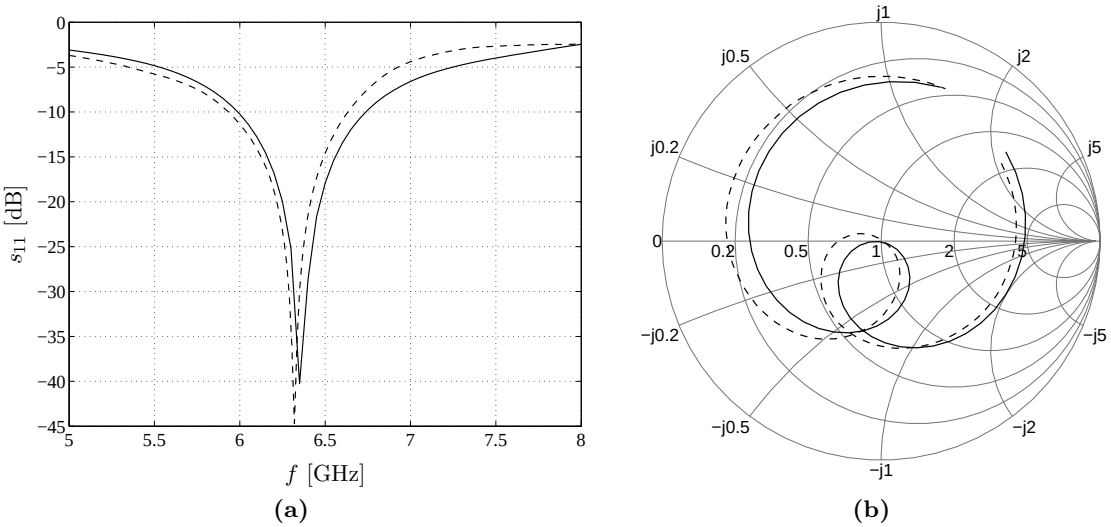

Figure 5.12: Reflection coefficient of the rectangular aperture antenna. Zero thickness case. Measurements (dashed)and presented approach (solid line).

5.4.4 Thick Dog-Bone Aperture Antenna: Comparison with Measurements

A more general shape of the thick aperture antenna is investigated. The layout of the antenna is shown in Fig. 5.15(a). The aperture is now extended to a dogbone-type shape, which can be easily milled in a metallic shield. Fig. 5.15(b) shows the realized antenna with two thick metallic shields of $t = 1$ mm and $t = 3$ mm.

The results of the three samples, with thicknesses $t = 0, 1$ and 3 mm are shown in the Figs. 5.16–5.18. Here, it must be pointed out that already for the zero thickness slot (Fig. 5.16), the theoretical prediction does not follow as closely the measurements as in the case of the rectangular slot antenna. This shows clearly the numerical degradation associated with the modeling of a complicated shape like the dog-bone. The good news is that, despite the thin substrate ($h = 0.51$ mm), the presented approach does not seem to degrade the performances of our integral equation code and the agreement remains quite fair. In particular, the qualitative trend of the input impedance resonant loop opening with increased aperture thicknesses is perfectly predicted.

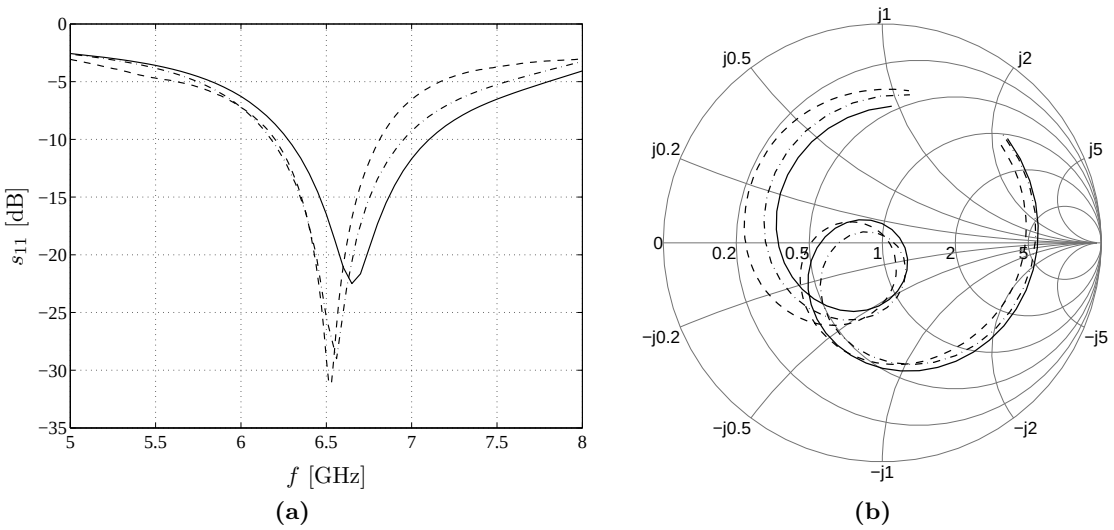

(a) **(b)**

Figure 5.13: Reflection coefficient of the rectangular aperture antenna. Aperture thickness $t = 1$ mm. Measurements (dashed), presented approach (solid), and full-wave cavity computation (dash-dotted line).

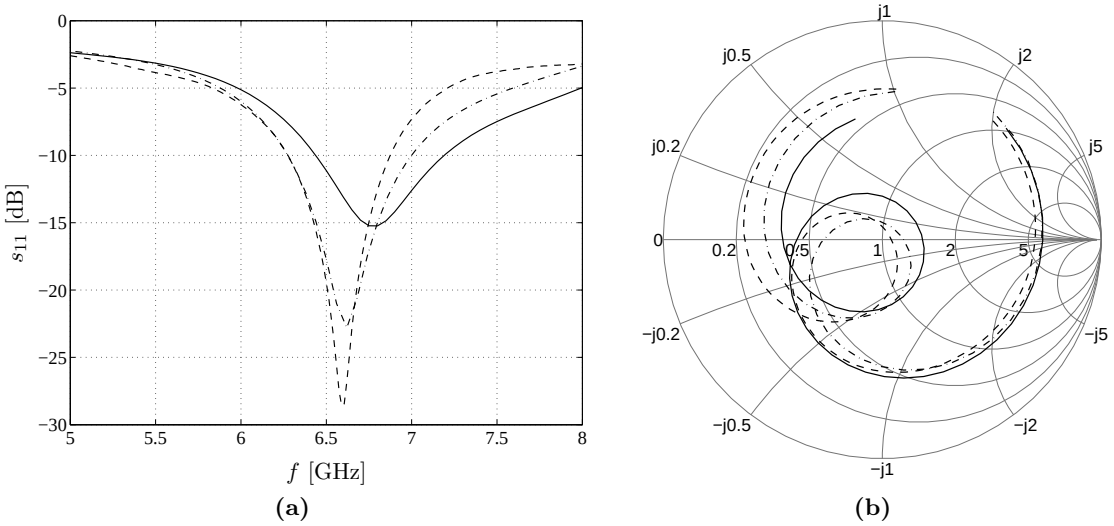

(a) **(b)**

Figure 5.14: Reflection coefficient of the rectangular aperture antenna. Aperture thickness $t = 3$ mm. Measurements (dashed), presented approach (solid), and full-wave cavity computation (dash-dotted line).

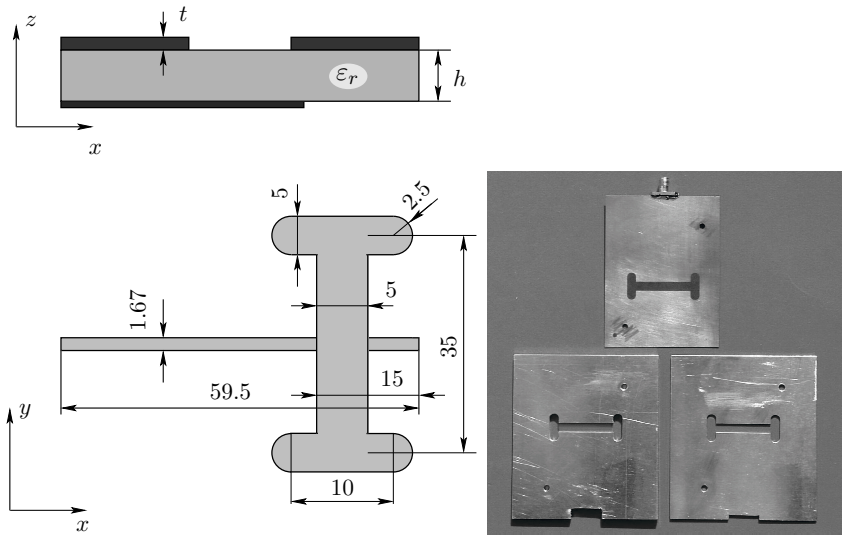

(a) **(b)**

Figure 5.15: Dog-bone aperture antenna. Dielectric: Duroid 5870, $\varepsilon_r = 2.33$, $\tan\delta = 0.0012$, $h = 0.51$ mm. All dimensions given in mm. (a) Layout of the antenna design. (b) Picture of the realized antenna samples.

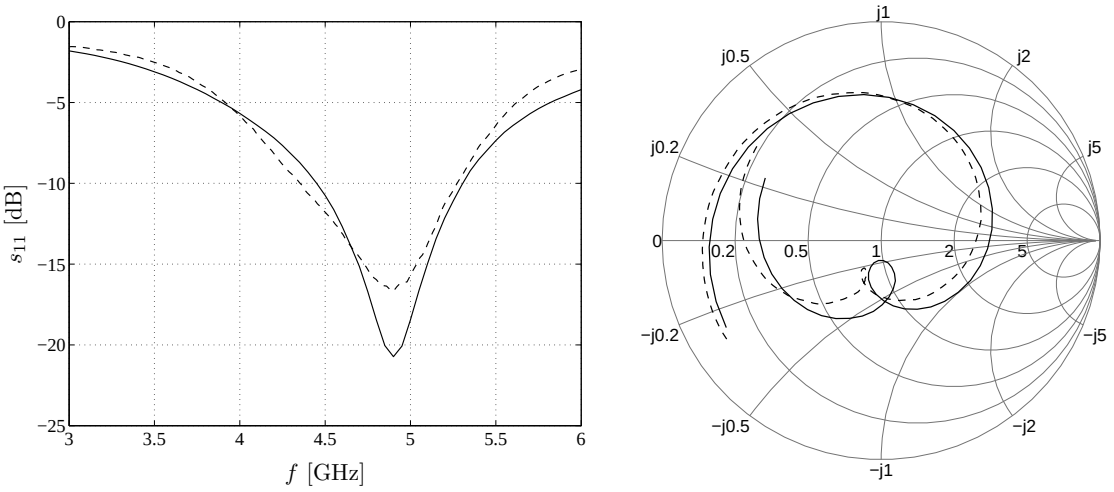

(a) **(b)**

Figure 5.16: The reflection coefficient of the dog-bone aperture antenna. Zero thickness case. Measurements (dashed line) versus simulation (solid line).

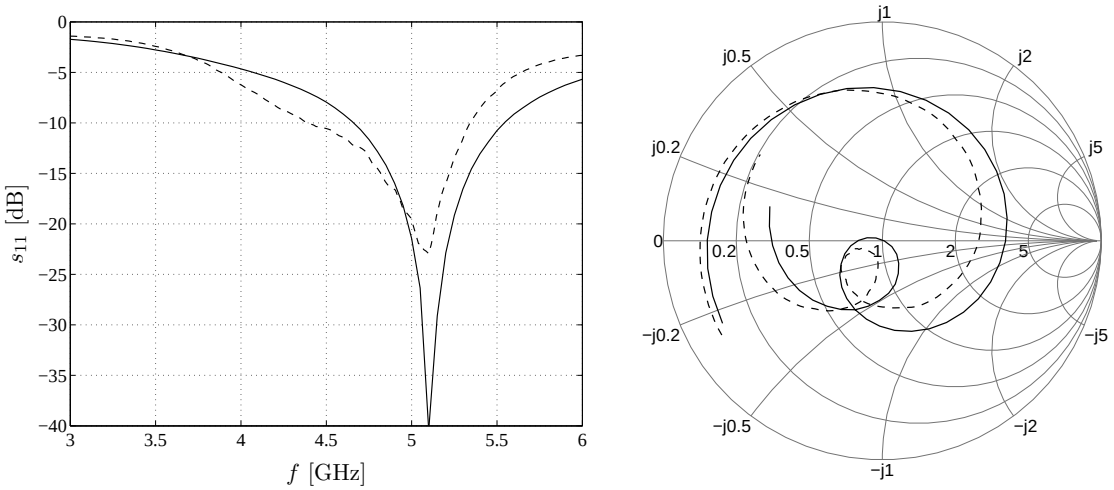

(a) **(b)**

Figure 5.17: The reflection coefficient of the dog-bone aperture antenna. Aperture thickness $t = 1$ mm $= 0.015\lambda_0$. Measurements (dashed line) versus simulation (solid line).

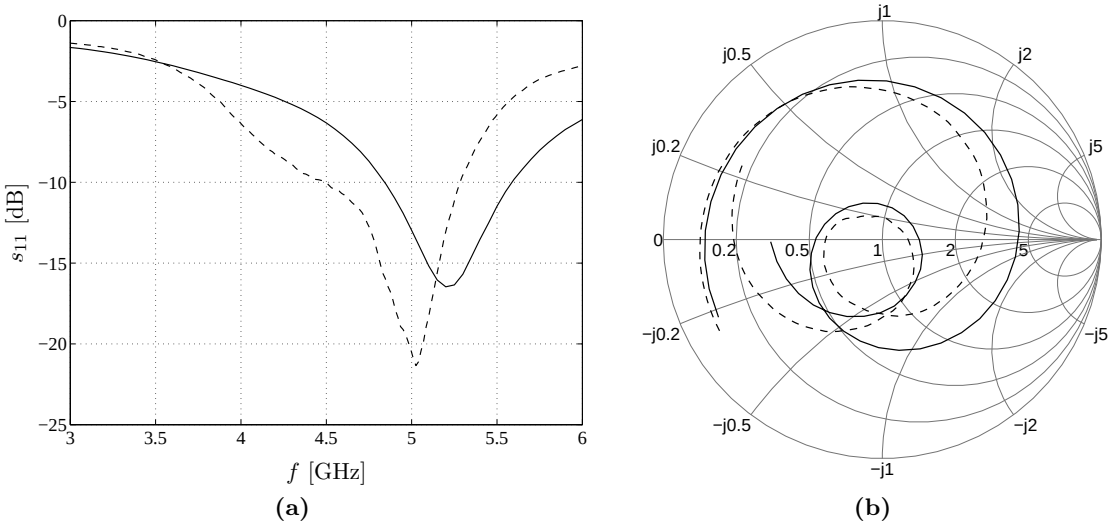

(a) **(b)**

Figure 5.18: The reflection coefficient of the dog-bone aperture antenna. Aperture thickness $t = 3$ mm $= 0.045\lambda_0$. Measurements (dashed line) versus simulation (solid line).

5.4.5 Error Analysis

The accuracy of a method is usually subjectively discussed by comparing the results of the method with other theoretical or experimental results. This is exactly what we have done in the previous sections, where we have compared the curves of reflection coefficients, obtained using the approximate approach, against the corresponding curves from the full-wave approach or measurements.

In order to treat the error quantitatively one needs to have [18]

- an accurate benchmark to which one may apply the metric,
- a metric to measure the error.

In this section, the reflection coefficients obtained from the full-wave cavity approach will be used as the accurate benchmark results. Again, this is not more than an empirical estimate of the true error, which could only be found by comparison to the exact solution of the problem, which is usually not available. A reasonably comprehensive and up-to-date survey of these issues can be found in [19]. Concerning the error metric, two different functions will be used, the correlation coefficient and the root-mean-square relative error (rms) that will give us the complementary information about the error estimation.

The correlation coefficient is a quantity that gives the quality of the least square fitting to the reference data [20, 21] and can be defined mathematically as follows. Let x_i and y_i, $i = 1, \ldots, N$ be two sets of complex data samples. Let us define the covariance and the standard deviation of these two data sets as

$$\sigma_{xy} = E\left\{(x - \bar{x})(y - \bar{y})\right\} \tag{5.10a}$$

$$\sigma_x^2 = E\left\{(x - \bar{x})^2\right\} \tag{5.10b}$$

$$\sigma_y^2 = E\left\{(y - \bar{y})^2\right\} \tag{5.10c}$$

where $E\{\cdot\}$ denotes the expectation operator, and $\bar{x}$ is the mean of the data set x_i, $\bar{x} = E\{x\}$. Now, the correlation coefficient is given by

$$r_{xy} = \frac{\sigma_{xy}}{\sigma_x \sigma_y}. \tag{5.11}$$

The correlation coefficient $r_{xy} = 1$ means that the data sets x and y are perfectly correlated or, in other words, that they behave in the same manner. However, since the correlation coefficient is independent on both origin and scale, we need an additional information in order to estimate how close the two data sets are one to another. For this, we can use the

root mean square relative error defined as

$$\varepsilon_{\text{rms}} = \sqrt{\frac{\sum_{i=1}^{N} |x_i - y_i|^2}{\sum_{i=1}^{N} |y_i|^2}}. \tag{5.12}$$

Using the adopted metric, we can quantitatively measure the error of predicted results in the approximate approach. Fig. 5.19 shows the reflection coefficients of the antenna from Fig. 5.11 for two aperture thicknesses: $t_1 = 0.05$ mm $\approx \lambda/1000$ (black lines) and $t_2 = 3.65$ mm $\approx \lambda/10$ (gray lines), the wavelength λ being computed at the maximum operating frequency in the simulation ($f = 8$ GHz). The reference results obtained from the full-wave cavity approach are shown in solid lines, and the results obtained from the approximate approach are presented with dashed lines. The predicted results for the thickness t_1 agree very well with the reference results. A correlation coefficient very close to one, $r_1 = 0.9999$, means that the two curves share exactly the same behavior. A very small rms-error of $\varepsilon_{\text{rms1}} = 0.01$ is a good indicator that the approximate solution fits perfectly with the reference one (black lines). In the case of a rather thick aperture, the approximate results are less good and this is reflected in both, the correlation coefficient $r_2 = 0.94$ and the rms-error which is now $\varepsilon_{\text{rms1}} = 0.35$ (gray lines).

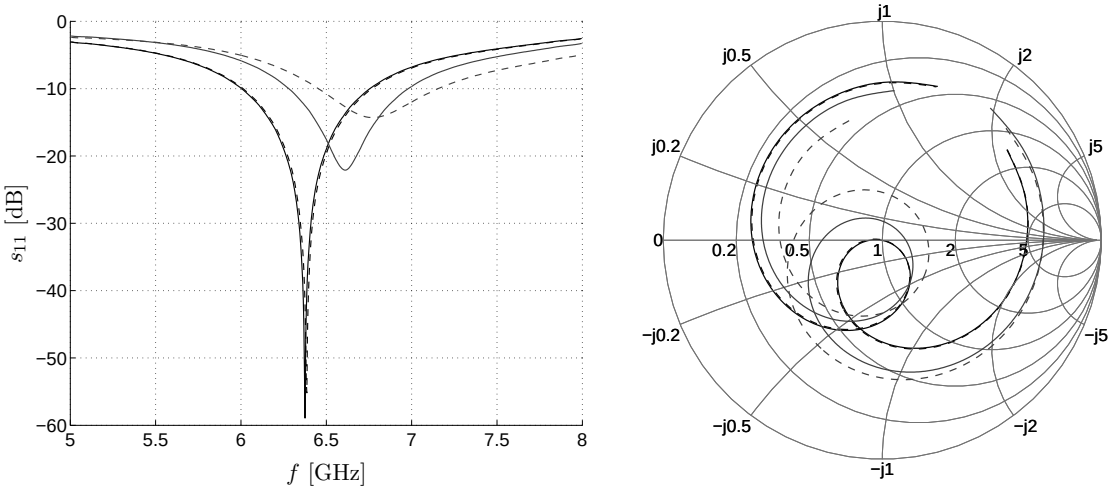

(a) The reflection coefficient. **(b)** The input impedance.

Figure 5.19: The reflection coefficient of the antenna from Fig. 5.11 for two aperture thicknesses: $t_1 = 0.05$ mm $\approx \lambda/1000$ (black lines) and $t_2 = 3.65$ mm $\approx \lambda/10$ (gray lines) at 8 GHz. Solid lines represent the full-wave cavity results (reference) and dashed ones the results obtained from the approximate approach. The correlation coefficients for the two pairs of curves are $r_1 = 0.9999$ and $r_2 = 0.94$ while the corresponding root-mean-square errors are $\varepsilon_{\text{rms1}} = 0.01$ and $\varepsilon_{\text{rms2}} = 0.35$.

Solid lines in Fig. 5.20 show the error in the reflection coefficient as a function of the normalized aperture thickness (λ being calculated for the maximum operating frequency in

the simulation, $f = 8$ GHz). The simulated structure is the rectangular thick aperture antenna from Fig. 5.11. As the aperture thickness grows, the error is increasing and becomes significant when the thickness starts to be comparable to the minimal lateral dimensions of the aperture ($b = 5$ mm $\approx 0.13\lambda$).

The same geometry, but with an additional high permittivity dielectric layer of the thickness h between the aperture and the feeding line, has been simulated. Two different layer thicknesses were used, $h_1 = 0.635$ mm $\approx 0.02\lambda$ (dashed lines), and $h_2 = 2h_1$ (dash-dotted lines). Much better prediction in the reflection coefficient may be noticed for the distances between the aperture and the feeding line that are larger than the aperture thickness. This behavior remains the same when instead of the high permittivity dielectric of $\varepsilon_r = 10.7(1 - \mathrm{j}0.0024)$, a foam layer ($\varepsilon_r = 1.0$) is used (see Fig. 5.21).

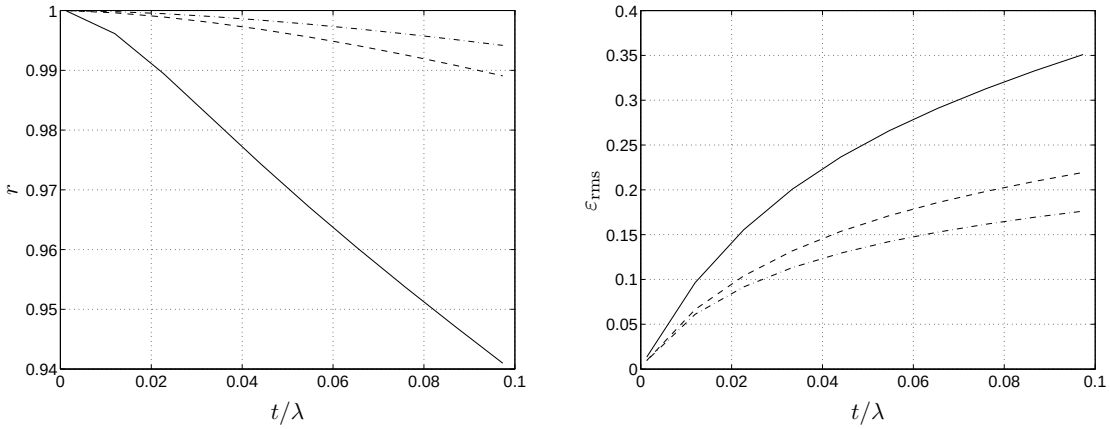

(a) The correlation coefficient. **(b)** The root-mean-square error.

Figure 5.20: The error in the reflection coefficient of the approximate approach as a function of the aperture thickness t. Solid lines: the antenna geometry from Fig. 5.11. The same antenna with an *additional high permittivity dielectric layer* of the thickness $h_1 = 0.635$ mm (dashed lines) and $h_2 = 2h_1$ (dash-dotted lines).

Finally, Fig. 5.22 illustrates the error vs. aperture thickness, for the square aperture antenna geometry. When compared to Fig. 5.20 and Fig. 5.21, much better predictions of the approximate model can be remarked. In this case, even for rather thick apertures, the minimal lateral dimension ($a = b = 25$ mm $\approx 0.7\lambda$) of the aperture still remains an order of magnitude bigger than its thickness.

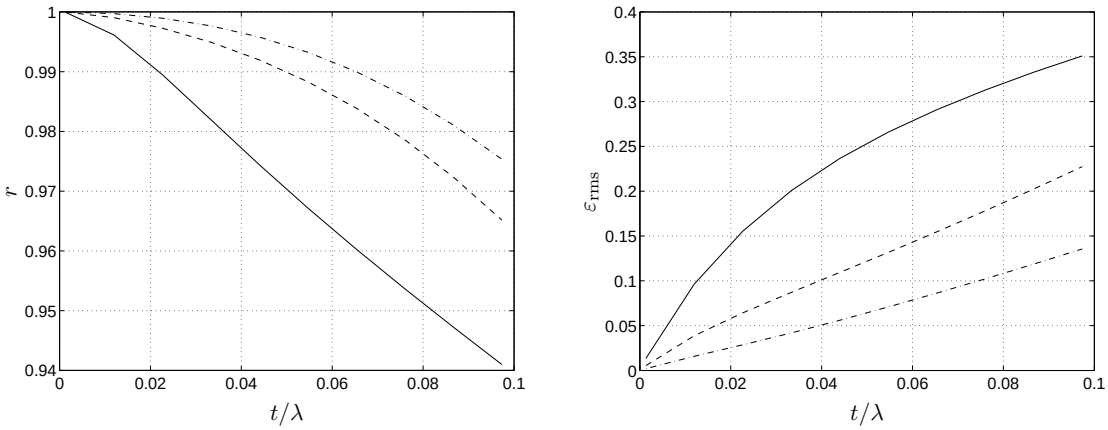

(a) The correlation coefficient. **(b)** The root-mean-square error.

Figure 5.21: The error in the reflection coefficient of the approximate approach as a function of the aperture thickness t. Solid lines: the antenna geometry from Fig. 5.11. The same antenna with an *additional air layer* of the thickness $h_1 = 0.635$ mm (dashed lines) and $h_2 = 2h_1$ (dash-dotted lines).

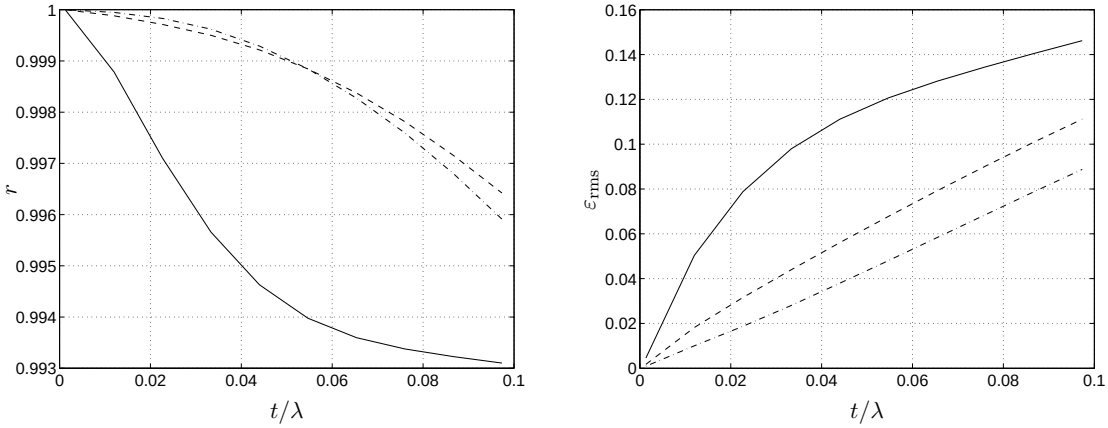

(a) The correlation coefficient. **(b)** The root-mean-square error.

Figure 5.22: The error in the reflection coefficient of the approximate approach as a function of the aperture thickness t. Solid lines: the antenna geometry from Fig. 5.11 with a *square aperture* of dimensions $a = b = 25$ mm. The same antenna with an *additional air layer* of thickness $h_1 = 0.635$ mm (dashed lines) and $h_2 = 2h_1$ (dash-dotted lines).

5.5 Conclusion

In this chapter we have presented the numerical and experimental study of the approximate technique for the numerical treatment of scattering from apertures in metal screens of finite thickness introduced in Chapter 4.

The original set of coupled integral equations developed and presented in this chapter is rigorous and exact from a full-wave point of view. There are two approximations introduced: one approximation has been introduced by replacing the cavity by parallel-plate Green's functions and another one in neglecting the magnetic current difference $\mathbf{M}_\Delta$.

The approach reduces significantly the simulation time compared to a full-wave cavity treatment of the thick apertures. The gain in computational time is due to, on one hand, the adoption of the parallel plate Green's function for the cavity and, on the other, the number of unknowns is halved as we consider the aperture having only one interface.

Various tests with increasing slot thicknesses have been performed and studied. The results are compared to a both full-wave cavity approach and measurements. The error study from the last section shows that the approximate model yields good predictions even for rather thick apertures, as long as the thickness of the aperture remains an order of magnitude smaller than its minimal lateral dimensions.

It must be pointed out that the upper limit reached in the current status of the method is already highly satisfactory. Many technologies using self-supporting metallic patches in *Ka*– and *Ku*–bands or thick conducting film in millimeter and submillimeter wave bands yield electrical thicknesses within this limit.

References

[1] R. F. Harrington and J. F. Mautz, "A generalized network formulation for aperture problems," *IEEE Trans. Antennas Propagat.*, vol. 24, no. 6, pp. 870–873, Nov. 1976.

[2] M. Himdi, J. P. Daniel, and C. Terret, "Analysis of aperture-coupled microstrip antenna using cavity method," *Electron. Lett.*, vol. 25, no. 6, pp. 391–392, Mar. 1989.

[3] O. Lafond, M. Himidi, and J. P. Daniel, "Aperture coupled microstrip patch antenna with thick ground plane in millimetre waves," *Electron. Lett.*, vol. 35, no. 17, pp. 1394–1395, Aug. 1999.

[4] P. R. Haddad and D. M. Pozar, "Characterisation of aperture coupled microstrip patch antenna with thick ground plane," *Electron. Lett.*, vol. 30, no. 14, pp. 1106–1107, July 1994.

[5] J. Jin and J. Volakis, "TM scattering by an inhomogeneously filled aperture in a thick conducting plane," *IEE Proc-H*, vol. 137, no. 3, pp. 153–159, June 1990.

[6] S. D. Gedney and R. Mittra, "Electromagnetic transmission through inhomogenously filled slots in a thick conducting plane-arbitrary incidence," *IEEE Trans. Electromagn. Compat.*, vol. 34, no. 4, pp. 404–415, Nov. 1992.

[7] A. Álvarez-Melcón and J. R. Mosig, "An efficient technique for the rigorous analysis of shielded circuits and antennas of arbitrary shapes," in *Proc. International Symposium on Antennas (JINA'98)*, Nice, France, Nov. 17–19, 1998, pp. 57–60.

[8] ——, "Two techniques for the efficient numerical calculation of the Green's function for planar shielded circuits and antennas," *IEEE Trans. Microwave Theory Tech.*, vol. 48, no. 9, pp. 1492–1504, Sept. 2000.

[9] J. R. Mosig and A. Álvarez-Melcón, "The summation-by-parts algorithm - A new efficient technique for the rapid calculation of certain series arising in shielded planar structures," *IEEE Trans. Microwave Theory Tech.*, vol. 50, no. 1, pp. 215–218, Jan. 2002.

[10] D. Llorens del Río and J. R. Mosig, "On the interaction of magnetic and electric currents in stratified media," *IEEE Trans. Antennas Propagat.*, vol. 52, no. 8, pp. 2100–2108, Aug. 2004.

[11] D. Llorens del Río, "Electromagnetic analysis of 2.5d structures in open layered media," Ph.D. dissertation, Ecole Polytechnique Fédérale de Lausanne, Switzerland, 2005, Thèse No. 3183.

[12] J. R. Mosig, "Scattering by arbitrarily-shaped slots in thick conducting screens: an approximate solution," *IEEE Trans. Antennas Propagat.*, vol. 52, no. 8, pp. 2109–2117, Aug. 2004.

[13] C. M. Butler, Y. Rahmat-Samii, and R. Mittra, "Electromagnetic penetration through apertures in conducting surfaces," *IEEE Trans. Antennas Propagat.*, vol. AP-26, no. 1, pp. 82–93, Jan. 1978.

[14] J. Van Bladel, *Electromagnetic Fields*. New York: McGraw-Hill, 1964.

[15] R. E. Collin, *Field Theory of Guided Waves*, 2nd ed. New York: McGraw-Hill, 1991.

[16] K. A. Michalski and J. R. Mosig, "Multilayered media Green's functions in integral equation formulations," *IEEE Trans. Antennas Propagat.*, vol. 45, no. 3, Mar. 1997.

[17] J. R. Mosig, "Integral-equation technique," in *Numerical Techniques for Microwave and Millimeter-Wave Passive Structures*, T. Itoh, Ed. New York: Wiley, 1989, ch. 3, pp. 133–213.

[18] B. M. Kolundžija, "Accurate solution of square scatterer as benchmark for validation of electromagnetic modeling of plate structures," *IEEE Trans. Antennas Propagat.*, vol. 46, no. 7, pp. 1009–1014, July 1998.

[19] K. F. Warnick and W. C. Chew, "Error analysis of the moment method," *IEEE Antennas Propagat. Mag.*, vol. 46, no. 6, pp. 38–53, Dec. 2004.

[20] A. L. Edwards, "An introduction to linear regression and correlation," in *The Correlation Coefficient.* San Francisco: W.H. Freeman, 1976, ch. 4, pp. 33–46.

[21] E. W. Weisstein. (2004) Correlation coefficient, from math-world – a wolfram web resource. [Online]. Available: http://mathworld.wolfram.com/CorrelationCoefficient.html

6 An Integral Equation Technique for Solving Thick Irises in Rectangular Waveguides[†]

6.1 Introduction

A thick iris, defined as an aperture in a metallic wall of finite thickness, is one of the most common types of discontinuities encountered in waveguides. These apertures can arise in the waveguide external walls (slot waveguide antennas, coupling holes between waveguides) or in additional walls filling the waveguide cross-section and dividing the waveguide into coupled cavities, useful to create filtering structures. From this second point of view, irises were first analyzed in the early fifties, by means of approximate analytical and variational techniques, well detailed in classical textbooks [1, 2, 3, 4]. Initially, these approximate expressions were derived for small apertures in zero-thickness conducting walls, but correction factors for larger apertures and/or finite thickness walls [5, 6, 7] were soon introduced. The first systematic technique for the full-wave analysis of irises in waveguides was the Mode Matching (MM) technique [8, 9]. Specific applications for several regular iris shapes can be found in [10, 11, 12, 13]. Nowadays, in order to cope with arbitrary shapes and more complicated geometries, so-called hybrid methods are used, where MM is combined with Integral Equation (IE) approaches [14] or with Finite Element (FEM) algorithms [15, 16, 17]. See the excellent review paper by Arndt *et al.* [18] for a comprehensive and up-to-date survey.

In parallel to these developments, slots in waveguides have been also analyzed with classical integral equation approaches using the equivalence principle [19]. In this context, the problem of thick irises inside waveguides is equivalent to the problem of apertures of a finite thickness in printed multilayered antennas. The theoretical development and its experimental validation, presented in Chapters 4 and 5, showed that the apertures of finite thicknesses can be treated as infinitely thin apertures (Fig. 6.1). The aperture thickness appears only as a modification in the Green's functions of the problem, but otherwise the aperture is treated as a two-dimensional object. This technique reduces two times the number of unknowns on the iris and allows to treat the irises of arbitrary cross-sections.

In the first part of this chapter, we present an Integral Equation (IE) technique for solving rectangular waveguide discontinuities including thick irises. Waveguide discontinuities here are considered in wider sense being not only irises and interconnections of waveguides with different cross-sections, but also dielectric layers of different dielectric properties and metallic patches and slots embedded inside dielectrics. The technique presented is based on [20, 21] and is recalled here for the sake of completeness. The new features added to it are the extension to the rectangular waveguides of different cross-sections and the modal excitation, which is

[†]I. Stevanović, P. Crespo-Valero, and J. R. Mosig, *IEEE Trans. on Microwave Theory Tech.*, submitted for publication on 20 Jan. 2005

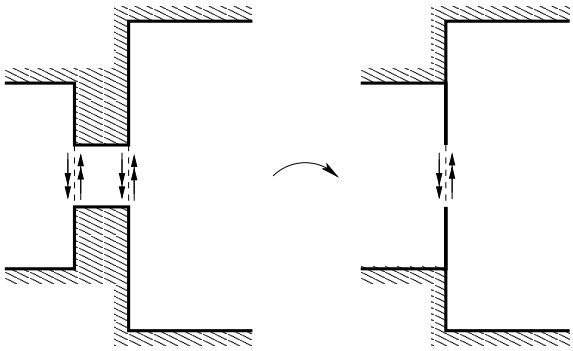

Figure 6.1: Thin iris modeled as a zero-thickness iris.

explained in detail in Section 6.4. This formulation is then verified by a series of test cases, where the results from our solver are compared to the simulations or measurements available in the open literature.

The second part of the chapter treats the problem of thick irises inside the rectangular waveguides. An original and efficient treatment, similar to the one presented in Chapters 4 and 5, is introduced. The technique is validated by comparing the results of simulations with both full-wave cavity approach, where the iris is treated as a new waveguide section, and with measurements of some real-life structures.

6.2 Integral Equations and Method of Moments

Consider a structure composed of a number of waveguides with different rectangular cross-sections (Fig. 6.2). Any interconnection between waveguides of different cross-sections and any zero-thickness iris is treated like a slot in the standard slot antenna formulation. An iris with a non zero-thickness will be considered *ab initio* as a new waveguide cross-section. However, for not very thick irises, an original and efficient treatment will be introduced later on. On the other hand, any waveguide section can be filled by stratified dielectrics and include conductive patches of arbitrary shapes localized in planes perpendicular to the propagation direction.

In the integral equation formulation of the problem, the boundary conditions for the fields are imposed. On every interconnection of two different waveguides and every slot, the surface equivalence principle is applied and magnetic surface currents $\mathbf{J}_{\mathrm{H}}$ (on both sides of the interface) are introduced in such a way as to insure the continuity of the tangential component of the total electric field

$$\mathbf{E}_{\mathrm{t}}^{+} = \mathbf{E}_{\mathrm{t}}^{-} \Leftrightarrow \mathbf{J}_{\mathrm{H}}^{+} = -\mathbf{J}_{\mathrm{H}}^{-}. \tag{6.1}$$

The continuity of tangential component of the total magnetic fields on the slots and the

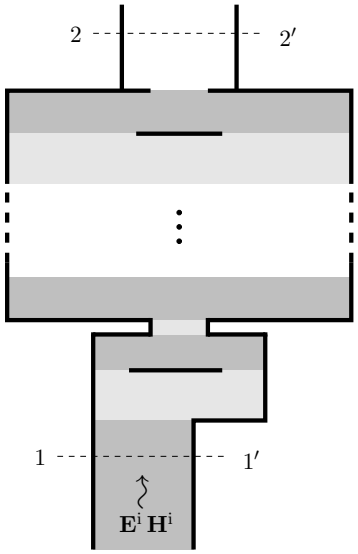

Figure 6.2: General multilayered waveguide structure composed of an arbitrary number of planar printed patches and slots.

interconnections of two different waveguides has to be satisfied

$$\mathbf{H}_{\mathrm{t}}^{+} = \mathbf{H}_{\mathrm{t}}^{-}. \tag{6.2}$$

Every patch surface is modeled using electric surface currents $\mathbf{J}_{\mathrm{E}}$. Considering all the patches to be made of perfectly conducting metallizations, the tangential component of the total electric field ($\mathbf{E}$) on them has to be set to zero

$$\mathbf{E}_{\mathrm{t}} = \mathbf{E}_{\mathrm{t}}^{\mathrm{i}} + \mathbf{E}_{\mathrm{t}}^{\mathrm{s}} = \mathbf{0} \tag{6.3}$$

where $\mathbf{E}^{\mathrm{i}}$ and $\mathbf{E}^{\mathrm{s}}$ are the incident and the scattered electric fields, respectively.

Introducing field Green's functions, the scattered fields can be expressed as convolution integrals of the electric and/or magnetic sources and the corresponding Green's functions. The boundary conditions evolve this way into a system of integral equations with unknown electric and magnetic surface currents.

The MoM technique has been used to numerically solve the system of integral equations. The unknown electric and magnetic currents are expanded into a set of basis functions. In order to model general shape of magnetic and electric planar sources, subsectional (rectangular/triangular) basis functions have been selected, so the unknown sources can be expanded as follows

$$\mathbf{J}_{\mathrm{Q}}(\mathbf{r}') = \sum_{k} \alpha_{\mathrm{Q}k} \mathbf{f}_{\mathrm{Q}k}(\mathbf{r}'), \quad k = 1, \ldots, N_{\mathrm{Q}} \tag{6.4}$$

where the source index Q is set to Q = E for an electric source (HED) or to Q = H for a magnetic source (HMD). In the same expression, $\alpha_{\mathrm{Q}k}$ are the unknown coefficients in the

expansion of the currents and $\mathbf{f}_{Qk}$ are the N_Q subsectional basis functions defined on electric (Q = E) or magnetic (Q = H) surfaces.

Using the Galerkin procedure, the same set of functions as the one used for the basis functions is chosen. This way, the original coupled system of integral equations is transformed into an algebraic linear system of equations, with the coefficients α_{Qk} as unknowns

$$\begin{bmatrix} [R_{EE}] & [R_{EH}] \\ [R_{HE}] & [R_{HH}] \end{bmatrix} \begin{bmatrix} [\alpha_E] \\ [\alpha_H] \end{bmatrix} = \begin{bmatrix} [\gamma_E] \\ [\gamma_H] \end{bmatrix}. \tag{6.5}$$

There are four different types of terms R_{PQ} that appear in the final MoM matrix. The term (k, l) in each submatrix can be written in a condensed form as

$$R_{PQ}(k,l) = \int_{S_k} \mathbf{f}_{Pk}(\mathbf{r})\, \mathrm{d}S \int_{S_l} \vec{\mathbf{G}}_{PQ}(\mathbf{r}|\mathbf{r}')\mathbf{f}_{Ql}(\mathbf{r}')\, \mathrm{d}S'. \tag{6.6}$$

Using the equivalent transmission line networks to represent the waveguide sections, the field dyadic Green's functions are given by

$$\vec{\mathbf{G}}_{PQ}(\mathbf{r}|\mathbf{r}') = \sum_i \widetilde{G}_{Pi}(z,z')\, \mathbf{p}_i(x,y)\, \mathbf{q}_i(x',y'). \tag{6.7}$$

It must be pointed out that the above is a compact notation where both the observer index P and the source index Q can be either E (electric field, electric source) or H (magnetic field, magnetic source). Accordingly, the vector modal functions $\mathbf{p}$ and $\mathbf{q}$ are either the modal functions of electric ($\mathbf{e}$) or of magnetic ($\mathbf{h}$) type. Finally, the term $\widetilde{G}_{Pi}(z,z')$, depending only on the observer index, is the associated spectral Green's function that corresponds to either the voltage ($\mathbf{p} = \mathbf{e}$) or the current ($\mathbf{p} = \mathbf{h}$). The index i represents the order number of the rectangular waveguide mode ($\mathrm{TE}_{m,n}$ where $m, n = 0, 1, 2\ldots$, $mn \neq 0$ or $\mathrm{TM}_{m,n}$ where $m, n = 1, 2, 3, \ldots$). The expressions for $\mathbf{e}_i$ and $\mathbf{h}_i$, the vector modal functions of electric and magnetic type for the waveguides of rectangular cross-sections, can be found in [1].

Introducing the rectangular waveguide Green's functions (6.7) into the expressions for MoM coefficients, (6.6) becomes

$$R_{PQ}(k,l) = \sum_i \widetilde{G}_{Pi} C_P(k,i) C_Q(l,i), \tag{6.8}$$

where

$$C_P(k,i) = \int_{S_k} \mathbf{f}_{Pk}(x,y)\mathbf{p}_i(x,y)\, \mathrm{d}x\, \mathrm{d}y. \tag{6.9}$$

It can be noticed from the above equations (6.8) that all MoM matrix coefficients are functions of only two different overlapping integrals. In particular, the overlapping integrals of the $\mathbf{e}$ and $\mathbf{h}$ vector modal functions with the vector basis functions. Having rectangular and/or triangular subsectional basis functions, these integrals can be computed analytically [21].

6.3 Efficient Evaluation of MoM Matrix

For efficient evaluation of the series in (6.8), the extraction of the quasi-static term of the spectral Green's functions is performed [20]. The main implication of this technique is that the original series are separated into frequency independent and frequency dependent series. The frequency independent series are evaluated only once for a given geometry, and are, therefore, not recomputed for each new point in frequency. As for the frequency dependent series, they are evaluated for each point in frequency, but due to the extraction of the quasi-static part, the convergence is enhanced considerably. As a result, an important saving in computational time for the analysis of multilayered media waveguide structures over a wide range of frequencies is achieved.

Dropping the P and Q indices, any MoM matrix coefficient in (6.8) can be written in the following general form

$$R(k,l) = \sum_i \widetilde{G}_i C_{eh}(i,k) C_{eh}(i,l), \tag{6.10}$$

where C_{eh} is an overlapping integral of the **e** or **h** vector modal functions with the vector basis functions, and $\widetilde{G}_i$ is a voltage or a current coefficient computed using equivalent transmission line networks (spectral quantity). The first step in the procedure is to add to and substract from (6.10) the quasi-static term of the spectral domain quantity $\widetilde{G}_i$

$$R(k,l) = \sum_i \left(\widetilde{G}_i - \widetilde{G}_i^0\right) C_{eh}(i,k) C_{eh}(i,l) + R_0(k,l), \tag{6.11}$$

where $\widetilde{G}_i^0$ is the quasi-static part of $\widetilde{G}_i$, and we have defined

$$R_0(k,l) = \sum_i \widetilde{G}_i^0 C_{eh}(i,k) C_{eh}(i,l). \tag{6.12}$$

To obtain the quasi-static part, the case of modes infinitely below the cut-off has to be considered. The equivalent network for the quasi-static part is then composed only of two semi-infinite transmission line sections, above and below the exciting generator, that is, the source point.

For the case of a HED as a source (Q = E), the quasi-static part of the voltage coefficient is non-zero only for the rooftops belonging to that electric interface and is given by [21]

$$R_0(k,l) = \mathrm{j} D^{\mathrm{TE}} R_0^{\mathrm{TE}}(k,l) + \frac{1}{\mathrm{j} D^{\mathrm{TM}}} R_0^{\mathrm{TM}}(k,l) \tag{6.13a}$$

with

$$R_0^{\mathrm{TE}}(k,l) = \sum_i \frac{1}{k_{\rho i}} C_{eh}^{\mathrm{TE}}(i,k) C_{eh}^{\mathrm{TE}}(i,l) \tag{6.13b}$$

$$R_0^{\mathrm{TM}}(k,l) = \sum_i k_{\rho i} C_{eh}^{\mathrm{TM}}(i,k) C_{eh}^{\mathrm{TM}}(i,l) \tag{6.13c}$$

$$D^{\mathrm{TE}} = \omega\mu_0 \frac{\mu_r^+ \mu_r^-}{\mu_r^+ + \mu_r^-} \tag{6.13d}$$

$$D^{\mathrm{TM}} = \omega\varepsilon_0(\varepsilon_r^+ + \varepsilon_r^-) \tag{6.13e}$$

where C_{eh}^{TE} and C_{eh}^{TM} are the overlapping integrals between the subdomain basis functions of a given electric interface with the $\mathrm{TE}_{m,n}$ and $\mathrm{TM}_{m,n}$ modal sets, respectively, $k_{\rho i}$ is the transverse wave number of the i^{th} mode, and the superscripts $+$ and $-$ are used to designate the dielectric parameters of the layers above and below the considered interface, respectively.

Analogously, for a HMD as a source, (Q = H), the quasi-static part of the current coefficient is non-zero only for the rooftops belonging to that magnetic interface and is given by [21]

$$R_0(k,l) = \frac{1}{\mathrm{j}D^{\mathrm{TE}}} R_0^{\mathrm{TE}}(k,l) + \mathrm{j}D^{\mathrm{TM}} R_0^{\mathrm{TM}}(k,l) \tag{6.14a}$$

where

$$R_0^{\mathrm{TE}}(k,l) = \sum_i k_{\rho i} C_{eh}^{\mathrm{TE}}(i,k) C_{eh}^{\mathrm{TE}}(i,l) \tag{6.14b}$$

$$R_0^{\mathrm{TM}}(k,l) = \sum_i \frac{1}{k_{\rho i}} C_{eh}^{\mathrm{TM}}(i,k) C_{eh}^{\mathrm{TM}}(i,l). \tag{6.14c}$$

The interesting feature of (6.13b), (6.13c), (6.14b) and (6.14c) is that all the quantities depend only on geometry, and are, therefore, frequency independent. Consequently, the series are computed only once for a given geometry and are not recomputed for each subsequent frequency point. Once they are summed up, the total quasi-static matrix coefficients are evaluated with the use of equations (6.13a) and (6.14a).

Substituting the quasi-static part in (6.11), the final MoM matrix coefficients are obtained, this time frequency dependent. It is important to note, that since the quasi-static term is extracted, the resulting series will converge much faster than the original ones.

6.4 Modal Excitation

Let the excitation of the waveguide be a source which produces a single mode, of unit amplitude. This mode (usually the dominant mode) is denoted by the index i. The field transverse to the z-direction can be expressed in terms of the incident power wave a_i as

$$\mathbf{H}^{\mathrm{i}} = \frac{a_i}{\sqrt{Z_i}} \mathbf{h}_i \tag{6.15}$$

where Z_i is the characteristic impedance, and $\mathbf{h}_i$ the vector modal function of the magnetic field for the considered mode.

Suppose that we want to compute the reflection coefficient in the reference plane $1-1'$ (Fig. 6.3). Let the aperture A_1 in that reference plane be discretized into a number of subsectional (rectangular and/or triangular) basis functions $\mathbf{f}_{\mathrm{H}k}$, for all indices $k = 1, \ldots, N_{\mathrm{H}}$ for which $S_k \subset A_1$.

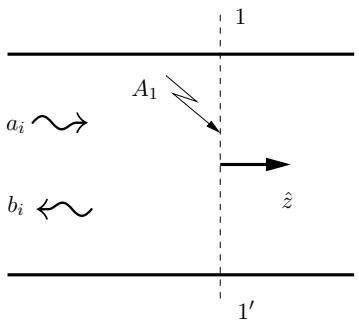

Figure 6.3: Waveguide excitation.

The excitation vector in the MoM system of equations (6.5) can be expressed then as follows

$$\gamma_{\mathrm{H}k} = -2 \int_{S_k} \mathbf{H}^{\mathrm{i}} \cdot \mathbf{f}_{\mathrm{H}k} \, \mathrm{d}S \tag{6.16}$$

where the coefficient 2 comes from the "mirrored" magnetic field [22].

After having solved the system, we obtain, among the others, the unknown coefficients β_k, used to expand the magnetic current on the aperture A_1 in a given set of basis functions

$$\mathbf{J}_{\mathrm{H}} = \sum_k \beta_k \mathbf{f}_{\mathrm{H}k}. \tag{6.17}$$

The tangential electric field in the aperture, now that magnetic current is known, can be expressed as

$$\mathbf{E} = \hat{z} \times \mathbf{J}_{\mathrm{H}} = \sum_k \beta_k \left(\hat{z} \times \mathbf{f}_{\mathrm{H}k} \right). \tag{6.18}$$

On the other hand, this field can be represented with a mode expansion, because it is also a field solution in the waveguide

$$\mathbf{E} = \sum_j (a_j + b_j) \sqrt{Z_j} \mathbf{e}_j. \tag{6.19}$$

By projecting the electric field onto the incident mode i over the aperture A_1 and using the orthonormality of the modes, (6.19) becomes

$$\int_{A_1} \mathbf{E} \cdot \mathbf{e}_i \, \mathrm{d}S = (a_i + b_i) \sqrt{Z_i} \int_{A_1} \mathbf{e}_i \cdot \mathbf{e}_i \, \mathrm{d}S = (a_i + b_i) \sqrt{Z_i}. \tag{6.20}$$

Taking into account (6.18), yields

$$b_i = -a_i + \frac{1}{\sqrt{Z_i}} \sum_k \beta_k \int_{S_k} (\hat{z} \times \mathbf{f}_{\mathrm{H}k}) \cdot \mathbf{e}_i \, \mathrm{d}S \tag{6.21}$$

and finally, using

$$(\hat{z} \times \mathbf{f}_{\mathrm{H}k}) \cdot \mathbf{e}_i = -\mathbf{f}_{\mathrm{H}k} \cdot \mathbf{h}_i \tag{6.22}$$

one obtains

$$b_i = -a_i - \frac{1}{\sqrt{Z_i}} \sum_k \beta_k \int_{S_k} \mathbf{f}_{\mathrm{H}k} \cdot \mathbf{h}_i \, \mathrm{d}S \tag{6.23}$$

for all indices k for which $S_k \subset A_1$. The reflection coefficient on the aperture A_1 can now be expressed as

$$\rho = \frac{b_i}{a_i}. \tag{6.24}$$

Suppose that a waveguide is short-circuited (there is no aperture). This means that $\beta_k = 0$ and from (6.23) directly follows $b_i = -a_i$, that is, the reflection coefficient in this case becomes $\rho = -1$. In the case of an infinitely long waveguide, the aperture has the waveguide's cross-section. If the incident electric field is

$$\mathbf{E}^{\mathrm{i}} = a_i \sqrt{Z_i} \mathbf{e}_i,$$

the magnetic current over the aperture will be given by

$$\mathbf{J}_{\mathrm{H}} = -\hat{z} \times \mathbf{E}^{\mathrm{i}} = -a_i \sqrt{Z_i} \hat{z} \times \mathbf{e}_i = -a_i \sqrt{Z_i} \mathbf{h}_i.$$

Then, from (6.23), we obtain

$$\begin{aligned} b_i = & -a_i - \frac{1}{\sqrt{Z_i}} \sum_k \beta_k \int_{S_k} \mathbf{f}_{\mathrm{H}k} \cdot \mathbf{h}_i \, \mathrm{d}S = \\ = & -a_i - \frac{1}{\sqrt{Z_i}} \int_{A_1} \left(\sum_k \alpha_{\mathrm{H}k} \mathbf{f}_{\mathrm{H}k} \right) \cdot \mathbf{h}_i \, \mathrm{d}S \\ = & -a_i + \frac{1}{\sqrt{Z_i}} \int_{A_1} a_i \sqrt{Z_i} \mathbf{h}_i \cdot \mathbf{h}_i \, \mathrm{d}S \\ = & -a_i + a_i \int_{A_1} \mathbf{h}_i \cdot \mathbf{h}_i \, \mathrm{d}S = 0 \end{aligned}$$

which means, that there is no reflected wave and $\rho = 0$.

Suppose our structure has another port, defined at the reference plane $2 - 2'$ and we would like to compute the transmission coefficient between the two ports. Let the second port be attached to the right-hand side of the aperture A_2 at this reference plane (Fig. 6.4) and let the incident power wave that excites the port attached to the aperture A_1 (Fig. 6.3) be a_i^1. The transmission coefficient between the two ports can be defined as (see Fig. 6.4)

$$\tau_{21} = \frac{b_i^{2'}}{a_i^1} = \frac{a_i^2}{a_i^1} \tag{6.25}$$

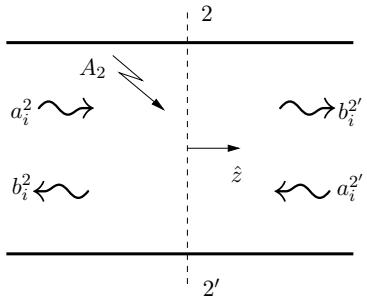

Figure 6.4: Port for which the transmission coefficient is computed.

Taking into account that, by definition, the second port is perfectly matched $a_i^{2'} = b_i^2 = 0$ and following the same procedure as in equations (6.17–6.23), for the transmission coefficient one obtains

$$\tau_{21} = -\frac{1}{a_i^1}\frac{1}{\sqrt{Z_i}}\sum_k \alpha_{\mathrm{H}k}\int_{S_k} \mathbf{f}_{\mathrm{H}k}\cdot\mathbf{h}_i\,\mathrm{d}S \tag{6.26}$$

for all indices k for which $S_k \subset A_2$.

The developments presented in this section are valid for a two port waveguide structure, but they can be easily extended to a structure with several ports.

6.5 Preliminary Numerical Results and Experimental Verifications

Before proceeding further towards the theory for the efficient solution of the thick irises, the above formulation has been carefully tried on several classical benchmark problems. In the following sections, the results of the numerical solutions using the presented theory are compared to theoretical predictions, simulations obtained using other numerical solvers, and with measurements.

6.5.1 Rectangular Waveguide Filled with Two Semi-Infinite Dielectrics

A rather simple example presented here is an infinitely long rectangular waveguide with dimensions $a = 22.86$ mm and $b = 10.16$ mm. The waveguide is oriented in the z-direction and filled with two semi-infinite dielectrics. The dielectric permittivity of the layer below $z = 0$ plane is $\varepsilon_{r1} = 1$ and the permittivity of the layer above $z = 0$ is $\varepsilon_{r2} = 80(1 - \mathrm{j}0.125)$.

The characteristic impedance of the mode TE_{10} is given by

$$Z_{\mathrm{c}} = \frac{\mathrm{j}\omega\mu_0\mu_r}{k_z} \tag{6.27}$$

where $k_z = \sqrt{k_0^2\varepsilon_r\mu_r - \left(\frac{\pi}{a}\right)^2}$ is the propagation constant of the mode.

The reflection coefficient of the mode TE_{10} at the interface $z = 0$ between the two dielectrics can be written as

$$\rho = \frac{Z_{c2} - Z_{c1}}{Z_{c2} + Z_{c1}} = \frac{k_{z1} - k_{z2}}{k_{z1} + k_{z2}} \tag{6.28}$$

In Figures 6.5 and 6.6, the reflection coefficient obtained using the solver is compared to the theoretical values obtained from (6.28), for frequencies bigger than the cut-off frequency of the dominant mode. The excellent agreement with theoretical predictions can be observed.

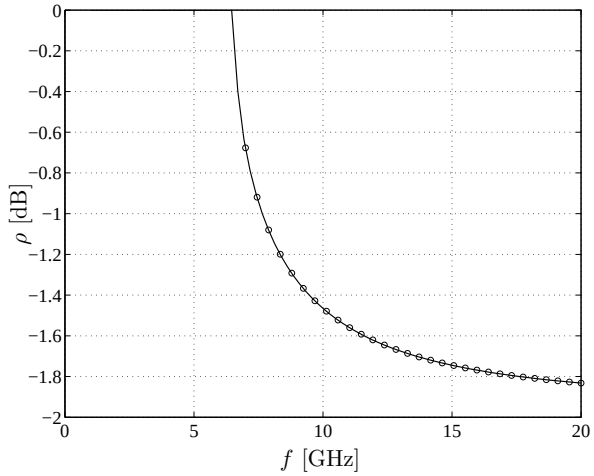

Figure 6.5: Simulated reflection coefficient (solid line) compared to the theoretical results (∘).

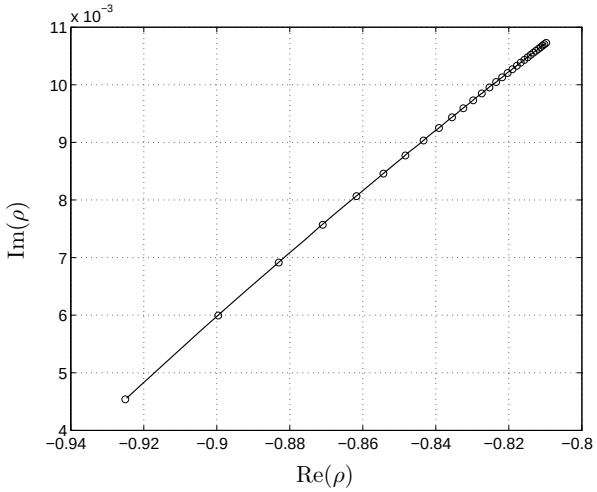

Figure 6.6: Simulated reflection coefficient (solid line) compared to the theoretical results (∘).

6.5.2 Capacitive and Inductive Irises

The following two test cases have been investigated in this section: a capacitive and an inductive iris shown in Fig. 6.7(a) and Fig. 6.8(a). The structures have been simulated using another program developed in our laboratory: `FEST3.0` [23, 24]. The results obtained using presented approach and shown in Fig. 6.7(b) and Fig. 6.8(b) are in excellent agreement with the values obtained from `FEST3.0`.

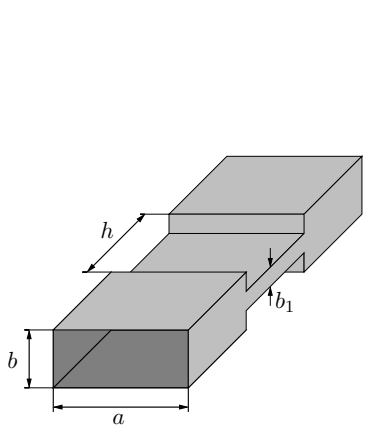

(a) The geometry.

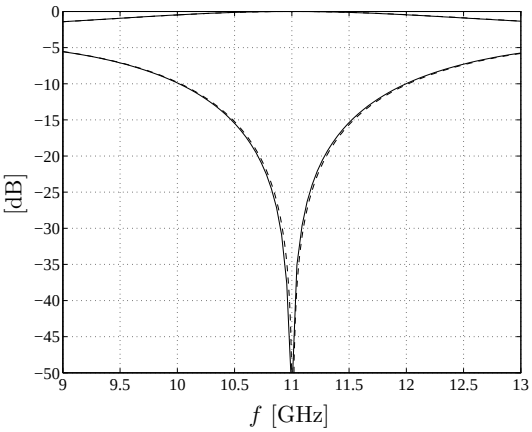

(b) Reflection and transmission coefficients.

Figure 6.7: Capacitive iris. Dimensions are in mm: $a = 22.86$, $b = 10.16$, $b_1 = 5.08$, $h = 15.2$. The results from the presented approach (solid lines) compared to results obtained from `FEST3.0` (dashed lines).

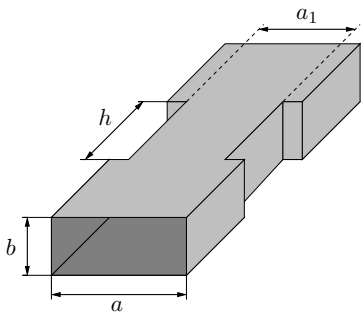

(a) The geometry.

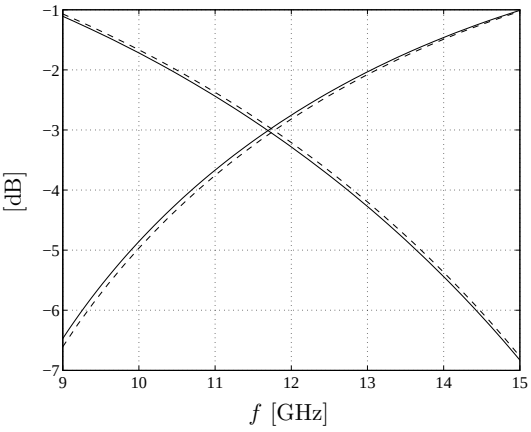

(b) Reflection (decreasing function) and transmission (increasing function) coefficients.

Figure 6.8: Inductive Iris. Dimensions are in mm: $a = 22.86$, $b = 10.16$, $a_1 = 11.43$, $h = 2$. The results from the presented approach (solid lines) compared to results obtained from `FEST3.0` (dashed lines).

6.5.3 Open-Ended Rectangular Waveguide

Reflection from an open-ended waveguide (Fig. 6.9) is a non-destructive technique used in measurement of material properties [25]. Several medical applications of microwave energy that use a rectangular waveguide placed against the surface of the body have been developed in order to heat the tissue (hyperthermia), measure the tissue temperature (thermography) or detect breast cancer (see [26] and the references therein).

The theory presented in this chapter and Chapter 2 is suitable for the efficient solution of the reflection from an open-ended rectangular waveguide terminated either by an infinite dielectric material or by a layered dielectric medium. Using the equivalence principle and magnetic currents, the problem is decoupled into two equivalent problems. One is inside the waveguide region and the other is in the laterally unbounded multilayered medium. The MoM coefficients that correspond to the magnetic currents at the interface are computed independently in the two equivalent problems, using the corresponding Green's functions, and then summed up in the global MoM matrix (Fig. 6.10).

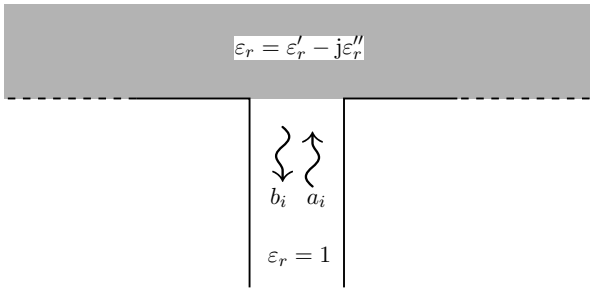

Figure 6.9: Open-ended waveguide.

Consider a rectangular waveguide WR90 (with dimensions $a = 22.86$ mm, $b = 10.16$ mm) open-ended on one side (Fig. 6.9). Suppose that the open-ended side is emerged in a dielectric medium of a complex permittivity $\varepsilon_r = \varepsilon_r' - \mathrm{j}\varepsilon_r''$.

This structure has been simulated at frequency $f = 10$ GHz for different values of the complex permittivity. The results of the reflection coefficients are shown in Fig. 6.11. The shaded rectangle in the lower left corner designates the area in the Smith's chart covered by the possible values of the reflection coefficient. Using these curves and the value of the measured reflection coefficient, it is easy to deduce the complex permittivity of the medium under test (inverse problem).

The numerical results for the homogeneous case have been verified against experimental values for the open waveguide radiating into air. Simulated results are compared with the measured ones [25] in Figs. 6.12 and 6.13, showing very good agreement with measurements.

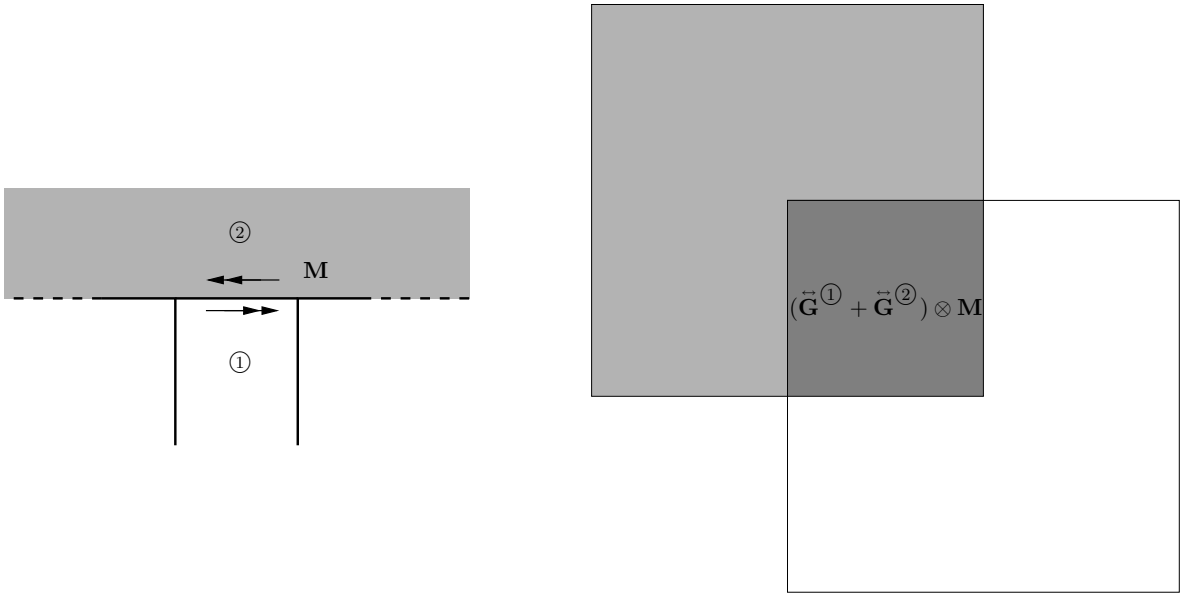

Figure 6.10: Combination of the MoM submatrices corresponding to the shielded ① and laterally unbounded ② regions.

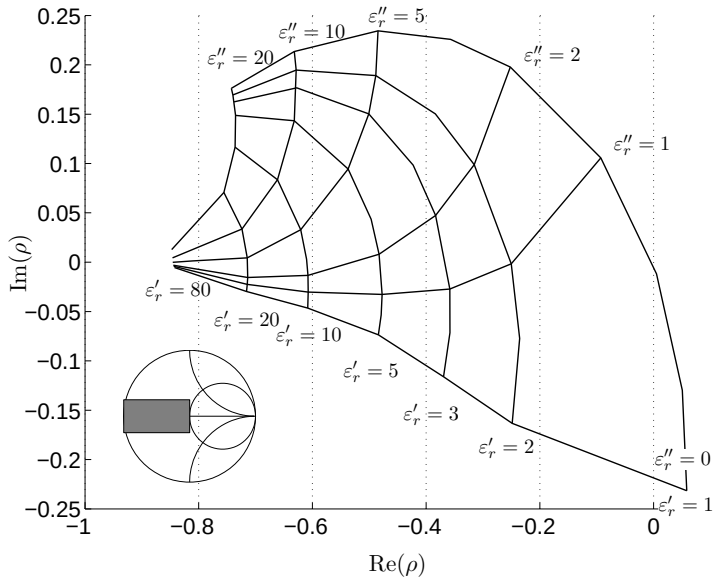

Figure 6.11: The reflection coefficient from the open-ended rectangular waveguide ($a = 22.86$ mm, $b = 10.16$mm) at $f = 10$ GHz for different values of the complex permittivity $\varepsilon_r = \varepsilon_r' - \mathrm{j}\varepsilon_r''$.

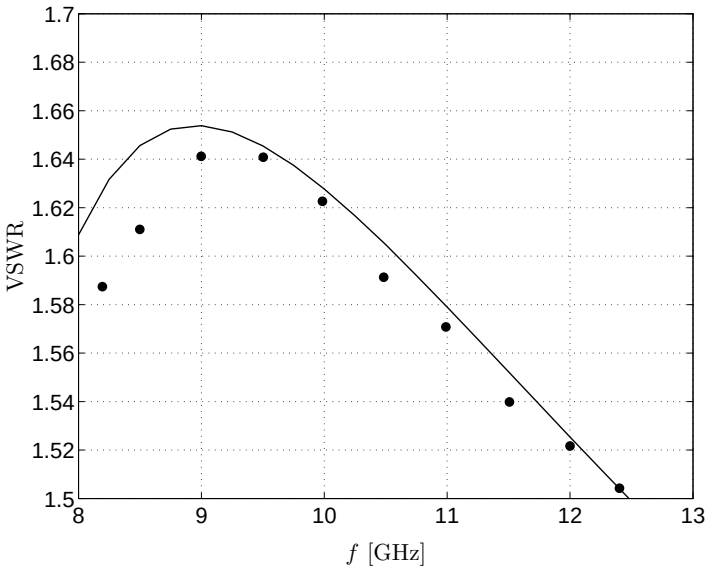

Figure 6.12: VSWR: comparison of simulated results (solid line) with the measured values (•) [25] for radiation in the air.

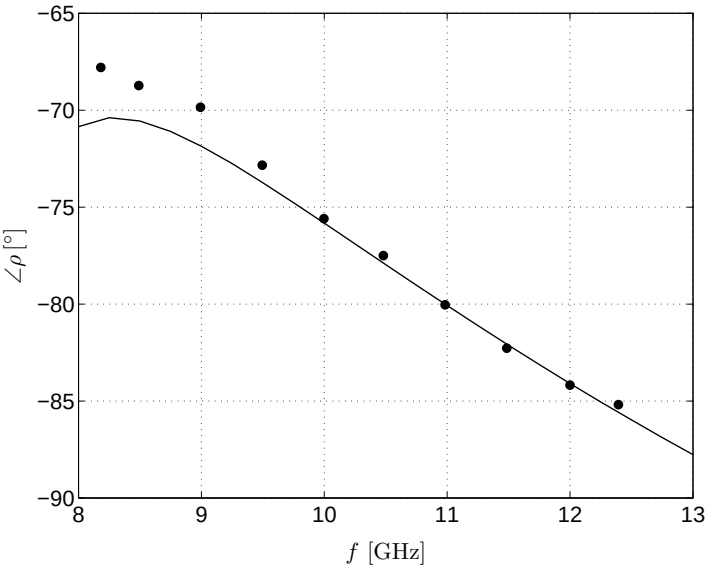

Figure 6.13: Phase of the reflection coefficient: simulated results (solid line) and measured values (•) [25].

6.5.4 Single Lattice of Printed Elements Inside the Rectangular Waveguide

In this section we present results of the scattering from the single lattice of printed elements inside the rectangular *Ka*-band waveguide. The geometry of the problem is presented in Fig. 6.14 and consists of a metallization embedded within the host dielectric layer. The reflection coefficient of the dominant TE_{10} mode obtained using our model agrees very well with the measured results taken from [27].

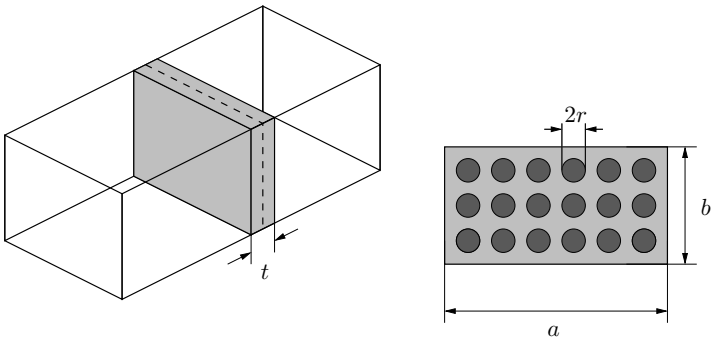

Figure 6.14: Rectangular waveguide in *Ka*-band with one printed PBG layer. Dielectric parameters of the host layer: $\varepsilon_r = 11.1$, $\tan\delta = 0.0028$. All dimensions in mm: $a = 7.112$, $b = 3.556$, $t = 2.68$, $r = 0.34a$ [27].

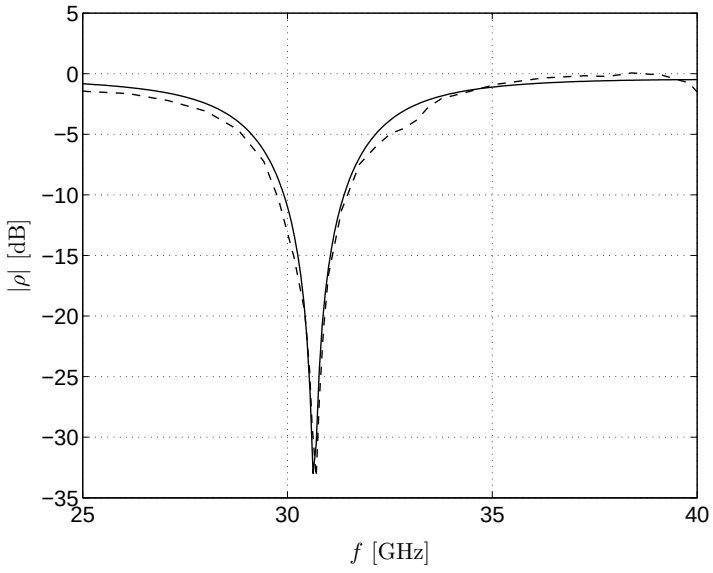

Figure 6.15: Reflection coefficient. Solid line: full-wave approach, dashed line: measurements taken from [27].

6.5.5 Assessment of the IE Model for Waveguides

The four different structures analyzed in this section show clearly the interest of an IE model for waveguides. The algorithm is flexible and general and can be applied not only to traditional discontinuities (waveguide steps and irises) but also to hybrid problems (open radiating waveguides) and to complex structures like geometry of Section 6.5.4. In all cases the accuracy of the IE model is good. But there is more. The IE model is by its own nature perfectly suited to include our thick slot formulation, also based on an IE approach. This will be shown conclusively in the next sections of this chapter.

6.6 Efficient Numerical Treatment of Thick Irises

An iris of a finite thickness inside the rectangular waveguide can be solved, using the theory presented in the previous sections, as a cavity region with magnetic currents on its both interfaces. This problem is equivalent to the problem of apertures of a finite thickness in the printed multilayered antennas. The theoretical development and its experimental validation in Chapters 4 and 5 showed that the apertures of finite thicknesses can be treated as infinitely thin (Fig. 6.1). The aperture thickness appears only as a modification in the Green's functions of the problem, but otherwise the aperture is treated as a two-dimensional object. This technique reduces two times the number of unknowns on the aperture and, depending on how the correction term is computed, allows to treat the apertures of arbitrary cross-sections. As shown in Chapter 4, the approximate treatment of thick apertures led to a perturbation term in the existing integral equation kernel. The integral equations remain the same, save for the correction factor that is added to the Green's functions at the aperture interface [see (4.67) on page 102]

$$\overleftrightarrow{\mathbf{G}}_{\mathrm{HM}} = \overleftrightarrow{\mathbf{G}}^{+}_{\mathrm{HM}} + \overleftrightarrow{\mathbf{G}}^{-}_{\mathrm{HM}} + 2\overleftrightarrow{\mathbf{G}}^{\Delta}_{\mathrm{HM}} \tag{6.29}$$

where the superscripts + and − designate the region above and below the thick aperture.

The possibility of not being forced to consider the volume defining the thick aperture/iris as a new waveguide region is the keystone of the efficient procedure presented in this chapter. However, to implement a particular computational algorithm, we shall need a fast and accurate way of evaluation of the GF correction term $\overleftrightarrow{\mathbf{G}}^{\Delta}_{\mathrm{HM}}$.

The correction term that accounts for a thick iris is given by [see (5.2b) on page 115]

$$\overleftrightarrow{\mathbf{G}}^{\Delta}_{\mathrm{HM}} = \overleftrightarrow{\mathbf{G}}^{=}_{\mathrm{HM}} - \overleftrightarrow{\mathbf{G}}^{\times}_{\mathrm{HM}} \tag{6.30}$$

where $\overleftrightarrow{\mathbf{G}}^{=}_{\mathrm{HM}}$ is the Green's function of the thick iris region when both source and observer points are on the same iris interface, and $\overleftrightarrow{\mathbf{G}}^{\times}_{\mathrm{HM}}$ the same Green's function when they are on the opposite iris interfaces.

One approach in efficient computing of the correction term is to neglect the iris' walls and use a parallel plate Green's function when computing the correction factor. We will designate this strategy as the "PP" approach. A second one, more accurate is to use the Green's functions of the rectangular waveguide. This will be called the "RW" approach. The "RW" approach will give the exact correction factor for the irises of rectangular cross-sections.

In the "PP" approach, the thick iris correction term is computed in the way presented in Chapters 4 and 5. This approximation will remain valid for all shapes of the thick irises as long as the iris' thickness is sufficiently small compared to its minimal lateral dimensions [28].

The correction terms for potential Green's functions are obtained applying the zero order inverse Sommerfeld transformation to the parallel plate spectral domain Green's function [29, 30]

$$G^{\Delta}_{\mathrm{F}xx} = G^{\Delta}_{\mathrm{F}yy} = \frac{\varepsilon}{2\pi}\mathcal{S}_0\left[\frac{1}{k_z}\tan\frac{k_z t}{2}\right] \tag{6.31a}$$

$$G^{\Delta}_{W} = \frac{1}{2\pi\mu}\mathcal{S}_0\left[\frac{1}{k_z}\tan\frac{k_z t}{2}\right] \tag{6.31b}$$

where t is the thickness of the considered iris and k_z is the propagation constant inside the iris in the z direction. The difference as compared to the approach presented in Chapters 4 and 5 is in the fact that the correction terms are not added on the level of the spectral domain Green's functions, but on the MoM coefficient level. The MoM coefficients of the iris are computed as if it were infinitely thin using the theory presented in the previous sections. Then, the correction terms in the MoM coefficients are computed using the mixed potential integral equation (MPIE) and the potential Green's functions (6.31), and added to the already computed MoM coefficients.

In the "RW" approach, the Green's function correction term for the field Green's functions is expressed as a sum of modes (rectangular waveguide modes), obtaining this way a consistent FIE approach that uses always (for closed regions) the modal field Green's functions. In this approach, the correction term will necessarily depend on the thick iris cross section.

If we consider a rectangular iris, the Green's function can be written as

$$\overleftrightarrow{\mathbf{G}}_{\mathrm{HM}} = \sum_i \widetilde{G}_{\mathrm{H}i}(z,z')\mathbf{h}_i(x,y)\mathbf{h}_i(x',y') \tag{6.32}$$

where $\widetilde{G}_{\mathrm{H}i}(z,z')$ is the current evaluated at the coordinate z along the equivalent transmission line network, when the exciting generator is set to one and placed at the coordinate z' in the direction of propagation, and $\mathbf{h}_i$ is the vector mode of magnetic type for waveguides with rectangular cross-sections.

Taking into account (6.30) and (6.32), the Green's function correction term can be expressed as

$$\overleftrightarrow{\mathbf{G}}^{\Delta}_{\mathrm{HM}} = \sum_i \widetilde{G}^{\Delta}_{\mathrm{H}i}\mathbf{h}_i(x,y)\mathbf{h}_i(x',y') \tag{6.33}$$

where

$$\widetilde{G}^{\Delta}_{\mathrm{H}i} = \frac{\mathrm{j}}{Z_{\mathrm{c}_i}}\tan\left(\frac{k_{z_i}t}{2}\right). \tag{6.34}$$

6.7 Numerical Results For Thick Iris Problems

6.7.1 Comparison with Rigorous Full Wave Approach

The first test-structure simulated is a simple rectangular waveguide WR90 with a thin rectangular iris of dimensions $a_1 = a/2$ and $b_1 = b/2$ placed at the center of the waveguide's cross-section (Fig. 6.16).

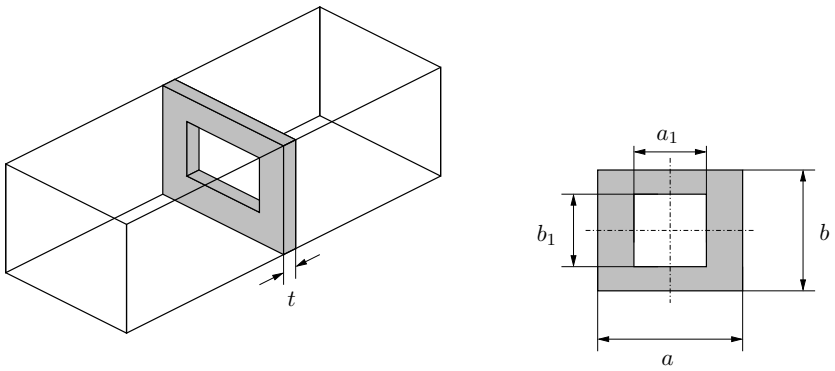

Figure 6.16: Thin iris. $a = 22.86$, $b = 10.16$, $a_1 = 11.43$, $b_1 = 5.08$. All dimensions given in mm. t is variable iris thickness.

The simulations were carried out for different iris thicknesses ($t = 0.01$, 0.05, 0.1, 0.5, and 1.0 mm). In Fig. 6.17, the reflection and transmission coefficients are shown simulated using the "PP" approach (○), the "RW" approach (+), the full-wave cavity approach (■), and supposing that the iris is infinitely thin (dashed line). In the full-wave approach, the simulations were done with 5000 modes used in computation of the quasi-static terms (frequency independent) and 1000 modes for computation of dynamic terms (frequency dependent). In the "RW" approximate approach, the correction factor was computed taking into account the dimensions of the rectangular iris cross-section. The quasi-static term was not extracted. Number of modes used for computing dynamic terms was 1000. The results reached the numerical convergence since we obtain the same response when the number of modes is doubled and even three times bigger. The almost perfect matching of the "PP" and "RW" approaches with the full-wave cavity approach taken as a reference, can be observed up to iris thicknesses of $t = 0.1$ mm $= \lambda/200$ at the center frequency $f = 15$ GHz. Above this thickness, the approximate models predict the scattering parameters less accurately but still better than the zero thickness approach (dashed lines in Fig. 6.17). As the thickness grows, the "RW" approach is shown to be more precise in predicting the scattering parameters than the "PP" approach, which is especially true for the transmission coefficient, where the ideal transmission (of 0 dB) is never reached [see the line with circles in Fig. 6.17(c)].

Fig. 6.18 shows the CPU time versus the number of unknowns for the problem from Fig. 6.16 solved using the full-wave approach (○), the "PP" approach (•), and the "RW" approach (×) on a PC with 2.4 GHz and 512 MB of RAM. The program is implemented in Compaq Visual Fortran, operating system Windows XP. As it can be seen from the figure, the problem solved using the approximate approaches with the same mesh density as in the full-wave cavity

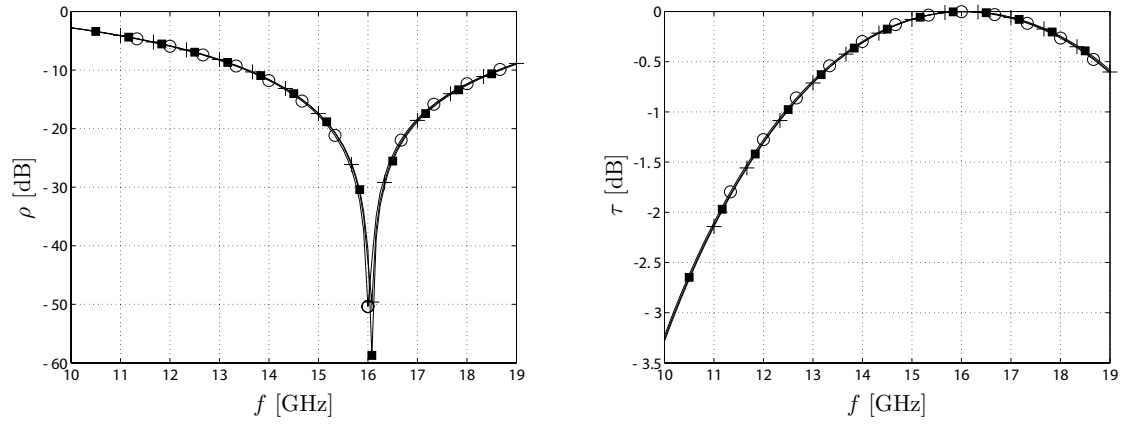

(a)

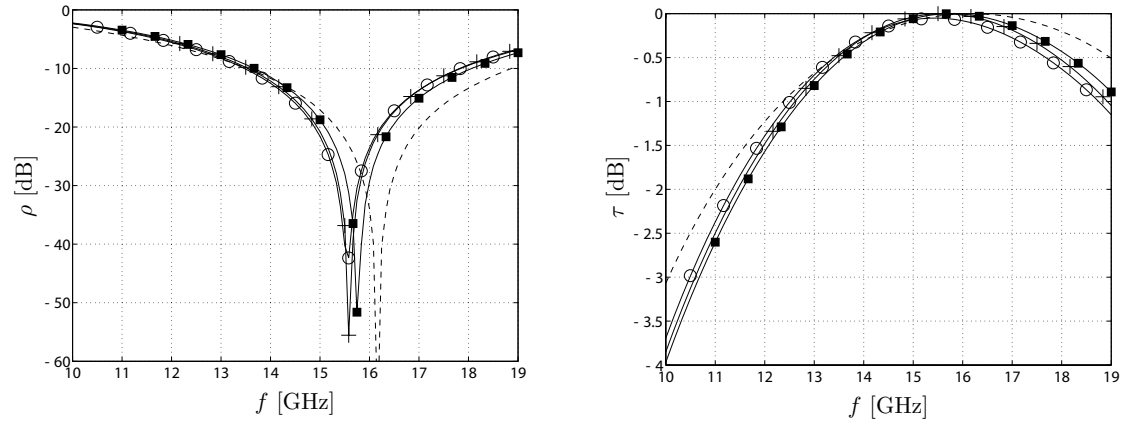

(b)

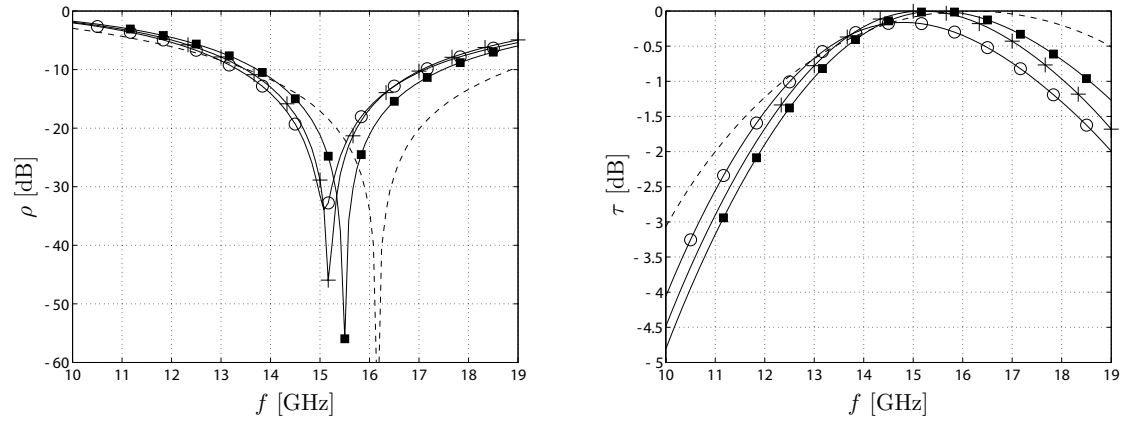

(c)

Figure 6.17: Reflection and transmission coefficients for different iris thicknesses: (a) $t = 0.1$ mm $= \lambda/200$, (b) $t = 0.5$ mm $= \lambda/40$, and (c) $t = 1$ mm $= \lambda/20$. "PP" (○), "RW" (+), full-wave cavity approach (■), and zero thickness iris (dashed line).

problem will have half the number of unknowns (the thick iris is accounted for as an infinitely thin iris with the correction factor in the Green's function) and the corresponding CPU time will be significantly smaller. Note that in Fig. 6.18, the number of unknowns N corresponds to the number of unknowns in the full-wave approach.

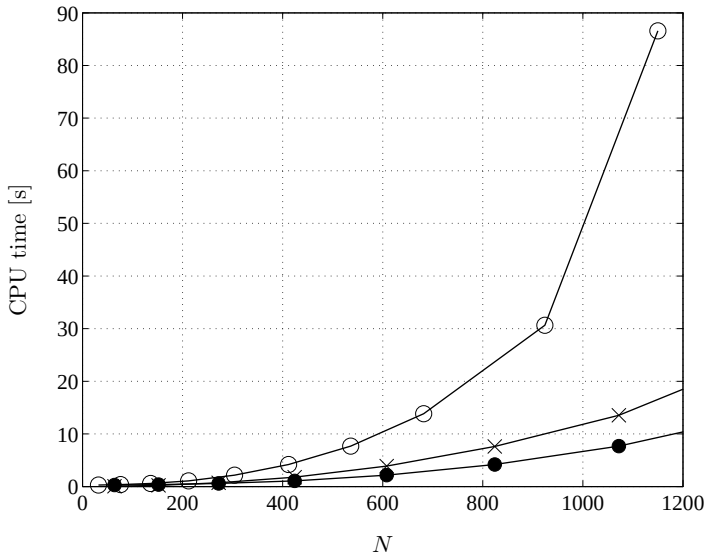

Figure 6.18: The CPU time versus number of unknowns for a problem from Fig. 6.16 solved using the full-wave cavity approach (○), the "PP" (●) and the "RW" approach (×) with the same mesh density.

6.7.2 Circular Iris Coupled Filter: Comparison with Measurements

The method has been verified by simulating a circular iris coupled resonator filter shown in Fig. 6.19. For this problem, the "PP" approach did not provide accurate enough results and the GF correction factor, calculated using the "RW" approach, has been prefered. For the correction factors, rectangular waveguides of the cross-sections that circumscribe the cross-sections of the circular irises are used. As can be seen from Fig. 6.20, the results of the insertion loss simulated using our approach are in excellent agreement with the measured values taken from [13], which demonstrates the precision of our technique.

The irises in this practical example are rather thin, being a hundredth of the operating wavelength. However, neglecting this thickness when simulating the structure would lead to erroneous results (dashed line in the same figure).

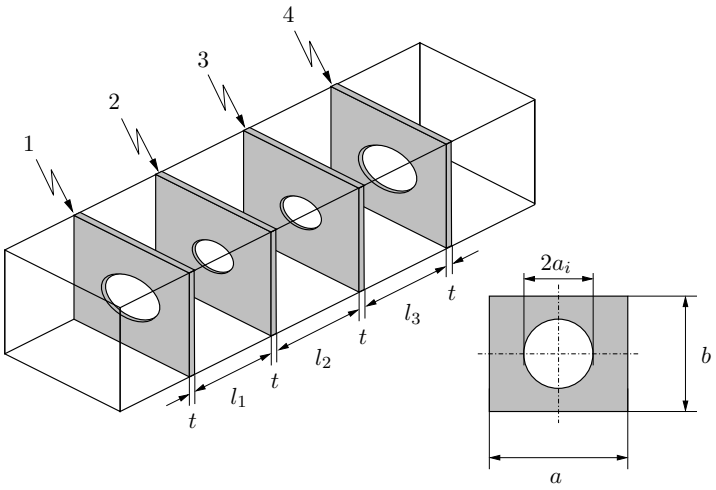

Figure 6.19: Circular iris coupled rectangular waveguide three-resonator filter [13]. Filter dimensions are in mm: $a = 15.8$, $b = 7.9$, $t = 0.218$, $a_1 = 2.577$, $a_2 = 1.142$, $a_3 = 1.125$, $a_4 = 2.592$, $l_1 = 12.499$, $l_2 = 12.819$, $l_3 = 12.461$.

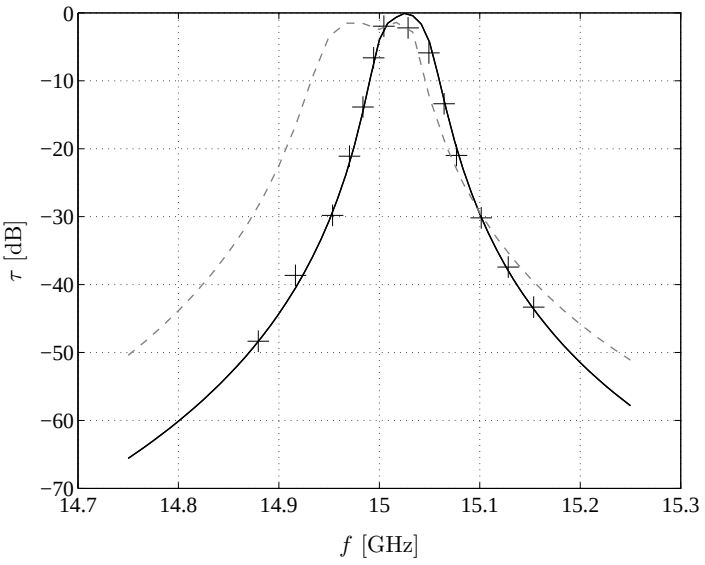

Figure 6.20: The insertion loss of the iris coupled resonant filter: simulation using the "RW" approach (solid line) and measured values (+) taken from [13]. The dashed line represents the simulation with infinitely thin irises.

6.7.3 Thick Resonating Iris: Comparison with Mode Matching

Finally, a structure consisting of two identical thick irises separated by a distance l (Fig. 6.21) has been analyzed. The iris thickness of approximately $\lambda/10$ in the operating frequency band is out of the reach of simplified formulation (PP/RW) so we use here the full-wave approach. The results are compared to the results that can be found in [31], obtained using the Mode Matching technique. Good agreement between the two methods is observed for both reflection and transmission coefficients (Fig. 6.22).

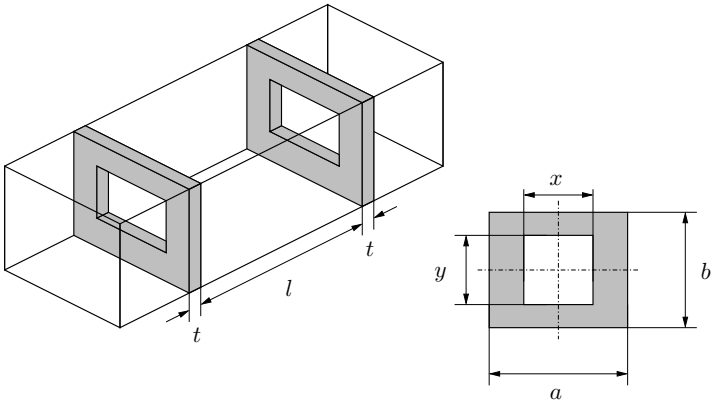

Figure 6.21: Structure consisting of two identical thick irises in rectangular waveguide WR90. $a = 22.86$, $b = 10.16$, $x = 14.79$, $y = 10.16$, $t = 2.67$, $l = 5.37884$. All dimensions given in mm [31].

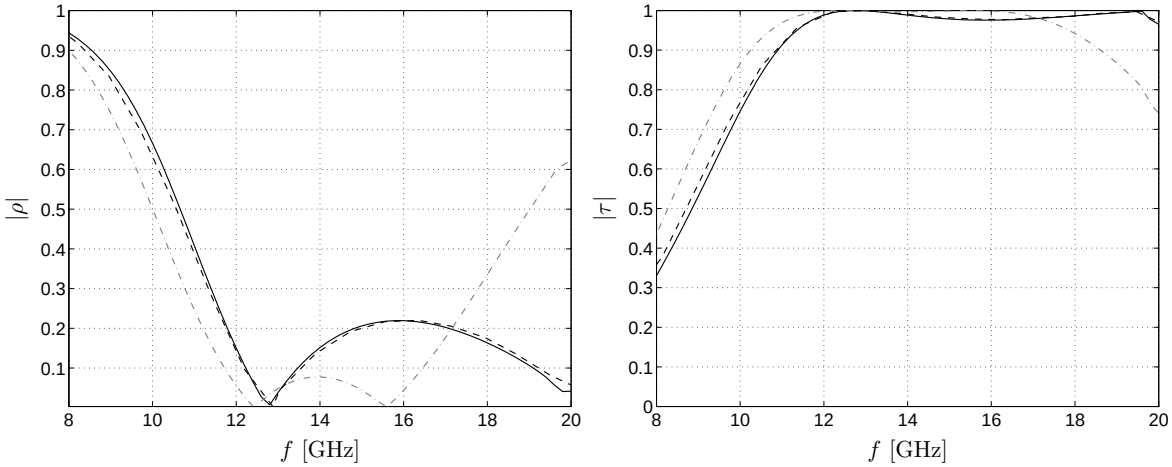

(a) Reflection coefficient for the TE_{10} mode. **(b)** Transmission coefficient for the TE_{10} mode.

Figure 6.22: Solid lines – our full-wave solver, dashed lines – the Mode Matching technique [31], and dash-dotted lines – the "RW" approximate method.

6.8 Conclusion

In this chapter, we have presented and IE-MoM technique for solving rectangular waveguide discontinuities including thick irises. Waveguide discontinuities here are considered in wider sense being not only irises and interconnections of waveguides with different cross-sections, but also dielectric layers of different dielectric properties and metallic patches and slots embedded inside dielectrics.

The theory for solving this kind of structures is presented in the first part of this chapter. It is based on the work presented by Eleftheriades *et al.* [20] and Álvarez-Melcón [21]. The possibility of having waveguides of different rectangular cross-sections and the modal excitation are the new features as compared to the cited publications.

The theory has been implemented in a Compaq Visual Fortran program and it has been verified using a set of benchmarks, ranging from the simple structure of a rectangular waveguide filled with two semi-infinite dielectrics, where the results are found to be in excellent agreement with the theory, through capacitive and inductive irises, where the results are compared to `FEST3.0` numerical solver [24], to the case of an open-ended rectangular waveguide and a single lattice of metallic patches printed on dielectric slabs, where the results are in good agreement with the measured values found in [25, 27]. The above results would suffice to justify the pertinence and interest of our developments.

The problem of irises of finite thickness is treated in the second part of this chapter. It is obvious that above a certain thickness, only a rigorous model treating the irises themselves as cavities can provide accurate results. But for moderate thicknesses, reasonable accuracy can be obtained by combining the approximate model for finite thickness apertures introduced in Chapter 4 with a classical integral formulation of waveguide discontinuities. Then, the proposed technique reduces by a factor of two the number of unknowns in every iris and thus includes the effect of irises' thickness with no increase in the computational complexity associated to zero-thickness irises. The key point of the approach is to include the thickness as an analytical correction in the Green's function that must be used when solving irises with the equivalence principle. Two practical formulations of this correction factor have been discussed and implemented with excellent results. The roughest and simplest one (called PP, parallel plate) can be applied to irises of any shape, but they must be large and not very thick, because the coupling phenomena corresponding to the irises' lateral walls are neglected. If this assumption cannot be made, an alternative way of computing the Green's function correction (RW, rectangular waveguide) is proposed, valid for shapes where the waveguide modes have an analytical expression. This second alternative represents only a slight overhead in computer time and hence it is always preferable to the zero thickness approach. Moreover, our approach remains accurate when compared with a full wave approach up to thicknesses of the order of several hundredths of wavelength. For these thicknesses, frequently encountered in current technologies, the zero-thickness model does not provide the accuracy requested in many modern applications.

References

[1] N. Marcuvitz, *Waveguide Handbook*. New York: McGraw-Hill, 1951.

[2] L. Lewin, *Advanced Theory of Waveguides*. London: Iliffe, 1951.

[3] R. E. Collin, *Field Theory of Guided Waves*. New York: McGraw-Hill, 1960.

[4] G. Matthaei, L. Young, and E. M. T. Jones, *Microwave Filters, Impedance-Matching Networks, and Coupling Structures*. New York: McGraw-Hill, 1964.

[5] R. J. Luebbers and B. A. Munk, "Analysis of thick rectangular waveguide windows with finite conductivity," *IEEE Trans. Microwave Theory Tech.*, vol. MTT-21, no. 7, pp. 461–468, July 1973.

[6] R. Levy, "Improved single and multiaperture waveguide coupling theory, including explanation of mutual interactions," *IEEE Trans. Microwave Theory Tech.*, vol. MTT-28, no. 4, pp. 331–338, Apr. 1980.

[7] A. Jennings and R. L. Gray, "Extension of Levy's large-aperture design formulas to the design of circular irises in coupled-resonator waveguide filters," *IEEE Trans. Microwave Theory Tech.*, vol. MTT-23, no. 11, pp. 1489–1493, Nov. 1984.

[8] P. J. B. Clarricoats and K. R. Slinn, "Numerical soution of waveguide-discontinuities," *IEE Proc-H*, vol. 114, no. 7, pp. 878–886, July 1967.

[9] A. Wexler, "Solution of waveguide discontinuities by modal analysis," *IEEE Trans. Microwave Theory Tech.*, vol. MTT-15, no. 9, pp. 508–517, Sept. 1967.

[10] H. Patzelt and F. Arndt, "Double-plane steps in rectangular waveguide and their application for transformers, irises and filters," *IEEE Trans. Microwave Theory Tech.*, vol. MTT-29, no. 5, pp. 771–777, May 1982.

[11] M. S. Navarro, T. E. Rozzi, and Y. Z. Lo, "Propagation in a rectangular waveguide periodically loaded with resonant irises," *IEEE Trans. Microwave Theory Tech.*, vol. MTT-28, no. 8, pp. 857–865, Aug. 1980.

[12] F. Arndt, J. Bornemann, D. Heckmann, C. Piontek, H. Semmerow, and H. Schueler, "Modal-s-matrix method for the optimum design of inductively direct-coupled cavity filters," *IEE Proc-H*, vol. 133, no. 5, pp. 341–350, 1986.

[13] U. Papziner and F. Arndt, "Field theoretical computer-aided design of rectangular and circular iris coupled rectangular of circular waveguide cavity filters," *IEEE Trans. Microwave Theory Tech.*, vol. 41, no. 3, pp. 462–470, Mar. 1993.

[14] M. Guglielmi, G. Gheri, M. Calamia, and G. Pelosi, "Rigorous multimode network representation of inductive steps," *IEEE Trans. Microwave Theory Tech.*, vol. 42, no. 2, pp. 317–326, Feb. 1994.

[15] L. Valor and J. Zapata, "Efficient finite element analysis of waveguides with lossy inhomogeneous anizotropic materials characterized by arbitrary permittivity and permeability tensors," *IEEE Trans. Microwave Theory Tech.*, vol. 43, no. 10, pp. 2452–2459, Oct. 1995.

[16] J. Rubio, J. Arroyo, and J. Zapata, "SFELP – An efficient methodology for microwave circuit analysis," *IEEE Trans. Microwave Theory Tech.*, vol. 49, no. 3, pp. 509–516, Mar. 2001.

[17] R. Beyer and F. Arndt, "Efficient modal analysis of waveguide filters including the orthogonal mode coupling elements by an MM/FE method," *IEEE Microwave Guided Wave Lett.*, vol. 5, no. 1, pp. 9–11, Jan. 1995.

[18] F. Arndt, J. Brandt, V. Catina, J. Ritter, I. Rullhusen, J. Dauelsberg, U. Hilgefort, and W. Wessel, "Fast CAD and optimization of waveguide components and aperture antennas by hybrid

MM/FE/MoM/FD methods – State-of-the-Art and recent advances," *IEEE Trans. Microwave Theory Tech.*, vol. 52, no. 1, pp. 292–305, Jan. 2004.

[19] H. Auda and R. F. Harrington, "A moment solution for waveguide junction problems," *IEEE Trans. Microwave Theory Tech.*, vol. MTT-31, no. 7, pp. 515–520, July 1983.

[20] G. V. Eleftheriades, J. R. Mosig, and M. Guglielmi, "A fast integral equation technique for shielded planar circuits defined on nonuniform meshes," *IEEE Trans. Microwave Theory Tech.*, vol. 44, no. 12, pp. 2293–2296, Dec. 1996.

[21] A. Álvarez-Melcón, "Application of the integral equation technique to the analysis and synthesis of multilayered printed shielded microwave circuits and cavity backed antennas," Ph.D. dissertation, Ecole Polytechnique Fédérale de Lausanne, Switzerland, 1998, Thèse No. 1901.

[22] J. V. Bladel, *Electromagnetic Fields*. New York: McGraw-Hill, 1964.

[23] M. Mattes, "Contribution to the electromagnetic modelling and simulation of waveguide networks using integral equations and adaptive sampling," Ph.D. dissertation, Ecole Polytechnique Fédérale de Lausanne, Switzerland, 2003, Thèse No. 2693.

[24] M. Mattes and J. R. Mosig, "Integrated cad tool for waveguide components," Final Report, Dec. 2001, ESTEC No. 12465/97/NL/NB.

[25] V. Teodoridis, T. Sphicopoulos, and F. E. Gardiol, "The reflection from an open-ended rectangular waveguide terminated by a layered dielectric medium," *IEEE Trans. Microwave Theory Tech.*, vol. 33, no. 5, pp. 359–366, May 1985.

[26] E. Cheever, J. B. Leonard, and K. R. Foster, "Depth of penetration of fields from rectangular apertures into lossy media," *IEEE Trans. Microwave Theory Tech.*, vol. MTT-35, no. 9, pp. 865–867, Sept. 1987.

[27] C. A. Kyriazidou, H. F. Contopanagos, and N. G. Alexópoulos, "Monolithic waveguide filters using printed photonic-bandgap materials," *IEEE Trans. Microwave Theory Tech.*, vol. 49, no. 2, pp. 297–307, Feb. 2001.

[28] J. R. Mosig, "Scattering by arbitrarily-shaped slots in thick conducting screens: an approximate solution," *IEEE Trans. Antennas Propagat.*, vol. 52, no. 8, pp. 2109–2117, Aug. 2004.

[29] ——, "Integral-equation technique," in *Numerical Techniques for Microwave and Millimeter-Wave Passive Structures*, T. Itoh, Ed. New York, USA: Wiley, 1989, ch. 3, pp. 133–213.

[30] I. Stevanović and J. R. Mosig, "Efficient electromagnetic analysis of line-fed aperture antennas in thick conducting screens," *IEEE Trans. Antennas Propagat.*, vol. 52, no. 11, pp. 2896–2903, Nov. 2004.

[31] J. M. Torre and J. M. Rebollar, "Multimode TLM characterization of 2-dimensional geometries," in *IEEE AP-Symposium Digest*, vol. 4, July 13–18, 1997, pp. 290–294.

7 Conclusions and Future Work

7.1 Thesis assessment

A commonly used numerical procedure for solving Maxwell's equations in planar microwave and millimeter wave structures is the Integral Equation in combination with the Method of Moments (IE-MoM). Although electromagnetic simulation based on Maxwell's equations is rigorous, any practical implementation requires some approximations either in the description of the structure and surrounding environment, or in terms of boundary conditions. IE-MoM simulators assume an infinite lateral extent of the dielectric layers and ground planes or a boundary often with rectangular electric walls, for boxed multilayered structures. These assumptions allow the efficient construction and evaluation of the associated Green's functions as shown in Chapter 2. At the same time, the thickness of metallic patches and ground planes is neglected. However, in many configurations such as cavity backed antennas, irises in waveguide filters, aperture-fed patches, and thick coplanar lines, the conducting screen thickness has to be accounted for, because of the technology (self-supporting metallic plates rather than printed sheets), the frequency (mm- and sub mm-waves) or both. The drive to analyze more complex environments yields the much more involved Green's functions, for which the older numerical tricks and recipes do not apply anymore and any speed-up in the calculation of Green's functions and of their convolutions is of paramount relevance.

A fine mesh density used to discretize large and complex planar geometries to guarantee good solution accuracy, brings, on the other hand, a heavy burden on the CPU in terms of both memory and time. In a problem of N unknowns, the memory allocation increases with $\mathcal{O}(N^2)$ and the simulation time with $\mathcal{O}(N^3)$. The efficient solution methods are needed to accelerate the MoM calculations and allow simulation of large structures using standard desktop computers.

In this thesis, both problems have been addressed. A computationally efficient way of filling the MoM matrix when solving large and complex electromagnetic problems has been dealt with in Chapter 3. An approximate but efficient Green's function computation for multilayered planar structures containing apertures and irises in ground planes with finite thicknesses has been presented in detail in Chapters 4–6.

The Subdomain Multilevel Approach (SMA), is an efficient technique for accelerating the Integral Equation Method of Moments analysis of large complex-shaped printed antennas. The basic idea of the method is to divide the large electromagnetic problem into several subproblems or subdomains, by inserting, where necessary, artificial ports. Each subdomain is simulated separately and current density profiles, called macro-basis functions (MBFs),

obtained. By demanding current continuity at the artificial ports introduced, the current distributions are combined to form a set of basis functions for the global MoM system. The SMA compresses the MoM matrix and reduces significantly the memory occupation. In consequence, the time needed for inverting the MoM matrix becomes comparable and in some cases even smaller than the time needed for filling it. This way, the computational bottleneck is displaced to the filling of the MoM matrix, especially when the interaction between two MBFs is concerned. Chapter 3 presented an efficient way of computing MBF reaction terms. The strategy is based on reducing MBFs to equivalent moments. Each subdomain is further subdivided into smaller subregions, the number of which depends on the size of the subdomain with respect to the operating wavelength, and in each subregion, the equivalent moment is found. The MBF reaction term is then computed as a sum of significantly lower number of equivalent moment-reaction terms bypassing the bottleneck of the standard unrefined SMA. The accuracy of the proposed method has been verified through several examples, in which this technique is compared with a conventional MoM approach, with the unrefined SMA and with measurements. The results showed excellent agreement between all the approaches for both input impedance and radiation patterns with an improvement in computational time that reaches 50 % of the CPU time needed for the unrefined SMA.

In parallel with the efficient solution of large complex-shaped antenna problems this thesis addressed the improvements in the Green's function computation for boxed and laterally unbounded multilayered media including thick apertures and irises.

In Chapter 4, a new approximate method for scattering from apertures on thick screens has been presented. The approximations introduced allow for the thick aperture to be modeled as an infinitely thin one, where the thickness appears only as a modification in the Green's functions of the problem. The correction factor in the Green's functions is computed supposing that the lateral dimensions of the aperture are an order of magnitude larger than its thickness. Under this hypothesis, the aperture's side walls could be neglected and the parallel plate Green's functions in computing the correction term are used. This approach allows to model thick apertures of arbitrary cross-sections and reduces significantly the simulation time needed when a full-wave cavity treatment of the thick apertures is employed. The gain in computational time is more than advantageous and it is due to, on the one hand, the adoption of the parallel plate Green's function for the cavity which accounts for the bulk of the computational savings (as it obviates the time consuming computation of the cavity Green's function). On the other hand, the number of unknowns is twice smaller as we consider the aperture having only one interface.

Chapter 5 showed that the thick aperture model can be, with minor modifications, fully incorporated into the traditional integral equations for slots and patch antennas embedded in stratified media. After having introduced the new complete set of integral equations for a printed-line fed slot antenna, which involves both electric and magnetic currents, Chapter 5 explored some computationally relevant aspects of the approximate thick aperture model and provided further numerical verifications. Various tests with increasing slot thicknesses have been performed and studied. The results have been compared to both a full-wave cavity approach (with the thick aperture modeled as a cavity section) and measurements. This study

showed that the approximate model yields good predictions even for rather thick apertures, as long as the thickness of the aperture remains an order of magnitude smaller than its minimal lateral dimensions. It must be pointed out that the upper limit reached in the current status of the method is already highly satisfactory. Many technologies using self-supporting metallic patches in *Ka*– and *Ku*–bands or thick conducting film in millimeter and submillimeter wave bands yield electrical thicknesses within this limit.

The problem of thick irises inside stratified media waveguides is equivalent to the problem of thick apertures in multilayered circuits and antennas. However, some waveguide structures, as resonator filters, are much more sensitive to tolerances and approximations than it is the case in multilayered media antennas. This calls for more accurate approximations of the correction factor that accounts for the aperture (or iris) thickness. Chapter 6 has discussed and implemented two different approaches in computing the Green's function correction term. The first approach is the same as in Chapters 4 and 5 of this thesis, where the lateral walls of the aperture are neglected and the correction term is computed using the parallel plate Green's function. This approach is designated as the "PP" method. A more accurate method in computing the Green's function correction term, denoted as the "RW" approach, does not neglect the lateral walls of the iris and uses the rectangular cavity Green's functions. Both methods have been compared to the full-wave approach for the case of a thick rectangular iris inside a rectangular waveguide. For very thin irises, both methods agree well with the full-wave approach taken as a reference. However, as the thickness grows, the "RW" approach is shown to be more precise than the "PP" approach. The "RW" approach gives very good results as compared to the measurements in predicting the transmission coefficient of the thin iris coupled resonator filter.

7.2 Perspectives

This thesis has resolved several problems in the efficient simulation of planar multilayered structures that include electrically thick apertures or irises, or that need a large number of unknowns to be accurately simulated. However, there are several possible improvements that can be carried out in addition to the developments presented. These and the new ideas that resulted from the work done in this thesis are discussed in the following paragraphs.

The accurate full-wave analysis of finite periodic structures is important, as they have wide applications in the electromagnetic engineering, ranging from frequency-selective surfaces, photonic or electromagnetic bandgap (PBG or EBG) materials and metamaterials with negative permittivity and permeability. These are all large-scale problems that require both excessive memory and computational time. The Subdomain Multilevel Approach with macro-basis functions is shown to be a successful technique for solving large-scale antenna arrays, and as such, it is a promising candidate for solving other periodic structures. Its implementation is simple since it does not depend on the type of the Green's functions used to characterize the problem and it can be easily extended to shielded structures. This would allow an efficient modeling of PBG filters similar to the example presented in Section 6.5.4. The number of lattices of printed elements in this example can be enlarged to five or more. Although

the number of unknowns can be such as to yield prohibitively large memory occupation and computational time when conventional MoM analysis is applied, the SMA technique would bring the study of the problem under the reach of the standard desktop PCs.

In parallel to the application of the SMA to the periodic structures different from the antenna arrays, some refinements in the definition of macro-basis functions can be investigated. In the current version of the SMA technique presented and used in Chapter 3 of this thesis, the MBFs are computed as solutions of small-sized problems that contain isolated subdomains in which the whole large antenna structure is decomposed. The mutual coupling effects between different subdomains are taken into account through the interactions between different MBFs defined on them. Instead of using isolated solutions to obtain MBFs, some dummy cells that represent the surrounding subdomains to the subdomain on which the MBF is computed, could be introduced. This would allow to accurately capture the mutual coupling effects already in the solution of a small-size problem. The number of dummy cells should be large enough to properly represent the surrounding subdomains and at the same time small enough not to influence the size and computational time needed to solve the small-size problem. The MBFs defined in such a way should increase the accuracy of the SMA technique and allow precise modeling of the mentioned periodic structures.

Thick aperture approximation could be applied to efficiently model the scattering from periodic apertures in thick metallic screens. To this aim, the approximation can be successfully combined with the Ewald transformation that is shown to have a very rapid convergence rate in computing the periodic Green's functions (Section 2.6.5). Applying the thick aperture approximation would significantly decrease the simulation time as compared to the one needed when the aperture is modeled as a waveguide (or cavity) section.

The thickness of the conductive patches and their resistivity are accounted for in most of the present solvers in approximate manners through an equivalent surface impedance. Taking into account the duality that exists between infinitely thin plates and apertures, it would be interesting to investigate the efficient modeling of thick conductive patches, using Green's function correction terms as it was the case with apertures in thick conducting screens. Recognizing, however, that there is no real duality between their thick counterparts, this problem remains far from trivial.

Conductor losses increase as the square root of frequency and additional losses due to surface roughness could also be considerably higher as we move from microwave to millimeter and sub-millimeter bands. An accurate characterization of these losses is a prerequisite in the mm-wave design. Our approximate model of thick apertures does not take into account ground plane losses. An interesting issue would be to investigate this problem and try to find an efficient way of introducing the ground plane losses into the existing model.

List of Figures

List of Tables

CV

Ivica Stevanović was born on April 2, 1976 in Kruševac, Serbia. He received the Dipl. Ing. degree from the School of Electrical Engineering (ETF), University of Belgrade, in September 2000. In February 2002 he enrolled the PhD studies at the Laboratoire d'Electromagnétisme et d'Acoustique (LEMA) of the Ecole Polytechique Fédérale de Lausanne (EPFL).

He was a Student Assistant at the Laboratory of Electronics of ETF (1998-2000) responsible for answering questions and grading reports during lab sessions in classes on Electronics and Pulse and Digital Electronics. During the summer 2000, he worked as an undergraduate research fellow at the Laser Interferometer Gravitational Wave Observatory (LIGO 40m), California Institute of Technology, Pasadena, CA. He was in charge of MATLAB/Simulink modeling and analysis of the LIGO mirror suspensions design, velocity damping and feedback control loops. In November 2000 he joined LEMA, EPFL, where he is currently a Research and Teaching Assistant. As a Research Assistant he has been responsible for several projects.

- Development of computer model to study the effect of intelligent antennas on radio system planning and on mitigation. Swiss Federal Office of Communication Project (2004-present).
- Development of computer model for Deep Brain Stimulation in collaboration with the Centre Hospitalier Universitaire Vaudois (2003-present).
- Development of computer program for analysis of planar multilayered media circuits and antennas. Integration of the software into the ADF-EMS framework with the programs of other partners in the project. European Space Agency Project (2002-2004).
- Research of the fundamentals of various approaches and signal processing techniques, the consequences of introduction as well as the potential of smart antenna and MIMO systems. Swiss Federal Office of Communication Project (2002-2003).
- Development of computer program to analyze wide-band dual-polarization antenna arrays; design, manufacture and measurements of breadboards to validate the model. European Space Agency Project (2000-2002).

As a Teaching Assistant he has led the exercises in classes on Electromagnetics I and II and Antennas and Propagation, graded exams, and proposed and supervised student semester projects.

Ivica Stevanović received a scholarship from the Serbian Ministry of Education (1996-2000) and a research fellowship (SURF) from the California Institute of Technology, Pasadena (summer 2000). He is a student member of the IEEE.

List of Publications

REFEREED JOURNAL PAPERS

1. I. Stevanović, P. Crespo-Valero, and J. R. Mosig, "An integral equation technique for solving thick irises in rectangular waveguides," *IEEE Transactions on Microwave Theory and Techniques*, under review.

2. I. Stevanović and J. R. Mosig, "Using symmetries and equivalent moments in improving the efficiency of the subdomain multilevel approach," *IEEE Antennas and Wireless Propagation Letters*, accepted for publication.

3. I. Stevanović and J. R. Mosig, "Efficient electromagnetic analysis of line-fed aperture antennas in thick conducting screens," *IEEE Transactions on Antennas and Propagation*, vol. 52, no. 11, pp. 2896–2903, Nov. 2004.

4. I. Stevanović and J. R. Mosig, "Efficient evaluation of Macro-Basis-Function reaction terms in the Subdomain Multilevel Approach," *Microwave and Optical Technology Letters*, vol. 42, no. 2, pp. 138–143, July 2004.

REFEREED CONFERENCE PAPERS

1. I. Stevanović and J. R. Mosig, "Thick slots in waveguides modeled with approximate integral equation techniques," *International Conference on Electromagnetics in Advanced Applications and European Electromagnetic Structures Conference*, Torino, Italy, Sept. 12–16, under review.

2. P. Crespo-Valero, M. Mattes, I. Stevanović, and J. R. Mosig, "A numerically stable transmission line model for multilayered Green's functions," *IEEE AP-S International Symposium and USNC/URSI National Radio Science Meeting*, Washington DC, July 3–8, 2005, accepted for publication.

3. F. De Vita, I. Stevanović, A. Freni, and J. R. Mosig, "Green's function factorization for the analysis of stratified media," *IEEE AP-S International Symposium and USNC/URSI National Radio Science Meeting*, Washington DC, July 3–8, 2005, accepted for publication.

4. K. Blagović, I. Stevanović, J. R. Mosig, and A. K. Skrivervik, "Numerical analysis of scattering by periodic apertures in conducting screens with finite thickness," *IEEE AP-S*

International Symposium and USNC/URSI National Radio Science Meeting, Washington DC, July 3–8, 2005, accepted for publication.

5. F. Nuñez, I. Stevanović, and A. K. Skrivervik, "Simulation of cavity backed 3D structures using Ewald's transformation," in *Proc. International Symposium on Antennas (JINA'04)*, Nice, France, Nov. 8–11, 2004, pp. 56–57.

6. I. Stevanović, P. Crespo-Valero, and J. R. Mosig, "Nearfield computation in planar multilayered structures," in *Proc. International Symposium on Antennas (JINA'04)*, Nice, France, Nov. 8–11, 2004, pp. 58–59.

7. I. Stevanović and J. R. Mosig, "Subdomain multilevel approach with fast mbf interactions," in *Proc. IEEE Antennas and Propagation Society Symposium (AP-S)*, vol. 1, Monterey, CA, USA, June 20–25, 2004, pp. 367–370.

8. I. Stevanović and J. R. Mosig, "Approximate full wave method for electromagnetic analysis of thick apertures," in *Proc. 17th International Conference of Applied Electromagnetics and Communications, ICECom 2003*, Dubrovnik, Croatia, Oct. 1–3, 2003, pp. 419–422.

9. K. Blagović, I. Stevanović, and A. K. Skrivervik, "Convergence of infinite periodic Green's functions for the mixed potential integral equation," in *Proc. 17th International Conference of Applied Electromagnetics and Communications, ICECom 2003*, Dubrovnik, Croatia, Oct. 1–3, 2003, pp. 423–426.

10. D. Llorens del Río, I. Stevanović, and J. R. Mosig, "Analysis of printed structures including thick slots," in *Proc. International ITG Conference on Antennas, INICA 2003*, Berlin, Germany, Sept. 17–19, 2003, pp. 165–168.

11. I. Stevanović and J. R. Mosig, "Electromagnetic analysis of planar structures with thin apertures," in *Proc. 11th Microcoll Conference*, Budapest, Hungary, Sept. 10–11, 2003, pp. 135–138.

12. I. Stevanović and J. R. Mosig, "A specially truncated set of images used for solving Green's functions for boxed planar structures," in *Proc. International Symposium on Antennas (JINA'02)*, vol. 1, Nice, France, Nov. 12–14, 2002, pp. 35–38.

13. A. K. Skrivervik, F. Nuñez, M.-E. Cabot, I. Stevanović, and J.-F. Zürcher, "Terminal antennas: developments and trends," in *Proc. Nordic Antenna Symposium, (Antenn 03)*, Kalmar, Sweden, May 13–15, 2002, pp. 13–22, invited paper.

WORKSHOP PRESENTATIONS

1. J. Iten Simões, I. Stevanović, and A. K. Skrivervik, "Interference mitigation using switched beam antennas," *COST 284 Mini-workshop*, Chexbres, Switzerland, March 2–4, 2005.

2. J. R. Mosig, I. Stevanović and F. Bongard, "Activities of the LEMA-EPFL Group within the Network Metamorphose," *First Workshop of the METAMORPHOSE Network of Excellence*, Lille - Louvain-la-Neuve, France-Belgium, Nov. 24–26, 2004.

3. I. Stevanović, F. Tiezzi, and J. R. Mosig, "Efficient electromagnetic analysis of planar structures with thick metallizations," in *Proc. 26th ESA Antenna Technology Workshop on Satellite Antenna Modelling and Design Tools*, ESTEC, Noordwijk, The Netherlands, Nov. 12–14, 2003, pp. 175–180.

4. D. Llorens del Río, I. Stevanović, and J. R. Mosig, "Analysis of printed structures including thick slots," in *COST-284 Meeting*, Budapest, Hungary, Apr. 2003.

5. J. R. Mosig, I. Stevanović, and M. Mattes, "Enhanced numerical modelling of waveguide networks and planar circuits," in *IEEE MTT-S International Microwave Symposium, Workshop: EM-based CAD and optimization of waveguide components, planar circuits and antennas*, Seattle, Washington, USA, June 2–7, 2002, invited presentation.

TECHNICAL REPORTS

1. I. Stevanović and J. R. Mosig, "Detailed design document (DDD) of the mixpatch solver," LEMA-EPFL, Technical Report, ESA-ESTEC Activity 15538/01/NL/JSC: Integrated Electromagnetic Modeling of Satellite Antennas, Aug. 2004.

2. I. Stevanović and J. R. Mosig, "Architecture design document (ADD) of the mixpatch solver," LEMA-EPFL, Technical Report, ESA-ESTEC Activity 15538/01/NL/JSC: Integrated Electromagnetic Modeling of Satellite Antennas, Aug. 2004.

3. I. Stevanović, F. Tiezzi, and J. R. Mosig, "Software user manual (SUM) of the mixpatch solver," LEMA-EPFL, Technical Report, ESA-ESTEC Activity 15538/01/NL/JSC: Integrated Electromagnetic Modeling of Satellite Antennas, Aug. 2004.

4. I. Stevanović, J. Iten, and A. K. Skrivervik, "Effect of intelligent antennas on radio system planning and on mitigation: Review of smart antenna systems," LEMA-EPFL, Task 1 Report, OFCOM Activity, Mar. 2004.

5. I. Stevanović, F. Tiezzi, and J. R. Mosig, "Software validation and verification plan (SVVP) of the mixpatch solver," LEMA-EPFL, Technical Report, ESA-ESTEC Activity 15538/01/NL/JSC: Integrated Electromagnetic Modeling of Satellite Antennas, Jan. 2004.

6. R. Koß, I. Stevanović, M. Mattes, and J. R. Mosig, "Using the Ewald transformation technique in computing potential and field Green's functions for cuboid cavities," LEMA-EPFL, Technical Report, ESA-ESTEC Activity RFQ/3-10382/02/NL/LvH, Aug. 2003.

7. I. Stevanović, F. Tiezzi, and J. R. Mosig, "Model design document (MDD) of the mixpatch solver," LEMA-EPFL, Technical Report, ESA-ESTEC Activity

15538/01/NL/JSC: Integrated Electromagnetic Modeling of Satellite Antennas, Feb. 2003.

8. I. Stevanović, F. Tiezzi, and J. R. Mosig, "Model validation plan (MVP) of the mixpatch solver," LEMA-EPFL, Technical Report, ESA-ESTEC Activity 15538/01/NL/JSC: Integrated Electromagnetic Modeling of Satellite Antennas, Feb. 2003.

9. I. Stevanović, A. K. Skrivervik, and J. R. Mosig, "Smart antenna systems for mobile communications," LEMA-EPFL, Final Report, OFCOM Activity, Jan. 2003.

10. I. Stevanović and J. R. Mosig, "Modelling of wide band dual polarization antenna arrays," LEMA-EPFL, Technical Report, ESA-ESTEC Activity 12996/98/NL/DS, WP6100, Aug. 2002.

11. E. Cabot, I. Stevanović, and J. R. Mosig, "Frequency-domain study of a printed meander antenna as an example of pre-fractal structure," LEMA-EPFL, Technical Report, European Project IST-2001-3305, June 2002.

12. I. Stevanović and J. R. Mosig, "Modelling of wide band dual polarization antenna arrays," LEMA-EPFL, Technical Report, ESA-ESTEC Activity 12996/98/NL/DS, WP4100, Feb. 2002.

13. I. Stevanović and J. R. Mosig, "Modelling of wide band dual polarization antenna arrays," LEMA-EPFL, Technical Report, ESA-ESTEC Activity 12996/98/NL/DS, WP3100, June 2001.

14. I. Stevanović and A. J. Weinstein, "Understanding the LIGO optics suspension controller electronics design," California Institute of Technology, Internal working Note of the LIGO project, Document type LIGO-T000097-00-R, Sept. 2000.